Integrated Computational Modeling of Run-Out Table Phase Transformations

by

Ry Karl

A thesis submitted in partial fulfillment of the requirements for the degree of

Master of Science

in

Materials Engineering

Department of Chemical and Materials Engineering
University of Alberta

Abstract

A thermal-microstructural model was developed to predict the effect of laminar cooling during TMCP on the through thickness microstructure of an X70 steel. Model development was conducted in three sections, beginning with microstructure modelling of dilatometer samples with cooling rates ranging from 1 - 120 ℃/s. This was followed by thermal modelling using a finite element method. The thermal and microstructure models were then unified into one using a modified form of the Scheil additive principle. Using this unified model, microstructure predictions for an industrially produced 15 mm X70 sample were made, and shown to be in good agreement with measured values.

A microstructure model was developed for the simultaneous transformation of two phases during continuous cooling. This model was used on the data acquired from dilatometry testing of samples cooled at 1-, 5-, 15-, 22-, 30-, 50-, 80-, and 120 ℃/s. As a result, transformation curves for high and low temperature phases were produced for each dilatometer sample. A combination of optical and scanning electron microscopy were then used to characterize the phases in each sample. From this, it was found that below 50 ℃/s, the primary phases were ferrite and acicular ferrite, while above this they were acicular ferrite and bainite. Model validation was done using EBSD band contrasting, where the fraction of each phase was determined based on the pattern quality of each pixel.

Thermal modelling was carried out in ABAQUS, and used to capture the effect of different laminar cooling configurations on the through thickness temperature profile. Infrared thermography and pyrometer temperature measurements were gathered during plant trials and used as model inputs, while a modified spray boiling curve was used as a fitting parameter. Assessment of infrared data lead to the observation of abnormal temperature fluctuations across the width of the skelp. A method was developed to

characterize these anomalous temperatures, and it was determined that they were the result of oxides on the skelp surface. A program in Python was developed to track the location and size of these oxides prior to coiling, and additional thermal models that included the presence of oxides were developed.

The thermal and microstructure models were then combined into one by using a modified form of the Scheil additive principle. In this approach, austenite decomposition curves were generated for predicted temperature profiles from thermal modelling, and then decomposed using the microstructure model. Validation of this combined model was done by conducting EBSD band contrasting on an industrially produced X70 sample. Once validated, the model was used to make predictions for alternate laminar cooling configurations: presence of oxides, lower coiling temperature, early cooling, and late cooling.

Based on the results from the thermal microstructure model, it was observed that changing the cooling configuration had little influence on the end microstructure. What this illustrates is the inability to produce significant changes to the microstructure through cooling. From dilatormety testing, it was shown that for this grade of steel, at cooling rates achievable on the ROT, a combination of ferrite ($\approx 80\%$) and acicular ferrite is always produced. From an industrial standpoint, these results emphasize the importance of chemistry and their pivotal role in determining the end microstructure of the steel. Further work should focus on determining how to manipulate steel chemistry to achieve desired types and fractions of phases.

Preface

This dissertation is an original work by Ry Karl. None of the text in this thesis has been published, but portions of chapter 5 were presented at the 2022 European Oxide Scale Conference. Parts of this thesis are intended to be submitted for publication.

All dilatometer testing presented in this work was done at CanmetMATERIALS, and the initial handling of this data was carried out by Maro Emakapor. The thermal model developed in chapter 4 is based on the original work by Barry Wiskel and Jonathan Prescott.

Due to the sensitivity of temperature measurements used/gathered in this project, they have all been normalized with respect to their finish rolling temperature.

"Nobody ever figures out what life is all about, and it doesn't matter. Explore the world. Nearly everything is really interesting if you go into it deeply enough"

–Richard P. Feynman

Acknowledgements

Before mentioning anyone else, I would like to express my utmost gratitude to Hani Henein who gave me the opportunity to learn and grow under his supervision. Over the past two years, I have learnt so much under your guidance, and as I move foreword in my career, I aspire to be the type of person and engineer you are. Also thank you Barry Wiskel for all those lengthy debates over ideas. I feel those meetings are where I did the most learning over these years.

To my friends and family, I could not have made it this far without you all. You have always been there for me through the good and the bad times. Mom, Dad (Steady Eddy), Travis, Dakota, Tyler, Andre, Jeff, Manny, thank you!

To all my colleagues who have become my friends, you made two more years of school not too bad. Tamara, Dylan, Marcelino, Jonas, Lucas, Quentin, Tailin, Remy, Kylian, Anne, and Anqi, I was lucky to meet you all.

Lastly, my amazing girlfriend, who through the hardest time of her life, was always there for me. Words cannot express how grateful I am to have you.

Table of Contents

List of Tables

List of Figures

Nomenclature

α	Alpha phase
β	Beta phase
ΔL	Length change
μ_p	Population mean
σ_p	Population standard deviation
τ	Incubation time
τ_o	Time constant
θ	Discretized step temperature
ζ	Phase fraction
A_{r3}	Austenite to ferrite transformation temperature upon cooling
BCC	Body centered cubic
BS	Bottom surface
CCT	Continuous cooling transformation
CHF	Critical heat flux
CL	Center line
CR	Cooling rate
CT	Coiling temperature
CTE	Coefficient of thermal expansion
d	Prior austenite grain size
$EBSD$	Electron back scattered diffraction

f	Fraction transformed
FCC	Face centered cubic
FEM	Finite element modeling
$FESEM$	Field emission scanning electron microscope
G	Growth rate
GRG	Generalized reduced gradient
$HSLA$	Hogh strength low alloy
HTC	Heat transfer coefficient
I	Nucleation rate
$JMAK$	Johnson Mehl Avrami Kologoromov
$K(T)$	Rate constant
K	Fraction transformed constant
M_s	Martensite start temperature
MA	Martensite with retained austenite
MRT	Multispectral radiation thermometry
n	Avrami constant
OM	optical microscopy
ONB	Onset of nucleate boiling
PQ	Pattern quality
Q	Activation energy
QT	Quarter line
R	Universal gas constant
ROT	Run out table
SEM	Scanning electron microscopy
t	time

$TMCP$	Thermal mechanically controlled processing
TS	Top surface
TTT	Time temperature transformation
V	Actual volume
V^e	Extended volume
w	Phase volume
XRD	X-ray diffraction

Chapter 1

Introduction

Microalloyed steels are a type of alloy produced through small additions of niobium (Nb), titanium (Ti), and/or vanadium (V), and thermomechanical controlled processing (TMCP). As a subset of high strength low alloy steels (HSLA), these materials are designed to exhibit high strength and toughness, and are used extensively in the automotive and pipeline industries [1] [2]. The mechanical properties are derived from the alloy microstructure, which is a result of both the microalloying additions, and the different stages of the production process. TMCP consists of a series of steps beginning with homogenization, followed by rough rolling, finish rolling, and then laminar cooling on the runout table (ROT). Homogenization is used to reduce micro segregation and put microalloying elements back into solution [3]. Next, rough and finish rolling are used to refine the grain size through reducing the skelp thickness [4]. Finally, the skelp is cooled from the finish rolling temperature ($\sim$ 800 ℃) to the coiling temperature (CT) ($\sim$ 550 ℃) on the ROT. The cooling rate on the ROT affects the phase transformation that occurs in the steel [5]. Changing the thermal history imposed on the ROT will result in microstructures with different mechanical properties. The ROT consists of a series of banks and headers that apply water to the surface of the skelp. To reach a specific CT, different configurations of these banks and headers are used. By altering the cooling configuration, different cooling rates are imposed on the skelp which changes its thermal

history, microstructure, and ultimately its mechanical properties. Process pyrometers are used to monitor the surface temperature after finish rolling and prior to coiling, but they cannot measure the cooling rate inside the skelp as it transits the ROT. To quantify the effect of ROT configuration on microstructural evolution, it is necessary to develop a thermo-microstructure model. This research aims to develop a thermo-microstructure model that can predict the effect of ROT cooling on X70 steel microstructure. To achieve this, the following objectives were undertaken:

1. Quantify the effect of cooling rate on phase transformations.
2. Develop a microstructure model that can predict transformations as a function of temperature and cooling rate.
3. Develop a thermal finite element model (FEM) to quantify the effect of ROT configuration on cooling rate.
4. Combine the thermal and microstructure models into a thermo-microstructure model to predict the effect of ROT configuration (cooling rate) on microstructure.

Dilatometer tests were conducted on X70 samples to determine the effect of cooling rate on the microstructure evolution. Cooling rates ranging from 1 ℃/s to 120 ℃/s were used, and the results were fit to a modified form of the JMAK equation that could handle the simultaneous transformation of multiple phases [6]. The phase fractions of each sample were then quantified using electron backscattered diffraction (EBSD) for validation.

A thermal model was developed to replicate the cooling on the ROT and determine the thermal history of the skelp. The model incorporated the different cooling mechanisms observed on the ROT, as well as a film boiling curve. Using infrared (IR) thermography, a series of videos were taken of 8-, 11-, and 12-mm gauge steel to measure the transverse

temperature profile across the surface prior to coiling. These temperature measurements were used to modify and validate the performance of the model.

From IR thermography of skelp surfaces, the presence of oxides were observed. Surface oxides have an effect on the imposed cooling rates experienced by the skelp, so a technique was developed to isolate them and track their location. Additional thermal models which account for oxides were also developed to illustrate the extent that they change cooling on the ROT.

The thermal and microstructure models were combined into a thermo-microstructure model to predict the microstructure evolution through the thickness of the skelp. For variable cooling rates encountered on the ROT, a form of the Scheil additivity principle was applied. Results from this model were validated using an X70 sample from a known ROT run, and four alternate configurations were analyzed to assess the sensitivity.

This thesis consists of 7 chapters. Chapter 2 is a literature review of the important topics regarding this research: microalloyed steels, TMCP, laminar cooling, IR thermography, austenite decomposition, and EBSD. Chapter 3 presents the steel used during this research, and the experimental techniques conducted on them. Chapter 4 examines the development and results from the thermal model. Chapter 5 presents a technique created to identify and analyze the presence of oxides on the skelp surface. Chapter 6 discusses how the thermal and microstructure models were combined into one to predict the effect of ROT cooling on the microstructure evolution. Lastly, chapter 7 presents the conclusions of this research and suggests future work to be conducted.

Chapter 2

Literature Review

In this chapter a review of microalloyed steels, TMCP, laminar cooling, IR thermography, austenite decomposition, and EBSD is presented.

2.1 Microalloyed Steels

Microalloyed steels contain niobium, vanadium, and titanium either singly or in combination, with their total weight percent not exceeding 0.1% [7]. Through these additions, steels with yield strengths in the range of 275 - 750 MPa can be produced [8]. High yield strength values are the result of the strengthening mechanisms and microstructure that is produced from microalloying elements. Alloying affects the strength through changes to dislocation densities, precipitates, solid solution elements, and grain size, but it is the latter strengthening mechanism that contributes the most [7] [9]. Certain microalloying elements also play a significant role in the austenite to ferrite transformation, which in turn effects the overall microstructure evolution.

2.1.1 Grain Refinement

The primary source of strengthening comes from grain refinement of the microstructure through carbide and nitride precipitation. During thermal mechanical processing, the

solubility of microalloying elements change leading to the formation of precipitates at different stages [7]. For grain refinement, the niobium carbides formed during rough rolling have a major influence on grain size. Niobium carbides are stable in the austenite phase at rough rolling temperatures, this leads to them pinning the austenite grains through a process called Zener drag [7]. Through having niobium carbide precipitates along the austenite grain boundaries, the surface area increases. As the austenite tries to grow, the grain boundary must distort around the precipitate which requires additional energy referred to as a pinning force. Grain growth stops when the driving force for growth is counterbalanced by the pinning force [7].

Grain refinement can also be achieved through delaying the austenite decomposition time. This can occur through the alloying additions of Mn, Mo, Ni, and Cr, each of which strongly effect the hardenability of the steel [9]. In the work of Lu et al [9], the effect of these elements and their subsequent influence on grain size strengthening were quantified as a function of steel chemistry. From this work, it was shown that with increasing $wt\%$ of each of these alloying elements, the grain size decreased linearly.

2.1.2 Effect of Alloying on Transformation Temperature

Alloying elements added to steel can be categorized as either austenite or ferrite stabilizers [4]. Elements such as carbon, nickle, manganese, and copper have been shown to stabilize the austenite phase, thus lowering the A_{r3} [1] temperature. While silicon, chrome, niobium, vanadium, and titanium stabilize the ferrite phase which increases the A_{r3} temperature. Ferrite stabilizers also slow down the phase transformation of austenite to ferrite by reducing the diffusivity of carbon in the austenite phase [4]. Furthermore, the enrichment of these elements along austenite grain boundaries can reduce their overall energy, decreasing their ability to act as heterogeneous nucleation sites for ferrite forma-

[1] Austenite to ferrite transformation temperature upon cooling

tion [10]. Hindering the austenite to ferrite phase transformation can be beneficial in microstructure design, as it can allow for the formation of a more beneficial phase such as acicular ferrite and/or bainite [11].

Focusing on the microalloying elements (niobium, vanadium, and titanium), additions of each of these have been shown to increase the formation of acicular ferrite and bainite. For higher carbon steels, additions of niobium have been shown to promote the formation of bainite during continuous cooling [10] [12]. With the addition of vanadium, at lower CTs (570 °C), the formation of acicular ferrite is observed [13]. Similarly, vanadium, titanium, and molybdenum can work together to facilitate the formation of acicular ferrite [14] [15]. In this process, the molybdenum and vanadium atoms assist in stimulating the nucleation of acicular ferrite on titanium carbide precipitates [16].

To develop models that can be applied generally to all steel types, it is important to determine equations that can capture the effect of varying alloying on austenite decomposition. In a study by Li et al [17], a computational model was created that took into account the chemical composition and prior austenite grain size to predict time-temperature (TTT) and continuous cooling (CCT) transformation curves. By solving for the isothermal kinetics of different reactions, and then applying the Scheil additive principle (reviewed in section 2.5.3), they were able to replicate both TTT and CCT curves to a good approximation, Figure 2.1. The equations used to model isothermal reactions were based on the original work by Kirkaldy et al [18], where Zener and Hillert type equations were used [17].

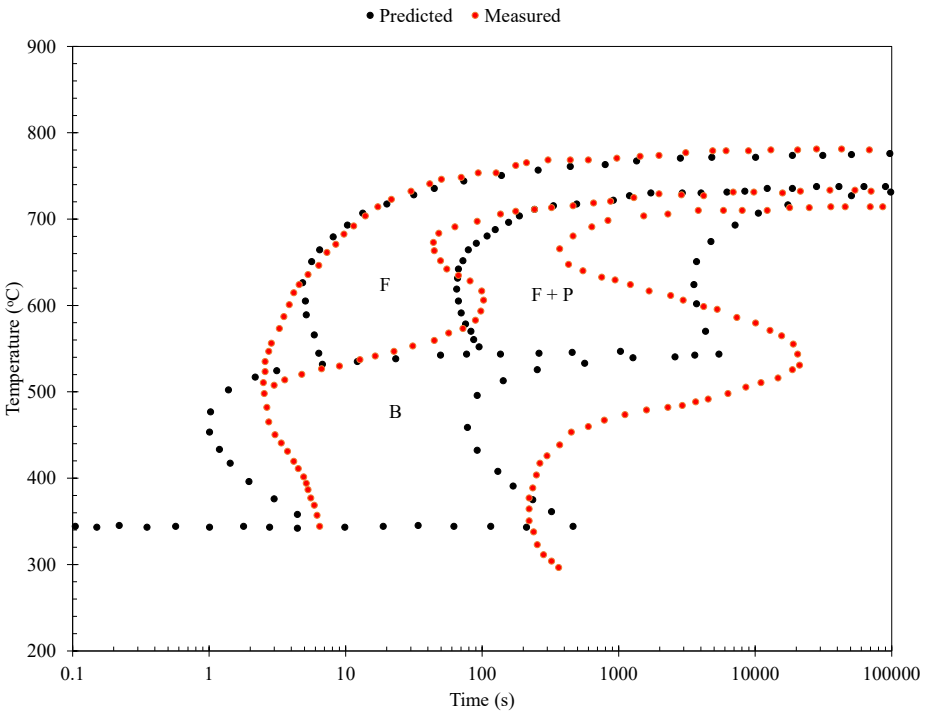

Figure 2.1: Model versus measured results for a CCT curve of 4140 steel using the model by Li et al [17]

2.2 Thermo Mechanical Controlled Processing

TMCP is a technique that allows for control of the final microstructure and thus properties of a steel skelp. During this process, the skelp piece goes through a high temperature homogenization treatment, which is then followed by rough and finish rolling, and then accelerated cooling. The temperature profile that the skelp will go through is shown in Figure 2.2, where homogenization takes place at approximately at 1200 ℃, rough rolling at 1100-1200 ℃, and finish rolling at 800-900 ℃.

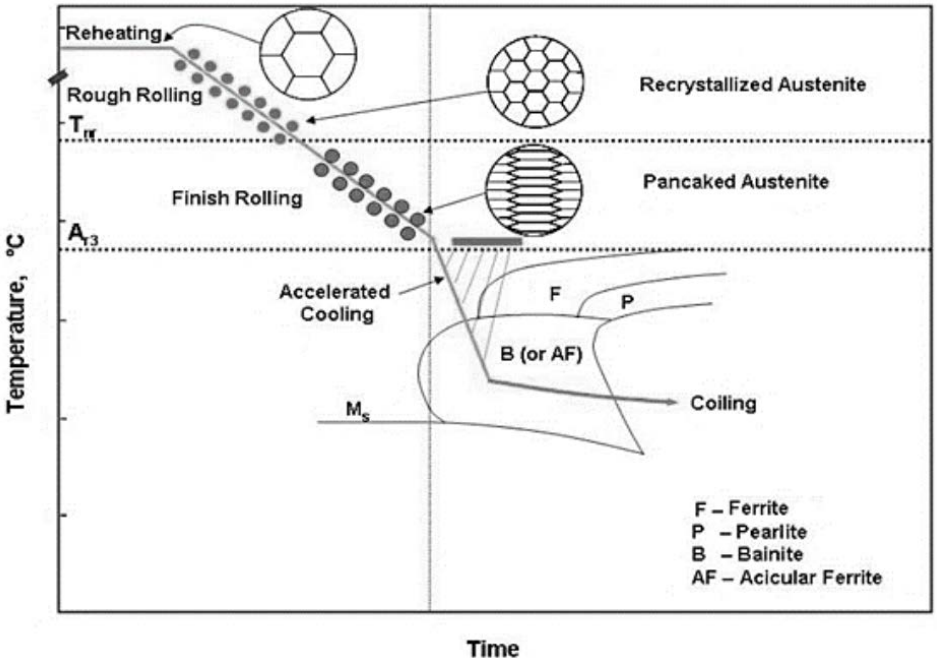

Figure 2.2: Temperature profile during TMCP [19]

2.2.1 Homogenization

The first step in the steel production process is continuous casting. During casting, liquid steel in a ladle is poured into a tundish, and then subsequently poured into a mold. The walls of the mold are cooled using water, and this leads to solidification of the liquid steel from the wall inwards. As the liquid metal solidifies, the solutes get rejected from the solid into the liquid, which results in a concentration gradient towards the center of the slab [20]. Since solidification from the mold wall occurs through the form of dendrites, the interdendritic regions are also solute rich. This rejection of solutes towards the center line of the slab is the result of the reduced solubility of alloying elements in the solid compared to the liquid. The degree of segregation can be classified as either macro or micro, where microsegregation occurs interdendriticly, and macrosegregation occurs at the centerline. Due to the segregation that occurs upon solidification, an inhomogeneous

through thickness composition is formed. To help mitigate this issue, homogenization of the slab in a reheat furnace is done. Through reheating the solidified slab at elevated temperatures (approximately 1200 °C), a localized redistribution of microsegragated alloying elements can be achieved. Although reheating helps with microsegregation, the theoretical time and temperature required to remove macrosegregation is not practical, meaning that a varying through thickness microstructure is unavoidable.

2.2.2 Rough and Finish Rolling

Following homogenization, the slab goes through a series of rolling processes aimed at refining the microstructure. The first rolling step is rough rolling at a temperature above the austenite recrystallization temperature where a majority of the thickness reduction occurs. The austenite recrystallization temperature has been shown to be significantly influenced by the Nb content in the steel [21]. As the solute content of Nb increases, the austenite recrystallization temperature increases drastically [22]. This results from both the Nb in solution and the Nb that has precipitated out to form NbC [21]. Nb in either of these forms generate a large pinning force which retards the motion of defects (dislocations, sub-grains, and grain-boundaries).

During rough rolling, various metallurgical processes are occurring such as work-hardening, dynamic recovery, and dynamic recrystallization. As the slab is plastically deformed, a portion of the energy used for deformation is stored in the steel in the form of dislocations [23]. This increase in energy associated with dislocations then provides the driving force for recovery and recrystallization. Recovery is a thermally activated process in which the strain energy is relieved through dislocation motion and reconfiguration, resulting in the formation of subgrains [23]. Following recovery, further stress relief is accomplished through recrystallization, where stress free grains are formed through

nucleation and growth along favorable subgrains [23].

Through the repeated recrystallization of deformed austenite grains at elevated temperatures, the continuous reduction of their size is achieved up until a limiting point [4]. For further reduction in grain size, the phase transformation from austenite to ferrite needs to be modified. Modification of the austenite to ferrite transformation can be achieved through finish rolling below the recrystallization temperature. By imparting deformation without recrystallization, the number of nucleation sites increases drastically [4]. Since the formation of ferritic phases are a nucleation and growth process, by increasing the nucleation and decreasing growth, smaller final grains are achieved.

The amount of deformation imparted into the steel prior to cooling will have an effect on the kinetics and CCT of the given sample. From previous research into this topic, it is suggested that an increase in deformation enhances the diffusion controlled austenite to ferrite and pearlite reactions [24] [25]. This is attributed to an increase in defects in the lattice which can help promote diffusion and serve as nucleation sites [26].

2.3 Laminar Cooling

Accelerated cooling at temperatures around the austenite transformation range is used to further refine the microstructure. This type of cooling occurs on the ROT where water is used to cool the skelp. Important parameters that must be addressed in ROT design are the skelp velocity and header type, each of which will have an impact on the cooling profile imposed. To predict the cooling during this stage, models are typically used.

2.3.1 Cooling Set-Ups

After exiting the finishing mill at temperatures between 850 - 900 °C, the skelp enters the ROT. The ROT consists of a series of banks and headers that supply water to nozzles that

expel water onto the surface of a hot skelp. Regarding the configuration of the header cooling systems, three basic set-ups are typically used: spray cooling, laminar flow, and water curtains, Figure 2.3 [27]. In a comparitative study between these configurations by Tacke et al [27], it was found that the water curtain system exhibited the highest degree of cooling efficiency, followed by laminar flow, and then spray cooling. Between each cooling system, there is also blow-off sprays that remove the water retained on the surface. This is done in order to both increase the efficiency of cooling from each bank, as well as allow the CT to be recorded with a pyrometer [28].

In the laminar cooling system, each header has the jets arranged in a 'U' shape [28] [29]. For narrow and thinner gauge material, these systems can supply adequate cooling rates, but struggle with wider and thicker gauges [29]. This is due to the non-uniform cooling it imposes, and its lower cooling capacity. For water curtains, along with their high cooling efficiency, they also have the the added benefit of improved uniform cooling in the transverse direction [30]. Although the high cooling capacity can be good for thicker gauge material, it can also be a drawback when cooling thinner gauges. Due to cooling efficiencies and times at the top and bottom surface, buckling is a common problem associated with this cooling system [29].

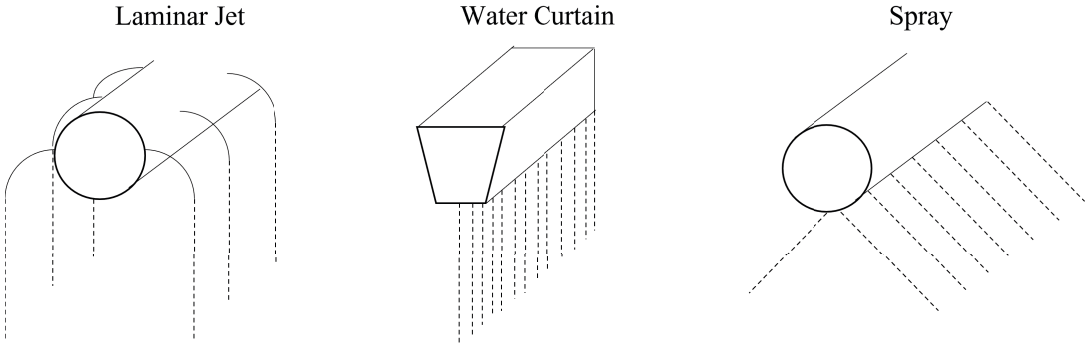

Figure 2.3: Different cooling configurations [31]

2.3.2 Cooling Mechanisms

As the skelp enters the ROT from the finishing stands, it goes through various cooling mechanisms as a result of its interactions with both air and water. In the regions where there is no exposure to water, the primary cooling mechanisms are convection and radiation. Directly underneath each header nozzle, multiple cooling mechanisms are taking place, namely single phase convection, nucleate boiling, transition boiling, and film boiling. A general schematic of the expected cooling regimes is shown in Figure 2.4.

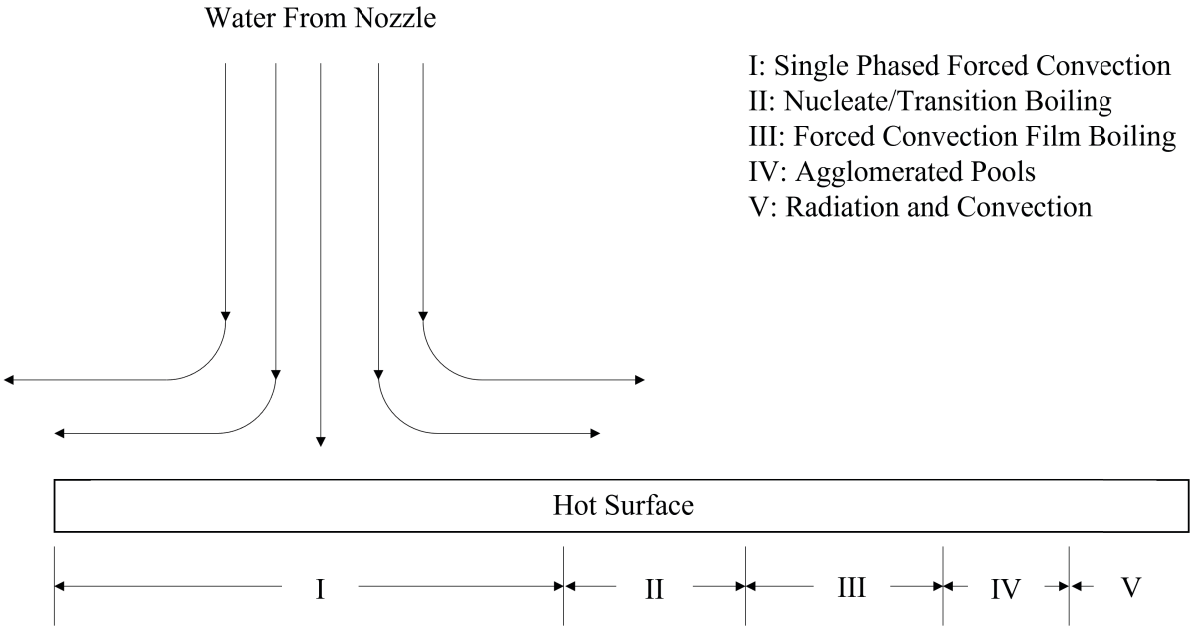

Figure 2.4: Expected cooling mechanisms produced from water jet impingement [32]

Referring to Figure 2.4, the region labelled (I) is the impingement zone in which the dominant mechanism of heat transfer is single phase forced convection. For this cooling mechanism, there is no boiling, and it is the result of the excess temperature (difference between surface temperature and liquid saturation temperature) being equal to or less than the saturation temperature of the liquid [33] [34]. The saturation temperature is the temperature needed for a liquid to boil and turn into a vapor.

As the excess temperature increases, a transition point called the onset of nucleate boiling (ONB) is reached, region (II). In this region, bubbles begin to detach from the skelp surface and induce a stirring action in the liquid [33] [34]. From this assisted motion, the heat transfer coefficient begins to rise. With increasing excess temperature, the bubbles begin to coalesce until a maximum heat transfer coefficient is reached; critical heat flux (CHF).

After the CHF is reached, a vapor film layer begins to develop which acts like an insulating layer that decreases the heat transfer coefficient, region (III) [33] [34]. This heat transfer mechanism usually takes place after the transition region where nucleate boiling changes to film boiling. Once the minimum heat flux, Leidenfrost, point is reached, a fully developed vapor layer separates the liquid from the surface. The vapor layer separates the liquid from the surface, and the heat transfer mechanism changes to both radiation and conduction [34].

As the distance from the stagnation point increases further, the water begins to agglomerate into pools, region (IV). This is due to the surface tension between water molecules causing them to pool on top of vapor layer previously formed [32]. In this region, heat loss is from convection between the vapor and skelp surface, and radiation from the exposed surface below the pool [32].

For the last region (V), the surface is not wet from the nozzle. Due to there being no water on the surface, heat is only transferred by radiation and convection to the surrounding [32].

Important for each of these mechanisms is the heat flux associated with them, which is a measure of the thermal energy transferred per unit time and area. To calculate heat flux, the corresponding heat transfer coefficient must be known for each region. In the radiation and convection regions, the effective heat transfer coefficient has been shown to vary between 100 - 200 Wm^{-2} depending on the air velocity [35]. For film boiling regions,

a spray cooling curve such as the one developed by Wendelstorf et al [36] can be used. Figure 2.5 illustrates a spray cooling boiling curve where convection (I), nucleate boiling (II), transition boiling (III) and film boiling (IV) regions and their corresponding heat transfer coefficients can be observed. For impact/impingement regions, the cooling is more complex, as multiple mechanisms are occurring. Various studies have investigated the magnitude of cooling in these regions, and results suggest the heat flux ranges between 10 - 12 MWm^{-2}, while the impact size is approximately two times the size of the nozzle [37] [38].

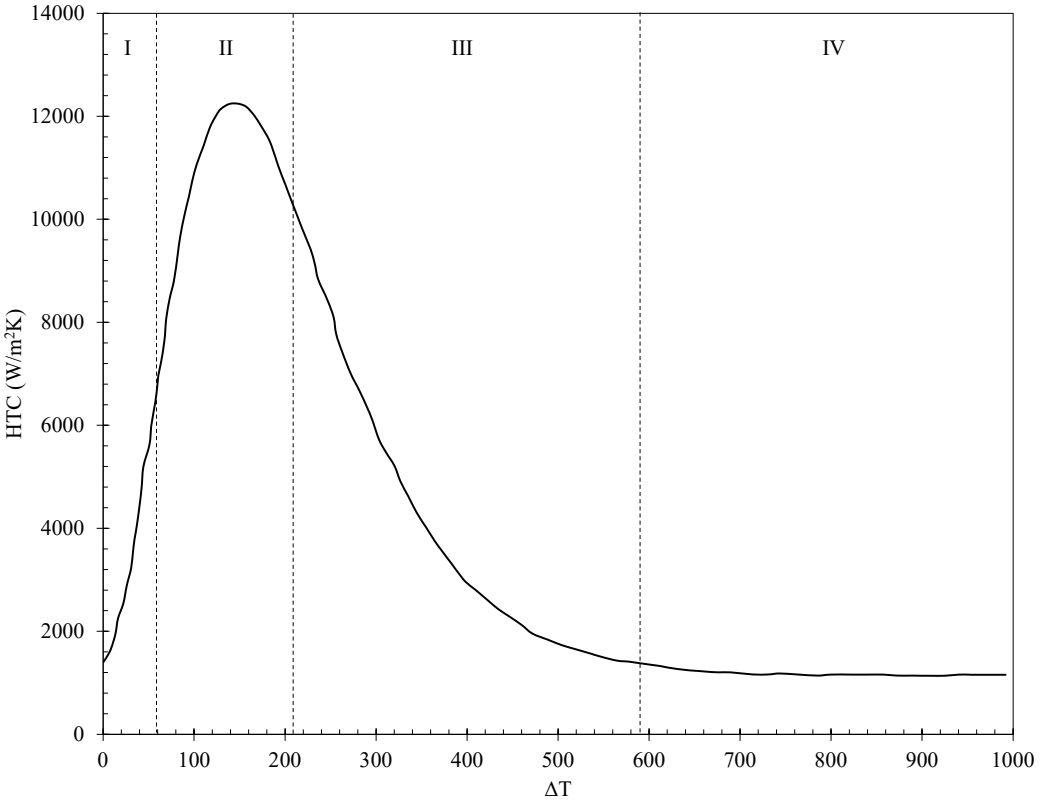

Figure 2.5: Spray cooling boiling curve for water [36]

2.3.3 ROT Models

As a result of the retained water on the skelps surface, and the vapor produced during cooling, it is difficult to measure the surface temperature of the skelp on the ROT. Instead, models have been developed to predict the time - temperature history of the skelp. Typically either finite difference or finite element methods are employed. Regardless of the method employed, one form of the heat equation (1-, 2-, or 3D) along with appropriate boundary conditions is used. Equation 2.1 shows the 3D version of the heat equation. Shown in Figure 2.4, there is also expected to be three unique types of cooling on the skelp surface with them being impingement (impact), film, and radiation. These cooling mechanisms define the boundary conditions that are used to solve the heat equation. Equations 2.2, 2.3, and 2.4 represent the boundary conditions for impingement, film, and radiation cooling. In these equations, ρ is the material density, c is the specific heat, T is temperature, t is time, k is the thermal conductivity, q is the rate of heat generation from transformation, Q is heat flux, and h is the heat transfer coefficient, ε is the Stefan-Boltzman constant, and σ is the emissivity.

$$\rho c\frac{\partial T}{\partial t} = \frac{\partial}{\partial x}(k\frac{\partial T}{\partial x}) + \frac{\partial}{\partial y}(k\frac{\partial T}{\partial y}) + \frac{\partial}{\partial z}(k\frac{\partial T}{\partial z}) + q \tag{2.1}$$

$$Q_{impact} = h_w(T - T_w) \tag{2.2}$$

$$Q_{film} = h_v(T - T_v) \tag{2.3}$$

$$Q_{radiation} = \varepsilon\sigma(T_s^4 - T_\propto^4) \tag{2.4}$$

In the study by Mukhopadhyay et al [39], a finite difference model based on the 1D heat transfer equation was used to describe the cooling on the ROT for a HSLA steel. For their model, three different heat transfer regimes were identified: radiation and convection between the finishing mill and first bank and the last bank and coiler, convection cooling from water jets, and conduction within the strip. Since the heat transfer in the longitudinal and transverse directions of the skelp were deemed substantially smaller than through the thickness, they were ignored. A film boiling curve was used to determine the heat transfer coefficient at the interface between water and skelp. In development of their model, the strip was first discretized into slices from top to bottom. The following assumptions were then made: heat flows from adjacent slices, the temperature of a slice is constant, and between two slices heat is transferred through conduction.

In the work by Serajzadeh [40], a finite element method was used to solve the 2D heat transfer equation for a low carbon steel. Similar to Mukhopadhyay et al [39], heat conduction was ignored in the longitudinal direction. Boundary conditions were defined for the jet impingement and film boiling zones, and the initial condition of the skelp was assumed to be equal to the exit temperature from the finishing mill. In addition, using the predicted temperature - time and cooling rate information simulated, microstructure predictions were made. This was done using the isothermal form of the Avrami equation and Scheil additive principle (section 2.5.3) in correlation to the material TTT.

In a similar approach as Serajzadeh, Wiskel et al [41] developed a 2D FEM in $ABAQUS/CAE^{TM}$. Three boundary conditions were used in this method compared to the two in the previously aforementioned 2D model. While both the impingement and film convection boundaries were applied, an additional radiation boundary was included, equation 2.4. Through inclusion of this third boundary condition, a more accurate representation of all the cooling mechanisms on the ROT was achieved. A film boiling curve adopted from Wendelstorf et al [36] was used to calculate the heat transfer coefficient

in the film boiling regime, while the jet impingement heat flux was used as a fitting parameter. Both the results and the validation of this model are shown in Figure 2.6.

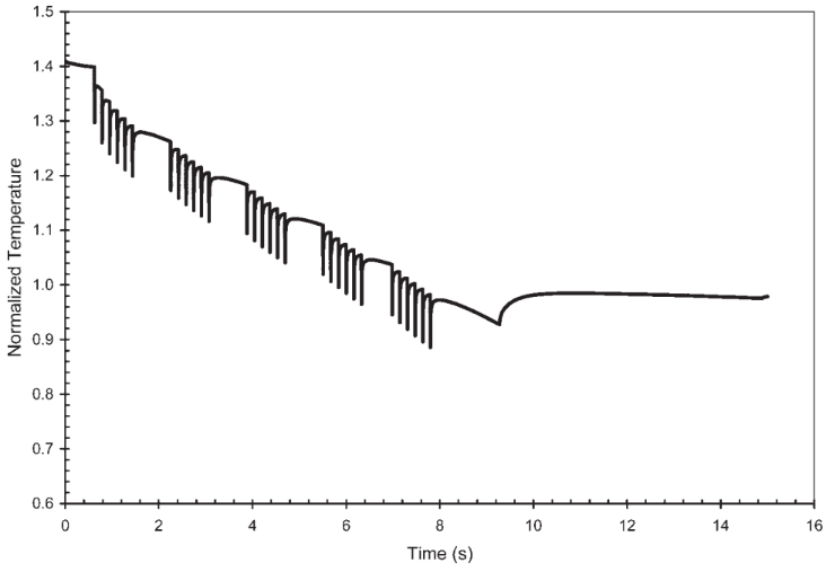

(a)

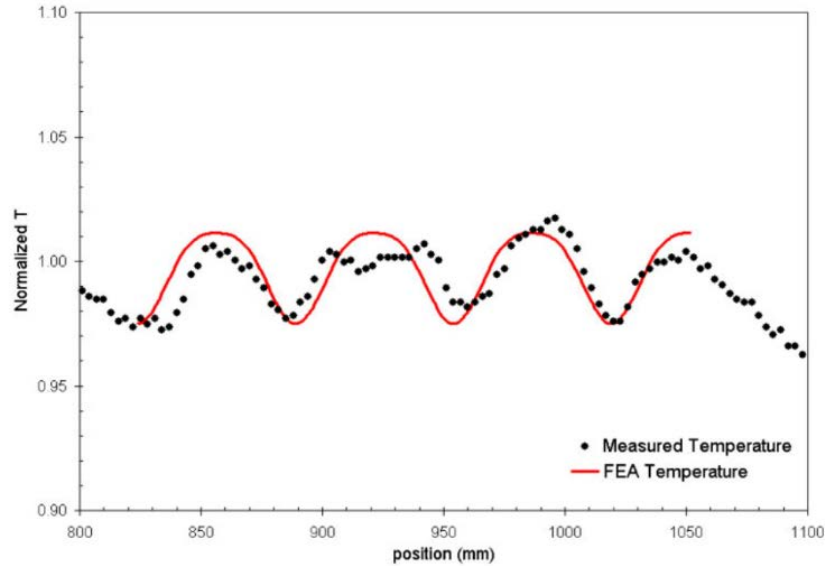

(b)

Figure 2.6: ROT model results (a) and validation (b) of time - temperature history

2.4 Infrared Thermography

IR thermography is a non-contact technique used for temperature measurement and visualization. It works through capturing the thermal radiation emitted by an object, and then converting the signal to an image [42]. IR radiation is a type of electromagnetic wave that has a wavelength range between 780 nm to 1 mm [43]. Only discrete bands within this spectrum can be utilized for imaging, and they are long wave (8 - 14 μm), mid-wave (3 - 5 μm), and short-wave (0.9 - 1.7 μm) [43]. By only detecting radiation in certain bandwidths, the influence of background radiation has minimal effect on measurements, specifically carbon dioxide, water vapor, and ozone [43].

2.4.1 Oxide and Steel Emissivity

The thermal radiation emitted from an object is a function of emissivity, which is the ability to radiate thermal energy compared to a blackbody. Emissivity is material-specific, which means that materials at the same temperature can exhibit different values of this property [43]. Other intrinsic factors that may affect this property include the surface condition and the measurement angle [43]. As an intrinsic property, emissivity can be used as a characterization tool to delineate between different materials [43] [44]. In the context of TMCP, oxidation regularly occurs on the surface of the skelp [45] [46] [47]. The oxide develops in various ways depending on the process parameters (roll deformation, CT, etc), which leads to varying end thicknesses [48] [49]. Due to the differences in emissivity between steel and oxides, the presence of these materials on the surface can be identified with IR thermography [50].

Depending on the point in the process that the oxide forms, it can be classified as either primary, secondary, or tertiary [51] [52]. Primary scale is formed during homogenization. This oxidation type is the most significant of the three due to the high temper-

ature and times associated with it, which leads to the oxide exhibiting strong interface bonding with the steel [51]. Upon entry into the roughing mill, the roughing descaler removes primary scale on the surface. Secondary scale continuously grows between deformation passes, and is either descaled after a a certain amount of passes or prior to finish rolling. Finally, during finish rolling, cooling, and coiling, a tertiary scale forms. Figure 2.7 shows the expected morphology of primary (a) and secondary (b) oxides [51]. Primary scale appears as large jagged teardrops, while secondary scale can look like either slightly jagged teardrops or smooth teardrops [51]. The scale that forms at each of these steps takes on a layered structure with a Wustite (FeO) inner layer, Magnetite (Fe_3O_4) middle layer, and Hematite (Fe_2O_3) outer layer [53] [54] [55] [56].

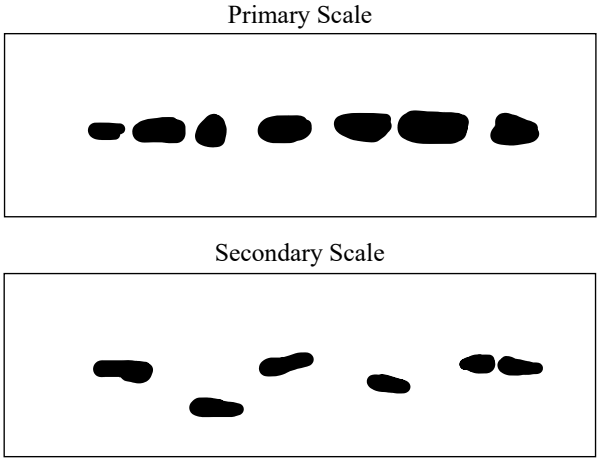

Figure 2.7: Expected morphology of primary and secondary scale [51] [57]

In a study by Campo et al [57], the emissivity of different thicknesses of oxides was investigated. Emissivity measurements were taken using a previously developed experimental device by the same author [58]. The newly developed device allowed for evaluation of emssivity values as a function of temperature for changing surface conditions. For a full description of the device design and functionality, refer to the authors paper [58]. Several disk shaped (66 mm diameter and 3 mm thick) Armco iron samples were pre-

pared by manually polishing down to 1000 grit and then cleaned in an acetone ultrasonic bath. The final surface roughness of each sample was approximately $0.083 \pm 0.006 \mu m$ and the emissivity of each sample was stabilized by annealing at 700 °C for 15 minutes in a $N_2 + 5\% H_2$ atmosphere. Oxygen was then slowly introduced to initiate oxidation. At four different temperatures (415, 480, 535, and 570 °C) the oxide emissivity was calculated as a function of thickness. After the pre-oxidation state (time t = 0), the emissivity exponentially increased until a maximun [57]. Following the maximum, as the thickness continued to increase, the emissivity exhibited a series of localized minima and maxima, Figure 2.8. Shown in Figure 2.8, after sufficient times, the emissivity of the oxide was always between the range of 0.75 - 0.85 (apart from 16 μm). The oxides were characterized through x-ray diffraction (XRD) which showed a predominately magnetite with a smaller amount of hematite composition.

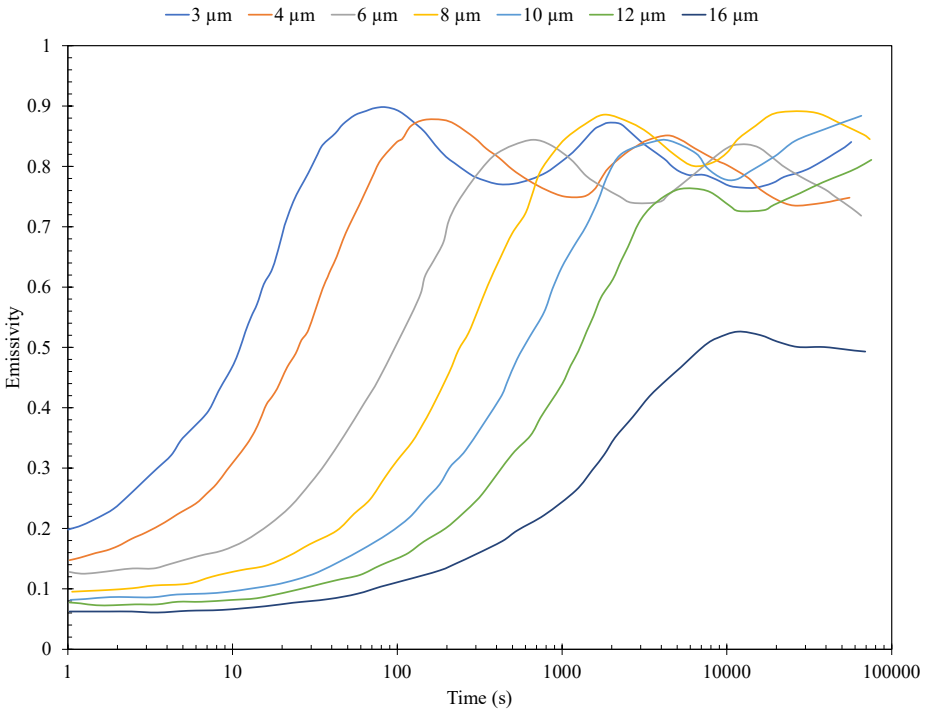

Figure 2.8: Iron oxide emissivity as a function of thickness at 480 °C [57]

Wen et al [59] investigated the emissivty behaviours of AISI 420, AISI 630, AISI H10, AISI H13, AISI A2, and AISI A6 steels under varying temperatures using multispectral radiation thermometry (MRT). Depending on the steel grade, temperature, and wavelength, large variances in emissivity were observed. In general, emissivity was shown to decrease with both decreasing temperature and/or increasing wavelength. Regarding the effect of chemistry, it was shown that chromium had the largest influence where higher contents resulted in lower observed emissivity values. This was suspected to be occuring due to the variations in oxidation behaviour on the steel surface. For the alloy with the closest chrome content to X70 (AISI A6), the reported emissivty value using a wavelength of 3 μm was approximately 0.82 [59].

2.4.2 Oxide Removal

Oxides are continuously removed from the skelp surface by descalers positioned before each rolling stage and across the width of the skelp. The typical descaler is a high-pressure water jet directed onto the skelp surface. Scale is removed by the physical impact of the water with the surface oxides and flashing [28]. A general schematic of a rough rolling descaler is shown in Figure 2.9, where the approximate nozzle spacing, spray width, and overlap are denoted as A, B, and C respectively. To maximize coverage over the skelp width, flat fan nozzles are used in descaling operations, where their performance is influenced by the specific standoff, pressure, flow rate, and nozzle configuration [28]. These nozzle parameters will all contribute to the resulting impact pressure which dictates the removal of oxides. Flat fan nozzles are advantageous over other styles, as they can produce a uniform impact pressure at proper standoff distances [28].

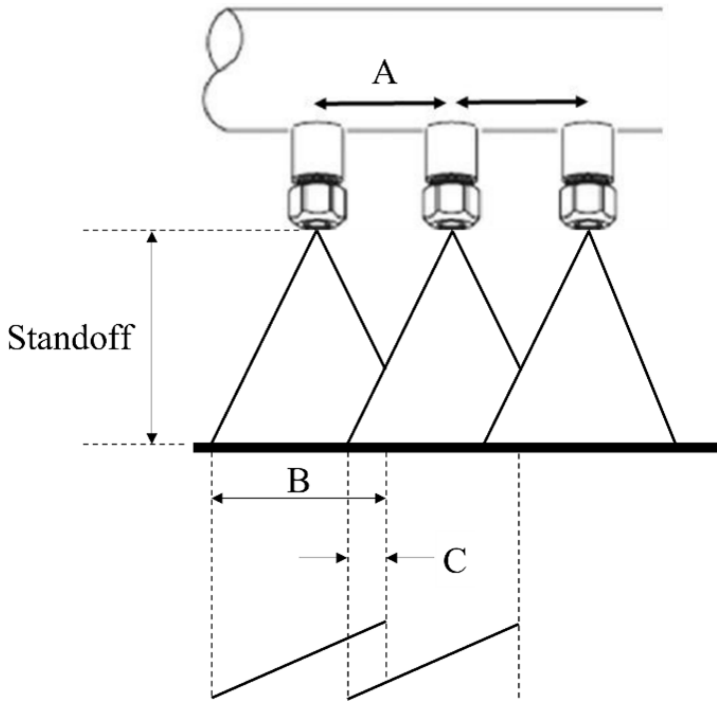

Figure 2.9: General schematic of three flat fan descaler nozzles

However, as shown through industrial observations, descalers are not capable of eliminating the problem of oxides completely [41] [60]. Interference between the spray from adjacent nozzles can result in so called overlap and washout regions where decreased descaling efficiency is observed [61] [62]. Furthermore, the ability of the descalers to remove the continuously formed oxides during TMCP has been shown to be influenced by processing parameters and strip chemistry [63] [64]. Both these variables effect the subsequent adhesion of the oxide to the strip surface. Oxides that are not removed prior to deformation steps also have the potential to exhibit enhanced adhesion, which results in decreased descalability [65]. Increased adhesion is due to the high plasticity of the oxide at elevated temperatures [66] [65]. Improper descaling can be problematic as it can have an effect on the imposed cooling profiles experienced on the ROT, resulting in regions of differing microstructure and mechanical properties [67] [68]. This is due to differences in thermal properties between oxides and steels.

2.5 Austenite Decomposition

To characterize the mirostructural evolution that occurs on the ROT, an understanding of the possible phases and mechanisms for which they form is needed. This can be accomplished by analyzing the phase diagram, TTT, and CCT curves for a given steel. Furthermore, to account for the cooling conditions on the ROT, an understanding of the relationship between isothermal and non-isothermal transformation kinetics is needed. First the thermodynamic stability of the steel phases will be presented.

2.5.1 Phase Diagrams

A phase diagram shows the thermodynamic stability of different phases for a given range of temperatures and compositions. Figure 2.10 shows a $Fe-Fe_3C$ phase diagram, where it can be seen that for TMCP steps prior to cooling, the equilibrium phase is austenite (above 850 °C at 0.2 wt% C). As the austenite is cooled below the A_3 temperature [2], ferrite begins to form. Further cooling to below the A_1 temperature [3] then results in the formation of pearlite. Since the phase diagram assumes equilibrium, it does not consider the kinetics (time) for different phase transformations. This leads to the omission of phases such as acicular ferrite, bainite, and martensite from showing up on it. Since cooling on the ROT is far from equilibrium, phase diagrams are not appropriate tools to model microstructural evolution. Instead, TTT and CCT curves which account for the kinetics of phase transformations can be used.

[2] Austenite to ferrite transformation temperature
[3] Austenite to pearlite transformation temperature

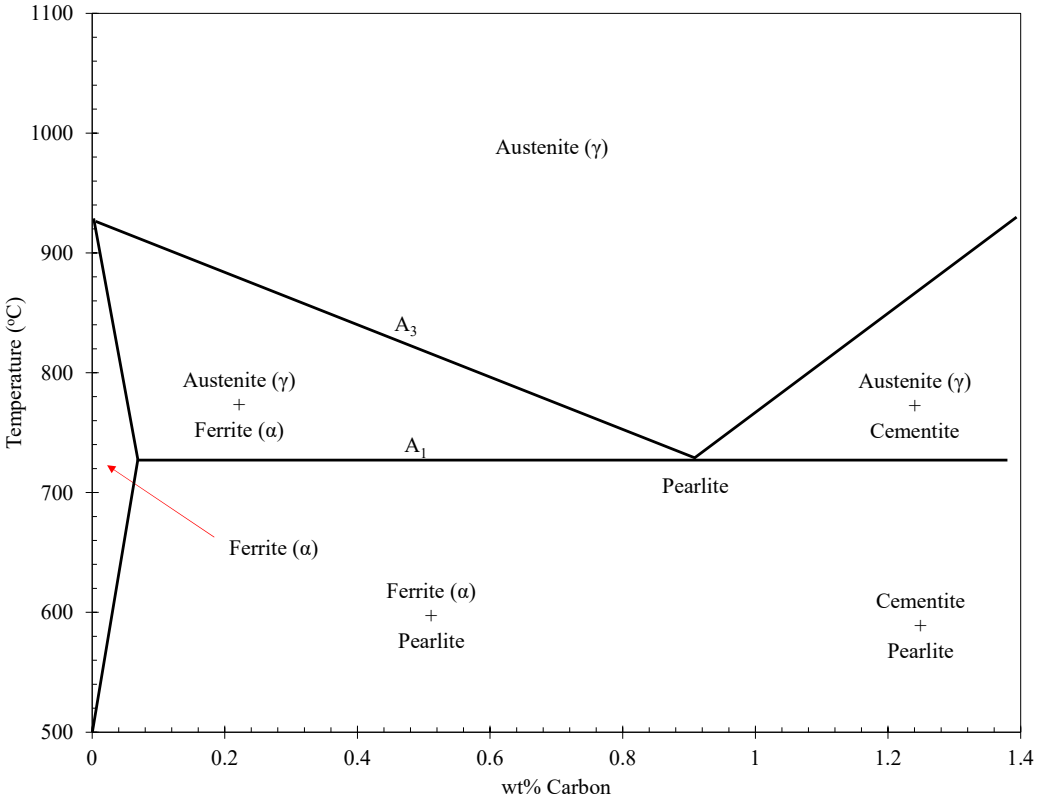

Figure 2.10: Iron - carbon phase diagram [69]

2.5.2 Isothermal Transformation

A TTT diagram is an isothermal plot of fraction transformed as a function of time and temperature. Figure 2.11 (a) shows a TTT diagram for an X70 steel (constructed using the model by Li et al [17]), where the production of multiple sections is the result of the different transformation mechanisms that can occur at varying temperatures. For the austenite to ferrite transformation, the reaction can either proceed in a reconstructive, displacive, or combination of the two manner. In the context of X70 steel microstructure, only the top (reconstructive 570 °C - 850 °C) and middle (combination 500 °C - 570 °C) regions of this diagram are of concern, as displacive phases such as martensite are minimal. For these transformations, different phases form through a nucleation and

growth mechanism. These two factors primarily influence the shape of the TTT curve, giving it a characteristic 'C' shape which reflects the variation of nucleation and growth with temperature [70].

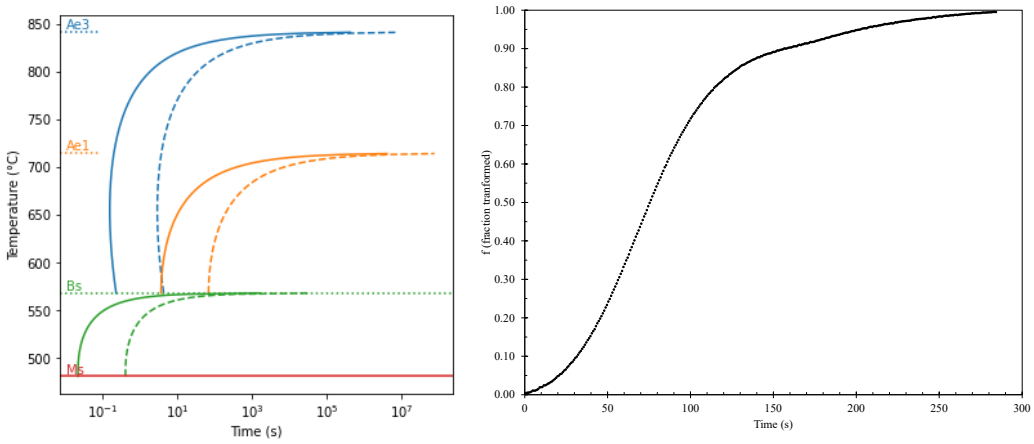

(a) **(b)**

Figure 2.11: TTT for a HSLA steel constructed using the model by Li et al [17] (a) and the sigmoidal isothermal transformation curve (b)

When modelling the kinetics of an isothermal phase transformation, assumptions regarding the type of nucleation and growth needs to be made. There are two predominate types of nucleation typically used in modelling and those are the constant rate and site-saturation modes [70]. In the constant nucleation and growth mode, nuclei continuously form throughout the transformation, while in site-saturation, all the nuclei are formed at the beginning [70]. Regardless of the mode assumed, the end equation used to model the sigmoidal curve shown in Figure 2.11 (b) takes the form of equation 2.5 which is the general Johnson–Mehl–Avrami–Kologoromov (JMAK) equation [71] [72]. In this equation, t is the time at the isothermal temperature, τ is the incubation time, $k(T)$ and $n(T)$ are rate constants, and f is the fraction transformed.

$$f = 1 - exp(-k(T)(t-\tau)^{n(T)}) \tag{2.5}$$

To account for the different austenite conditions that may occur during TMCP, various adaptations of equation 2.5 have been made. In a study by Chen et al [73], the isochronal phase transformation of austenite to ferrite was investigated. JMAK kinetics were employed, but the effect of site-saturation, alternating growth methods (interface and diffusion), and impingement of nuclei were also incorporated into the model [73]. Umemoto et al [74] incorporated the effect of austenite grain size on the decomposition kinetics into pearlite, equation 2.6. In this adaptation, d is the austenite grain size, and m is a constant related to the nucleation mode: 1 = surface, 2 = edge, and 3 = corner.

$$f = 1 - exp(-k(T)\frac{t^n}{d^m}) \tag{2.6}$$

It can be assumed that the formation of product phases occur in either a sequential or simultaneous manner, with the former case being less likely [6]. Jones et al [6], modified the JMAK equation to account for the simultaneous transformation of two or more phases. As this model is used for this work, a thorough walk through of the modification is presented, where a derivation of the JMAK is first presented.

When a product phase particle first nucleates after time τ, and subsequently grows, the volume (w) of the phase after time t is given by equation 2.7. In this equation, G is the growth rate and the phase shape is assumed to be spherical.

$$w_t = (\frac{4\pi}{3})G^3(t-\tau)^3 \tag{2.7}$$

As multiple product phase particles continue to grow, they will eventually impinge on one another [70] [6]. This aspect of nucleation and growth can be accounted for by first calculating the extended product phase volume, equation 2.8. In this equation, V_β is the volume of phase β, V is the total volume, I is the nucleation rate, and $d\tau$ is the time interval.

$$V_\beta = (\frac{4\pi V}{3}) \int_{\tau=0}^{t} G^3 I (t-\tau)^3 d\tau \tag{2.8}$$

The nucleation and growth that occurred in already transformed regions can then be omitted by calculating the actual volume. This is accomplished through introducing a probability factor that is proportional to the amount of un-transformed parent phase available at any instance during the reaction, equation 2.9. In this equation, dV_β^e is the rate of extended volume change of product phase β. The integrated form of equation 2.9 can then be substituted into equation 2.8 to yield the classic JMAK equation for a spherical product phase, equation 2.12.

$$dV_\beta = (1 - \frac{V_\beta}{V}) dV_\beta^e \tag{2.9}$$

$$V_\beta^e = -V ln(1 - \frac{V_\beta}{V}) \tag{2.10}$$

$$-ln(1 - \frac{V_\beta}{V}) = (\frac{4\pi}{3}) G^3 \int_0^t I (t-\tau)^3 d\tau \tag{2.11}$$

$$\zeta_\beta = \frac{V_\beta}{V} = 1 - exp(-\frac{1}{3}\pi G^3 I t^4) \tag{2.12}$$

Equation 2.12 is appropriate for multiple product phases when the reaction occurs sequentially, but when it is simultaneous, the addition of an α phase to the probability proportionality factor can be done [6]. Both product phases can then be related through a constant K which eliminates the need to analytically/numerically solve the final phase fractions [6]. The final equations for the volume fraction of α and β following the same procedure for one phase are then represented by equations 2.13 and 2.14.

$$\zeta_\alpha = (\frac{1}{1+K})(1 - exp[-\frac{1}{3}(1+K)\pi G_\alpha^3 I_\alpha^3 t^4]) \tag{2.13}$$

$$\zeta_\beta = (\frac{K}{1+K})(1 - exp[-\frac{1}{3}(\frac{1+K}{K})\pi G_\beta^3 I_\beta^3 t^4]) \tag{2.14}$$

2.5.3 Non-Isothermal Transformation

A CCT curve is used to illustrate phase transformations under non-isothermal conditions (cooling). To construct these types of curves, the ideas utilized in isothermal kinetics can be extended. This is done through two different approaches, either modifications to the JMAK equation, or applying the Scheil additive principle along a cooling path.

In a study by Venkatraman et al [75], the development of a CCT diagram was done through use of a modified JMAK equation on dilatometric data. Equation 2.15 shows the form of the JMAK equation used, where τ was calculated using an Arrhenius equation, equation 2.16. For the model, the constants Q and R were the activation energy and universal gas constant, respectively, and a site-saturation mode was assumed. Using a linear regression method, the constants were solved for and found to be in good agreement with literature (n was between 0.52 and 1, and Q was between 88 kJ and 188 kJ) [75]. Although values for τ were not reported, the magnitude of it was stated to be high meaning that transformation above equilibrium temperatures was not possible [75].

$$f = 1 - exp(-(\frac{t}{\tau})^n) \tag{2.15}$$

$$\tau = \tau_o exp^{\frac{-Q}{RT}} \tag{2.16}$$

The more common approach to non-isothermal transformations is the application of the Scheil additive principle. A vast number of studies rely on this method in order to approximate transformations along arbitrary cooling paths as the sum of short isothermal holdings [76] [77] [78]. Figure 2.12 shows the discretization of a arbitrary cooling path and how it relates to isothermal kinetics (TTT).

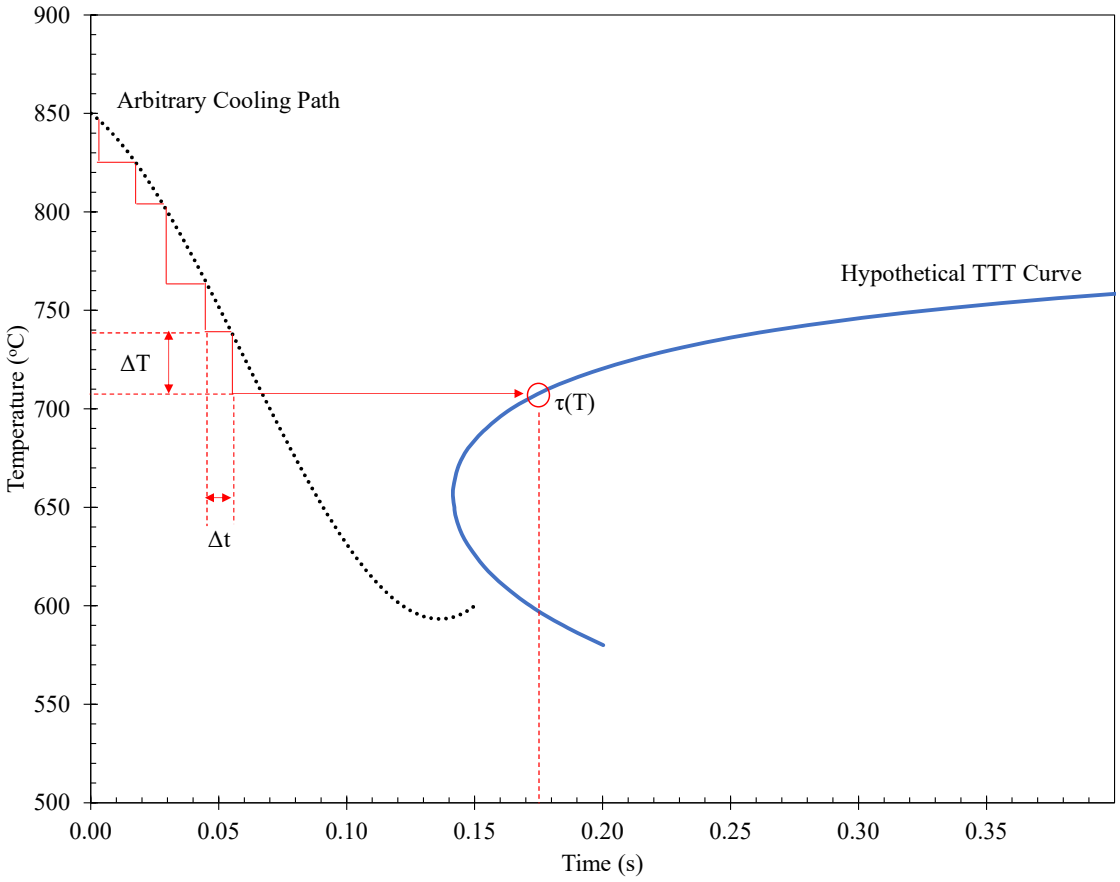

Figure 2.12: Approximation of arbitrary cooling path as small isothermal steps

In this process, the cooling path is first divided into a series of temperature steps (ΔT) with a corresponding time step (Δt). At each step, the isothermal incubation time ($\tau(T)$) required to transform a given amount of parent phase is given by the corresponding TTT, and can be used to calculate the fractional incubation time [76]. This is done by dividing

the time step by the isothermal incubation time at each temperature along the cooling path. When the sum of these fractional incubation steps equal unity, the transformation begins. This process can be expressed by equation 2.17 and 2.18.

$$f(T) = \sum_{T_e}^{T} \frac{\Delta t}{\tau(T)} \tag{2.17}$$

$$\int_{t=0}^{t=tn} \frac{dt}{\tau(T)} = \int_{T_e}^{T} \frac{dt}{dT} \frac{dT}{\tau(T)} = 1 \tag{2.18}$$

Equation 2.18 can then be inserted into the JMAK equation to yield an expression that can be used to calculate the the fraction transformed at a given temperature along an arbitrary cooling path, equation 2.19. In this equation, $Q(T)$ is the temperature dependant cooling rate and T_e is the end temperature.

$$X(T) = 1 - exp(\int_{T}^{T_e} (\frac{K(T)^{\frac{1}{n}}}{Q(T)} dT)^n \tag{2.19}$$

For a transformation to be additive, there are certain criteria that need to be met. Regarding equation 2.5, a proof conducted by Agarwal et al [79] was done where it was shown that if n is constant (not a function of temperature), then additivity applies. When the value of n is constant, the reaction is considered isokinetic, meaning that the the nucleation, growth, and impingement mechanisms during the transformation do not vary [80]. The criteria for additivity was further expanded on by the work of Christian [81] who proposed that additivity applies when the instantaneous transformation rate is a separable function of both temperature and fraction transformed, equation 2.20.

$$\frac{dX}{dt} = f(X)g(X) \tag{2.20}$$

2.6 Characterization With EBSD

EBSD is a quantitative analysis tool that can be used to characterize microstructure. Through the interaction of backscattered electrons with the crystallographic structure of the material, Kikuchi patterns are formed. Based on these Kikuchi patterns, information about the phases present can be determined.

2.6.1 Band Contrast

Different phases can be delineated from one another using the band contrast of the mapped regions. Band contrast is a measure of the diffraction pattern quality (PQ), and has been used extensively for characterization of austenite decomposition products [82] [83] [84] [85]. Depending on the PQ of the scan, the contrast of the pixels varies, where darker regions indicate poor pattern quality. Poor PQ can result from high dislocation densities which reduce the average intensity of the Kikuchi bands [83]. Based on this, the phases of ferrite, bainite, MA, and acicular ferrite can be distinguished between one another [83]. As the transformation temperature decreases, there is an observed increase in the intrinsic dislocation density of the product phase [85] [86], Figure 2.13. This is attributed to the different mechanisms by which each phase is formed. At higher temperatures, reconstructive phase transformations occur, resulting in polygonal and non-polygonal ferrite microstructures with low dislocation densities. As the transformation temperature decreases, quasi-displacive and displacive mechanisms occur resulting in acicular, bainitic, and martensitic microstructures with high dislocation densities [85] [86]. Based on this trend, the expected order of lowest to highest dislocation density for the phases would be polygonal ferrite, non-polygonal ferrite, acicular ferrite, bainite, and then martensite [85] [87] [88] [86].

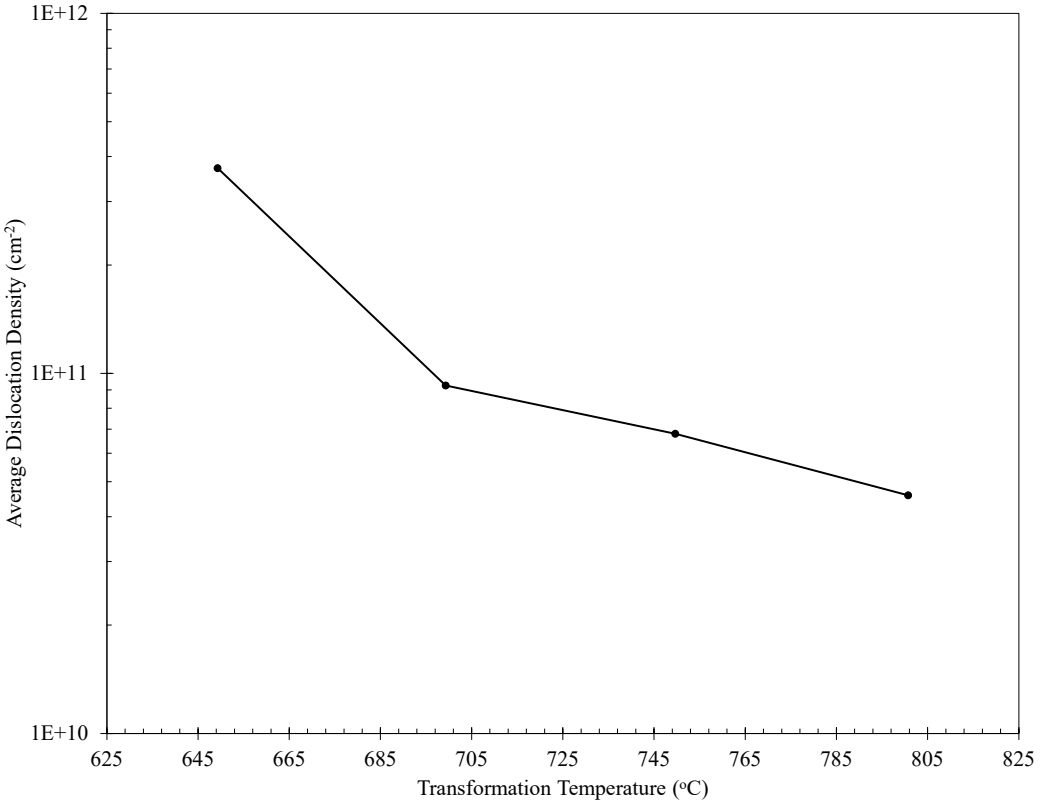

Figure 2.13: Variation in dislocation density for Fe-0.21Ti-0.08C phases as a function of transformation temperature (°C) [89]

When utilizing PQ to discriminate between phases, there are many user controlled factors that will influence the quality of the data. The major factors include the surface finish and the step size. Since the sample is typically tilted 70° and the interaction volume is small, the PQ is sensitive to any surface defects. The step size will also dictate the ability to resolve the finer details in the microstructure. A small step size will allow for full resolution of smaller features, but will result in excessively long test times. While a large step size will result in exclusion of the finer details needed for full characterization.

2.7 Summary

As described in this chapter, the final microstructure is a function of all the processing steps involved in TMCP, with the most important being the laminar cooling on the ROT. All steps prior to cooling condition the austenite for the subsequent phase transformations. Deviation from the expected microstructure (and thus properties) may occur when there are disruptions to the temperature profile imposed on the steel while traversing the ROT. Things that may disrupt the cooling profiles include improper ROT configurations or the presence of oxides on the surface. Techniques exist that allow us to asses these factors such as thermal models for imposed cooling profiles, IR thermography for the presence of oxides, and EBSD to assess the final microstructures produced, but few studies account for them all. This study aims to fill this gap in the research by developing an integrated computational materials engineering model that links models for phase transformations, ROT cooling, and surface oxides into one to allow for a better understanding of the expected microstructures formed on the ROT.

Chapter 3

Materials and Methodology

This chapter covers the materials and methodology used throughout the duration of this project. In section 3.1, the chemical composition, optical microscopy (OM), scanning electron microscopy (SEM), and EBSD conducted on the ROT steel are presented and discussed. Section 3.2 will cover the dilatometer analysis conducted on eight X70 samples prepared with cooling rates of 1-, 5-, 15-, 22-, 30-, 50-, 80-, and 120 ℃/s. Within section 3.2, details regarding testing specifics, treatment of dilation curves, and microstructural modelling are provided. Section 3.3 will show the CCT constructed from dilatometer testing which will be used later in the thermo-microstructure model.

3.1 X70 Runout Table Sample

In this section, the composition and processing of a 15.2 mm X70 steel will be presented. Furthermore, the results from OM, SEM, and EBSD analysis will be discussed. Using OM and SEM, the primary phases present in the sample were determined. EBSD was used to quantify phase fractions, as well as determine the distribution of grain area, aspect ratios, and misorientation angles.

3.1.1 Chemical Composition and Processing

A 15.2 mm thick X70 steel provided by Stelco Ltd. was the subject of analysis during this project. The composition of the provided steel is presented in Table 3.1.

Table 3.1: Composition of X70 steel produced at Stelco (wt.%)

C	Mn	Si	Cu	Cr + Mo + Ni	Nb	Ti + V
0.05	1.52	0.24	0.20	0.25	0.059	0.061

TMCP rolling parameters for the steel are summarized in Tables 3.2 and 3.3. Initially the sample was homogenized at $1.49T_{finish}$ before being cooled to $1.22T_{finish}$. At $1.22T_{finish}$, rough rolling reduced the skelp thickness from 240 mm to 33.9 mm. Following rough rolling, the skelp began finish rolling at $1.17T_{finish}$, where the thickness was further reduced to 15.2 mm. The final temperature of the steel prior to laminar cooling was T_{finish}. This information was used to replicate TMCP conditions on dilatometer samples (section 3.2).

Table 3.2: Rough Rolling parameters for 15.2 mm X70 steel

Homogenization (°C)	Exit (°C)	Starting Thickness (mm)	Finish Thickness (mm)
$1.49T_{finish}$	$1.22T_{finish}$	240	34

Table 3.3: Finish Rolling parameters for 15.2 mm X70 steel

Start T (°C)	Finish T (°C)	Starting Thickness (mm)	Finish Thickness (mm)
$1.17T_{finish}$	T_{finish}	34	15

Following finish rolling, the skelp entered the ROT at a speed of 2 m/s, where 34 sprays were used to reduce the temperature to the aim CT. Specific ROT spray configurations will be addressed in chapter 4 during the presentation of the thermal model.

3.1.2 Optical Microscopy

OM was conducted on an Olympus optical microscope with Stream Motion software. The sample was prepared by manually grinding and polishing down to 0.1 µm using a Buehler EcoMet 250 Grinder-Polisher. Silicon carbide abrasive grinding papers of P120, P280, P400, P800, and P1200 were used before changing to alumina, silica, and diamond polishing solutions. After grinding and polishing, samples were etched with a 2% nital solution. In low carbon steels, nital etching reveals the ferrite grain boundaries and colors them white, while leaving phases such as bainite and pearlite dark [90]. Furthermore, it dissolves the ferrite grains, resulting in a topographical surface [90]. Images were taken at the top (TS) and bottom (BS) surfaces, and the quarter (QT) and center lines (CL), at 500X magnification. QT and CL images are shown in Figures 3.1 and 3.2, respectively. Due to the complex nature of cooling at the TS and BS, only the CL and QT results are presented. Micrographs of the surfaces can be found in Appendix A.

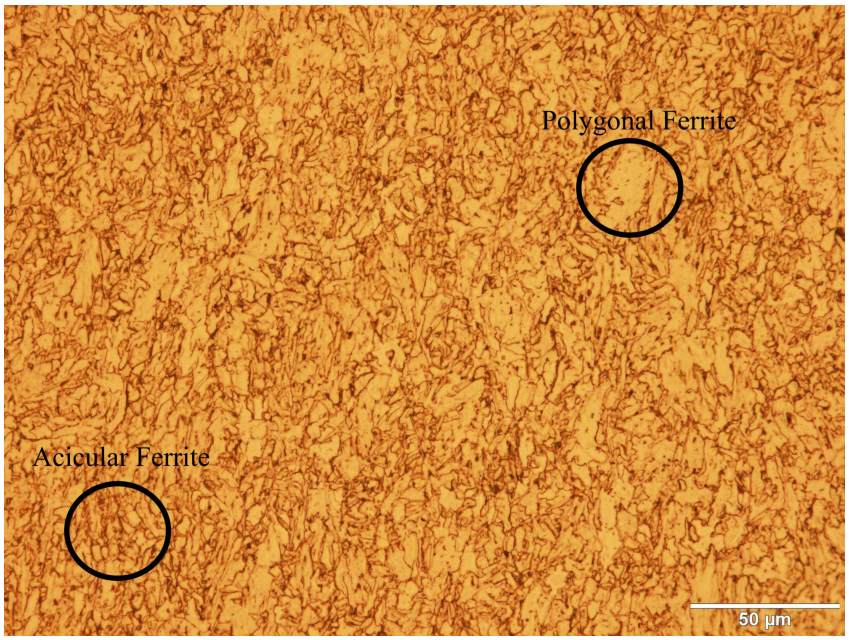

Figure 3.1: OM image of ROT sample taken at QT

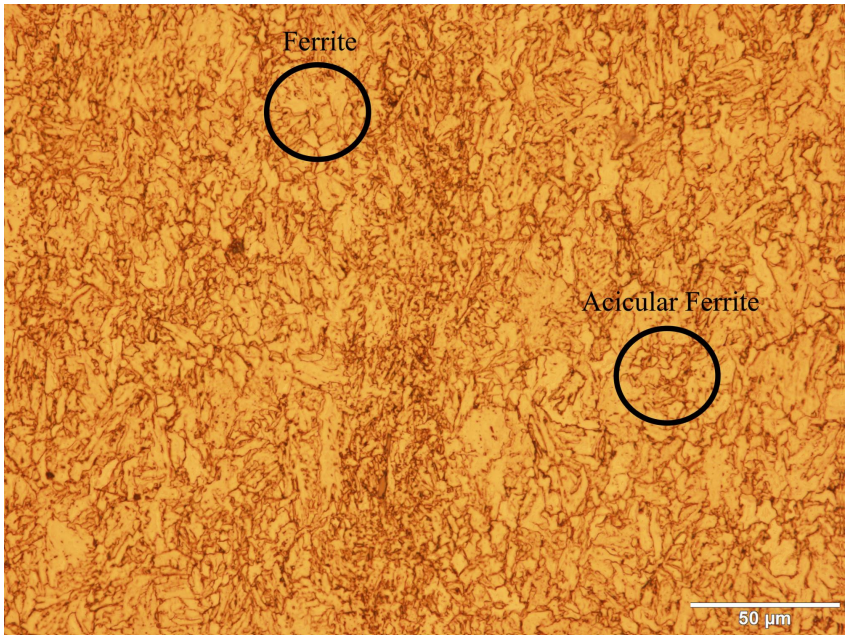

Figure 3.2: OM image of ROT sample taken at CL

From the images taken, two predominant microstructures were observed at the QT and CL. The first microstructure exhibited a large/blocky appearance, which is typical of polygonal ferrite. The second microstructure was much smaller in size, irregularly shaped, and had no apparent arrangement. Based on the characteristics of the second observed phase, it was determined to be acicular ferrite. In both micrographs, there is more ferrite present than acicular ferrite.

3.1.3 SEM

SEM imaging was conducted on a Tescan Vega3 SBH microscope. Images were taken at the QT and CL locations to verify results from OM. Samples were prepared the same way as with OM, where manual grinding and polishing down to 0.1 µm was done before being etched with a 2% nital solution. All SEM images were taken at the same locations as OM using an accelerating voltage of 20 kV and magnification of 2000X. Images were obtained using secondary electrons to observe the topography. 2000X magnification images of the

QT and CL are shown in Figure 3.3 (a) and 3.3 (b). Similar to the results of OM, the phases observed were polygonal ferrite and acicular ferrite. Supplementary images of the surfaces, QT, and CL can be found in Appendix A.

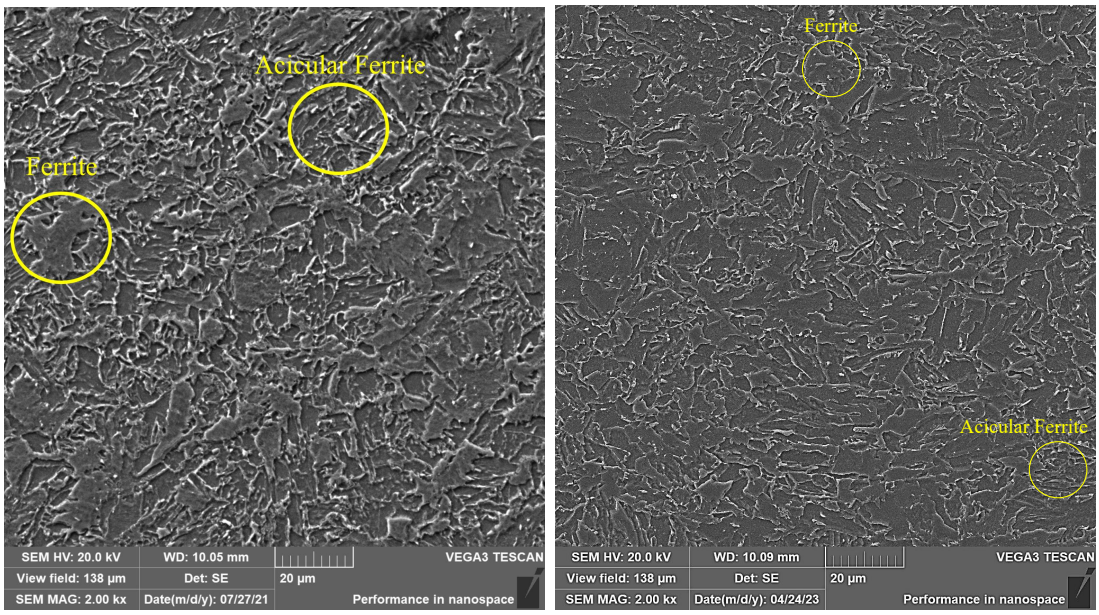

(a) **(b)**

Figure 3.3: SEM image taken at QT (a) and CL (b)

3.1.4 EBSD

EBSD was used to quantify the fraction of each phase present, grain area distribution, aspect ratio distribution, and misorientation angle distribution. Samples were prepared the same way as with OM and SEM, but without the final etching step. Prior to analysis, each sample was also cleaned with acetone in an ultrasonic bath for 10 minutes. Testing was conducted on a Zeiss Sigma FESEM using an operating voltage of 20 kV. Within the FESEM, the vacuum pressure was below 2E-5 torr, the aperture size was 60 µm, tilt was set to 70°, and the working distance was within 10-16 mm.

Band contrast images at the QT and CL were generated for the steel using a map size and step size of 90 x 63 µm and 0.1 µm, respectively. Figure 3.4 shows the band

contrast images which have been converted to a grayscale where a value of 0 is low contrast and a value of 255 is high contrast. As stated in section 2.6, the image quality (band contrast) is proportional to the sharpness of the Kikuchi pattern, which is influenced by crystalline defects such as dislocations. Based on this, low temperature ferritic phases (acicular ferrite and bainte) can be distinguished from those formed at higher temperatures (polygonal ferrite) through differences in pixel values.

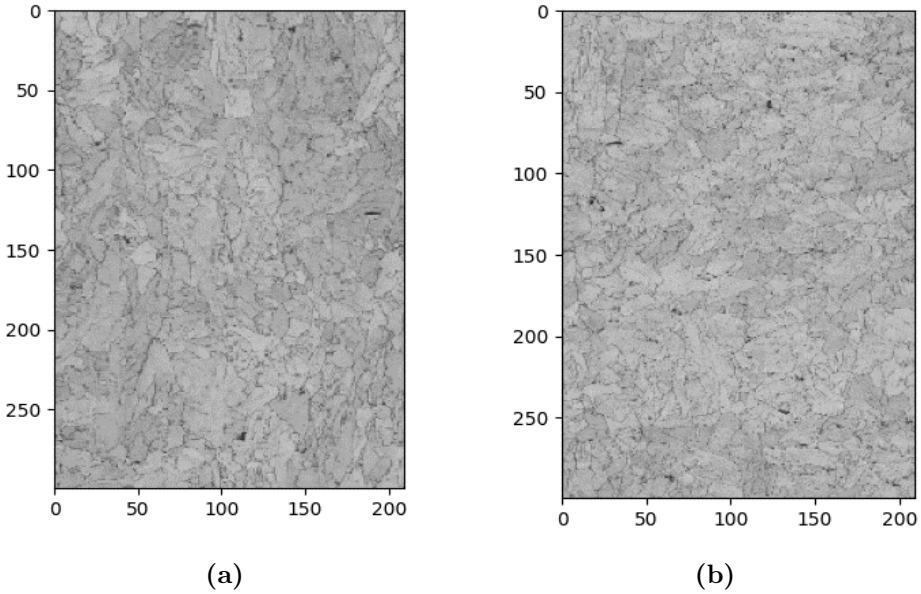

Figure 3.4: Band contrast images for X70 sample at QT (a) and CL (b)

The threshold pixel value that separates the phases was determined using a method developed by Wu et al [91]. In this method, it is assumed that the overall distribution of pixel intensity values in a band contrast map is the summation of Gaussian peaks derived from the phases present [91]. Deconvolution of the pixel distributions into Gaussian peaks was done using OriginLab 2022b. Using their Gaussian curve fitting module, the corresponding curves for each phase were determined. Only two curves were used for fitting, as the volume fraction of MA was deemed negligible. This was based on observations made during OM and SEM analysis. The effect of adding a third curve was

also found to have minor influences on the position of the other two. A deconvolution curve for the QT is shown in Figure 3.5.

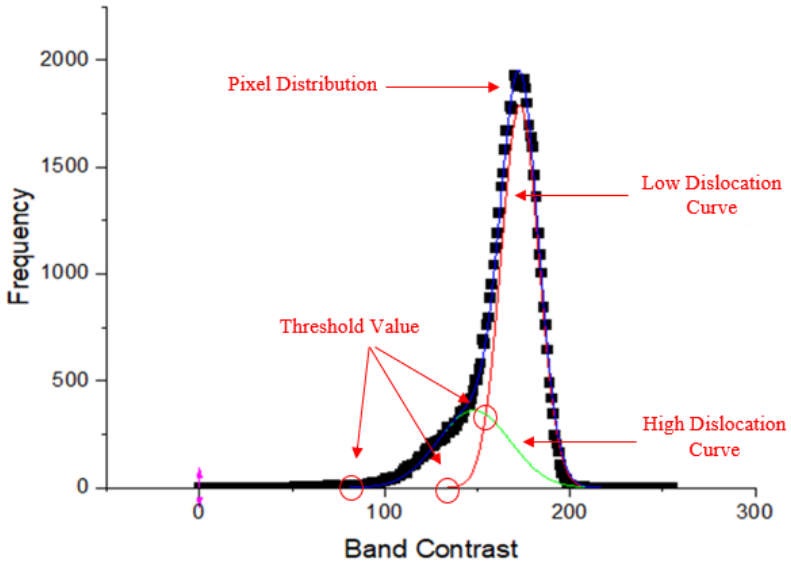

Figure 3.5: Gaussian curve fitting of X70 band contrast distribution at the QT

According to the method by Wu et al [91], to determine the threshold pixel value for the maps, the intersection point of the two Gaussian curves is taken. But by taking this point, portions of the low dislocation phase curve are not accounted for. This results in an under-reported volume fraction. Conversely, if the beginning of the curve is used, the high dislocation phase is under-reported. To mitigate these issues, the threshold value between ferrite, acicular ferrite, and/or bainite was selected based on the predominate phase present. From OM and SEM, it was shown that the X70 steel consisted of predominately ferrite. Based on this, the beginning of the low dislocation phase curve (ferrite for this sample) was used rather than the intersection.

With the threshold pixel values determined for all band contrast maps, a coloring module was run on each image. Based on the pixel intensity and the threshold value, a color was assigned to each point. Blue was assigned to ferrite, green to acicular ferrite,

and red to MA. Figure 3.6 shows the colored images after thresholding was applied. From this process, the phase fractions of ferrite, acicular ferrite, and MA were determined to be 78%, 21%, and 1% at the QT, and 74%, 24%, and 2% at the CL.

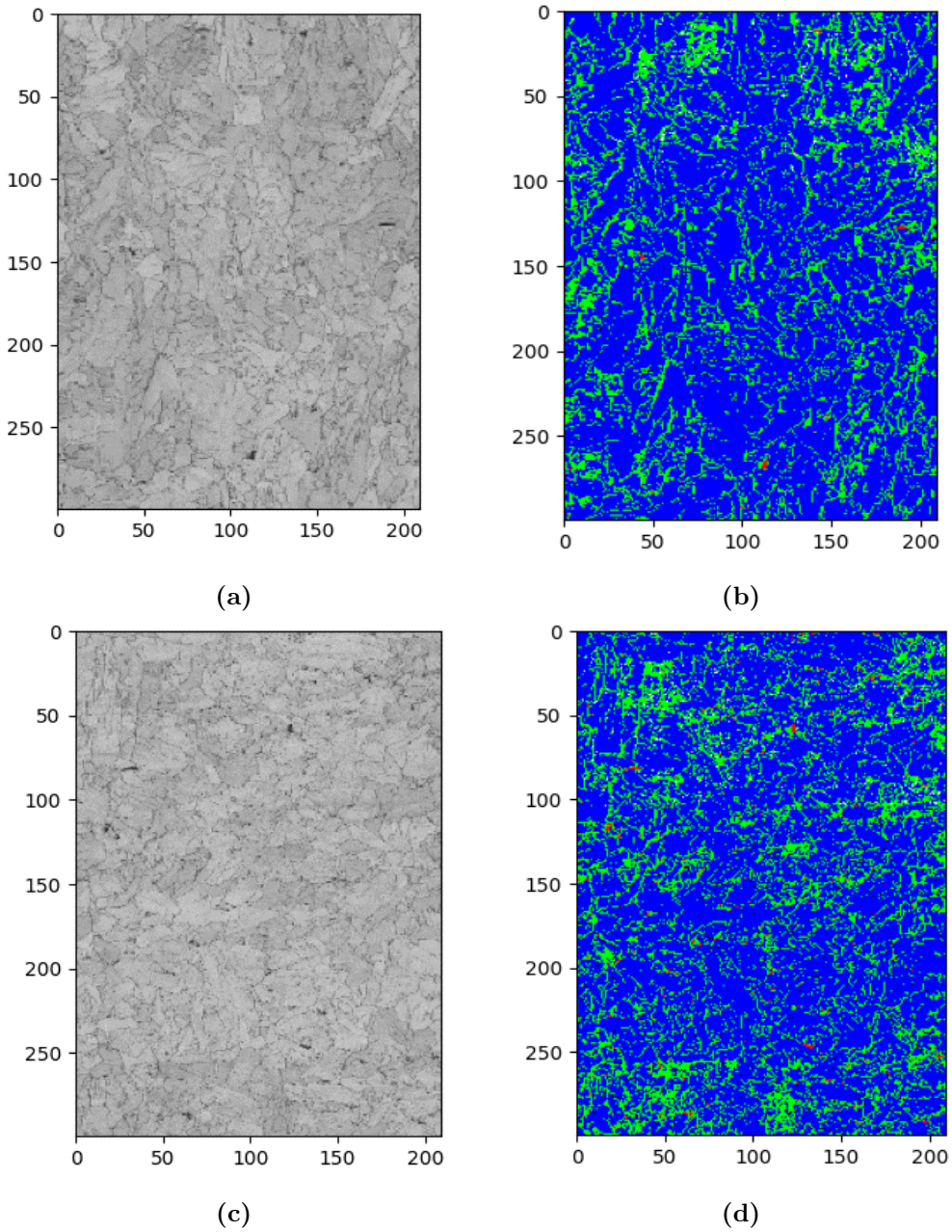

Figure 3.6: Conversion of X70 QT (a and b) and CL (c and d) band contrast maps to colored maps with ferrite (blue), acicular ferrite (green), and MA (red) highlighted

Using the crystallographic orientation data from EBSD, the grain size, aspect ratio, and misorientation angle distributions were also determined. These were calculated for later comparisons with dilatometer samples.

Figure 3.7 shows the distribution of grain area at the QT, where the average, median, and standard deviation were 7.53 μm^2, 3.51 μm^2, and 11.9 μm^2, respectively. The morphology of these grains were further described using the aspect ratio, Figure 3.8, which is the ratio between the height and diameter. Due to the different growth behaviors of phases, the aspect ratio can be used to indicate the presence of ferrite and acicular ferrite, as well as approximate the amount of each. Acicular ferrite can exhibit lath and plate morphologies with aspect ratios ranging between 1 – 11, but it has been suggested that 95% of these grains have aspect ratios above 2 [92]. Conversely, due to the blocky nature of polygonal ferrite, it has a low aspect ratio. Aspect ratio data was smoothed to reduce scatter so that further comparison with dilatometer samples would be easier.

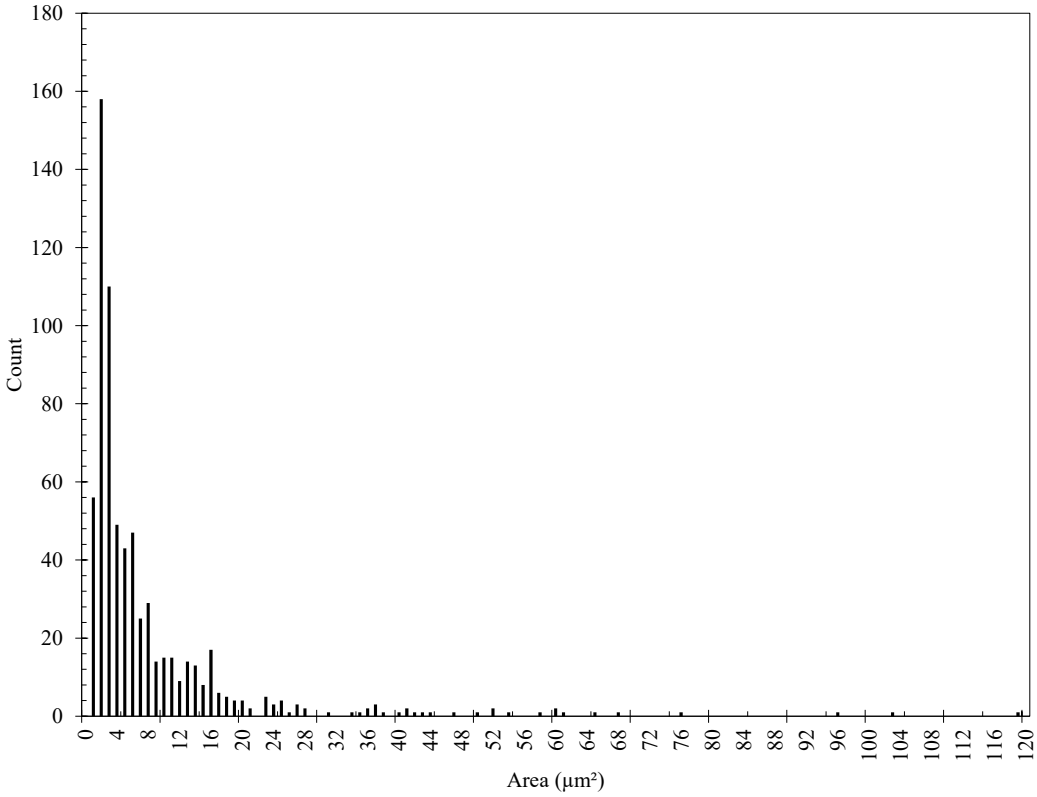

Figure 3.7: Grain area distribution of X70 sample

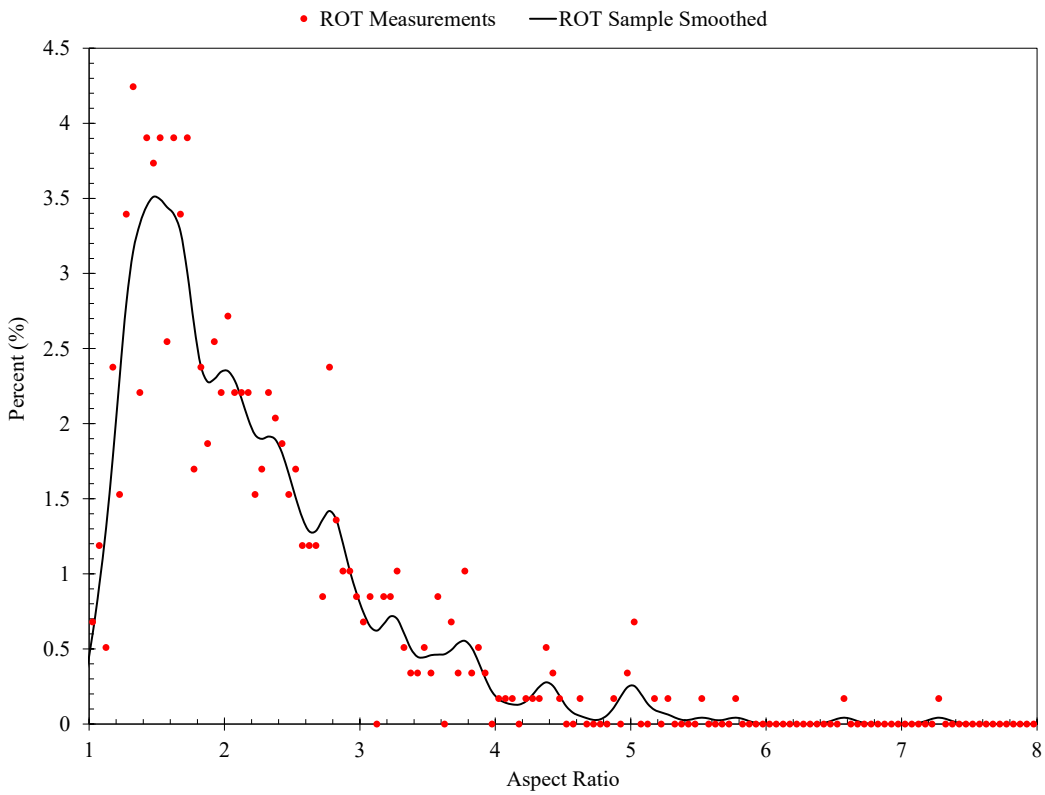

Figure 3.8: Aspect ratio distribution of X70 sample; raw (red) smoothed (black)

The misorientation angle that is observed between crystallographic planes is the result of the phase transformation of austenite to either ferrite, acicular ferrite, bainite, or martensite. Depending on the parent and product phase, preferential distributions of orientations are observed. Ferrite, acicular ferrite and bainite tend to exhibit a Kurdjumov-Sachs (KS) relationship with the parent austenite, which results in a characteristic double peak between the angles of 50 – 60° and a single peak below 25° [92] [93] [94] [95]. In the X70 misorientation frequency plot, Figure 3.9, three peaks are observed at 2°, 54°, and 59°. The one low angle and two high angle peaks correspond well with the OM and SEM observations of a predominate ferrite microstructure with some acicular ferrite [96].

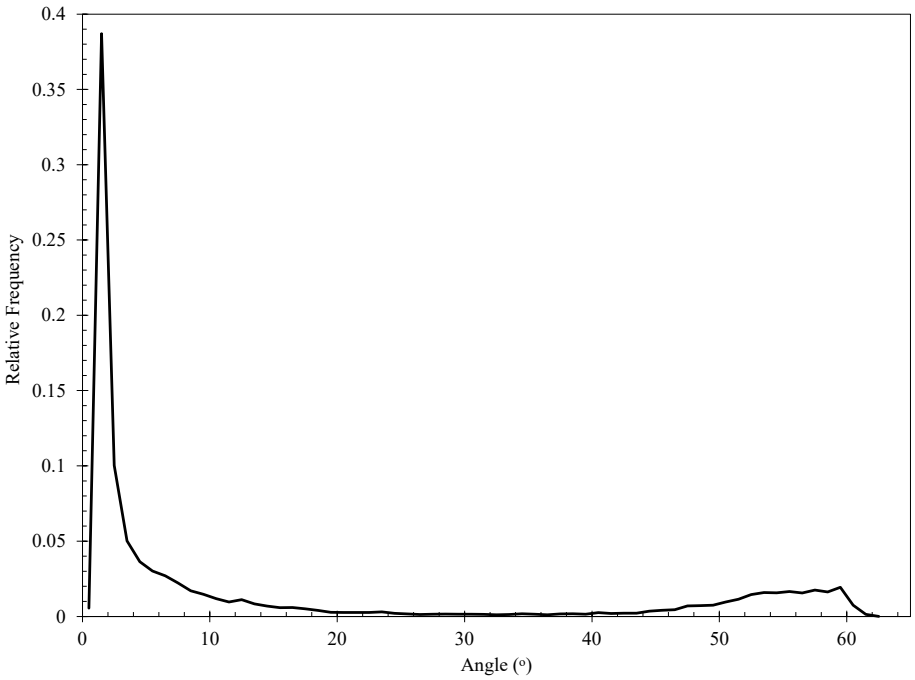

Figure 3.9: Misorientation angle plot of X70 sample

3.2 Dilatometer Samples

In this section, the dilatometry testing, results, and analysis are presented. Eight dilatometer tests were conducted using conditions similar to those in Tables 3.2 and 3.3. Using the dilation curves produced from these tests, fraction transformed curves were generated. With a modified form of the JMAK equation, a microstructure model was then utilized to decompose fraction transformed curves into distinct curves for individual phases. The predicted fractions from microstructure modelling were validated by doing OM, SEM, and EBSD on individual dilatometer samples. Using the EBSD data from each sample, the grain area, aspect ratio, and misorientation angle distributions were then compared to the X70 ROT sample.

3.2.1 Dilatometry Testing

Dilatometer tests were conducted on X70 samples to determine the effect of cooling rate on austenite decomposition. Eight tests were done using cooling rates of 1-, 5-, 15-, 22-, 30-, 50-, 80-, and 120 ℃/s. Samples were taken from the QT thickness of the 15.2 mm X70 sample, and then machined into cylinders with a diameter and width of 5 mm and 10 mm, respectively. Testing parameters were approximated to those in Tables 3.2 and 3.3. Samples were heated up to 1200 ℃ at a rate of 10 ℃/s, and then held for 1 minute. They were then cooled to 1050 ℃ at 3 ℃/s and held for 5 seconds with 0.25 strain (0.1/s). This was followed by a cooling step to 850 ℃ at 5 ℃/s where they were held for 5 seconds with 0.25 strain (0.1/s) before being cooled at the rate being tested. Figure 3.10 shows the processing route for dilatometer testing.

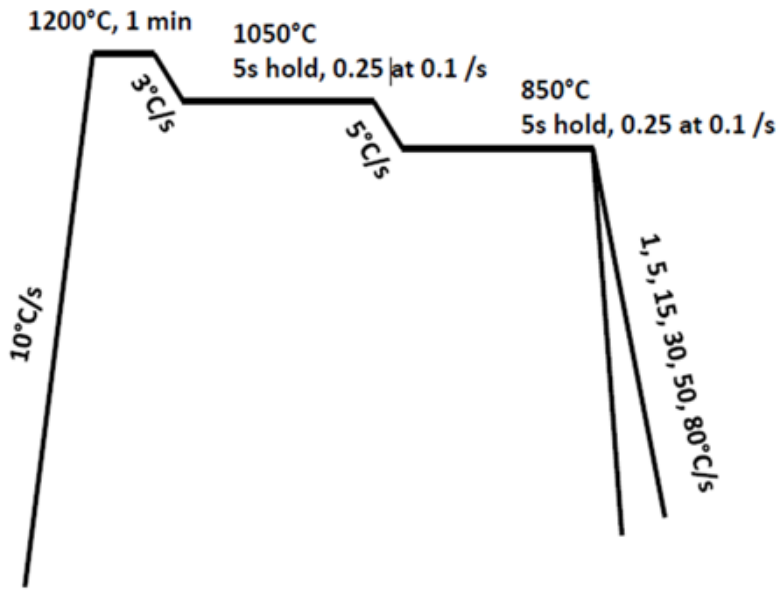

Figure 3.10: Processing route of dilatometer tests

3.2.2 Dilation Curves

Dilatometry measures the volume change of a sample at a fixed heating or cooling rate. In the case of this work, the dilation as a function of temperature was determined and then related to the phase transition occurring. Prior to cooling at the testing rate, the sample is fully austenite. Austenite has a face centered cubic (FCC) structure, where the packing factor is 0.74. As the sample cools, FCC austenite transforms into a body centered cubic (BCC) product. These BCC transformation products have a packing factor of 0.68, which results in dilation.

The dilation curve for the 15 ℃/s sample is shown in Figure 3.11. As illustrated in Figure 3.11, tangent lines for both ferrite and austenite were included in the dilation curves. Equations for the tangent lines were determined by finding the slope and intercept for the linear regions on the dilation curve corresponding to austenite and ferrite where no phase change is occurring. The regions considered predominately austenite and ferrite were above the A_3 temperature, and the end of the transformation, respectively. From these tangent line equations, the value of the slope is representative of the coefficient of thermal expansion (CTE) of either phase. Table 3.4 summarizes the calculated CTE values for austenite and ferrite at each cooling rate tested. Shown by these results is that there was a slight decrease in CTE for austenite with increasing cooling rate and a subsequent increase in CTE with cooling rate for ferrite. These values are close to what are expected from literature, with the value determined for austenite varying slightly ($2.3E-5$ ℃$^{-1}$ and $1.6E-5$ ℃$^{-1}$ for austenite and ferrite, respectively) [97] [98]. These differences may be attributed to large variations between the chemsitry of the dilatometer samples and those from the reported literature. Notably, the samples from the reported literature had much higher (0.12 and 0.17 wt%) carbon content.

Table 3.4: Variation of austenite and ferrite CTE with cooling rate

Cooling Rate (℃/s)	Austenite CTE ($℃^{-1}$)	Ferrite CTE ($℃^{-1}$)
1	$1.77E-5$	$1.09E-5$
5	$1.73E-5$	$1.17E-5$
15	$1.46E-5$	$1.16E-5$
22	$1.56E-5$	$1.18E-5$
30	$1.45E-5$	$1.19E-5$
50	$1.48E-5$	$1.29E-5$
80	$1.34E-5$	$1.30E-5$
120	$1.25E-5$	$1.33E-5$

Using these tangent lines in correlation with the dilation curve, the transformation start and stop temperature could be determined. At approximately 740 ℃ a rebound is observed which signifies the beginning of the austenite decomposition which continued until 450 ℃.

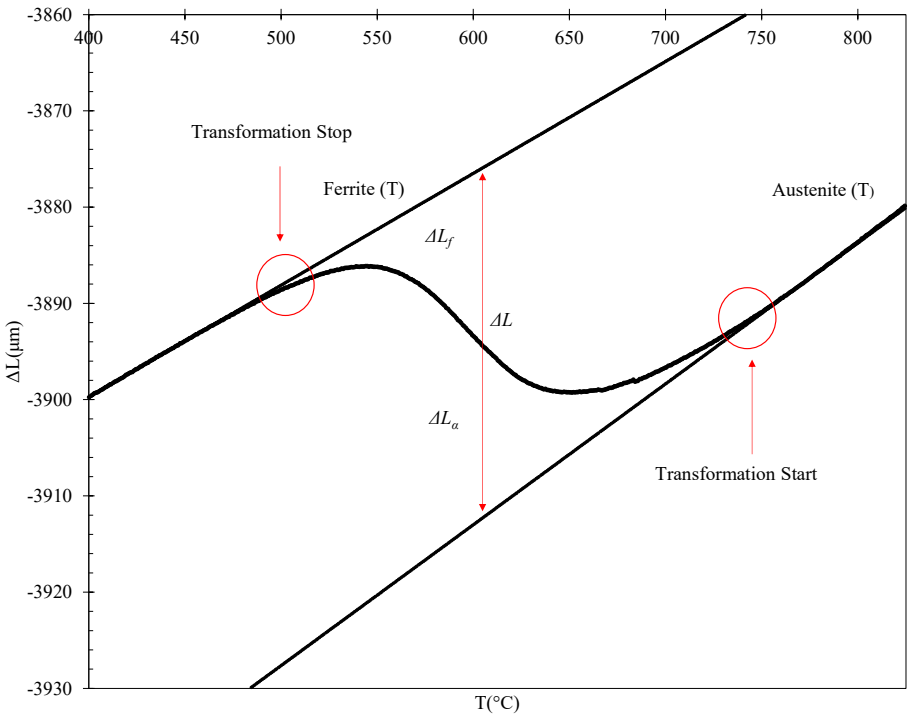

Figure 3.11: Dilatometer dilation curve for 15 ℃/s sample

Using the tangent lines, the fraction transformed at each temperature was then calculated using the lever rule [99]. In this method, the fraction of phases formed from austenite is assumed to be given by the ratio of dilation to maximum dilation. This is represented in equation 3.1, where Δ L$_a$, Δ L$_f$, and Δ L are the austenite tangent, ferrite tangent, and the maximum dilation, respectively, at a given temperature.

$$f = \frac{\Delta L - \Delta L_\alpha}{\Delta L_f - \Delta L_\alpha} \tag{3.1}$$

By calculating the fraction transformed at each temperature between 740 ℃ and 450 ℃, a complete fraction transformed plot was generated for each dilatometer sample. The fraction transformed for the 15 ℃/s dilatometer test is shown in Figure 3.12. A complete set of fraction transformed curves can be found in Appendix B.

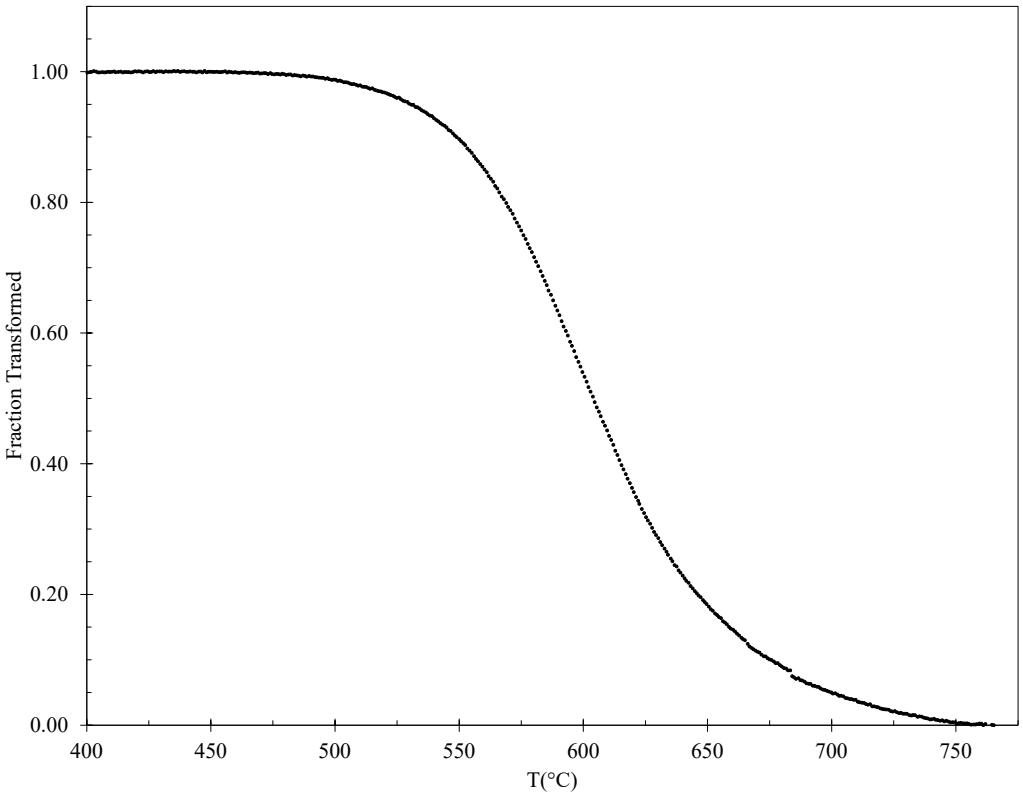

Figure 3.12: Fraction transformed plot for 15 ℃/s

3.2.3 Microstructure Modelling

A drawback of using the lever rule to quantify austenite decomposition is that it assumes that only a single phase is being formed [99]. This is rarely the case, as was illustrated through the OM and SEM images of the ROT sample. To circumvent this issue, a microstructure model was fit to the fraction transformed data.

A modified form of the JMAK equation developed by Jones et al (2.5.2) was used to decompose the fraction transformed curves into several phase curves. To fit the model to the fraction transformed data, the following equations 3.2, 3.3, and 3.4 were used.

$$\tau = \tau_o \exp\left(\frac{-Q}{RT}\right) \tag{3.2}$$

$$\zeta_\alpha = \left(\frac{1}{1+K}\right)\left(1-\exp\left(-(1+K)(\frac{t}{\tau})^{n_\alpha}\right)\right) \tag{3.3}$$

$$\zeta_\beta = \left(\frac{K}{1+K}\right)\left(1-\exp\left(-(\frac{1}{1+K})(\frac{t}{\tau})^{n_\beta}\right)\right) \tag{3.4}$$

To make the modified JMAK equation more general, the nucleation, growth, and time dependency in the exponential of the Jones model was replaced with τ. τ is defined by equation 3.2 and is used to calculate the incubation time for a particle of a given phase. In this equation, τ_o is the time constant, Q is the activation energy, R is the universal gas constant, and T is temperature. As shown in section (2.5.2), the modified JMAK equation developed by Jones et al is specific to a spherical particle. This is demonstrated in their equations through the $-\frac{1}{3}\Pi G_\beta^3 I_\beta t^4$ dependency in the exponential, where the shape factor n is assumed to be 3. Instead of assuming spherical particles, this dependency was replaced with $\left(\frac{t}{\tau}\right)^n$ which is used to describe the kinetics of phase transformations under continuous cooling [75]. Doing this allows for the possibility of different geometries of particles and cooling rates to be accounted for. Using τ, the volume fractions of each phase can be calculated with equations 3-3 and 3-4, where K and n are constants relating to the fraction of each phase and time, respectively.

The constants in equations 3.2, 3.3, and 3.4 (τ_o, K, n) were determined using a generalized reduced gradient (GRG) method within excel. GRG allows for the solution of complex problems with multiple independent variables affecting a single dependent variable [100]. Optimization of the modified JMAK equation was done through minimizing the sum of squares of the residuals between the measured fraction transformed and the theoretical fraction transformed. Upper and lower limits were placed on the independent variables being solved for and were based on a range of values found from literature. A summary of the constants and bounds for each cooling rate are shown in Appendix B.

Using the constants determined through GRG and the modified JMAK equation de-

rived from Jones et al, fraction transformed curves for both high and low temperature phases were generated. The austenite decomposition curve for the 15 ℃/s dilatometer test is shown in Figure 3.13. In each plot, the low temperature and high temperature phases are the green and blue curves, respectively. Furthermore, the experimental dilatometer data is the black curve and the predicted total fraction transformed (phase 1 and phase 2 summed) is the red curve. A summary of the final fraction transformed for each phase at different cooling rates is presented in Table 3.5. For the complete set of decomposition curves of all cooling rates, refer to Appendix B.

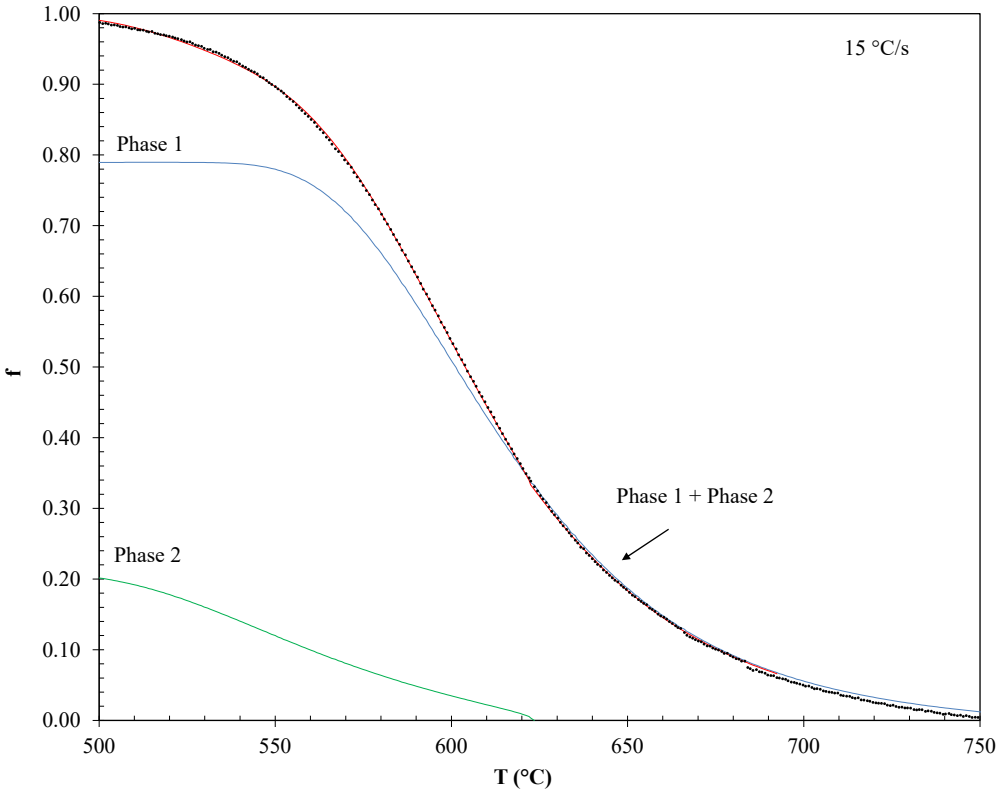

Figure 3.13: Microstructure modeling results for 15 ℃/s showing high and low temperature phases

Table 3.5: Fraction transformed at 1-, 5-, 15-, 22-, 30-, 50-, 80-, and 120 ℃/s

Cooling Rate (°C/s)	Phase 1	Phase 2
1	83 %	16 %
5	86 %	14 %
15	79 %	21 %
22	20 %	80 %
30	12 %	88 %
50	38 %	61 %
80	79 %	21 %
120	70 %	29 %

Figure 3.14 is a plot of transformation start temperatures predicted from modelling versus cooling rate. From this plot it was observed that the second phase formed at cooling rates below 50 ℃/s had approximately the same start temperature as the first phase formed above 50 ℃/s. In this plot, the region between 30 ℃/s and 50 ℃/s was interpolated as no data within this region was available. These start temperatures align well with those found in literature for ferrite, acicular ferrite, and bainite [101]. Verification of these observations are presented in the following section.

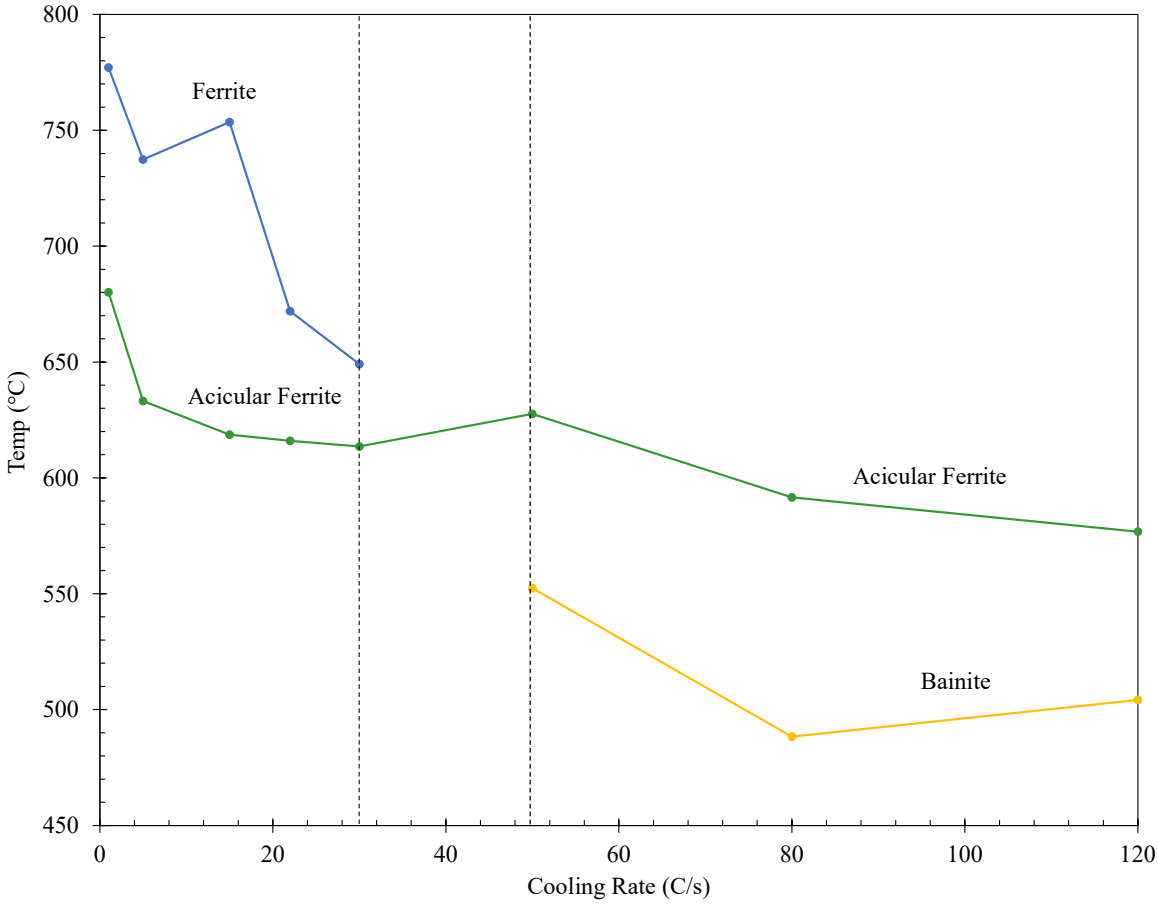

Figure 3.14: Transformation start temperatures for phases at different cooling rates

3.2.4 Phase Identification

OM, SEM, and EBSD were used to classify the high and low temperature phases in each dilatometer sample, as well as quantify the amount of each formed. Analysis work and preparation was carried out the same as with the ROT X70 steel where prior to OM, SEM, and EBSD, samples were prepared by manually polishing down to 0.1 um, and then etched using a 2% nital solution.

Optical Microscopy of Dilatometer Samples

Images taken at 500X on an OM are shown in Figures 3.15 and 3.16. For all cooling rates less than 50 ℃/s, the predominate microstructures observed were polygonal ferrite and acicular ferrite. As the cooling rates increased, the observed amount of polygonal ferrite seemed to decrease while the amount of acicular ferrite increased. At cooling rates of 50 ℃/s and above, the predominate microstructures changed to acicular ferrite and bainite. In the 50 ℃/s sample, there appeared to be a majority bainite, while in the 80 ℃/s and 120 ℃/s samples there was more acicular ferrite.

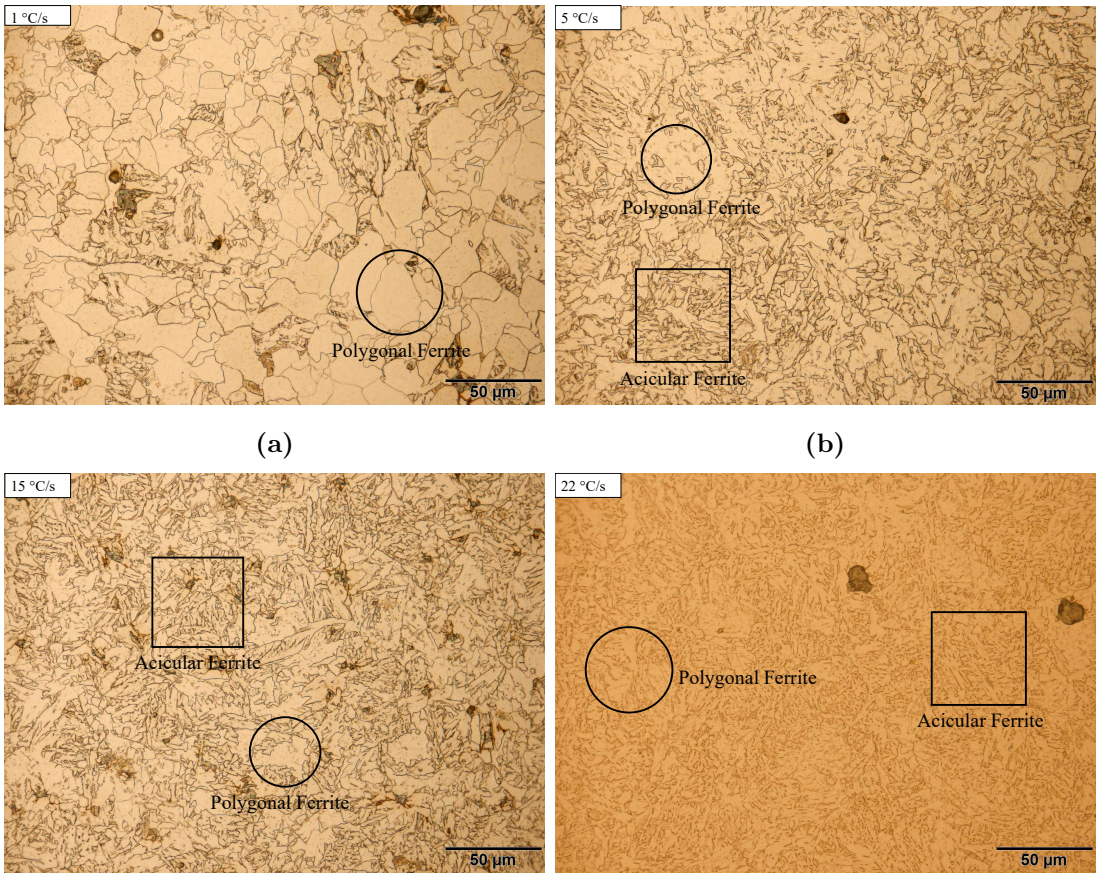

Figure 3.15: OM images at cooling rates of 1-, 5-, 15-, and 22 ℃/s

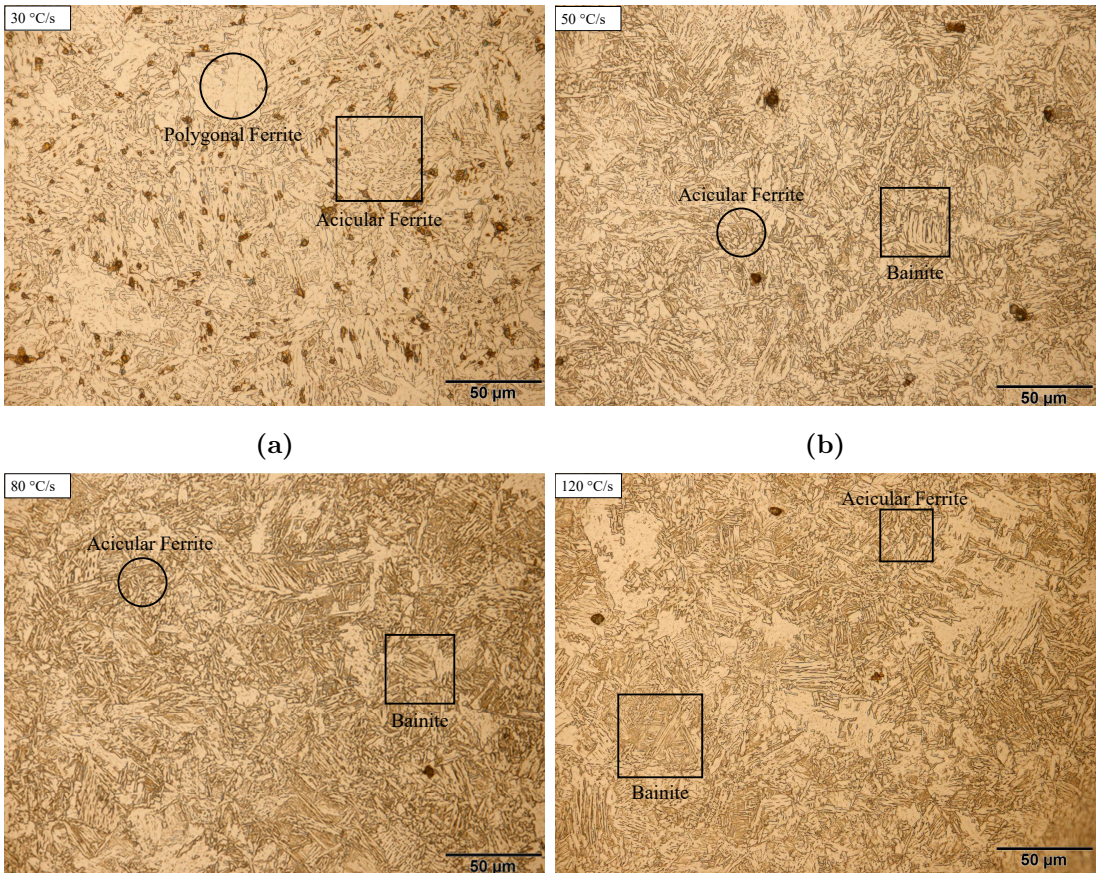

Figure 3.16: OM images at cooling rates of 30-, 50-, 80-, and 120 ℃/s

The observation of decreasing volume fraction of ferrite with increasing cooling rate is a commonly reported phenomena [102] [103] [104] [105] [106]. This is a result of the reconstructive mechanisms that occur during the austenite to ferrite phase transformation which are facilitated by carbon diffusion [70]. As the cooling rate is increased, there is less time for the carbon to diffuse which decreases nucleation and growth rates [70] [106] [107].

Acicular ferrite forms through a shear diffusional mechanism, where nucleation occurs within the austenite grain on either an inclusion or dislocation band [108] [109]. Since the density of deformation bands is far greater than the amount of inclusions, this nucleation type is expected to dominate the formation of the acicular ferrite in both dilatometer and

ROT samples. Deformation bands are formed during finish rolling where no recrystalization occurs. These sites do not solely act as nucleation sites for acicular ferrite, which is why for the 1 ℃/s sample (Figure 3.15 (a)) there is minimal acicular ferrite given the same deformation band density [4]. But, as the cooling rate increases, the kinetics of polygonal ferrite formation are reduced through the inhibiting of carbon diffusion [110]. This inhibiting of the polygonal ferrite phase then promotes the formation of acicular ferrite as more nucleation sites are available at lower temperatures [107] [110]. Multiple studies have suggested that increased cooling rates promote the formation of acicluar ferrite [110] [107] [108].

Shown in Figure 3.16, little to no bainite was observed when polygonal ferrite was present. This can be attributed to the competing nucleation mechanisms of the two. Both polygonal ferrite and bainite nucleate at austenite grain boundaries [70]. Thus by forming polygonal ferrite at higher temperatures first, the nucleation sites for subsequent bainite transformations are exhausted and it does not occur [111]. By inhibiting the bainite transformation, acicular ferrite formation is promoted instead [111].

SEM of Dilatometer Samples

Based on Figure 3.14 and OM, there was an observed switch between microstructures at 50 ℃/s, where below this the phases were polygonal ferrite and acicular ferrite, and above, it was acicular ferrite and bainite. To supplement these findings, SEM images of all dilatometer samples were taken at 2000X magnification. Using the 15 ℃/s and 50 ℃/s samples as representatives of low and high cooling rates, their microstructures were contrasted, Figure 3.17. From these images, it was confirmed that at 50 ℃/s, there was a transition between the primary phases being formed. SEM images of all dilatometer samples can be found in Appendix B

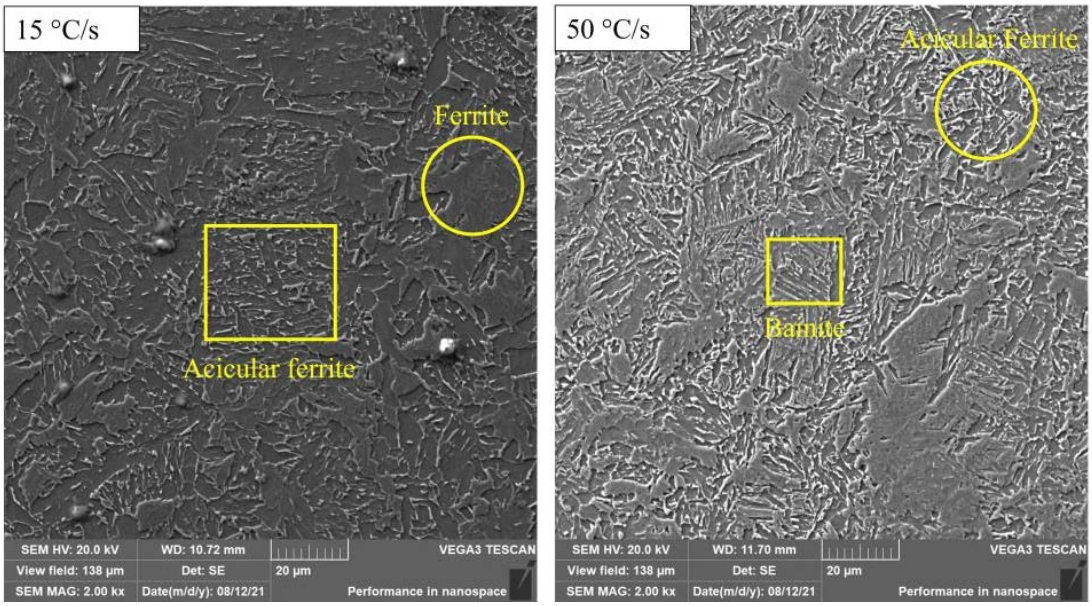

(a) **(b)**

Figure 3.17: SEM images of 15 ℃/s (a) and 50 ℃/s (b) dilatometer samples

EBSD of Dilatometer Samples

The grain area distribution, aspect ratio distribution, misorientation angle distribution, and phase fractions were determined for each dilatometer sample. Results for the 5 ℃/s and 15 ℃/s sample are shown in Figures 3.18 , 3.19 , 3.20 , and 3.21. The complete set of dilatometer EBSD results can be found in Appendix B. These samples were chosen for comparison as they produced results closest to the ROT steel previously assessed.

The significance of these comparisons is that it suggests that the microstructure evolution experienced by the ROT steel is close to that of the 5 ℃/s and 15 ℃/s samples. During thermo-microstructure model development, this can be used as a validation criterion where the kinetics should be close to those obtained from 5 ℃/s and 15 ℃/s samples. Tables 3.6 and 3.7 summarize the phase fractions determined for each dilatometer sample using the band contrast method.

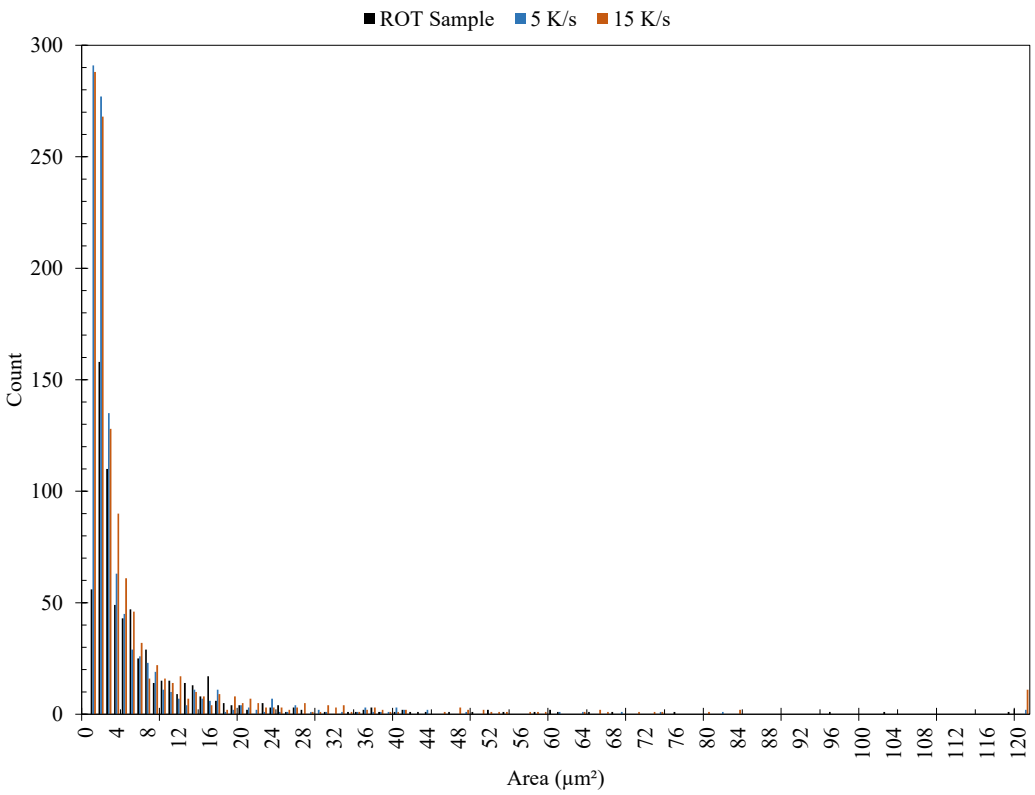

Figure 3.18: Grain area distribution comparison between ROT, 5 ℃/s, and 15 ℃/s samples

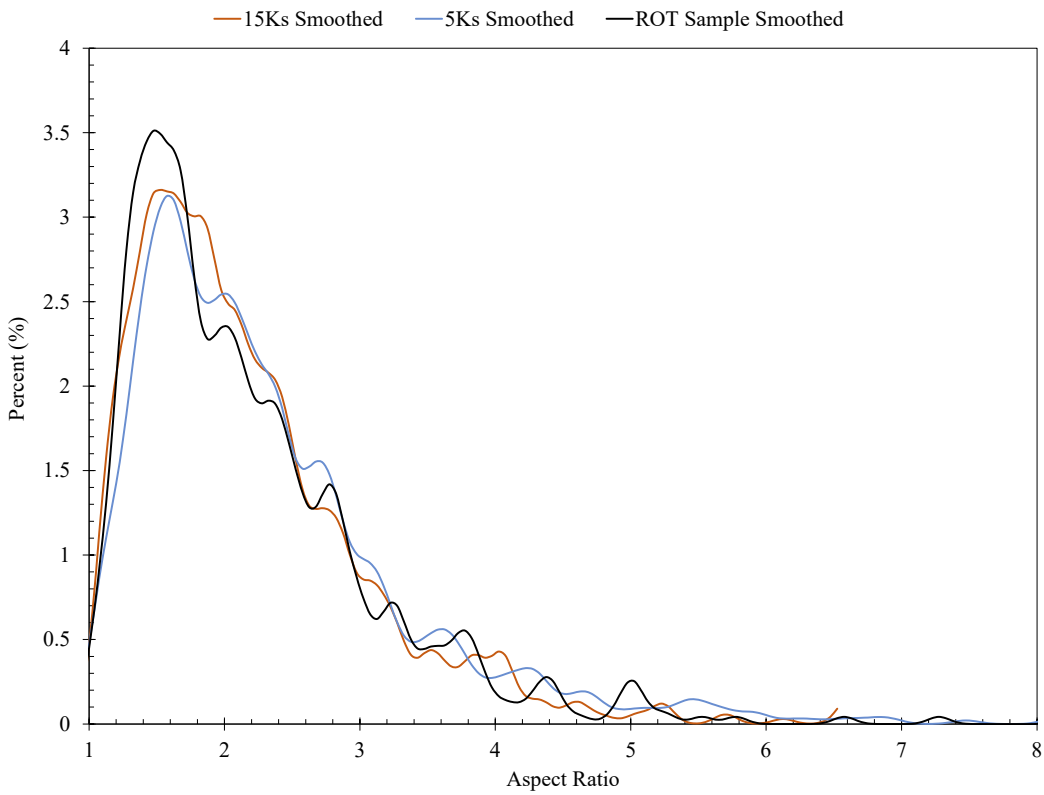

Figure 3.19: Aspect ratio distribution comparison between ROT, 5 ℃/s, and 15 ℃/s samples

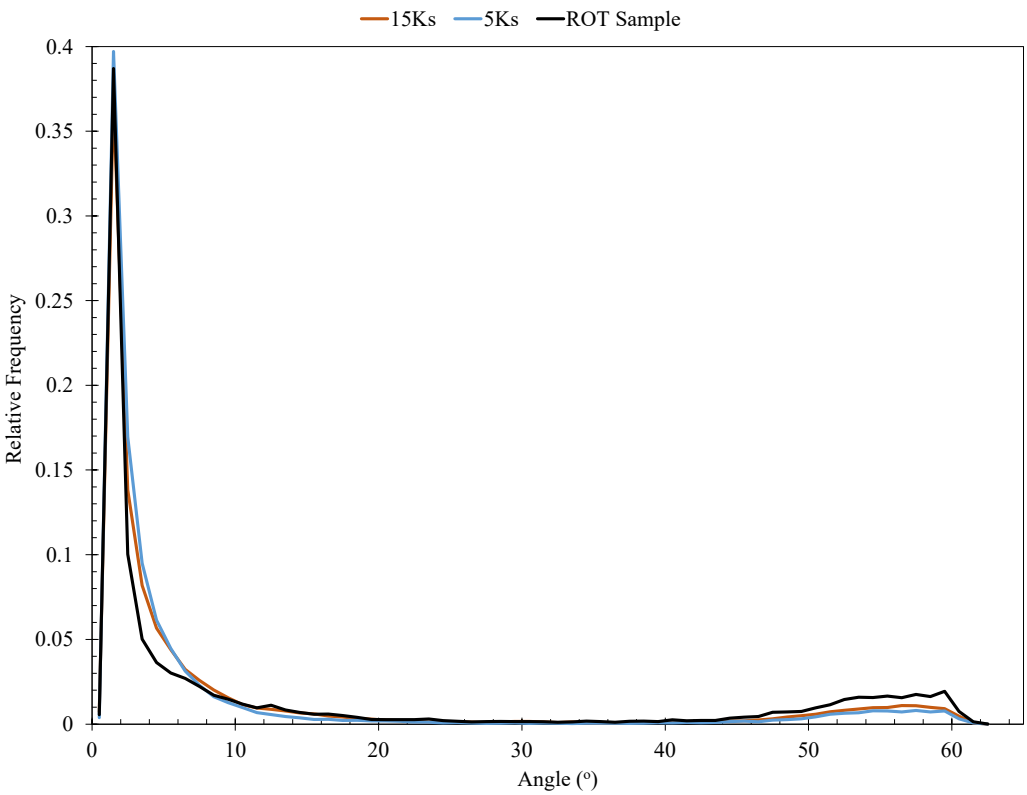

Figure 3.20: Misorientation angle distribution comparison between ROT, 5 ℃/s, and 15 ℃/s samples

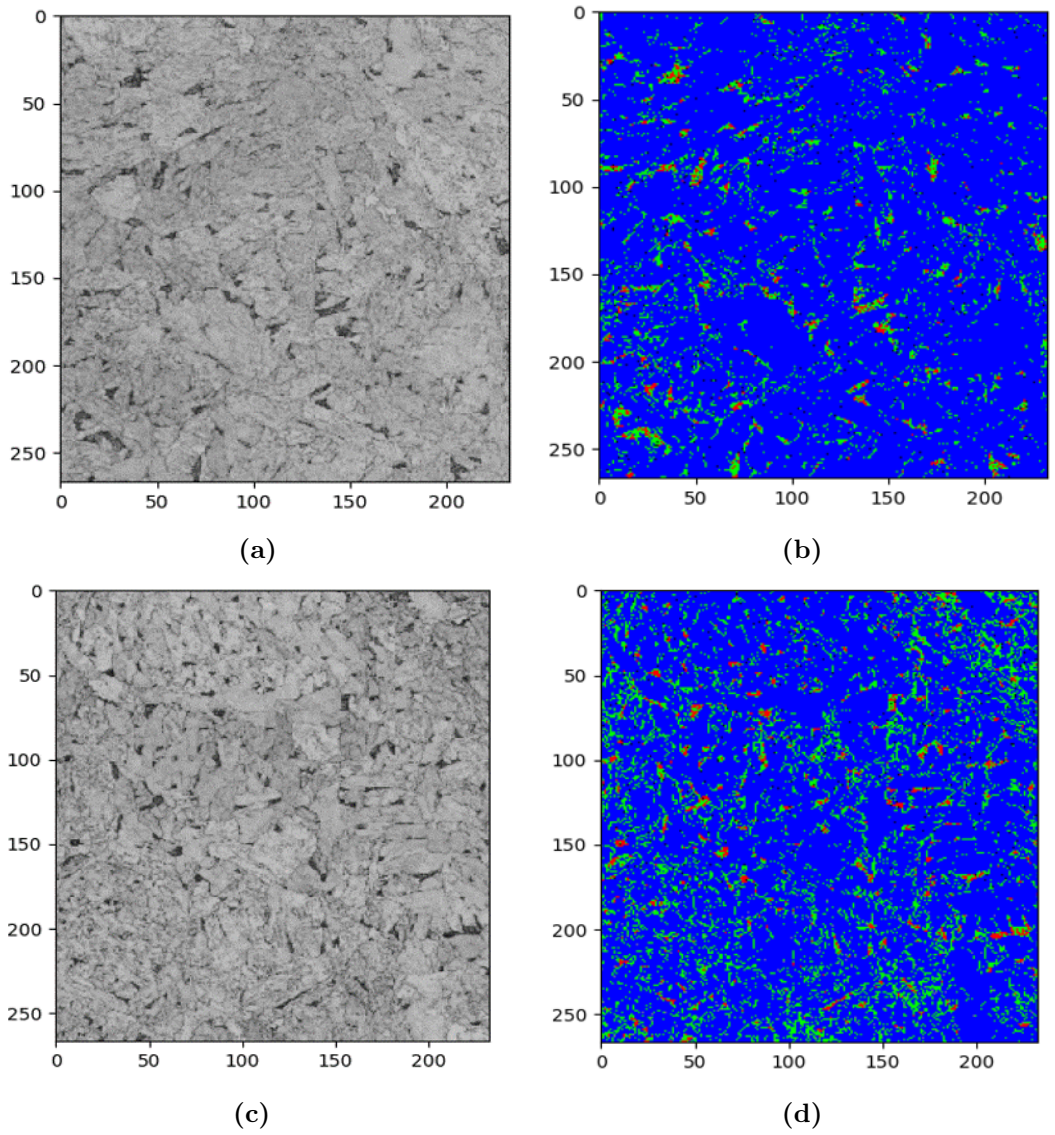

Figure 3.21: EBSD phase quantification of 5 ℃/s (a and b) and 15 ℃/s (c and d) samples with ferrite (blue), acicular ferrite (green), and MA (red) highlighted

Table 3.6: Fraction transformed at 1-, 5-, 15-, 22-, and 30 ℃/s using band contrast

Cooling Rate (°C/s)	Ferrite	Acicular Ferrite	Phase 3
1	63 %	33 %	4 %
5	89 %	9 %	2 %
15	81 %	16 %	3 %
22	36 %	55 %	9 %
30	22 %	76 %	2 %

Table 3.7: Fraction transformed at 50-, 80-, and 120 ℃/s using band contrast

Cooling Rate (°C/s)	Acicular Ferrite	Bainite	Phase 3
50	42 %	56 %	2 %
80	76 %	22 %	2 %
120	72 %	27 %	1 %

3.2.5 Microstructure Model Validation

To assess the efficacy of the microstructure model, a parity plot between EBSD (Tables 3.6 and 3.7) and predicted phase fractions (Table 3.5) was used. Individual plots were generated for each phase at a given cooling rate, Figure 3.22 and 3.23. MA was not assessed, as it was taken as the balance of each austenite decomposition plot in Figure 3.13. One standard deviation from the proportionality line (dashed red lines) was used to identify any potential outliers in the data, but as shown in the plots, all data fell within an acceptable range. Based on these results, the data from each dilatometer experiment was used in the development of both the CCT and thermo-microstructure model.

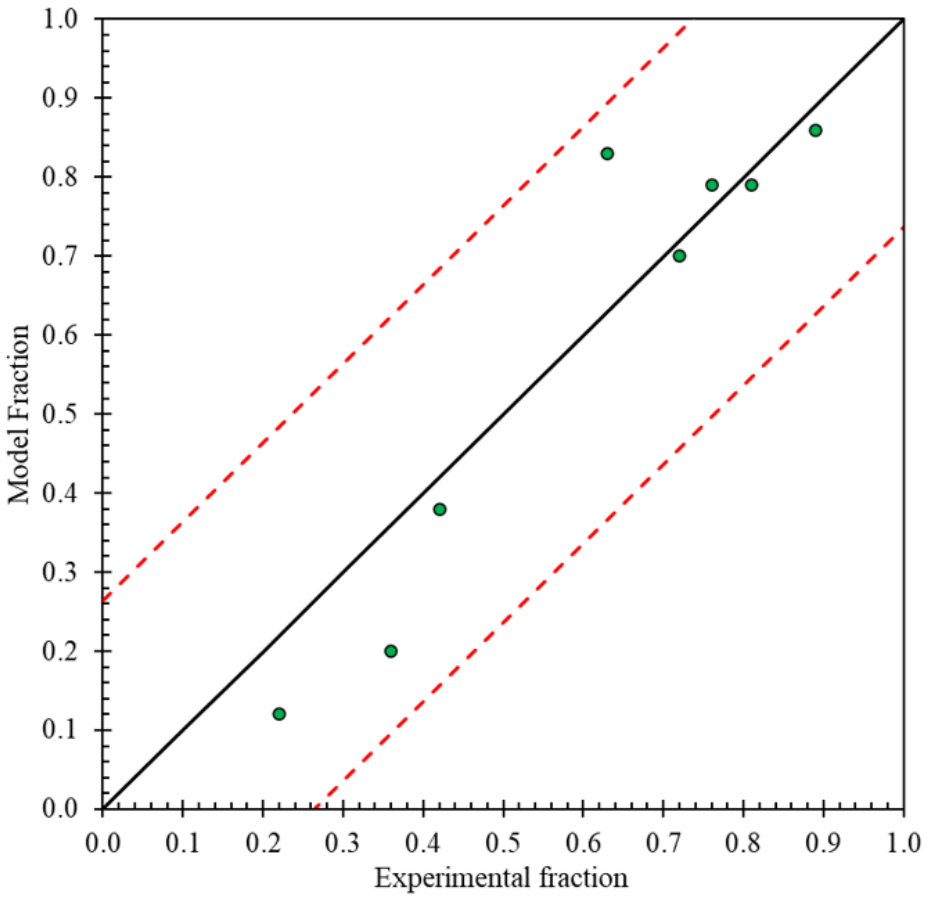

Figure 3.22: Parity plot for phase 1

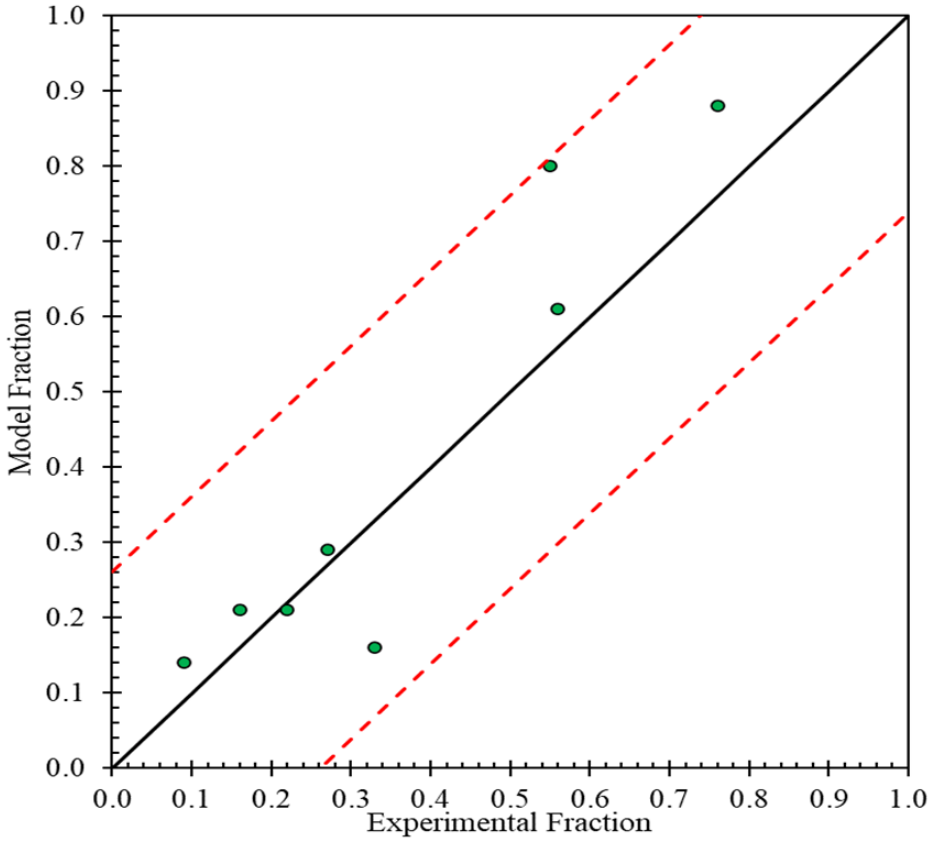

Figure 3.23: Parity plot for phase 2

3.3 CCT Curve Development

Using the start and stop temperatures determined from microstructure modelling, a CCT was constructed for Stelco Ltds. X70 steel, Figure 3.24. From this CCT, regions of single- and two-phase transformation can be seen. The start temperature of each phase was considered the temperature at which 1% had been formed. For end points, the temperature at which the transformation curve plateaued (99%) was used. This CCT will be used later during the construction of the thermo-microstructure model found in chapter 6.

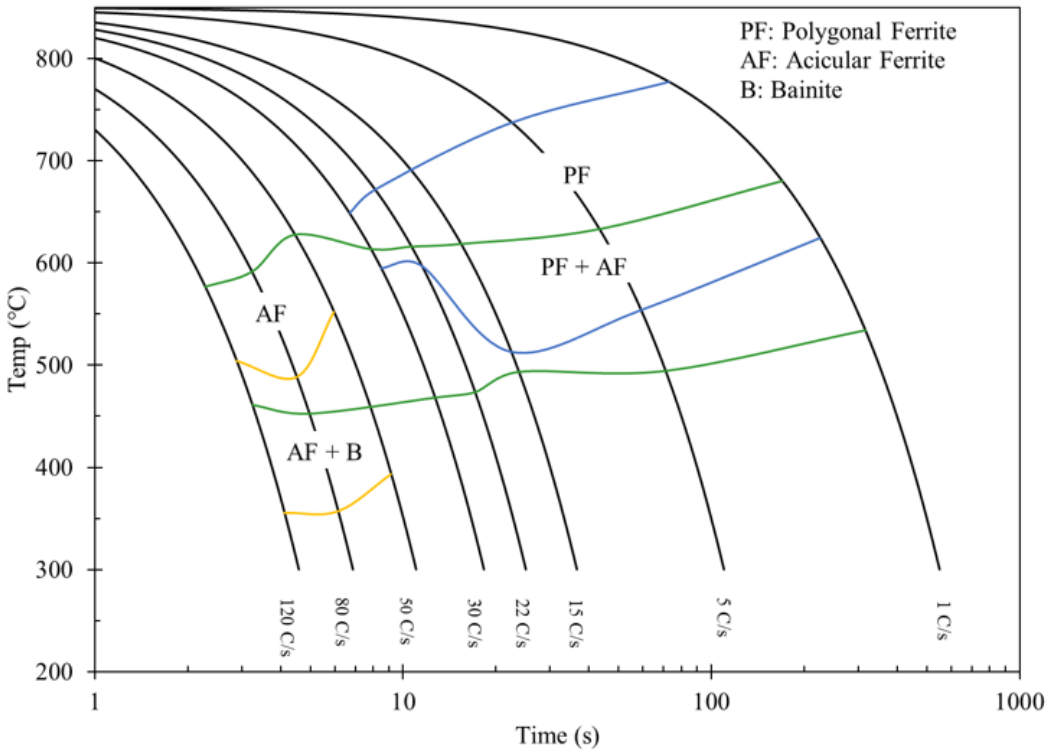

Figure 3.24: CCT diagram for X70 sample

3.3.1 Summary

As shown through the results from OM, SEM, and EBSD, the primary phases present in the X70 ROT sample were ferrite and acicular ferrite. This was based primarily on observations of phase morphology. These results align well with the reported/aim microstructures from the industrial sponsor, where a predominately ferrite microstructure with some acicular ferrite is targeted. Table 3.8 shows the reported microstructures and corresponding fractions of each through the thickness of the sample. Although analysis of the surface was difficult due to the complex cooling, an average phase fraction from all band contrast maps is still included. Shown from these results, apart from the surface, is that there was little observed differences in phase fraction through the thickness.

Table 3.8: Through thickness microstructure and phase fraction for X70 sample

Location	Ferrite (%)	Acicular Ferrite (%)
QT	78 %	21 %
CL	74 %	24 %
TS	55 %	45 %

Using dilatometer samples cooled at rates of 1 to 120 °C/s, a microstructure model that could handle both continuous cooling and the simultaneous formation of phases was developed. Model phase fraction predictions closely matched those measured using EBSD as illustrated through parity plots for the primary and secondary phases formed. Regarding the phases formed, below 50 °C/s, a combination of ferrite and acicular ferrite was observed, while above this, the phases were acicular ferrite and bainite. The results from microstructure modelling were then used to construct a CCT for the steel under investigation. Based on OM, SEM, and EBSD, the X70 ROT sample was best approximated as a combination of the 5 °C/s and 15 °C/s dilatometer samples. This observation will be used later as a validation criteria for predictions made with the thermo-micostructure model in chapter 6.

Chapter 4

Thermal Modelling of Run-Out Table

To determine the thermal history of the skelp as it traverses the ROT, a thermal FEA model was developed in ABAQUS CAE. The model was used to capture all the cooling mechanisms after finish rolling and prior to coiling. Using the model framework previously developed by Wiskel et al [41], modifications were made to appropriately represent the Stelco Ltd ROT used in this research. Thermal models were made for 8-, 11-, 12-, and 15 mm thick skelps. In section 4.1 an overview of the ROT will be presented, where a schematic of the system will be shown to illustrate dimensions of the banks and headers. Section 4.2 will highlight the major assumptions made during model development. Boundary conditions and meshing used will be shown in sections 4.3 and 4.4, respectively. Section 4.5 will show the results for the 15.2 mm model, while the 8-, 11-, and 12 mm models are shown in Appendix C. Validation of the model will be covered in section 4.6, where the IR thermography is presented. Lastly, section 4.7 will show the results from the sensitivity analysis conducted. For a complete table of thermophysical properties used in the model, refer to Appendix A.

4.1 Run-out Table Schematic

Cooling of the skelp occurs in three stages as it exits the finish roller. First is the radiative/convective cooling zone, followed by the laminar water-cooling zone, and then ending with another radiative/convective zone prior to upcoiling. Due to these different mechanisms, defining the segments over which each mechanism cools the skelp is critical for model development. The ROT modelled is approximately 151 m in length and consists of 7 evenly spaced banks that are 7.2 m wide. Banks are 9.6 m from one another, and the distance from the first and last banks to the finishing and coiling pyrometers are 12.4 m and 30 m, respectively. To monitor the temperature of the skelp, process pyrometers are positioned after finish rolling and before coiling. A general schematic of this setup is shown in Figure 4.1.

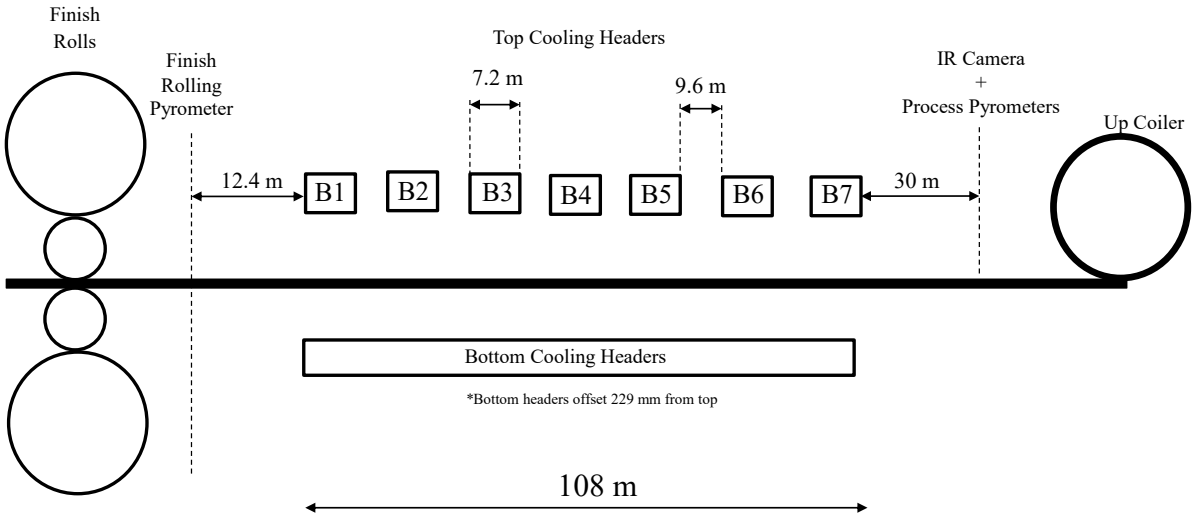

Figure 4.1: General schematic of ROT

The ROT utilizes a laminar jet cooling system, where water freely flows through the header and is expelled through circular nozzles onto the skelp. Each header consists of 2 columns of nozzles. Within the columns, the nozzles are evenly spaced in the Y-direction by 67 mm, but between columns they are offset by 34 mm. In total there are 53 nozzles

per header, each of which contributes to the cooling of the skelp. A schematic of the header and nozzles is shown in Figure 4.2.

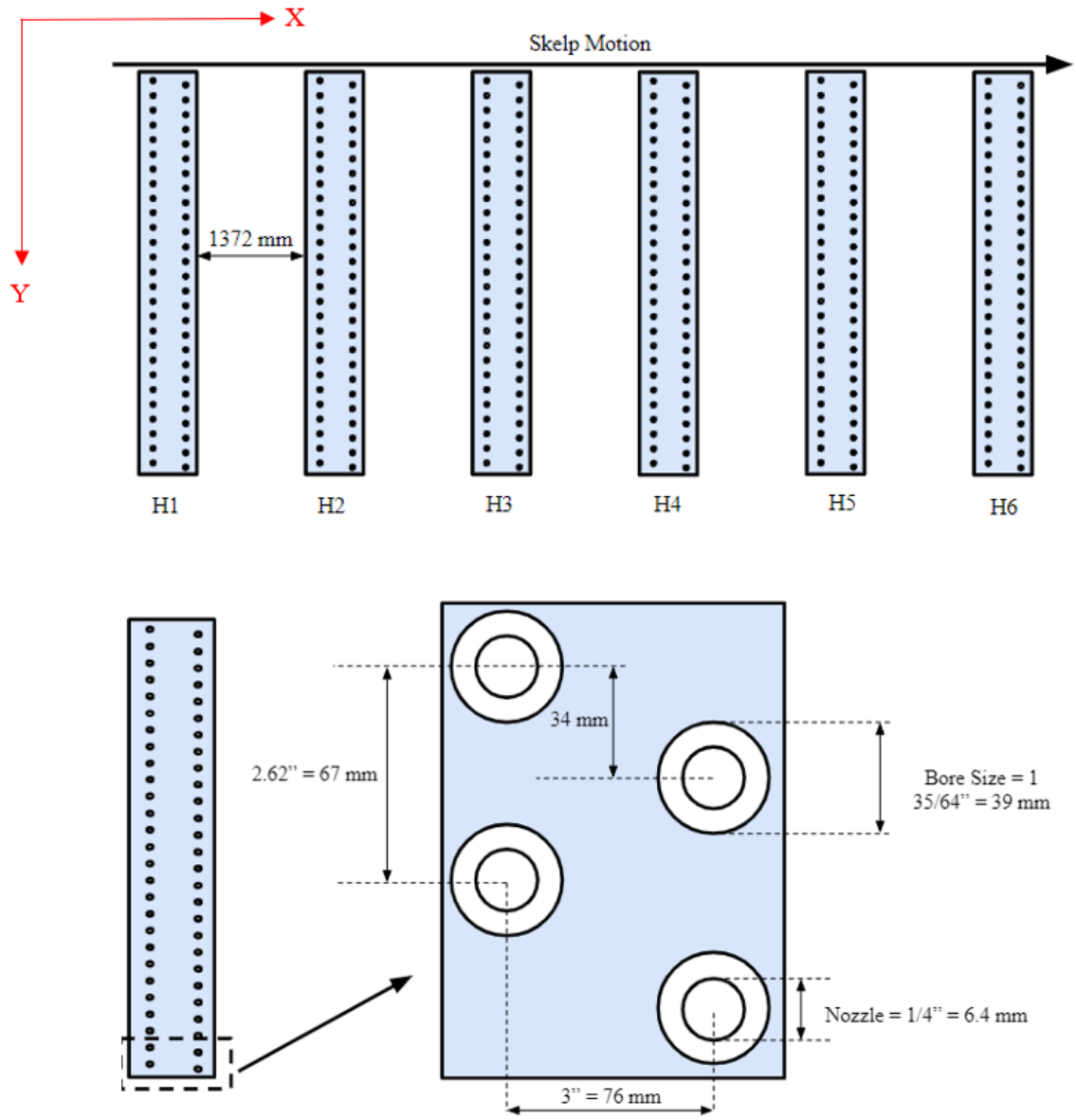

Figure 4.2: Schematic of headers within a bank (top) and their nozzle configuration (bottom)

4.2 Thermal Finite Element Model Assumptions

To simplify ROT model development, assumptions regarding the heat transfer mechanisms and nozzle configuration were made:

1. No longitudinal heat flow in the skelp.
2. Symmetry between the top and bottom heat flow.
3. Each nozzle contributes identical cooling.
4. Radiation/convection cooling occurs everywhere where there is no exposure to water.
5. Header nozzles are configured in one evenly spaced column, and not offset.
6. Water is removed from the skelp surface due to travel velocity and by side sprays.
7. Latent heat is released linearly over the transformation temperature range.

The first assumption was made based on the velocity of the skelp as it traverses the ROT. Through ignoring longitudinal heat flow, a 2D transverse slice of the skelp can be used as a representative of the total cooling conditions. Assumptions 2 and 3 were made to define points of symmetry in the model, so that only a region of the transverse slice needed to be modelled. Symmetry between the top and bottom of the skelp allows the centerline to have a heat flux of zero. As will be shown later in section 4.3, assumption 4 was made to clearly define where radiation/convective cooling occurs. To keep the model 2D, the two nozzle columns were superimposed into one, Figure 4.3. As shown in Figure 4.3, this is a valid approximation as there is no overlap in the X-direction between nozzles. Regarding water retention on the surface, side sprays are positioned between each bank. Due to the header configuration within each bank, water can either be assumed to be

retained on the surface or removed. From observations made previously, ROT skelp velocities were fast enough to remove retained water. Based on this, the assumption was made that water is removed by the both travel velocity and side sprays.

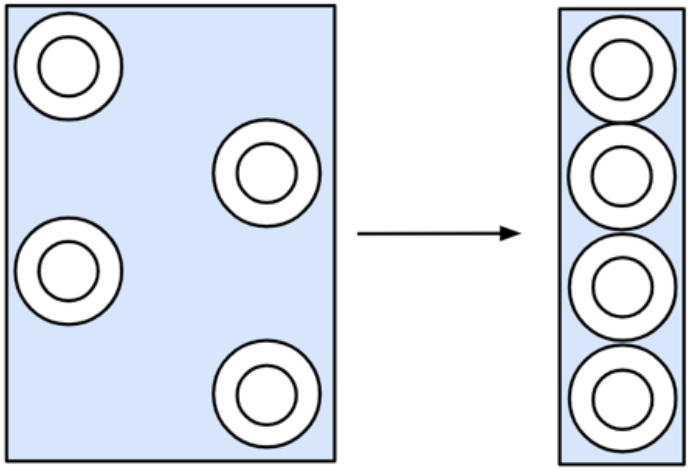

Figure 4.3: Assumed nozzle configuration for modelling

4.3 Boundary Conditions

Shown in section 2.3.3, impact, film, and radiation cooling boundary conditions are required to solve the heat equation. These boundary conditions are represented by equations 2.2, 2.3, and 2.4, where values for heat transfer coefficients and fluxes were gathered from literature (section 2.3.2)

Table 4.1 is a summary of ranges for impact cooling heat fluxes and sizes. Heat flux values ranged between 10 - 12 MWm^{-2}, and the impact size was best approximated with a width similar to the nozzle diameter and a length of two diameters [37] [38].

Table 4.1: Impact cooling experimental results from literature [41] [37] [38]

Plate Condition	impact Size	Flux (MWm^{-2})
stationary	2-times nozzle width	11-12
stationary	2-times nozzle width	n/a
Transient	n/a	10-12

Based on the work of Wiskel et al [41], a value of 10.5 MWm^{-2} was shown to provide good results, so it was selected for this model. Using a heat flux value of 10.5 MWm^{-2} resulted in the corresponding boundary condition for impact cooling, equation 4.1. In this equation, T_s and T_w are the temperatures of the skelp surface and water, respectively.

$$HTC_{impact} = \frac{10.5}{T_s - T_w}[MWm^{-2}] \tag{4.1}$$

Outside of the water impact zone, the heat transfer is governed by the water boiling curve. A modified version of the spray cooling curve developed by Wendelstorf et al [36] was used to approximate the resulting heat transfer coefficient in this region, and was treated as a fitting parameter for the model. A power equation was fit to the film boiling portion of the original spray cooling curve, and then varied until the predicted CT from modelling agreed with measurements from the coiling pyrometer. For the 15 mm skelp model, the boiling curve shown in Figure 4.4 was used, where the film boiling portion was modelled with equation 4.2. In Figure 4.4, the red curve is the modified boiling curve. Based on the temperature of the ROT water (21 °C) and the skelp surface, cooling only occures in the region denoted by the red box.

$$HTC_{film} = 2.15e^7 * \left(\Delta T^{-1.508}\right) \tag{4.2}$$

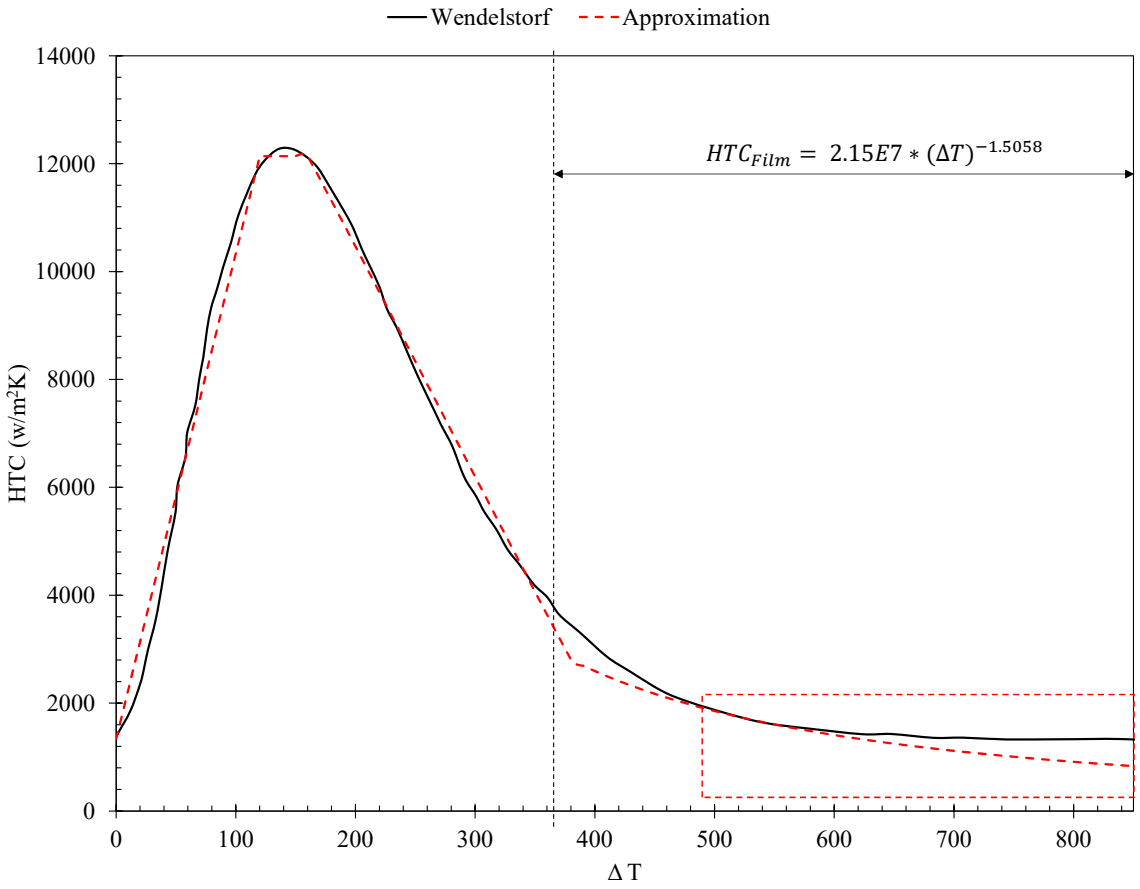

Figure 4.4: Boiling curve for 15 mm skelp thermal model

As the skelp traverses the ROT, the water that is retained on the surface will be removed either from side sprays stationed in between banks, or from the travel velocity. When the water is removed, a constant radiative heat transfer (h_∞) is assumed to occur with a value of 150 $Wm^{-2}K^{-1}$.

A general schematic of the different cooling regions to be modelled is shown in Figure 4.5. For simplicity, only two nozzles are illustrated. Blue and white regions denote areas where film boiling and impact cooling occur, respectively.

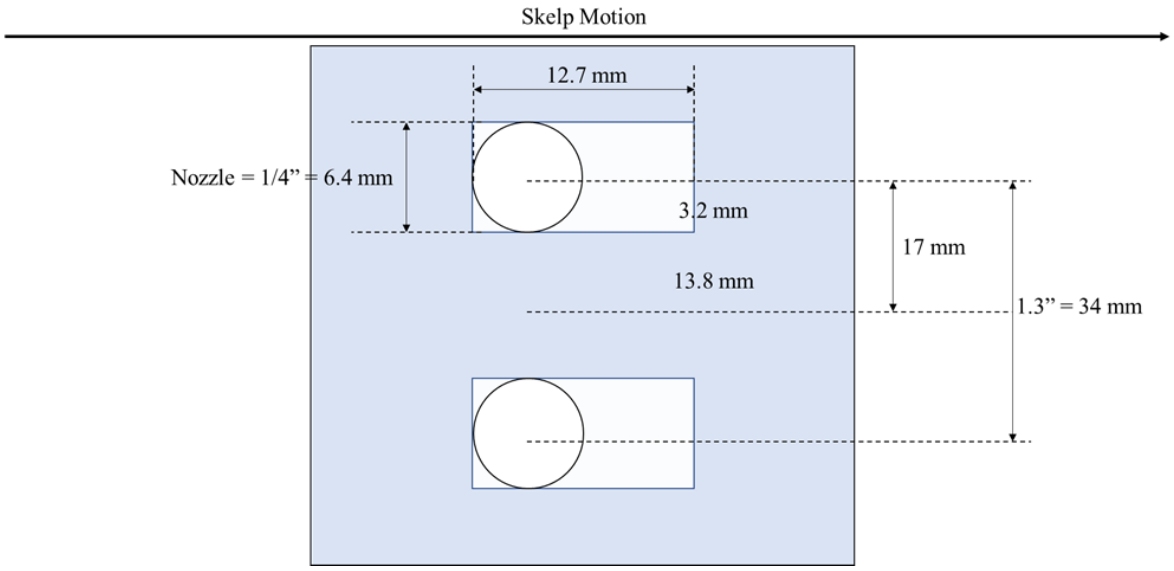

Figure 4.5: Defined boundary conditions for direct impact (white) and film boiling (blue)

Based on the boundary conditions defined in Figure 4.5, a representative 2D transverse slice was taken from the skelp width. Figure 4.6 shows a schematic of the skelp where the black box denotes the region where FEA was conducted. Only a small portion of the skelp was required to be modelled due to symmetry between nozzles and surfaces.

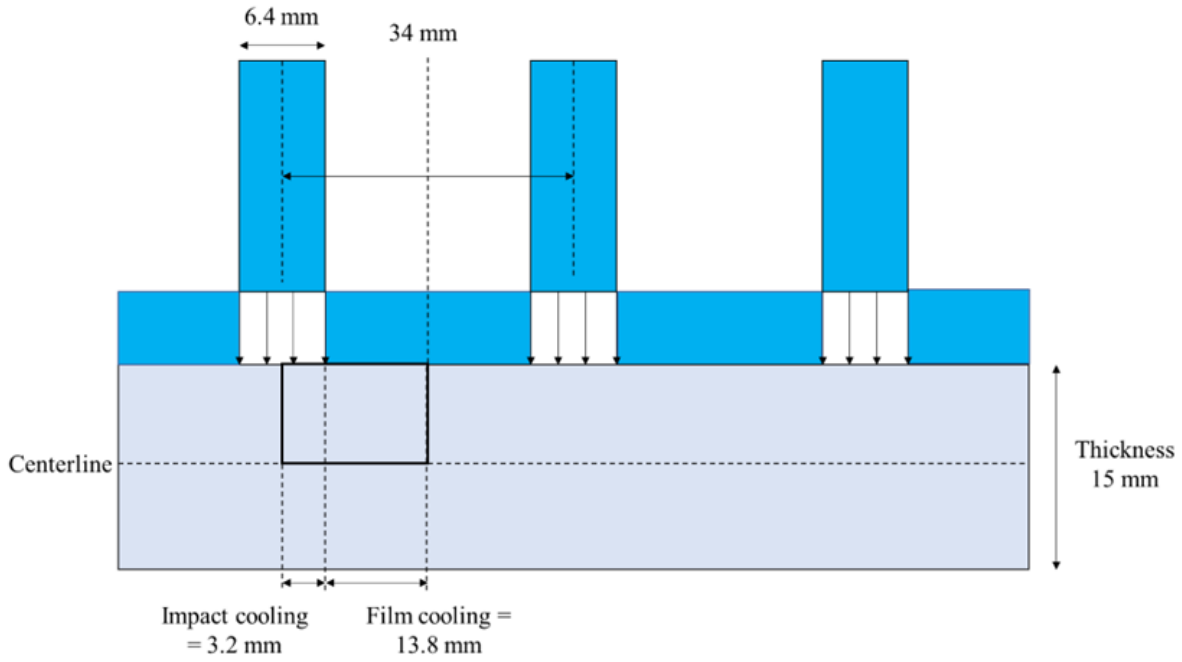

Figure 4.6: Transverse slice of skelp width highlighting FEA region (black box)

4.4 Thermal Finite Element Model Meshing

The FEM was constructed using structured 8-node quadrilateral elements as shown in Figure 4.7. As stated in section 4.3, there is a higher magnitude of cooling under the nozzle that results from the water impact. To more accurately capture the cooling in this region, a finer mesh was used, while in the film boiling region, a coarser mesh was used. Under the impact and film boiling regions, a 4 x 12 and 10 x 12 mesh were used, respectively. In section 4.7, a sensitivity analysis on the effect of mesh size on predicted temperatures is presented.

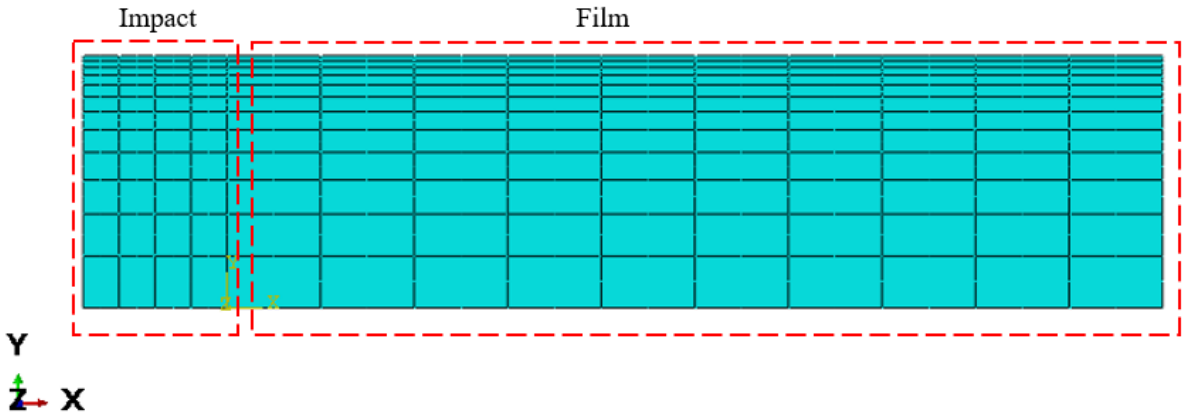

Figure 4.7: Meshing of FEM, illustrating impact and film boiling regions

4.5 Thermal Finite Element Model Results

Simulations replicated the part of the TMCP process between the finish rolling pyrometer and the coiling pyrometer (Figure 4.1). The finish rolling temperature was used as the starting point for the simulation. Using the FILM subroutine in ABAQUS, the ROT cooling parameters (velocity, banks, headers, and heat transfer coefficient values) were input into the model. In Figure 4.8, H1-H6 denote the different headers associated with each bank found on the ROT, and "On/Off" indicate whether they were in operation. Tables of spray patterns for 8-, 11-, and 12 mm products can be found in Appendix C.

	H1	H2	H3	H4	H5	H6
Bank 1	Off	Off	Off	Off	Off	Off
Bank 2	On	On	On	On	On	On
Bank 3	On	On	On	Off	Off	Off
Bank 4	Off	Off	Off	Off	Off	Off
Bank 5	Off	Off	On	Off	On	Off
Bank 6	Off	Off	Off	Off	Off	Off
Bank 7	Off	Off	Off	Off	Off	Off

Figure 4.8: Run out table configuration for X70 sample

To capture the effect of impact cooling from each header, a step size of 2E-3s was used. Considering the velocity of the skelp (2 m/s), this results in approximately 4 mm per increment during simulation.

Figure 4.9 illustrates the final temperature profile of the FEA model prior to coiling. Of note here is that the final predicted surface temperature ($0.650T_{finish}$) varied minimally from the measured value ($0.649T_{finish}$). Through this simulation, the temperature history of each node is index-able, which allows for the determination of the non-continuous cooling rate at any point in the model. Nodes of interest for microstructure evolution predictions are labelled CL1-3, QL1-3, and S1-3 left to right in Figure 4.9. CL, QL, and S stand for center line, quarter line, and surface, respectively. The temperature versus time profiles of nodes CL1-3, QL1-3, and S1-3 were plotted in groups as illustrated by the black boxes in Figure 4.9 (Figures 4.10, 4.11, and 4.12).

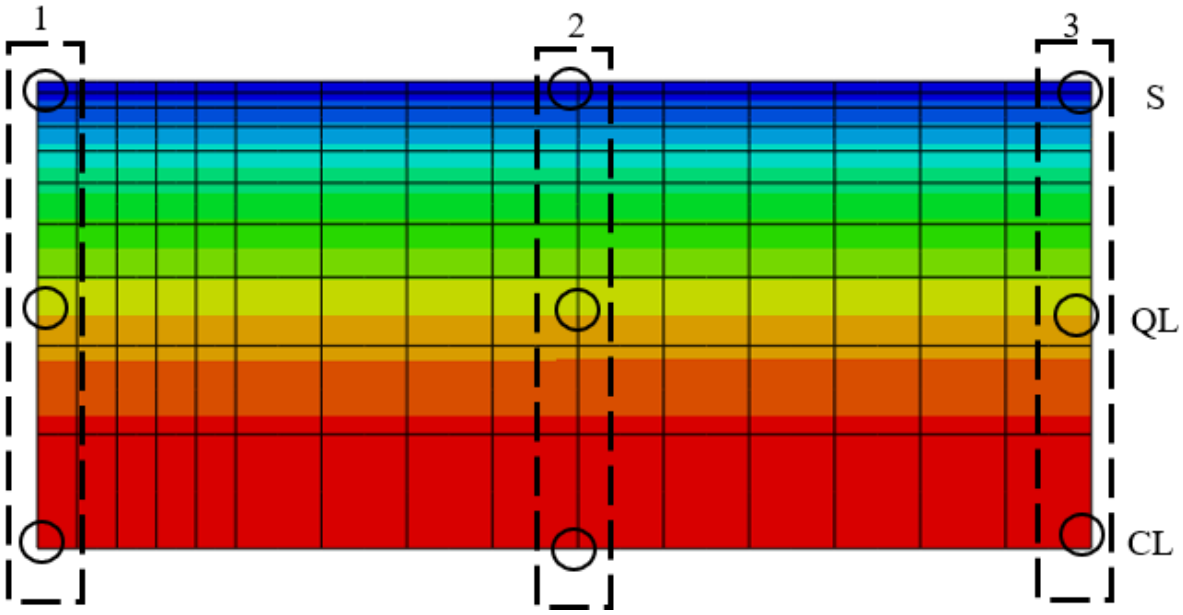

Figure 4.9: Final temperature profile of model prior to coiling

Figure 4.10 is the temperature profile through the thickness of the skelp directly below the nozzle. Underneath the nozzle (node S1) the cooling mechanism is single-phase convection which yields a high heat transfer coefficient and thus a higher heat flux. This results in the observed vertical lines shown in Figure 4.10. Following the last operational header in each bank, the water on the skelp surface is removed resulting in only radiation cooling occurring. Radiation cooling is unable to maintain the previously imposed temperature gradient, and this results in a partial reheating of the surface [112]. At the quarter (QL1) and center lines (CL1), the cooling rates are more stable as they do not experience cooling from the direct impact of water from the nozzle. The cooling rates imposed by the banks at the quarter and centerline are approximately 15 ℃/s and 10 ℃/s, respectively. For all 3 nodes, the radiative cooling rates are approximately the same at 2 ℃/s. Figures 4.11 and 4.12 show the through thickness temperature profiles for the regions denoted by black boxes 2 and 3 in Figure 4.9. There is little variation between these two regions.

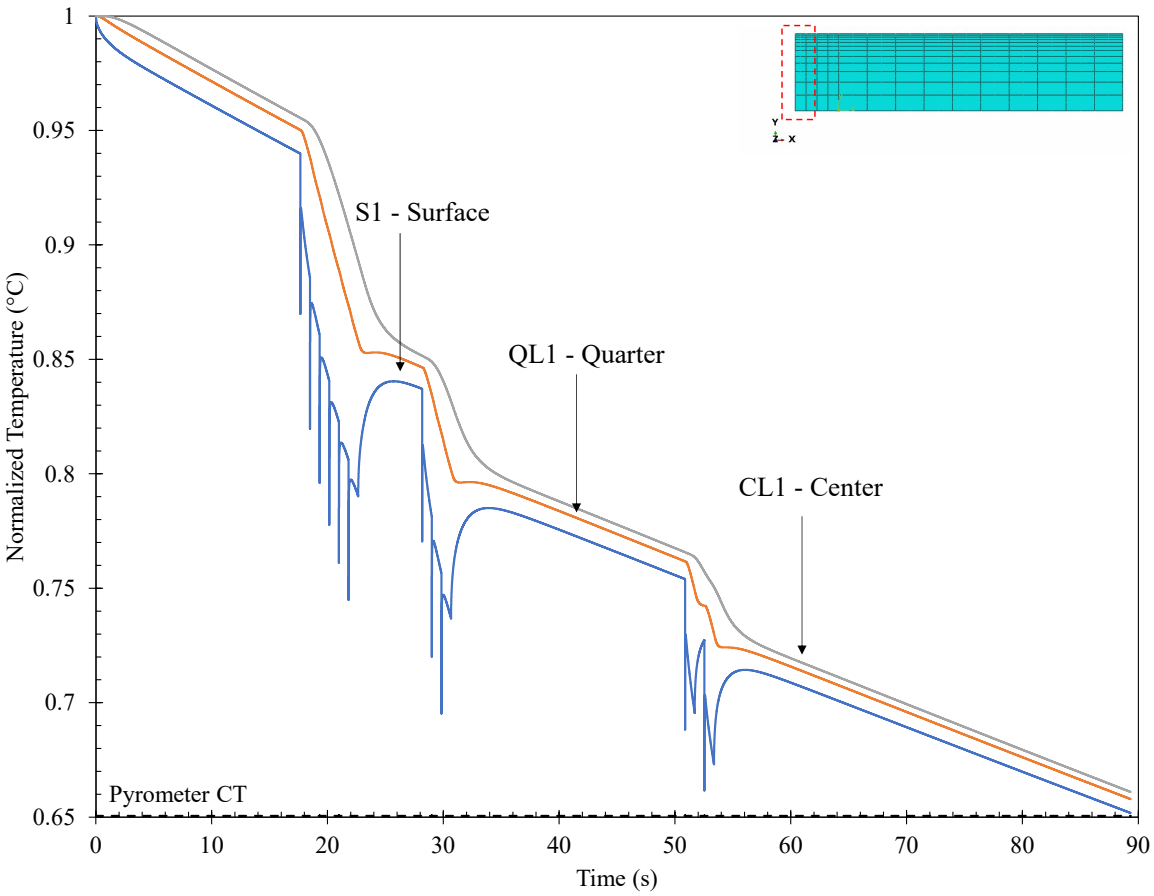

Figure 4.10: Temperature history of nodes QL1, CL1, and S1

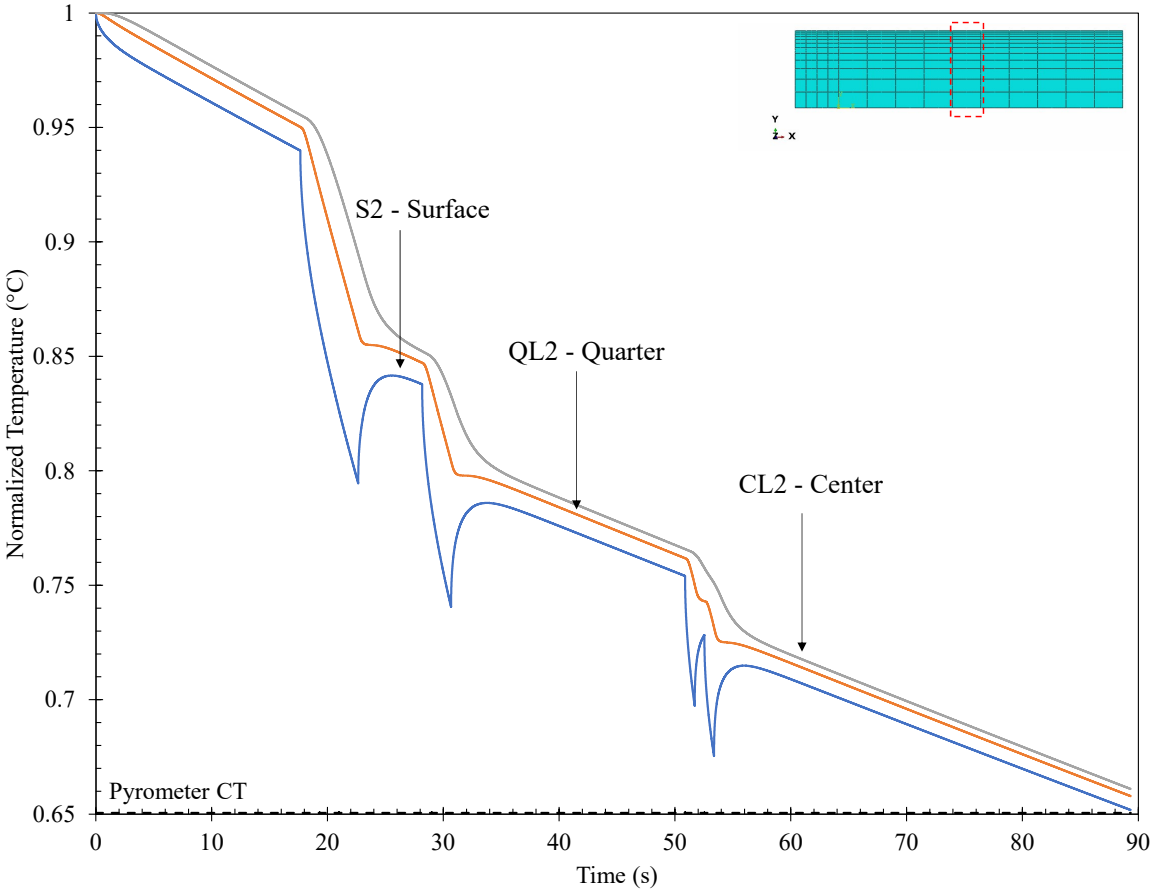

Figure 4.11: Temperature history of nodes QL2, CL2, and S2

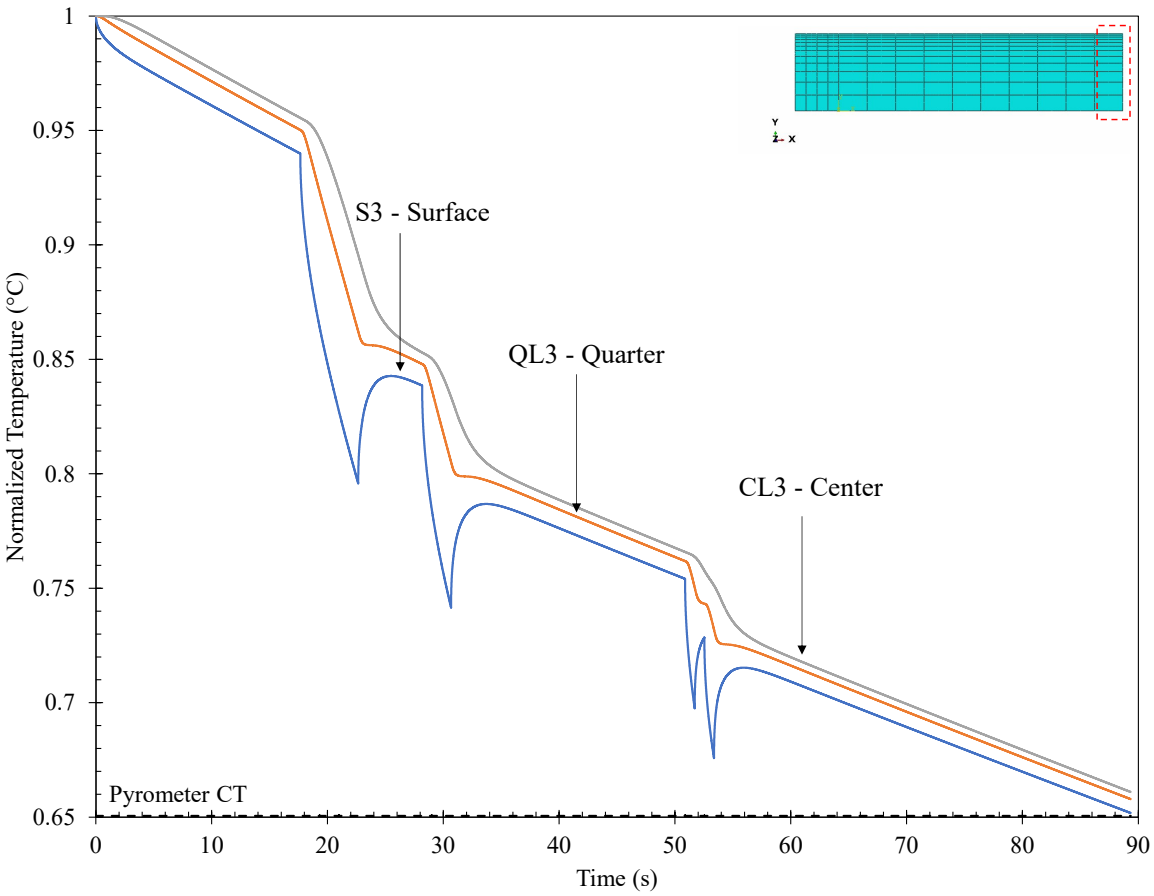

Figure 4.12: Temperature history of nodes QL3, CL3, and S3

4.6 Validation of Thermal Finite Element Model

A process pyrometer is used to measure the temperature of the skelp surface prior to coiling. This gives the instantaneous temperature of a specific region on the skelp surface and not the full transverse temperature profile. To circumvent this problem, an IR camera was installed in parallel to the pyrometer to measure the full temperature profile of the skelp surface. For the 15 mm sample, the coiling pyrometer measurement ($0.65T_{finish}$) was used as the validation temperature, while for 8-, 11-, and 12 mm simulations, IR camera readings were used. No 15 mm skelp were available during IR plant trials.

A Telops FAST IR camera (detection band of 3 – 5 μm) was used to measure the entire surface temperature profile of the skelp. The camera was positioned 5 m above the surface to capture approximately the full width (field of view was 1.8 m by 1.4 m) of the skelp as it moved from the laminar cooling system to the coiler. The pixel resolution of the camera was 2.7 mm x 2.7 mm with a total of 327,680 pixels in the field of view. A camera acquisition rate of 0.2 s was used and coordinated with the skelp velocity to ensure that the entire skelp surface was imaged. Lastly, an exposure time of 50 μs was used. The IR camera was calibrated to the pyrometer to ensure that both reported the same CT. Figure 4.13 compares the pyrometer and IR camera measurements after calibration for the 12 mm skelp (15 mm skelps were not run during plant trials), all other calibration curves can be found in Appendix C. The calibration process included varying the probing size, probing region, and emissivity to match the pyrometer readings. For the 12 mm skelp, a 200 mm diameter circle at the $\frac{1}{4}$ width with an emissivity of 0.86 was found to be the best match.

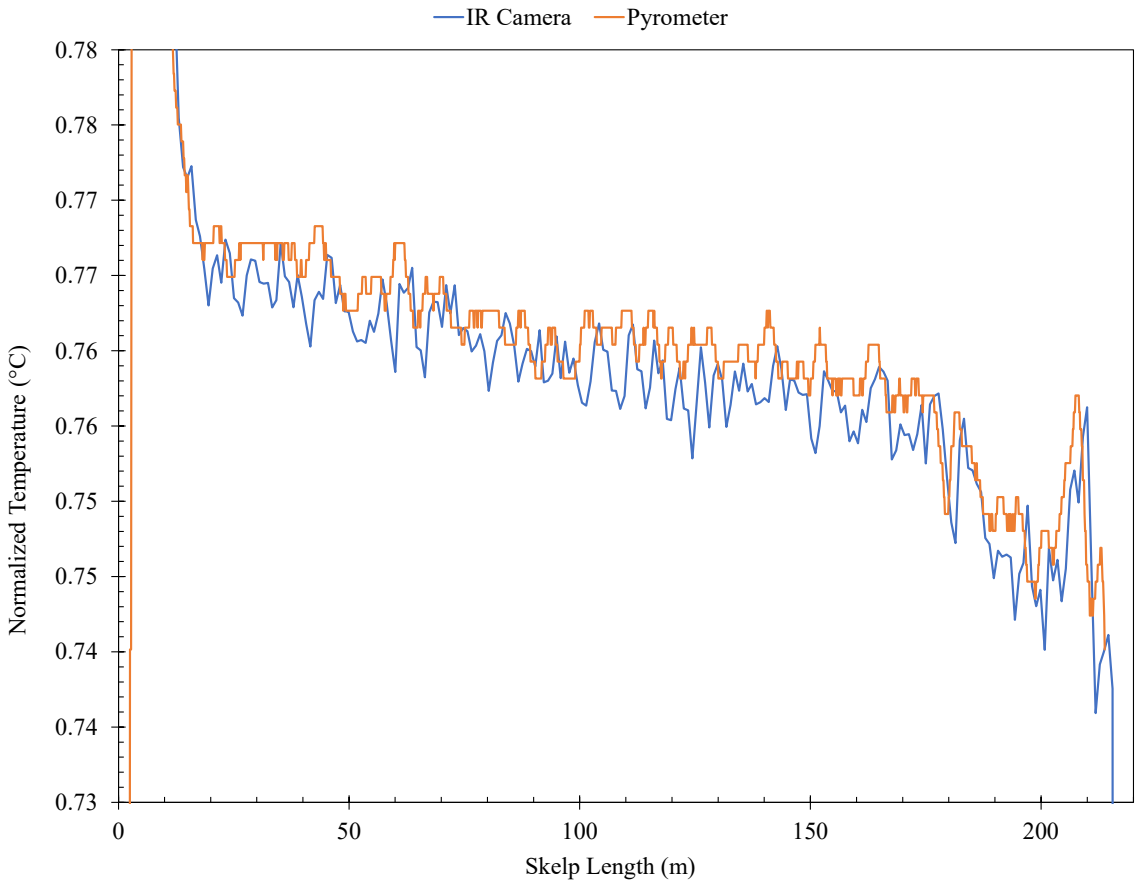

Figure 4.13: Process pyrometer and IR temperature measurements for 12 mm skelp

Using the calibrated IR videos, the transverse temperature profile of individual frames were measured. Figure 4.14 is a temperature map for a single image captured (Frame 280 of 12 mm skelp) along the length of the skelp. The dashed line shown in the figure is the location of a single transverse temperature profile.

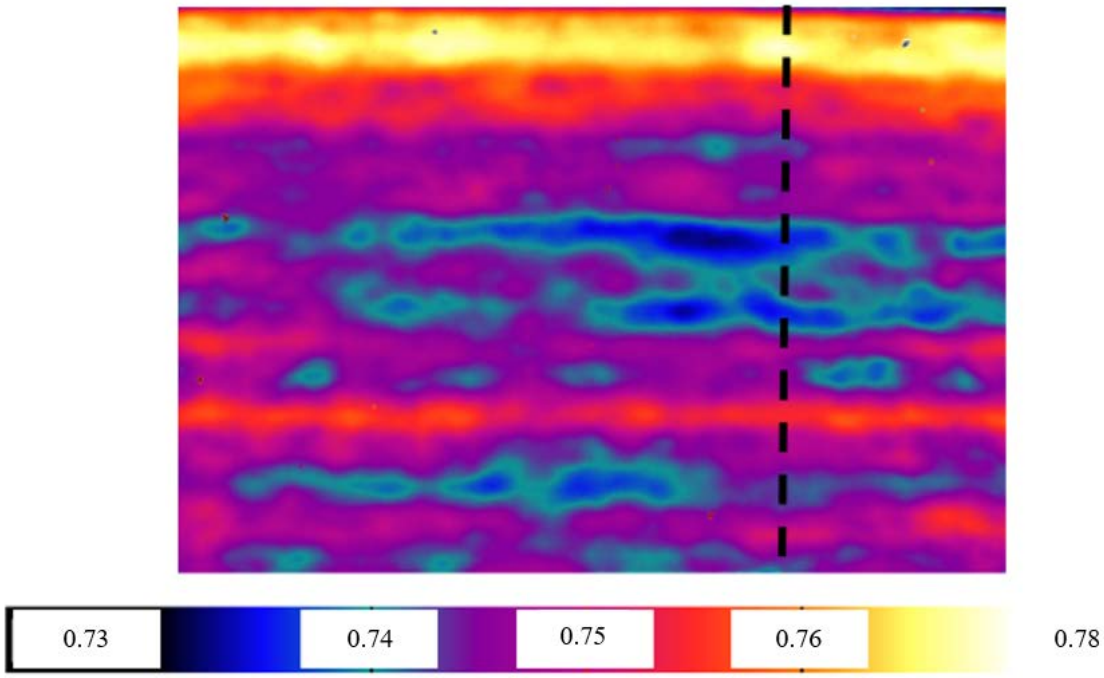

Figure 4.14: Surface temperature profile of a 12 mm skelp prior to coiling (Frame 280)

Figure 4.15 graphs the surface temperature across the width of Frame 280 (dashed line in Figure 4.14). The temperature fluctuations observed in this figure were present in all the IR frames measured for every skelp assessed during plant trials. For Frame 280, the temperature oscillations reached a max of $0.03T_{finish}$. The magnitude of these oscillations exceeds the predicted surface temperature fluctuations observed from FEM. From FEM, minimal temperature variations (< 1 °C) were predicted across the skelp width.

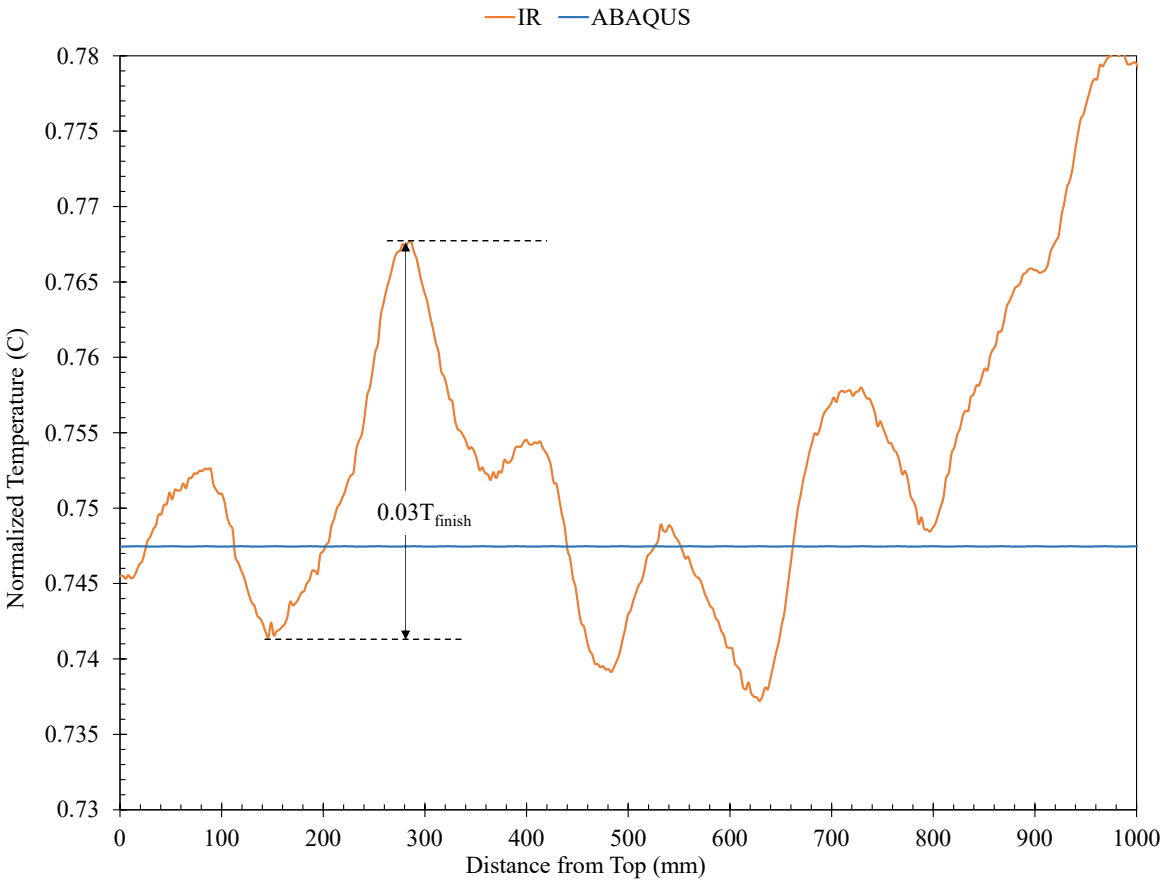

Figure 4.15: Transverse temperature profile across dashed line in Figure 4.14 compared to FEM (Frame 280)

For the thermal model results shown in Figures 4.10, 4.11, and 4.12, it was assumed that there was nothing on the surface of the skelp that would affect the cooling profile. Since this is not the case, as is evident through the results illustrated in Figure 4.15, in the following section a methodology to correctly identify and analyze these spots will be presented. Once analyzed, their effect on the subsequent cooling profile through the thickness of the skelp was assessed in chapter 6.

4.7 Sensitivity Analysis

A sensitivity analysis was conducted on the thermal model, where the impact of three parameters were examined. The first was the latent heat of transformation between austenite and ferrite. Next, the effect of increasing and decreasing the mesh was investigated. Lastly, varying the step size was examined. For all sensitivities, only the surface node under the nozzle was analyzed.

4.7.1 Latent Heat of Transformation

Shown in Appendix A, the latent heat of transformation was taken to be 18 kJ/kg and assumed to be be released linearly over the temperature range of 550 ℃ - 700 ℃ [41]. By doing this, variation of ferrite transformation start and stop temperatures with cooling rate were ignored. To determine the effect that the transformation range has on the cooling profile, two additional simulations were conducted. Figure 4.16 shows the effect of increasing the range to 500 ℃ - 775 ℃ and decreasing the range to 550 ℃ - 650 ℃.

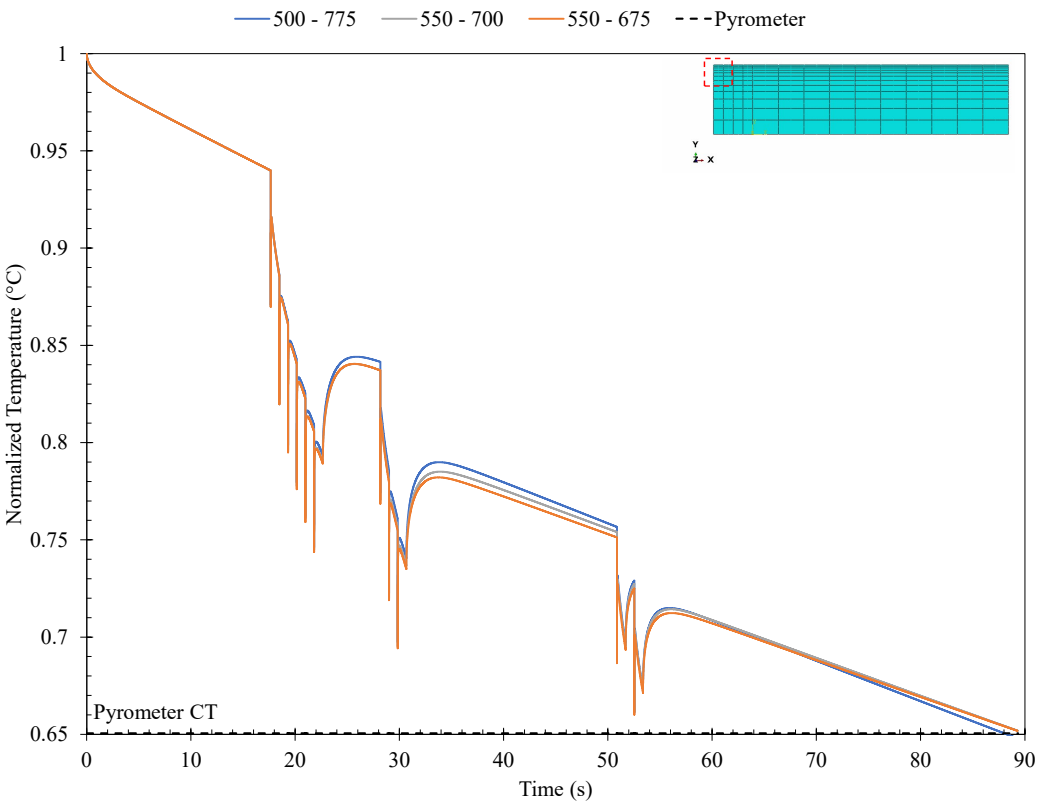

Figure 4.16: Effect of varying austenite to ferrite latent heat of transformation range to 500 ℃ - 775 ℃ and 550 ℃ - 650 ℃ (Surface node under nozzle)

The value of latent heat was also taken as an approximate value. From literature, this value has been shown to be very sensitive to various process parameters such as carbon content [113]. To assess its effect on temperature profiles, two more simulations were run with latent heat values of 14 kJ/kg and 25 kJ/kg. Figure 4.17 shows the results from these tests.

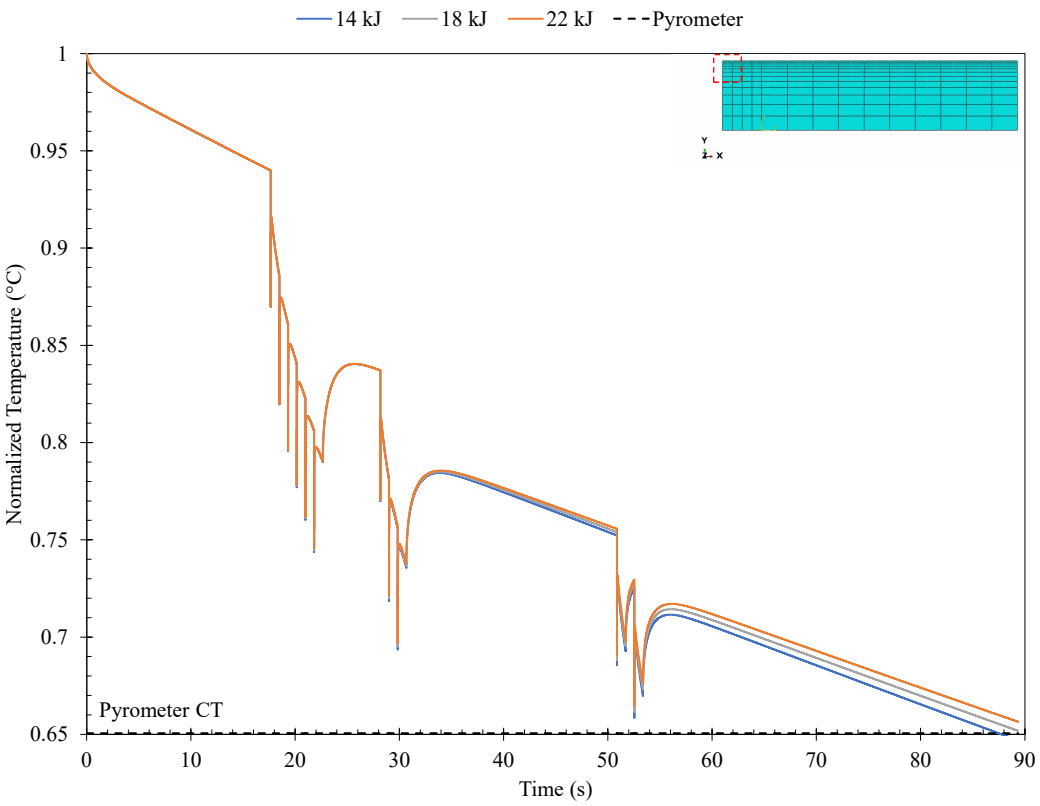

Figure 4.17: Effect of varying latent heat value between 14 kJ/kg, 18 kJ/kg, and 22 kJ/kg (Surface node under nozzle)

4.7.2 Mesh Size

Since the mesh determines both the accuracy and computation time of the simulation, the effect of varying this parameter is needed. The original model utilized 50 elements underneath the impact cooling region and 100 elements underneath the film boiling region. In each of these regions, the total number of elements were first increased and then decreased to elucidate any changes. Total element amounts were initially increased to 600, and then subsequently decreased to 40. Results from these simulations are shown in Figure 4.18. As can be seen in these images, the resulting CT from doubling the mesh ($0.652T_{finish}$) was the same compared to the mesh originally used. For the halved mesh,

the CT was slightly colder at $0.649T_{finish}$. The most significant effect that mesh size had on model performance was how it varied the magnitude of impact cooling. For normal and larger mesh sizes, the magnitude of impact cooling converged to the same values, but with a small mesh, it was reduced and varied.

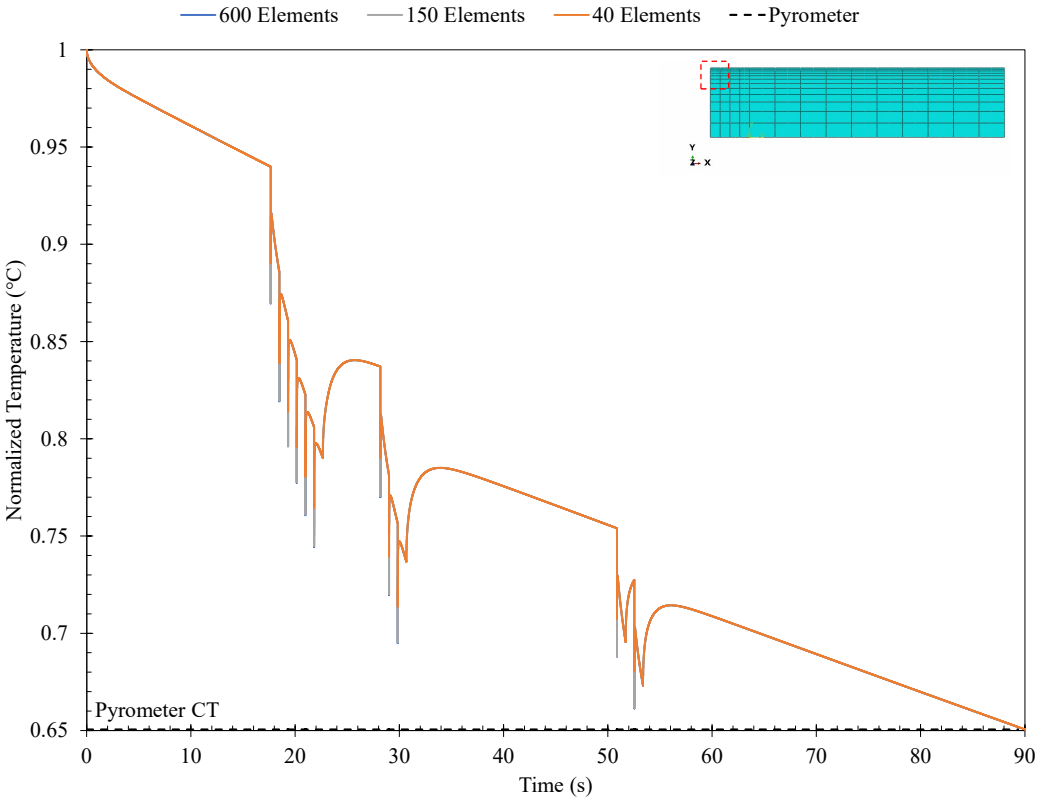

Figure 4.18: CT profile when node amount is increased and decreased

4.7.3 Step Size

The step size was found to have the largest effect on model performance. This was due to the two different cooling mechanisms occurring on the ROT. Shown by Figure 4.5, the region in which impact cooling occurs is very small. If the step size is too large, then the effect of direct impact between the water and the skelp surface will be missed. For the original model, shown in the previous section, a step size of 0.002 seconds was used,

but by using a small step size, this increases the computational time needed for each simulation. As such, the effect of increasing this parameter was examined to determine whether or not the effect of direct impact could still be captured while also decreasing computational time. Figure 4.19 shows the cooling paths for step sizes of 1 second and 0.01 seconds, respectively. Shown by these figures is the inability of the model to pick up the effect of direct impact at larger step sizes, this is illustrated by the lack of some extreme cooling regions (vertical lines) where a header is on.

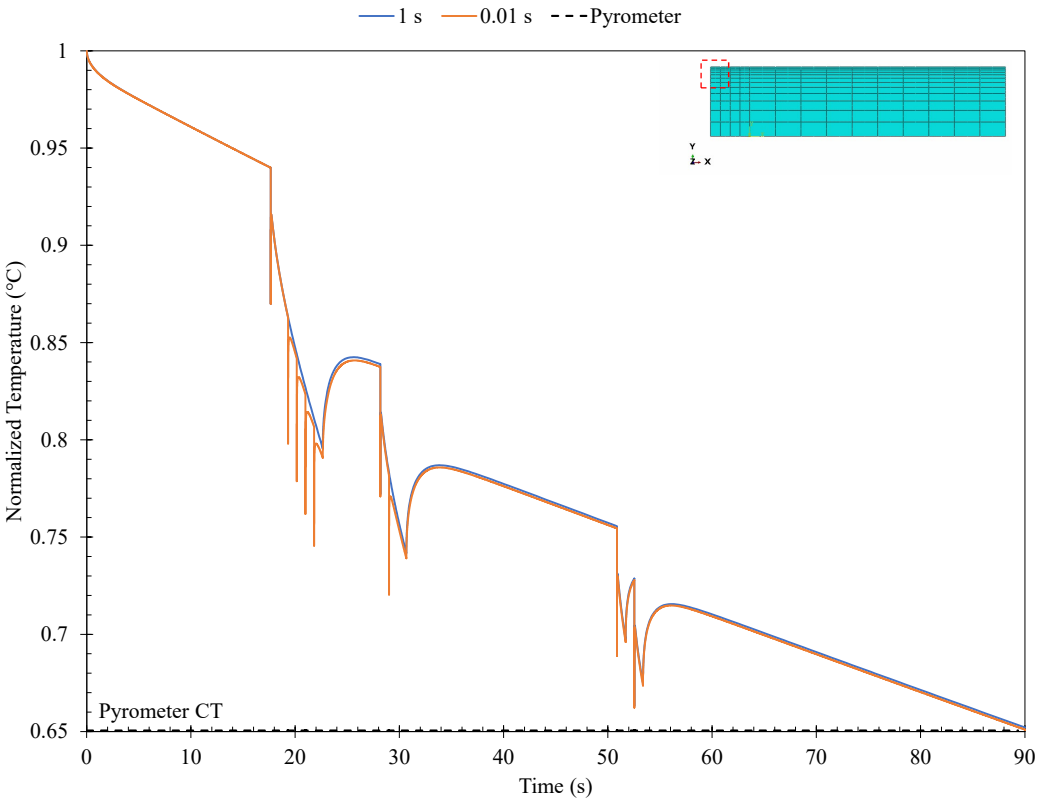

Figure 4.19: CT profile for 1 and 0.01 second step size

4.8 Summary

Thermal models for 8-, 11-, 12-, and 15 mm thick skelps traversing the ROT were made. The models analyzed the 2D heat transfer of a transverse slice of the skelp, ignoring heat flow in the longitudinal direction. Specific ROT spray configurations were programmed into the model through use of the FILM user-defined subroutine within ABAQUS. A modified film boiling curve based on the work of Wendelstorf et al [36] was used as a fitting parameter for the model. Through varying the film boiling curve, the model was able to accurately predict the coiling temperature while also exhibiting the different cooling mechanisms expected on the ROT. Both a pyrometer and IR camera were used for validation of the model. From comparing the IR measurements taken of the 12 mm skelp to those predicted from the model, large discrepancies were observed. Large temperature fluctuations were recorded with the IR camera which had not been predicted through modelling. These fluctuations were observed in all IR videos taken, so a method to characterize and assess them is presented in chapter 5.

Chapter 5

Cold Spot Classification and Analysis

Based on the observations made during IR video imaging of the skelp, it was determined that there were anomalous temperature values present on the surface. These temperature anomalies were attributed to the presence of surface oxides (scale). In this chapter, the techniques developed to identify and analyze the anomalous temperatures are presented, and their subsequent effect on cooling rate is explored. Section 5.1 presents the distribution of surface temperatures for a full skelp. In section 5.2 a classification technique is developed to isolate abnormal temperatures from normal ones. Section 5.3 illustrates the effect of surface oxides on the skelp temperature profile. Lastly, in section 5.4 an analysis of the oxide area fraction and location is shown, and then related to the descaler nozzle positions.

5.1 Temperature Distributions of Individual Frames

Within an IR video, there are approximately 132 million individual temperature measurements. Although there are many factors that influence the recorded temperature values (air quality, angle, surface roughness, etc.), the most impactful parameter is the emissivity. Since calibration is conducted for a single region and not for every pixel,

this is assumed to cause the overall temperature distribution to be normal. Figure 5.1 shows the distribution of temperatures for the entire 12 mm skelp run, calibrated to a single emissivity (0.86). The measured data (blue curve) was fit to a normal distribution (orange curve), resulting in a mean and standard deviation of $0.75T_{finish}$ and 7 ℃, respectively. Of note in this distribution is the presence of peaks at higher temperatures (A1 and A2) and one at lower temperatures (B1). After assessing all IR videos taken, the edge of the skelps consistently showed higher temperature values then the rest of the surface. This may be a result of skelp buckling which effects the emissivty. Buckling may be occuring due to either non-uniform cooling across the skelp width, a mis-match of coolings between the top and bottom, or the cooling rate being too large for how thin of a gauge the skelp is. For the low temperature peak (B1), this was the result of the anomalous cold temperatures. This was suggested by the observation that the temperature of these colder regions aligned well with the position of this peak.

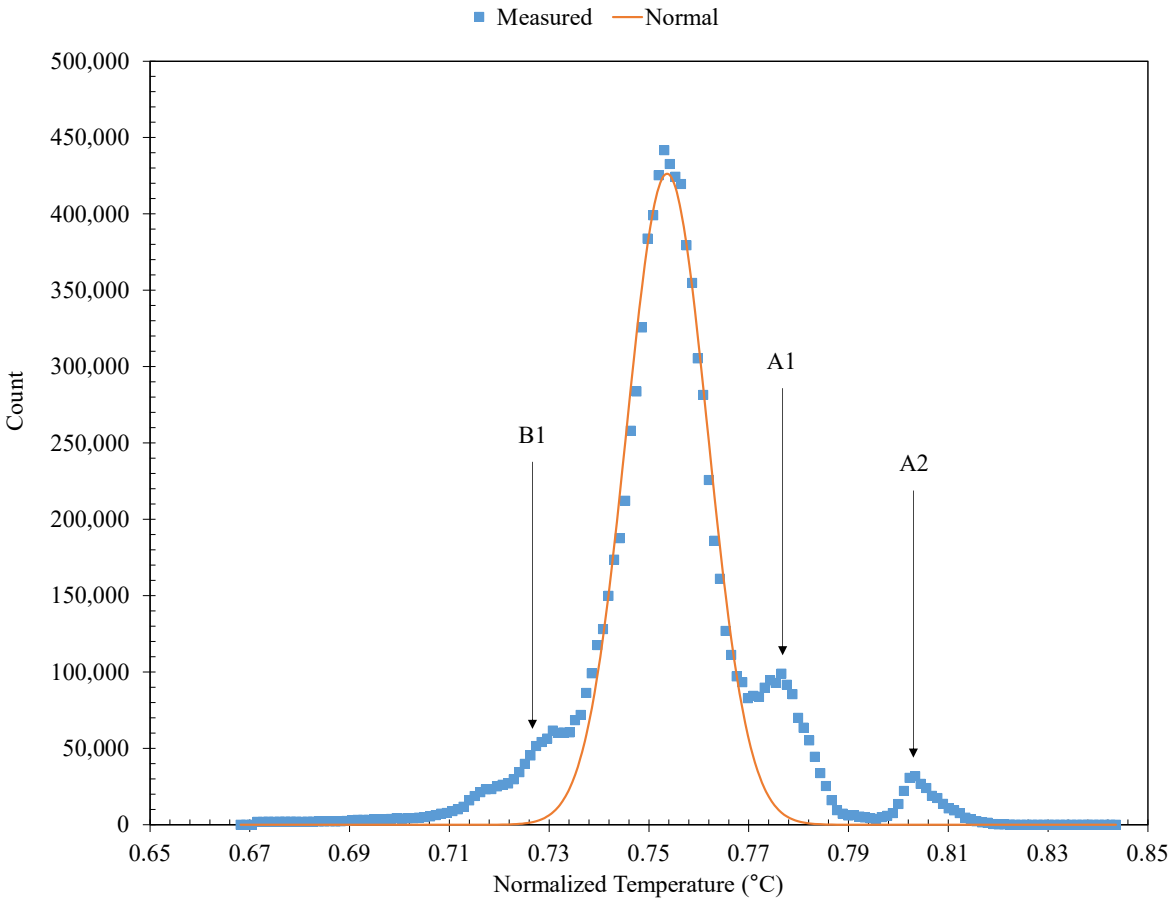

Figure 5.1: Temperature measurement of entire 12 mm skelp surface fit to a normal distribution

According to the central limit theorem, for a population with mean μ_p and standard deviation σ_p, if large enough sample sizes are taken from it, then the distribution of the samples will be normal. Within the IR video, individual frames consist of 327,680 temperatures which constitutes a large enough sample size that it should follow a normal distribution. Figure 5.2 is the temperature values fit to a normal distribution for Frame 280. Highlighted by the dashed red box is the region where the measured data begins to deviate from the normal distribution. A magnified view of the region encompassed by the dashed red box is shown in Figure 5.3.

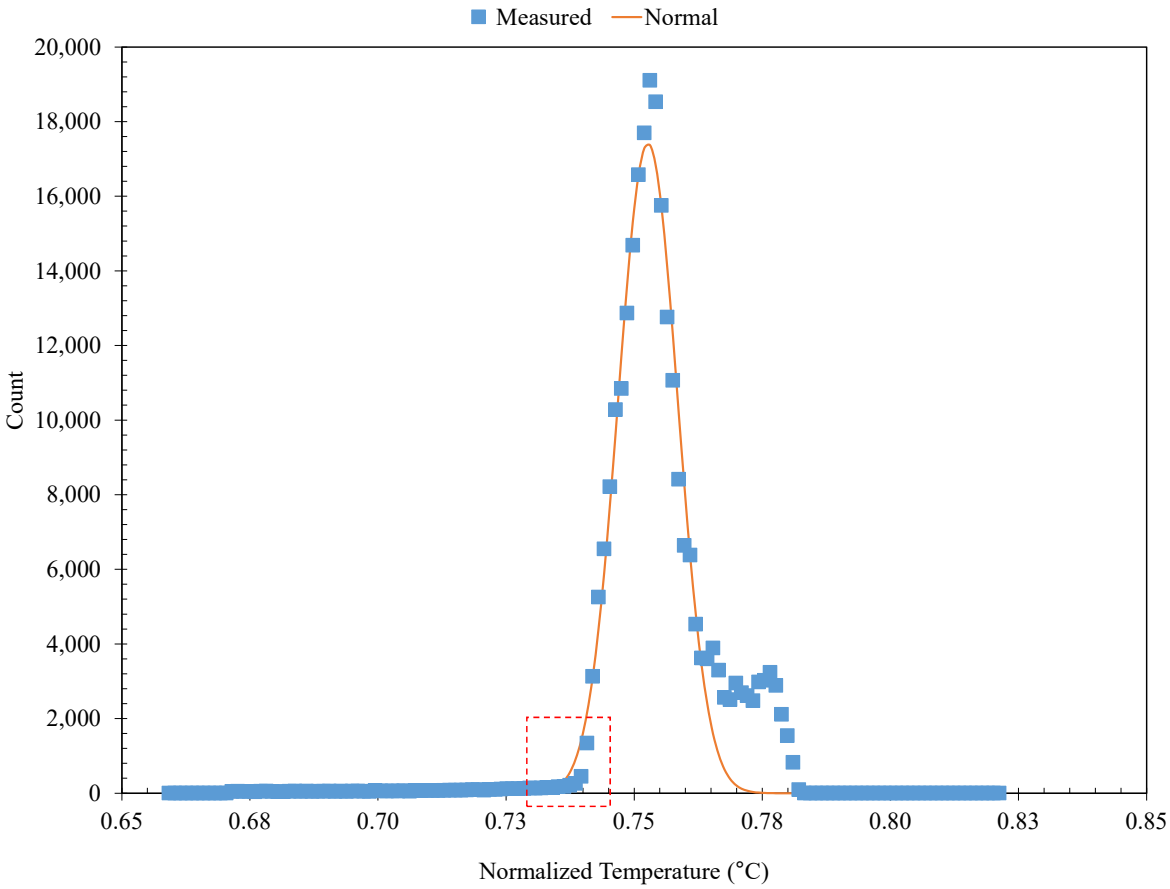

Figure 5.2: Temperature measurements for Frame 280 fit to a normal distribution

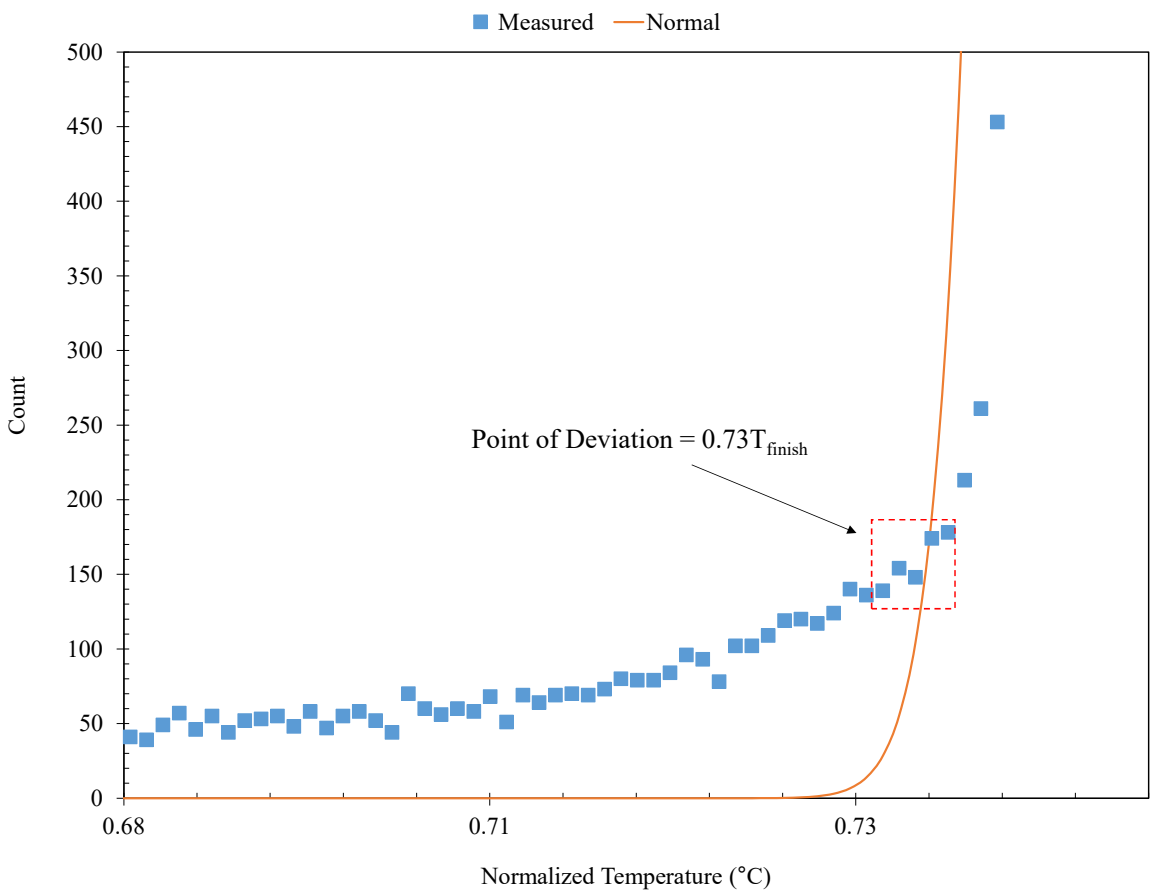

Figure 5.3: Magnified view of red box in Figure 5-2 illustrating the point of deviation

Using this point of deviation to delineate between lower temperatures natural to the process and those that are abnormal, a temperature threshold value was determined for individual frames in 10 m intervals. Through using 10 m intervals, the assumption was made that within those intervals the threshold value does not vary. Figure 5.4 shows Frame 280 before and after applying the threshold temperature of $0.73T_{finish}$. Regions that appear black fell below the determined threshold value for the frame.

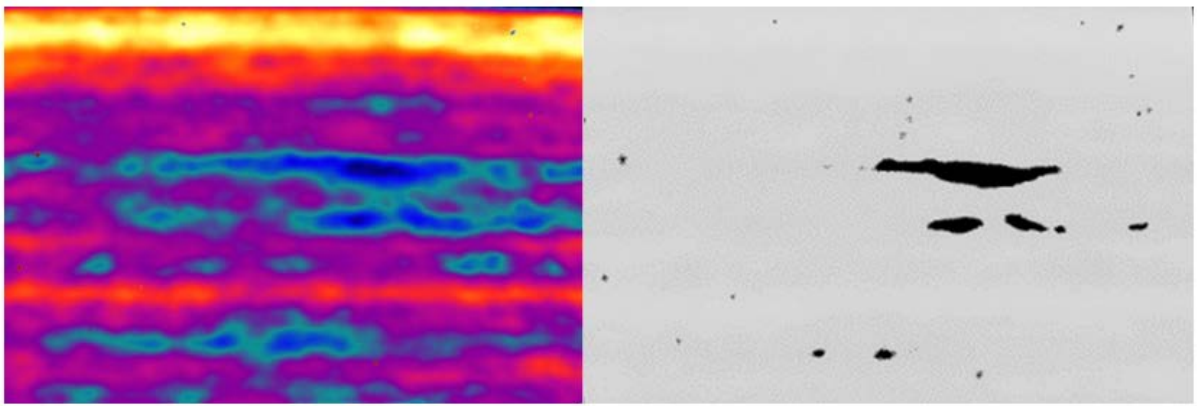

Figure 5.4: IR video frame before (left) and after (right) applying temperature threshold

5.2 Classification of Cold Spots

It was hypothesized that these cold spots were the result of oxides present on the surface of the skelp. From this hypothesis, a FEM was used to predict the surface temperature of the skelp before coiling with the presence of oxides. The model presented in chapter 4 was modified to include the presence of a 100-, 200-, 300- , 400-, and 500 μm oxides. Material properties for different oxides are shown in Appendix D. Since the oxide formed during TMCP is a combination of three iron oxides (wüstite, magnetite, and hematite), a linear combination of the expected volume fraction multiplied by the property value was assumed for the overall oxide, equation 5-1. Expected volume fractions for wüstite, magnetite, and hematite were taken as 46 %, 44 %, and 10 %, respectively, as suggested by the work of Abuluwefa et al [114].

$$P_{avg} = \sum_{i=1}^{n} f_i * P_i \tag{5.1}$$

In this equation, P_{avg} is the average property, f_i is the fraction of each component, and P_i is the property of each component.

The results for 12 mm model simulations with and without a 500 μm oxide are

shown in Figure 5.5, where the node analyzed was at the surface underneath the nozzle. Although the minimum temperatures reached by each varies ($0.60T_{finish}$ with oxide and $0.76T_{finish}$ without oxide), they both converge at the same CT ($0.75T_{finish}$). The same observations were made for the 100-, 200-, 300- , and 400 μm oxide simulations which suggests that the surface CT is independent of the presence and thickness of oxides.

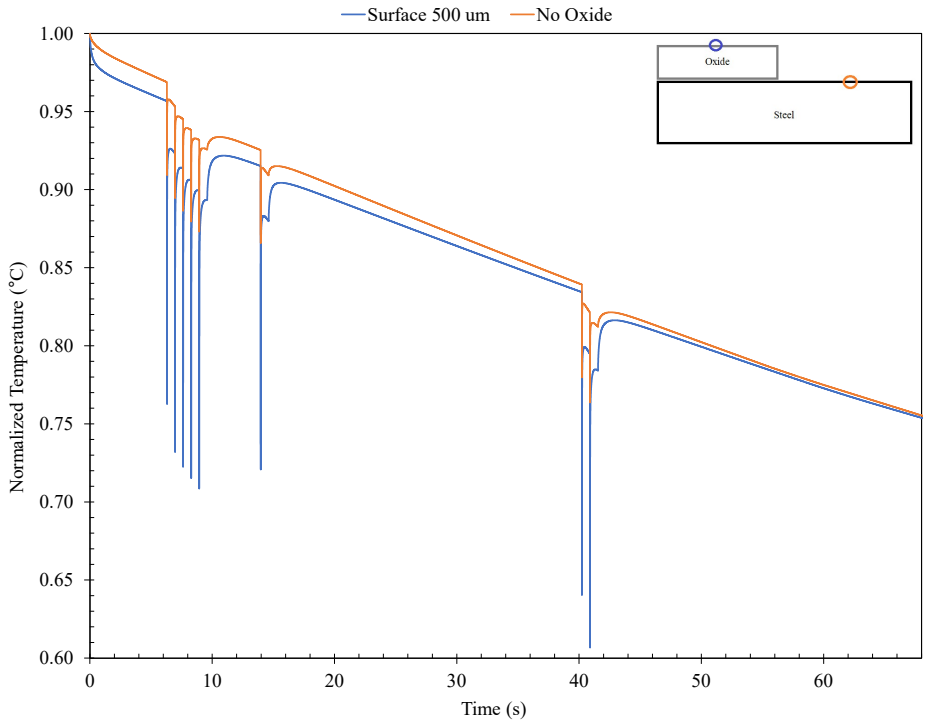

Figure 5.5: Surface temperature during laminar cooling with and without the presence of 500 μm oxide

Based on the observation that coiling surface temperature is independent of oxides, the emissivity required to correct each temperature anomaly was determined. Emissivity values of cold spots ranged from 0.78 – 0.83. This range agrees well with reported values of oxidized steel from literature [57]. From this, it was concluded that the large temperature fluctuations observed were due to differences in localized emissivity values arising from oxides.

5.3 Effect of Oxides on Steel Temperature Profile

Through the presence of an oxide on the skelp surface, there are slight variations in the imposed cooling profiles observed from FEM. Figure 5.6 illustrates the predicted differences in cooling profiles at the steel surface for a 500 μm oxide compared to no oxide underneath the nozzle. Although the regions of radiative cooling (linear regions) are very similar with only approximately 0.3 ℃/s differences in cooling rates, the regions of interest are where the water directly impacts the skelp (vertical drops). The oxide shields the skelp surface, reducing the magnitude of cooling imposed from each header.

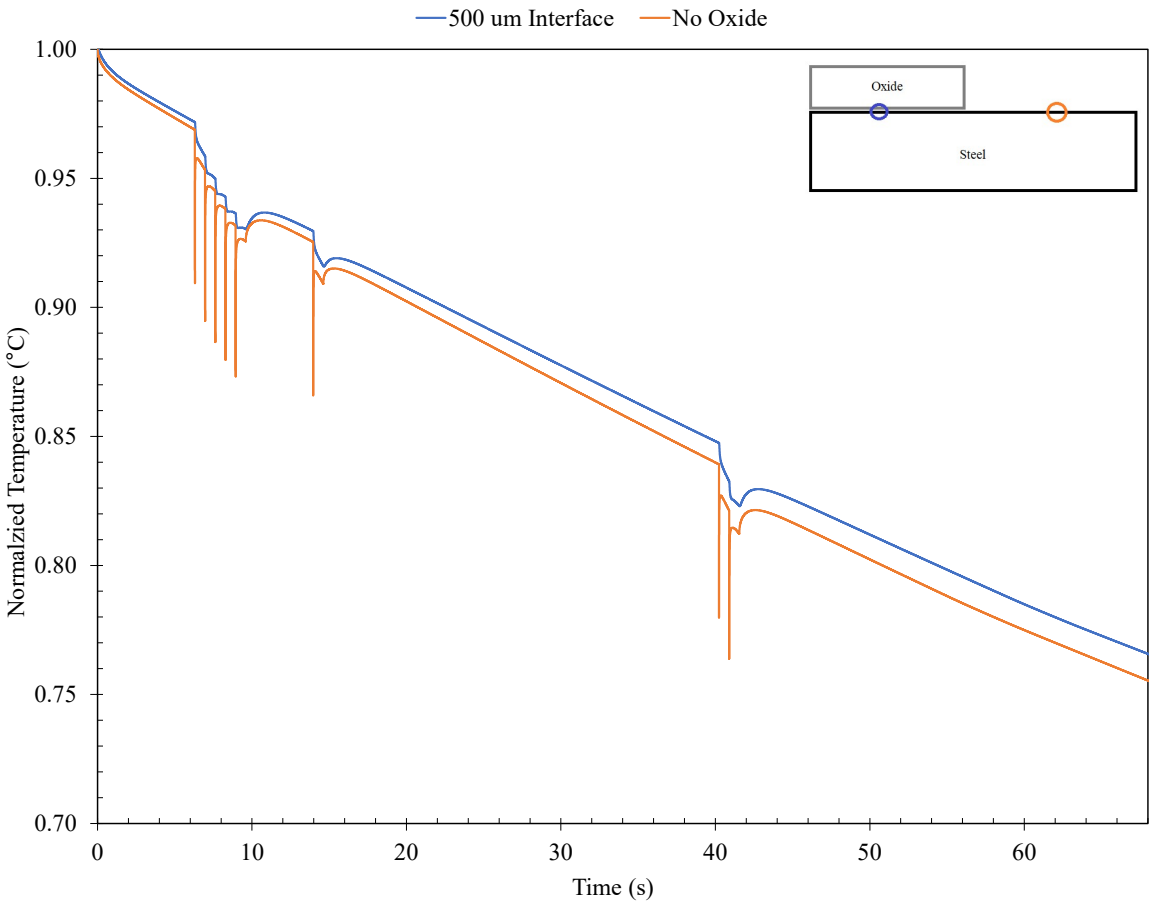

Figure 5.6: Steel surface cooling profile with and without the presence of a 500 μm oxide underneath the nozzle

Through thickness temperature profiles underneath the nozzle, quarter distance to the next nozzle, and halfway to the next nozzle were also generated, Figures 5.7, 5.8, and 5.9. In each instance, the oxide slightly reduced the cooling rates experienced by the skelp, resulting in CTs that varied by approximately 8 ℃ in each location. In chapter 6, when the thermo-metallurgical model is presented, the effect of changing the cooling profile on the microstructure will be explored.

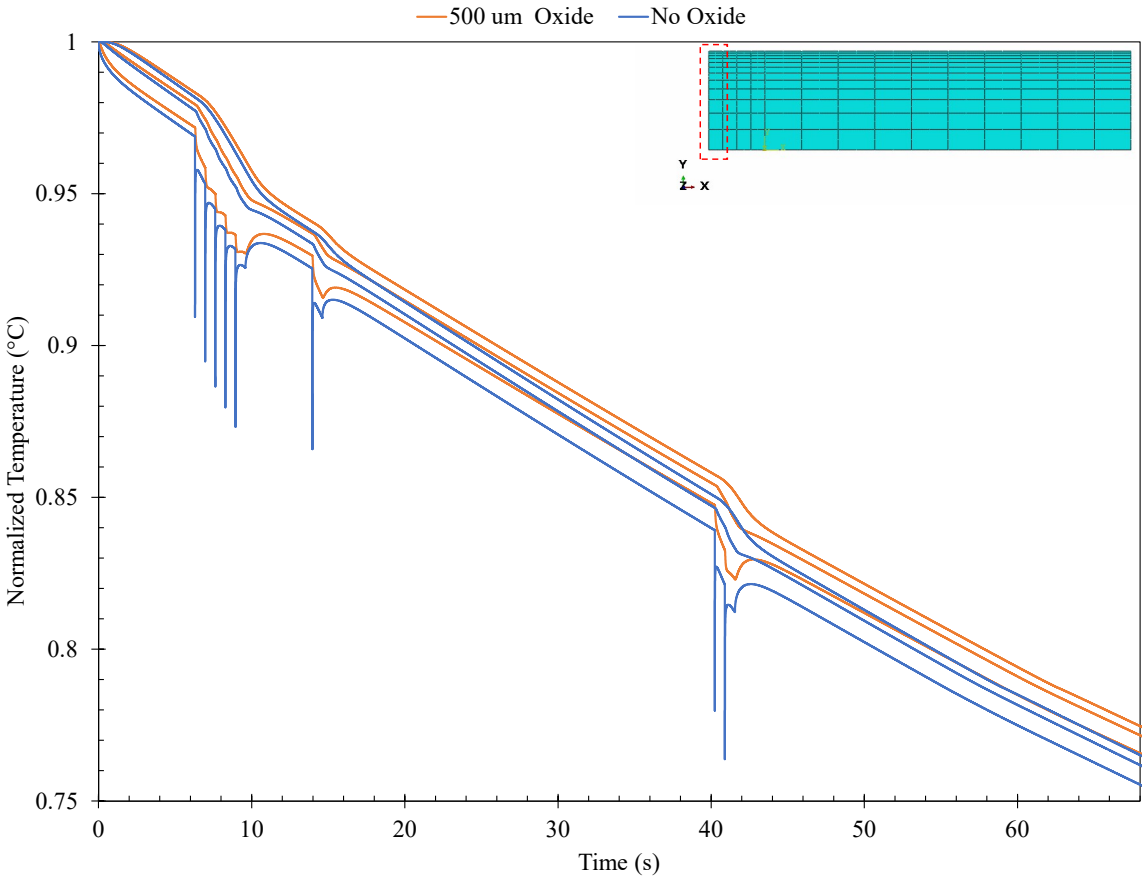

Figure 5.7: Through thickness temperature profile under nozzle with and without oxide

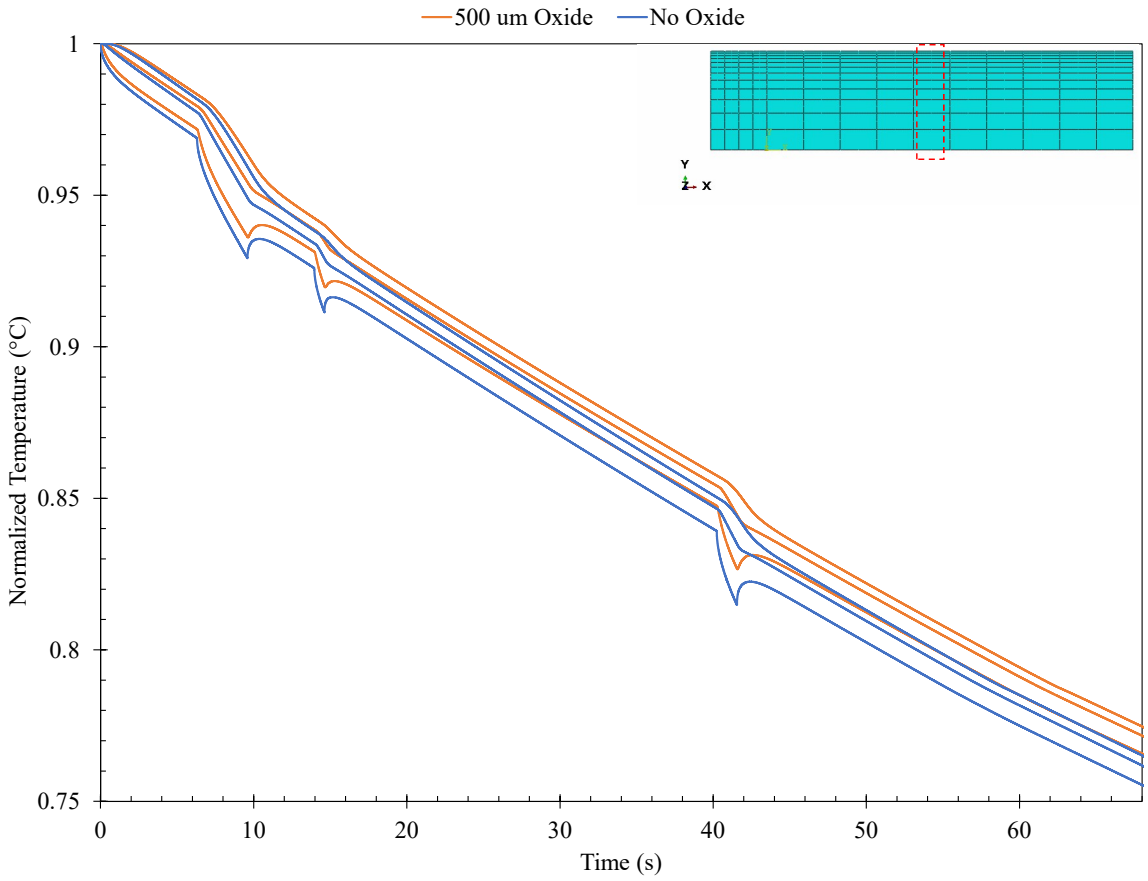

Figure 5.8: Through thickness temperature profile quarter distance between nozzles with and without oxide

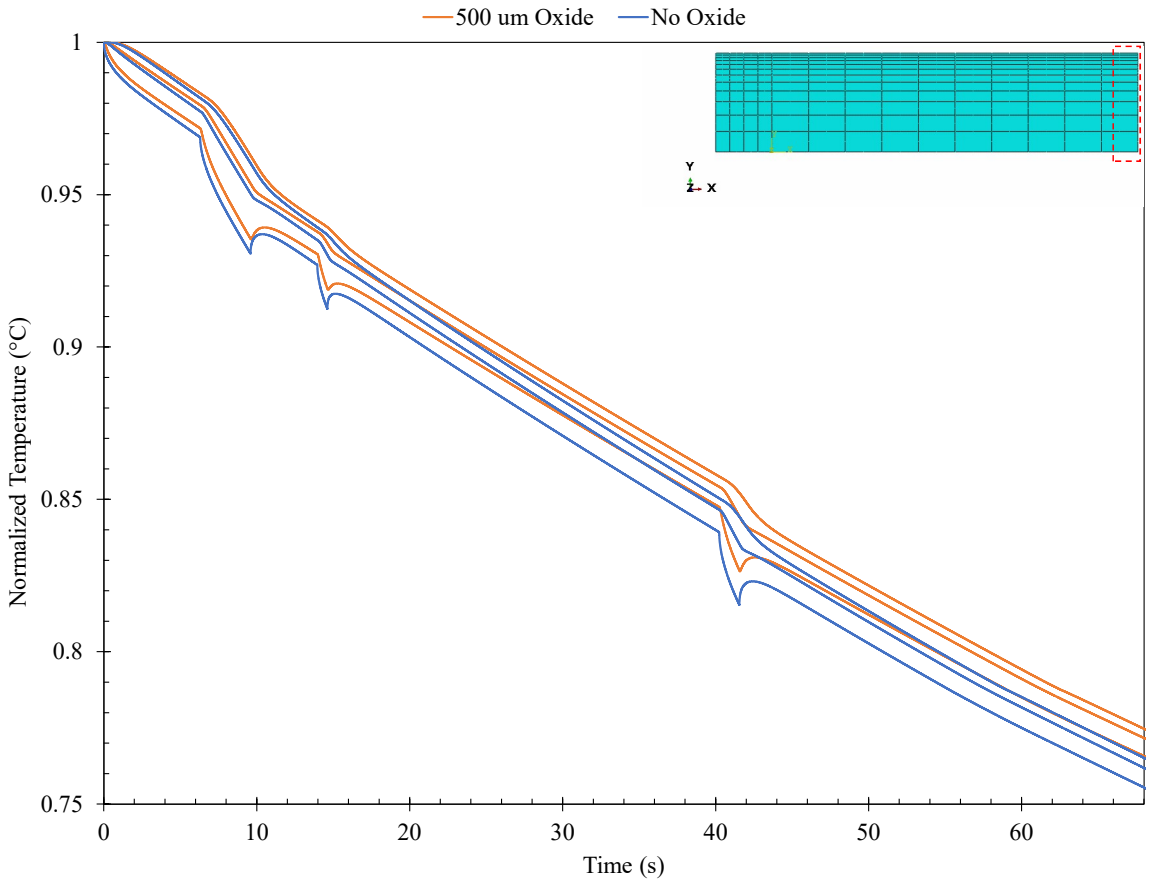

Figure 5.9: Through thickness temperature profile halfway between nozzles with and without oxide

5.4 Location and Area Fraction of Oxides

With the potential effect that oxides have on cooling rates elucidated, it becomes important to be able to predict their location and size. From knowing this, regions of varying microstructure can be estimated. Using the threshold temperatures found with the technique presented in section 5.1, a binary black and white IR video can be generated with oxides represented by black regions (Figure 5.4). Shown in Figure 4.13, the mean temperature at different points along the skelp length varies. To accommodate for this, oxide

threshold temperature values were determined in 10 m intervals along the skelp length. Figure 5.10 shows a schematic of this process, where for frames 120 and 383, two different threshold values were used.

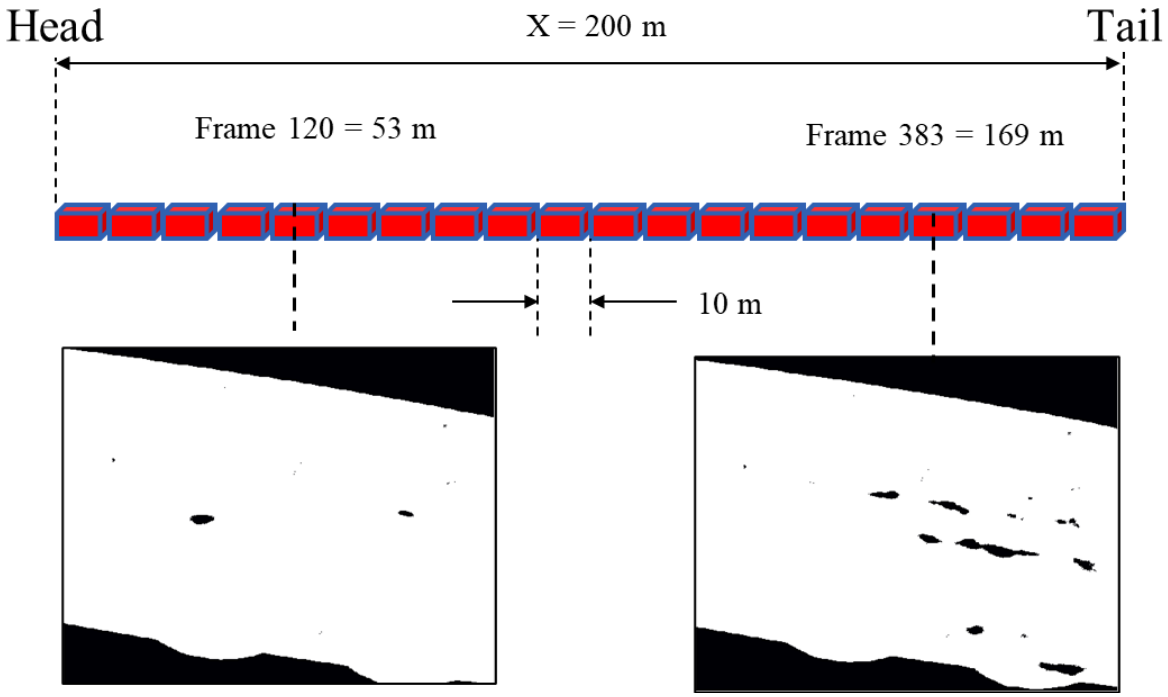

Figure 5.10: Schematic of 200 m skelp segmented into 10 m intervals

With the threshold values determined for each interval, a modified IR video was generated to highlight all anomalous temperatures. An object detection script written in Python was then used to track their location and size for an entire skelp run.

Figure 5.11 is a spatial distribution plot of the detected oxides. Two prominent bands can be observed, where band one and two are approximately 68 mm and 46 mm in width, respectively. These bands are situated towards the center of the skelp width, and the average spacing between them is 129 mm. Due to the spread within each band, the spacing between them accounting for the standard deviation (15 mm for band one and 10 mm for band two) was also calculated with the maximum spacing being 154 m and the minimum being 103 mm.

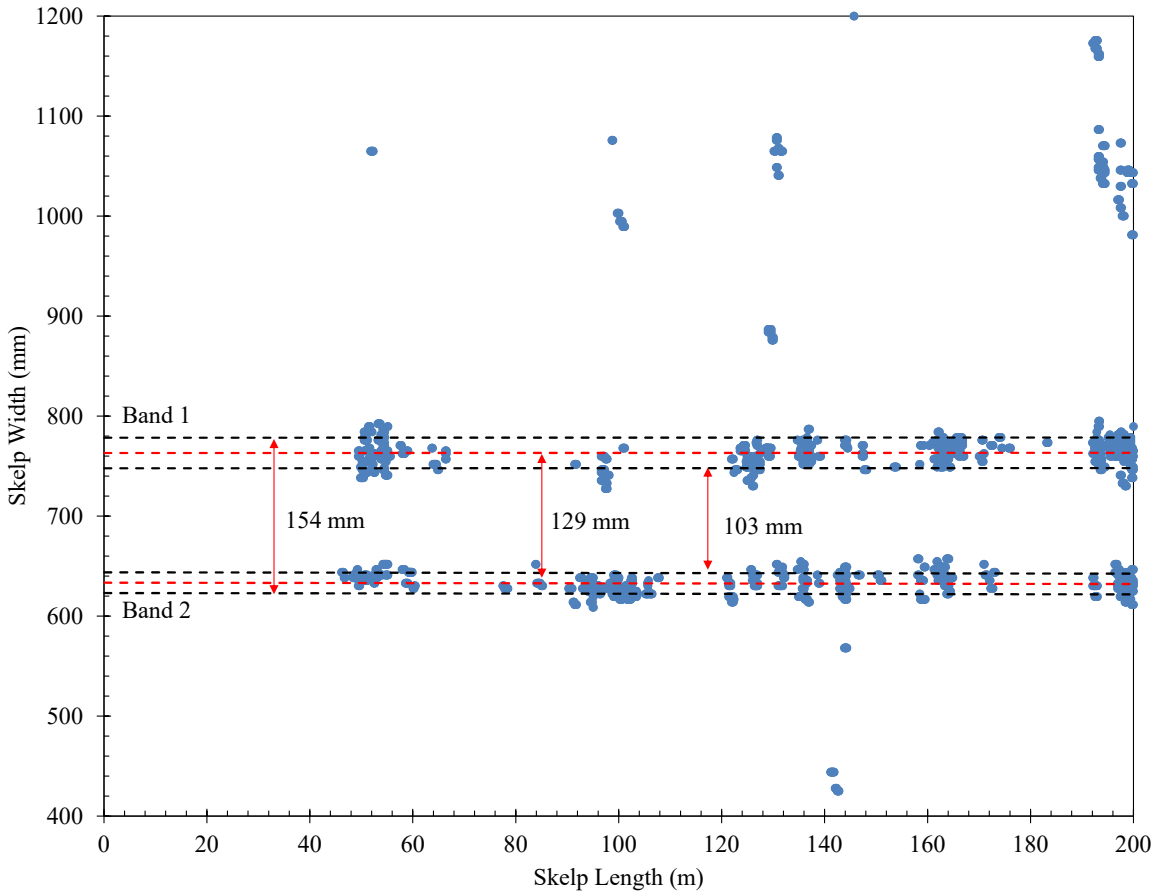

Figure 5.11: Spatial distribution of oxides detected along the skelp width

With the same object detection program, the size distribution and total area fraction of oxides at different lengths along the skelp was also determined, Figure 5.12 and 5.13. Oxide shapes were approximated as rectangles leading to an over estimation in their size. The mean size was calculated to be 16.9 cm^2, and the largest observed oxide was 426 cm^2. Based on the total calculated area fraction, it was determined that approximately 1% of the total skelp surface had oxide presents. This value is expected to be lower due to the overestimation due to approximating shapes as rectangles.

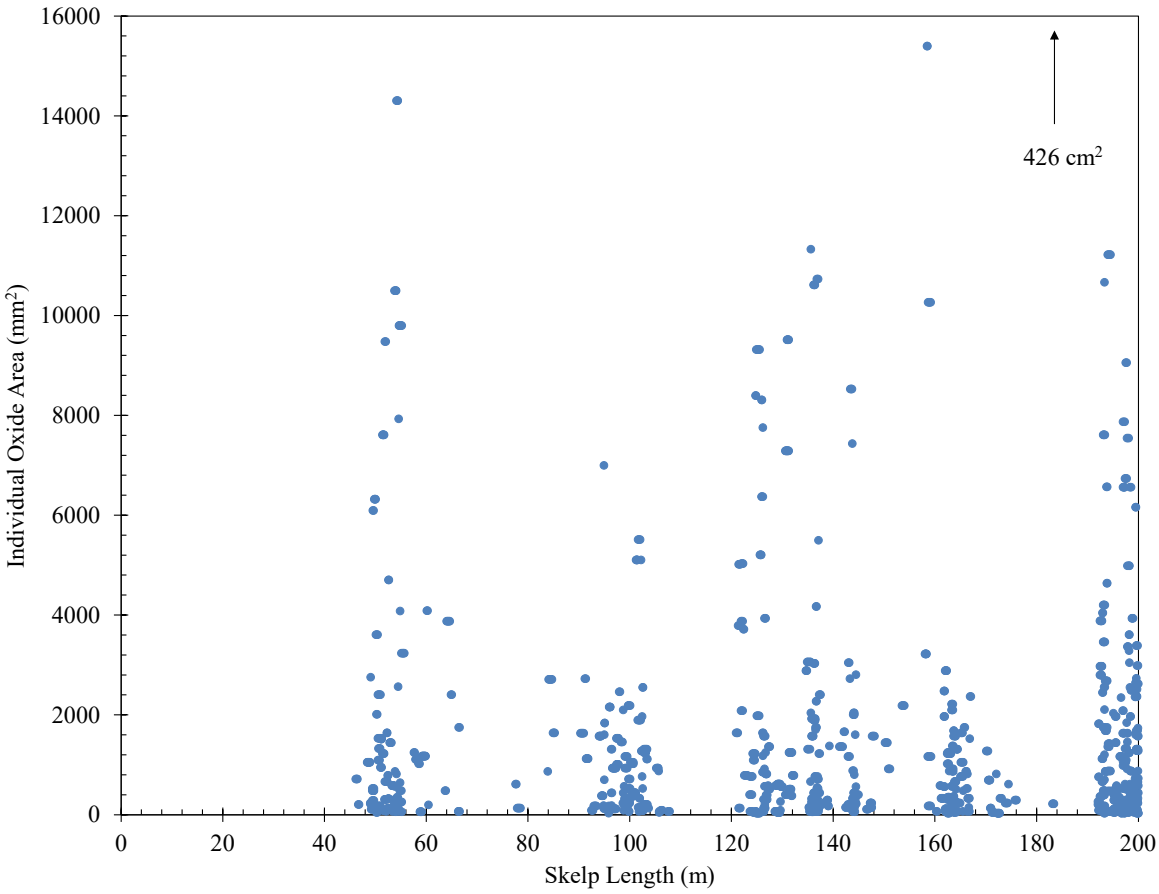

Figure 5.12: Size distribution of oxides along skelp length

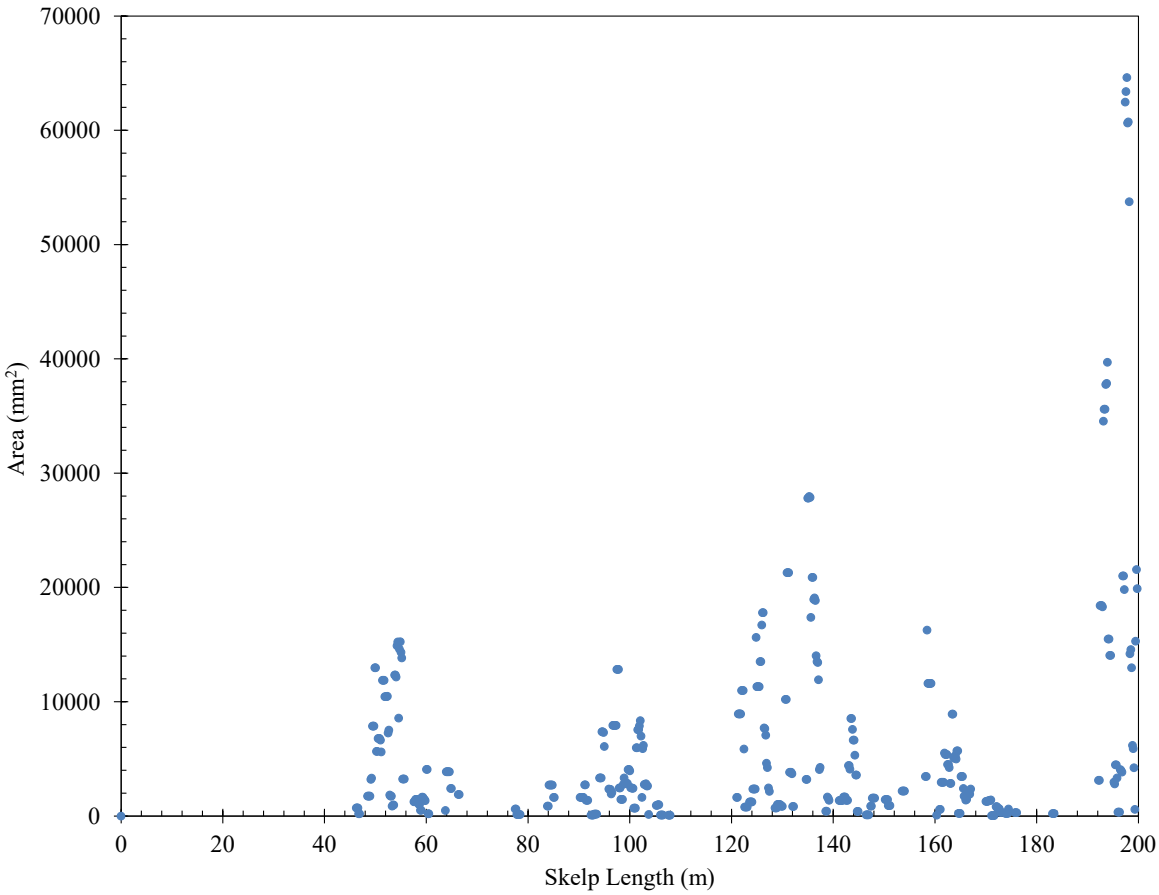

Figure 5.13: Total area of oxides at different lengths along skelp length

Based on the spacing between the two prominent bands, it is suggested that the oxide descalers adjacent to the middle nozzle are not working adequately and/or the oxides formed in this region are more strongly adhered to the surface. The oxides in these regions also exhibit an elongated shape along the skelp length (Figure 5.4), which suggests they were deformed during rolling. Outside of the region defined by the middle descaler nozzles, the presence of oxides was found to be minimal (Figure 5.11). This indicates that the nozzles positioned towards the edges of the skelp were functioning as intended. Minimal oxides were also detected at the center point between the two middle nozzles.

5.5 Summary

Figure 5.14 shows a 3D rendering of the entire 12 mm skelp made in Blender using all the temperature data gathered from the IR video. As can be seen, there were constant cold (blue) regions that ran along the whole length of the skelp with similar transverse spacing. In this chapter, a method to isolate and analyze these abnormally cold regions was developed. Using this method, these cold spots were found to be the result of oxides on the surface which were changing the local emissivty. When the transverse spacing of these oxides were measured, the spatial distribution was in good agreement with the spacing of the descaling nozzles. With the location of the oxides always being biased towards the center, and their spacing being similar to the descaler nozzle spacing, it is suggested that there are issues with the middle descaling nozzles.

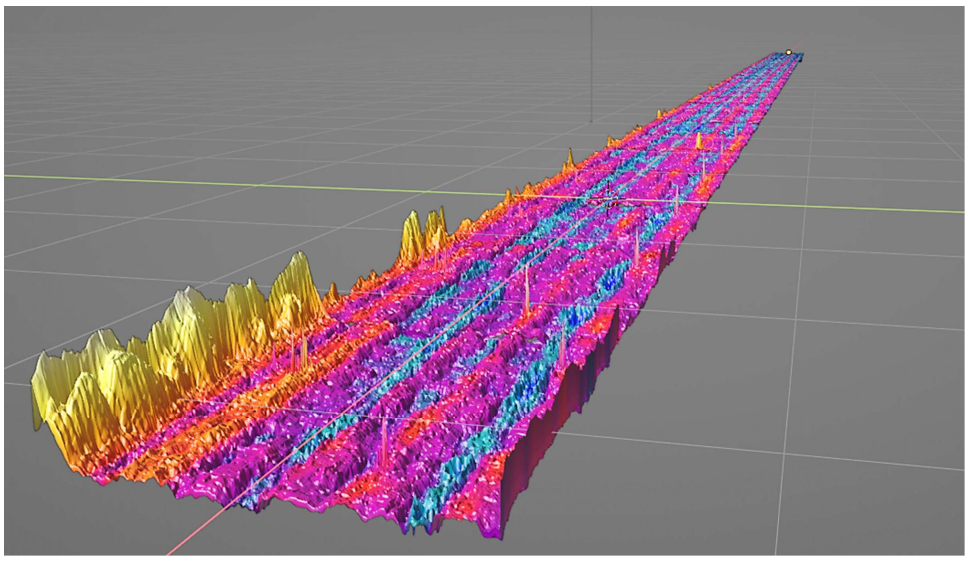

Figure 5.14: 3D rendering of a 12 mm skelp showing temperature distribution along the length

Chapter 6

Thermal Microstructure Model

In this chapter the temperature data from thermal modelling, and the thermodynamic and kinetic data from microstructure modelling, are combined into a single model to predict microstructure evolution on the ROT. The final microstructure of the provided X70 sample will be predicted using this model and then compared to results from OM and EBSD analysis. After validation of the model, different scenarios potentially encountered on the ROT will be explored. Scenarios of interest included oxides on the surface, a lower CT, and early/late cooling.

6.1 Model Development

From the thermal FEM, the temperature profile of the skelp on the ROT is known. In contrast to a dilatometer test which consists of continuous cooling at a single cooling rate, non-continuous cooling occurs on the ROT where the cooling rate constantly changes. Shown in section 2.5.3, Scheil developed a method to account for non-continuous cooling where the reaction is approximated as a series of small isothermal reactions. To utilize the method developed by Scheil, isothermal data in the form of a TTT is needed. For the sample under investigation in this work, no TTT is available, so instead a modification of the additivity principle developed by Rios will be used [115]. In the modified approach

to additivity, isothermal data can be extracted from the CCT diagram constructed in chapter 3. By applying this approach to the temperature profile of individual nodes in the thermal FEM, the austenite decomposition at different locations through the thickness of the steel can be determined. With the austenite decomposition known in each location, the same microstructure model used on dilatometer samples can be used to determine the phase fraction of ferrite and acicular ferrite present. A limitation to using this approach is its inability to account for the temperature rebounds that occur towards the surface of the steel. Due to this, an approximation of the cooling profiles is required to predict microstructure. A workflow of the model is shown in Figure 6.1.

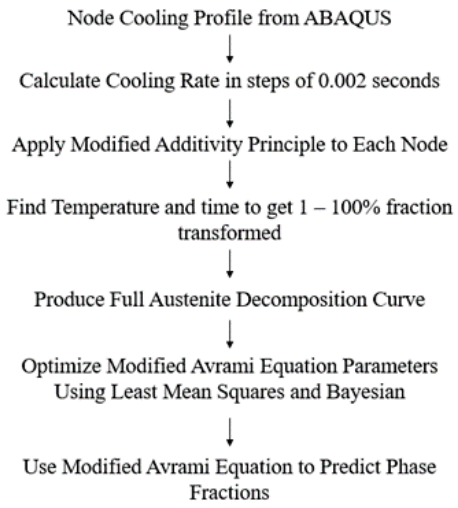

Figure 6.1: Thermo-Microstructure model workflow

6.1.1 Non-Continuous Cooling Rates

The complete cooling profile of the 15 mm model under the impact zone, as well as the point of no temperature rebounding, is shown in Figure 6.2. Due to limited literature on the effect of intermittent temperature rebounding on phase transformations, no nodes that exhibit this characteristic could be analyzed as is. From thermal modelling, temperature rebounding was shown to stop at a depth of 4 mm from the surface. To

circumvent this problem, the assumption that nodes that exhibited rebounding could be approximated as shown in Figure 6.3 was made. For those nodes, cooling was assumed to only occur up to the point of intersection with the tangent line of the following segment. Furthermore, for the surface nodes that exhibit instantaneous extreme cooling and rebounding (vertical lines), it was assumed that because the time increment of this event is so small, that it could be ignored.

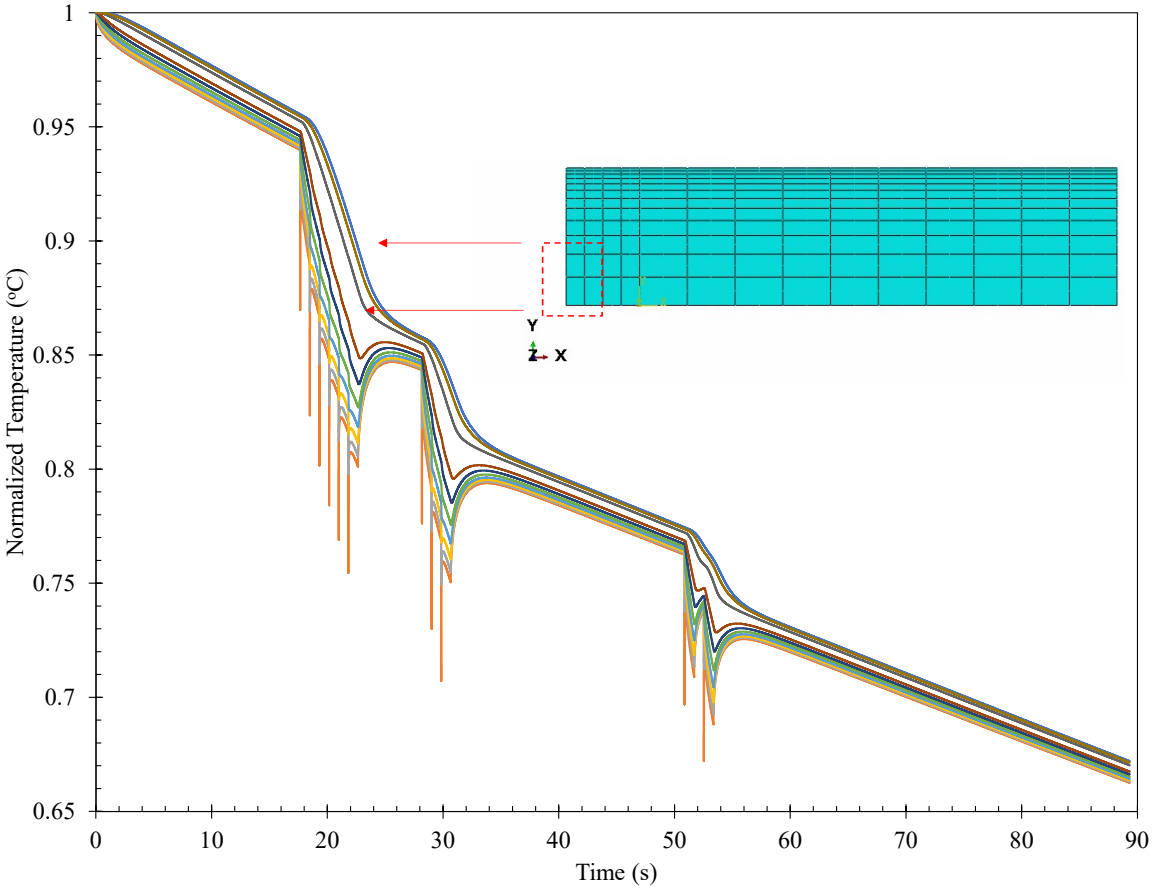

Figure 6.2: Through thickness temperature of each node under nozzle. The red box illustrates the point where rebounding stops

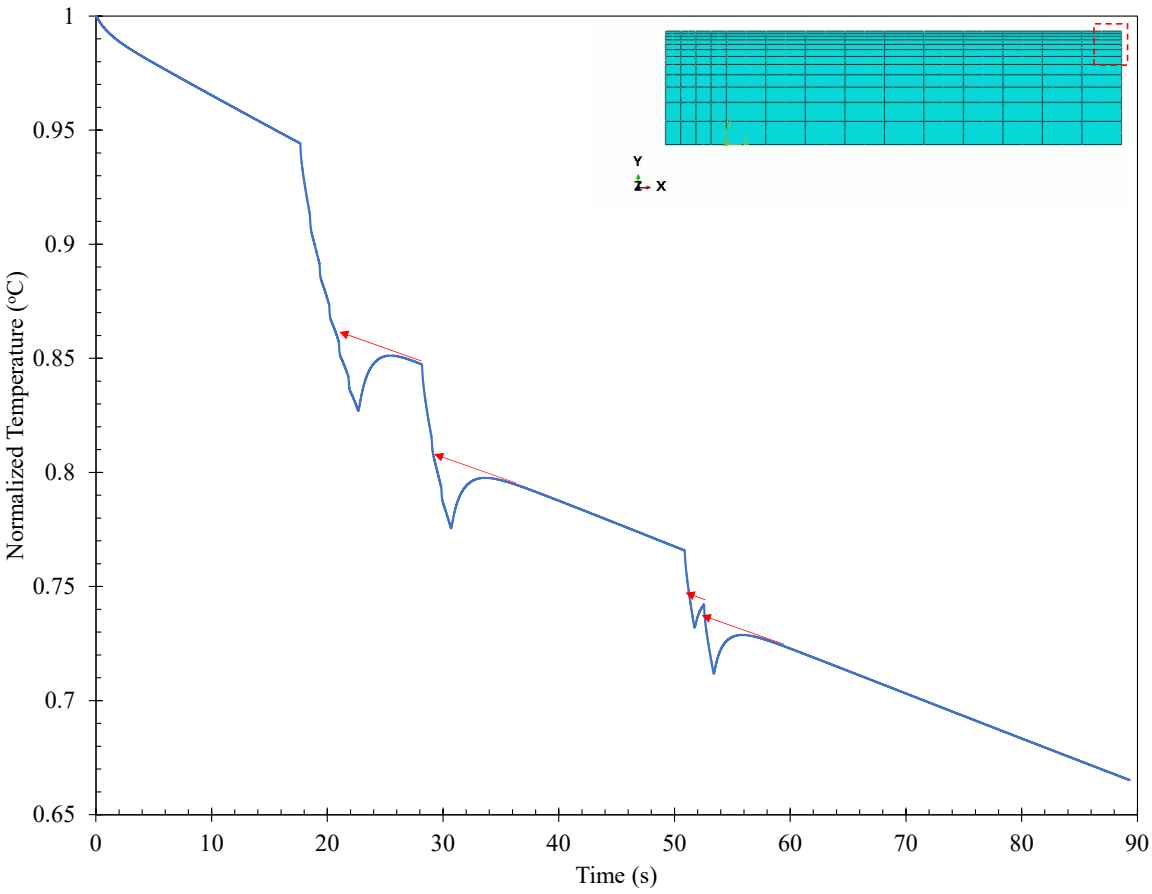

Figure 6.3: Approximation of temperature rebounding nodes (node 501)

With the normal and approximated non-continuous cooling profiles of each node, they were then divided into small segments, Figure 6.4. This was done to determine the instantaneous cooling rate at various points along the ROT (see inset in Figure 6.4). Segments were constructed using a step size of 0.002 seconds as this was found to elucidate the minor changes in cooling profiles between nodes.

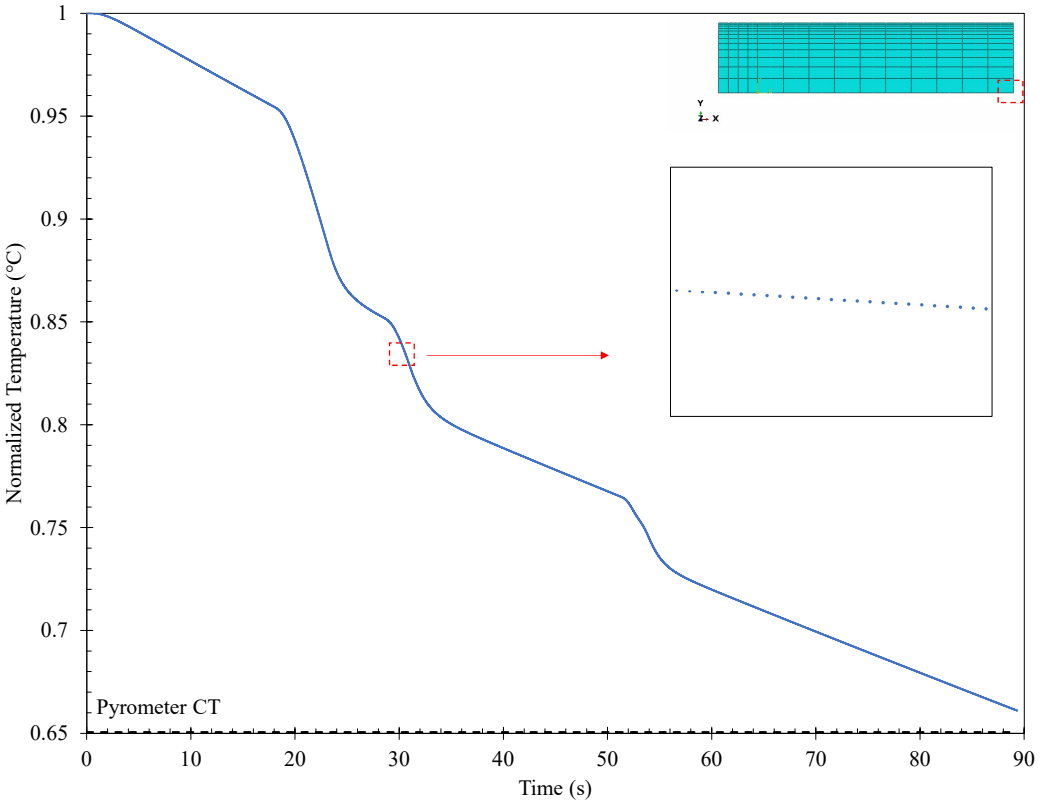

Figure 6.4: Segmented non-continuous cooling curve for node 360

6.1.2 Rios Method for Additivity

As stated in section (section 2.5.2), Scheil developed a method to convert non-isothermal data to isothermal data using TTT diagrams. By discretizing the continuous cooling profile into small steps, the fractional incubation of the reaction can be tracked, and the temperature to achieve a certain fraction of transformation can be approximated. This process is illustrated in equation 6.1, where dt is the time step, t_f is the transformation time for the reaction, and τ is the isothermal transformation time.

$$\int_{t}^{t_f} \frac{\mathrm{dt}}{\tau\left(X,T\right)} = 1 \tag{6.1}$$

This method is commonly used when isothermal data is available, but when it is not, a modified approach needs to be taken. Rios developed a method to solve for the inverse problem where one wants to extract isothermal data from non-isothermal kinetics.

In the method devised by Rios [115], the CCT is presented on the T – CR plane instead of the more common T-t plane. By doing this, specific fractions transformed can be plotted as contour plots as a function of cooling rate and temperature (X(q,T)). Contours for 20-, 30-, 40-, 50-, and 60% fraction transformed are presented in Figure 6.5. For each contour, a power equation was determined by fitting a trendline to the respective data points.

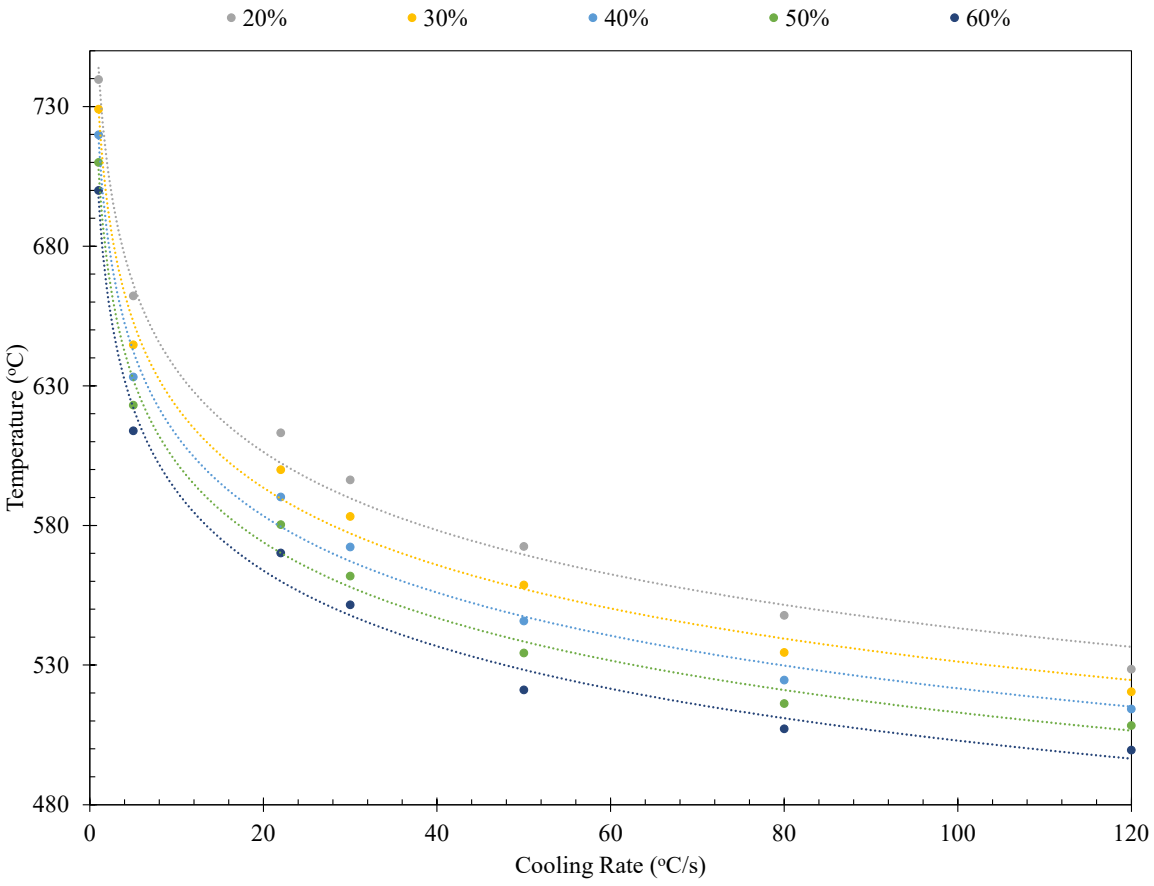

Figure 6.5: Alternative CCT plot showing X(q, T) contours for 20-, 30-, 40-, 50-, and 60% fraction transformed

Using the contours produced from data obtained from the CCT curve, the generalized additivity rule can be used on the arbitrary cooling paths experienced on the ROT. Of interest is the determination of the transformation temperature (T_f) where the specific fraction transformed will be obtained. By calculating this value for 1 – 100% fraction transformed, the austenite decomposition curve for an arbitrary cooling path can be generated. To illustrate this procedure, a two-step cooling path is illustrated in Figure 6.6.

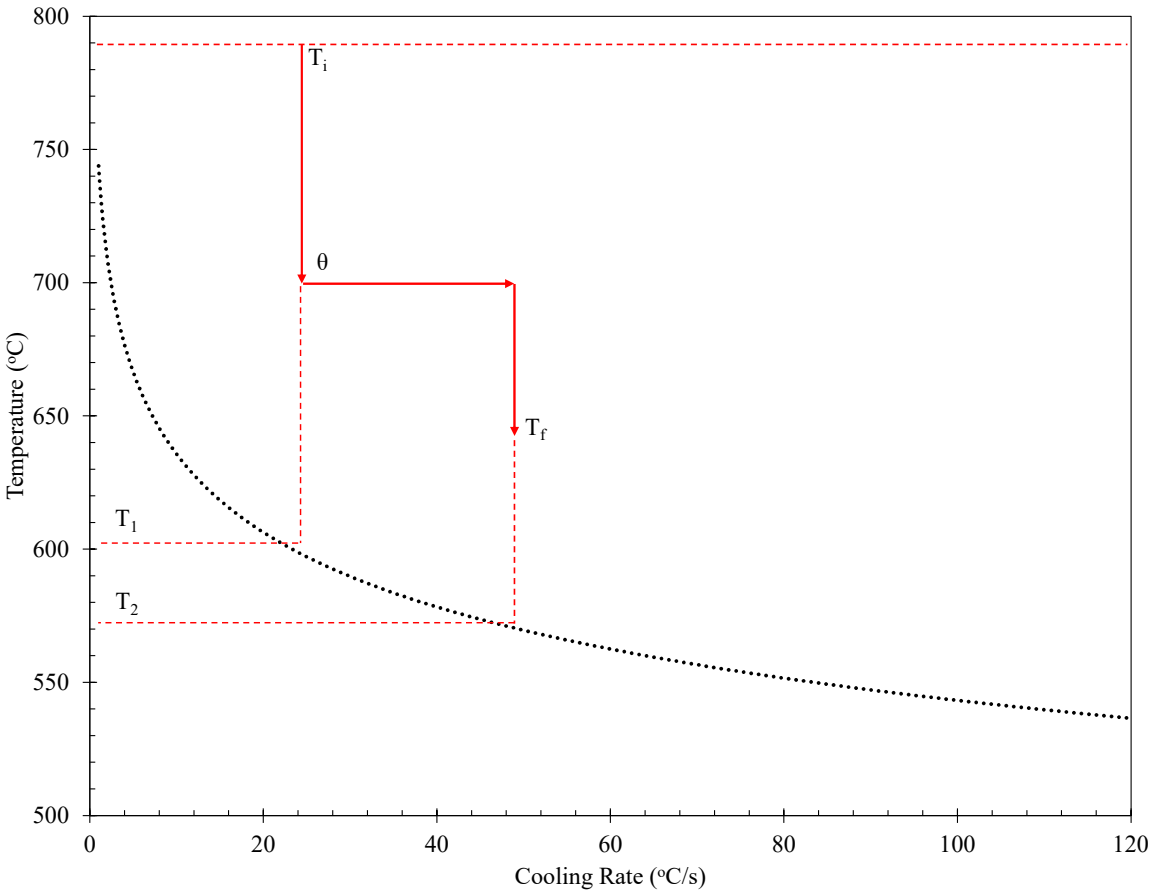

Figure 6.6: Application of Rios method of additivity for arbitrary two-step cooling process

For this example, the sample begins at the initial temperature (T_i). In the first step, it is cooled to θ at a cooling rate q_1. In the second step, it is cooled from θ

to the transformation temperature (T_f) at a cooling rate of q_2. For each step, the fractional incubation time is calculated as the difference between the transformation (T_1 and T_2) and step (T_i and θ) temperatures divided by the instantaneous cooling rates. This relationship is derived by taking the partial derivative of equation 6.2, which yields equation 6.3.

$$q = \int_{T_i}^{T} \frac{\mathrm{dT}}{\tau\left(X,T\right)} \tag{6.2}$$

$$\tau(X,T) = \left(\frac{\partial T}{\partial q}\right)_x \tag{6.3}$$

Based on the definition of additivity represented by equation 6.1, and the relationship derived in equation 6.3, the Scheil additive principle can be written in terms of temperature. The conversion of the Scheil additive principle to being in terms of temperature is shown below for the two-step example in Figure 6.6.

$$\int_t^{t_f} \frac{\mathrm{dt}}{\tau(\mathrm{X},\mathrm{T})} = \frac{dt_1}{\tau_1} + \frac{dt_2}{\tau_2} = \frac{\frac{T_i-\theta}{q_1}}{\frac{T_1-T_i}{q_1}} + \frac{\frac{T_f-\theta}{q_2}}{\frac{T_2-T_i}{q_2}} = \frac{T_i-\theta}{T_1-T_i} + \frac{T_f-\theta}{T_2-T_i} = 1 \tag{6.4}$$

When the summation of these steps equals unity, the transformation temperature has been reached. Since the transformation temperature is a function of the specific fraction transformed contour and the temperature dependent cooling rate, the method devised by Rios can be surmised with the generalized equation 6.5.

$$\int_{T_i}^{T_f} \frac{d\theta}{T(X_o, q(\theta)) - T_i} \tag{6.5}$$

Validation for Additivity

The criteria to apply additivity to a non-isothermal reaction is heavily debated as illustrated in section 2.5.3. Most models that apply additivity use an equation based on the JMAK theory, equation 6.6, where k(T) and n(T) are functions of temperature.

$$X(\tau, T) = 1 - exp(k(T) * \tau^{n(T))}) \tag{6.6}$$

In equation 6.6, some work has stated that n must be constant in order to apply additivity, while others state that the instantaneous reaction rate must be a separatable function of temperature and fraction transformed, equation 6.7.

$$\frac{\mathrm{dX}}{\mathrm{dt}} = f(T) * g(X) \tag{6.7}$$

For continuous cooling, a modified version of the JMAK equation shown by equations 6.8 and 6.9 can be used to describe the reaction [75]. The constants n, Q, and τ_o are constant for a specific transformation and can be solved for through fitting experimental data to the equation.

$$f = 1 - exp(\frac{-t}{k(T)})^n \tag{6.8}$$

$$k(T) = \tau_o exp^{\frac{-Q}{RT}} \tag{6.9}$$

A hand-tuning and Bayesian optimization technique were used to calculate reaction constants, with a least mean square cost function. Results from fitting the 5 ℃/s and 15 ℃/s data are shown in Figure 6.7 and 6.8. Furthermore, the variation of reaction constant n with cooling rate is shown in Figure 6.9. For each data set, a constant

activation energy of 200 kJ was used, as this is close to the activation energy for carbon diffusion in austenite. A complete set of fitted curves and reaction constants can be found in Appendix E. As seen in Figure 6.9, the constant n appears to be independent of cooling rate between 1 - 15 ℃/s. Deviation from this trend occurs at 22 ℃/s where the constant increases from 0.68 to 0.87. Since cooling does not reach rates of 22 ℃/s (apart from the surface), it was assumed that the value of n was constant for all situations encountered on the ROT, which satisfies the first criteria for additivity.

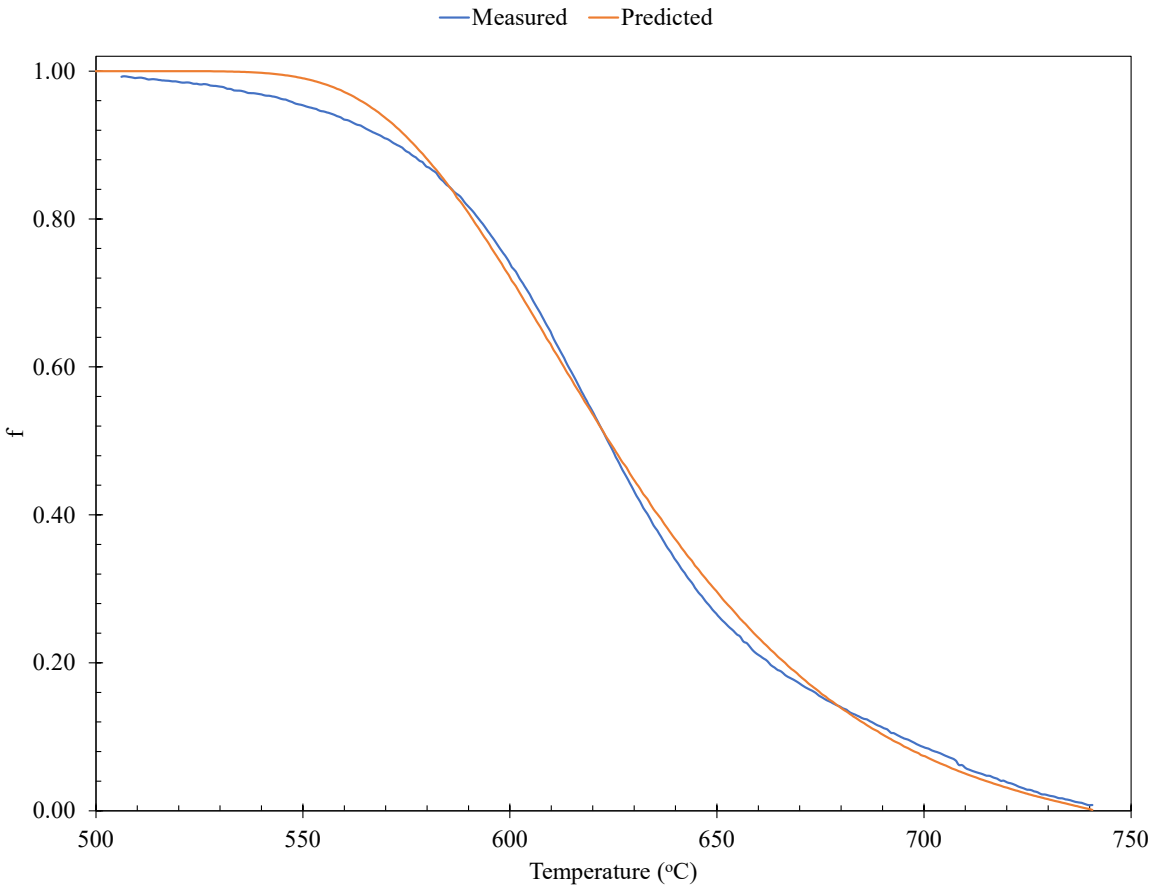

Figure 6.7: Experimental 5 ℃/s dilatometer data fit to equation 6-4 and 6-5

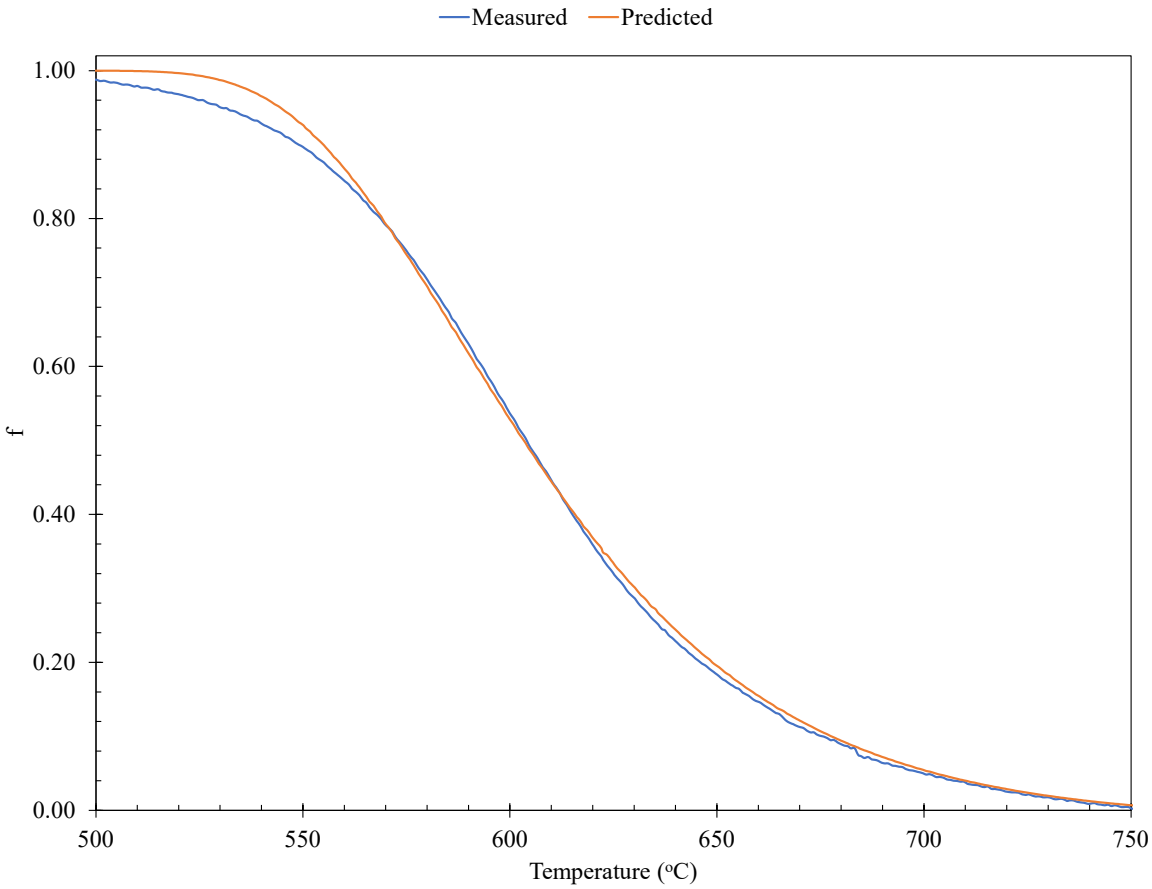

Figure 6.8: Experimental 15 °C/s dilatometer data fit to equation 6-4 and 6-5

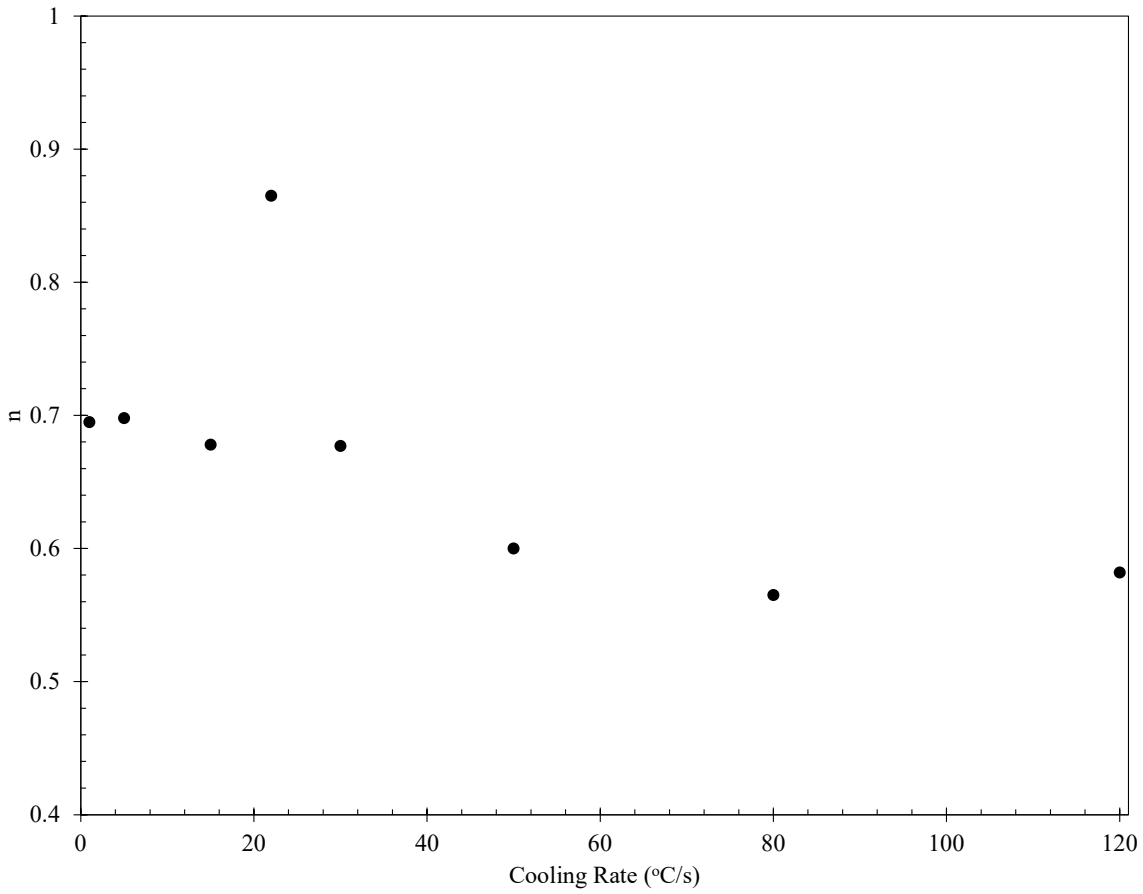

Figure 6.9: Variation of n constant in JMAK equation for different cooling rates

Assuming n is independent of temperature and cooling rate, the second criteria shown by equation 6.7 is also fulfilled. This is shown by taking the inverse of equation 6.8 which yields equation 6.10.

$$t = -k(T) * Ln(1 - f)) \tag{6.10}$$

6.1.3 Austenite Curve Construction

Using the method presented in section 6.1.2, the austenite decomposition curves for through thickness nodes were produced. Figure 6.10 shows the decomposition curves for

nodes 5, 360, and 501, where the location of each node is indicated in the figure in the top right-hand corner. The cooling path for node 501 was approximated as shown in Figure 6.3.

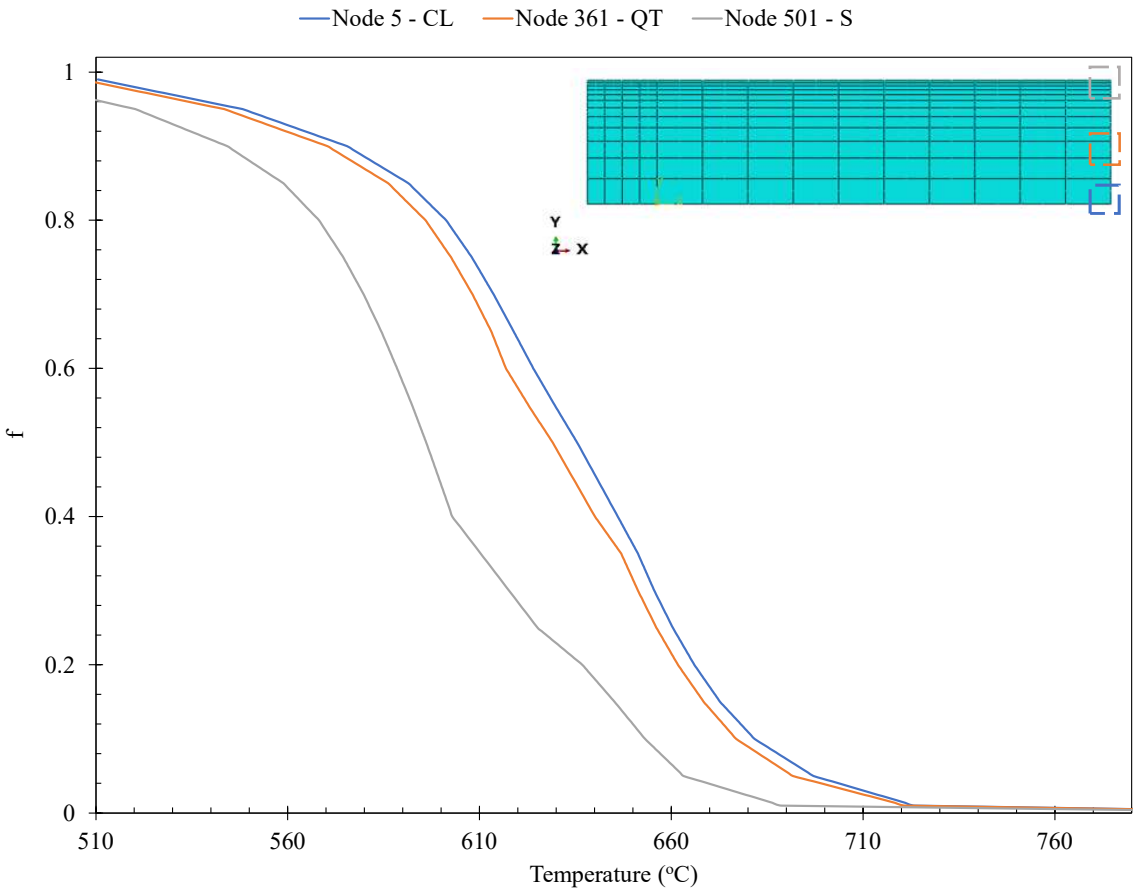

Figure 6.10: Nodes 5, 360, and 501 austenite decomposition curves

Of note with these curves is that they are constructed using temperature values for 1-, 10-, 20-, 30-, 40-, 50-, 60-, 70-, 80-, 90-, and 100% fraction transformed. Using these values as reference points and then interpolating the data in-between results in the linear regions observed in Figure 6.10. Furthermore, it can be seen that at the CT ($0.65T_{finish}$), the transformation has not gone to 100%. This observation of incomplete transformation prior to coiling is also reflected in the CCT for the sample (Figure 3.24). According

to the CCT, the transformation should be completed at around $0.59T_{finish}$. From this observation, it can be concluded that the coiling cooling rate will have an effect on the final microstructure of the steel. As this study focuses on the ROT, the effect of coiling on cooling rate and microstructure was not investigated. To accommodate for this portion of untransformed austenite, the cooling rate was approximated as radiative until all the austenite was transformed.

6.2 Model Predictions for X70 Sample

Using the austenite decomposition curves and the modified JMAK equation presented in chapter 3, microstructure evolution predictions were made using the developed model.

6.2.1 Model Assumptions

Through using this model, two assumptions were made regarding the microstructural evolution:

1. Only ferrite and acicular ferrite form.

2. Each phase transformation can be modelled with a single set of constants

Assumption one was based on dilatometer results, where under 50 ℃/s, only ferrite and acicular ferrite formed. Apart from surface and near surface nodes, cooling rates that produce bainite and martensite are not reached. In addition, the time spent at higher cooling rates for these nodes is small such that the fractional incubation time never reaches unity (i.e. bainite can be assumed to not form). The temperatures at which higher cooling rates occur are also well above the martensite start temperature for this steel. Based on equation 6.11, a M_s of 484 ℃ was predicted.

$$M_s = 545 - 330C + 2Al + 7Co - 14Cr - 13Cu - 23Mn - 5Mo - 4Nb - 13Ni - 7Si + 3Ti + 4V \tag{6.11}$$

The second assumption was made based on the observation that the austenite decomposition curves shown in Figure 6.10, to a good approximation, could be modelled by a single set of parameters. This is illustrated in Figure 6.11 where the austenite curve for node 5 is shown to be modelled by a single set of constants. Shown in 6.11, the beginning portion of the curve exhibits a strong fit. Around 610 ℃ the fitted curve begins to deviate. This is expected to be the result of phase two initiating. Since only one activation energy is used during fitting, the transformation of phase two is most likely not accounted for.

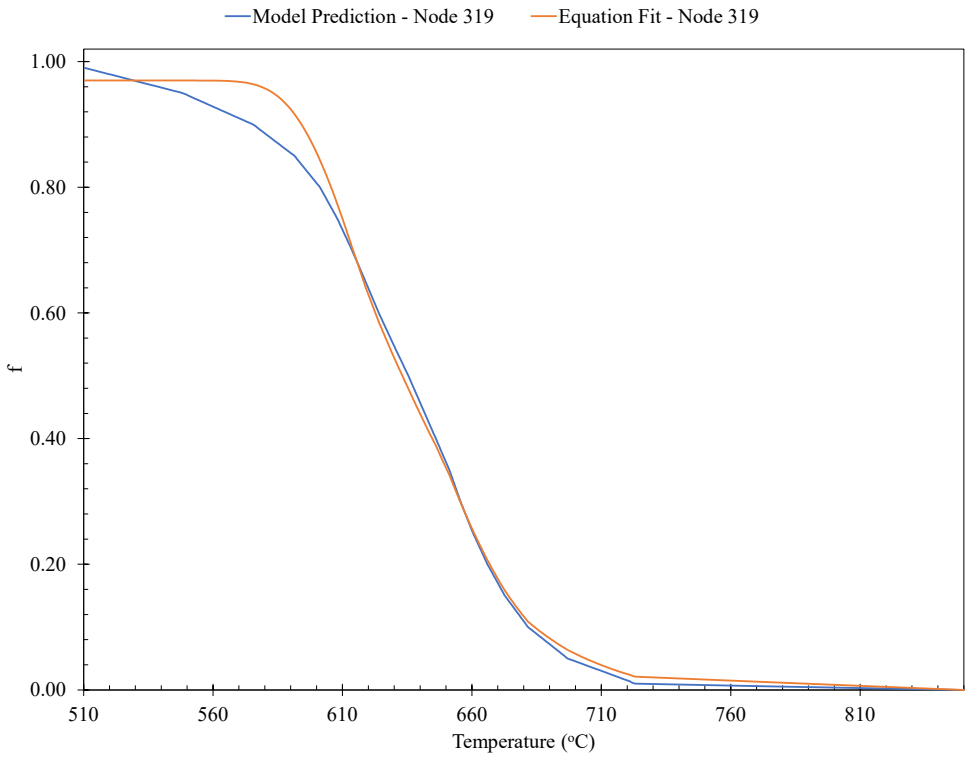

Figure 6.11: Node 5 austenite decomposition curve modelled with single set of constants

6.2.2 Transformation Start Temperatures

A critical component of the microtructure evolution model is the the determination of the transformation start temperatures of each phase. The beginning of austenite decomposition correlates to the transformation start temperature for ferrite. For acicular ferrite, a 1% fraction transformed contour can be generated using the microstructure modelling results shown in section 3.2.3. Using the same approach as with austenite decomposition curve construction shown in section 6.1.3, the start temperature of acicular ferrite can be determined. Table 6.1 shows the calculated start temperatures for each phase at nodes 5, 360, and 501.

Table 6.1: Transformation start temperatures for nodes 5, 281, and 501

Node	Ferrite T_s (℃)	Acicular Ferrite T_s (℃)
5	723	643
360	721	639
501	689	608

6.2.3 Model Predictions

The constants used to model each product phase were determined using a two-step fitting procedure. Initially, a hand-tuning method was used to find suitable boundaries for each constant. This was done by manually varying each parameter until a good fit was found. Using these boundaries, a subsequent Bayesian optimization technique with a mean-squared error (MSE) cost function found the overall best fit. Figures 6.12, 6.13, and 6.14 show the results for the center, quarter, and surface. In each figure the black curve represents austenite, blue is ferrite, orange is acicular ferrite, and yellow is the summation of both product phases. Table 6.2 shows the predicted phase fractions at nodes 5, 360, and 501.

Table 6.2: Predicted phase fractions at nodes 5, 360, and 501

Node	Ferrite (%)	Acicular Ferrite (%)
5	84	16
360	78	22
501	54	46

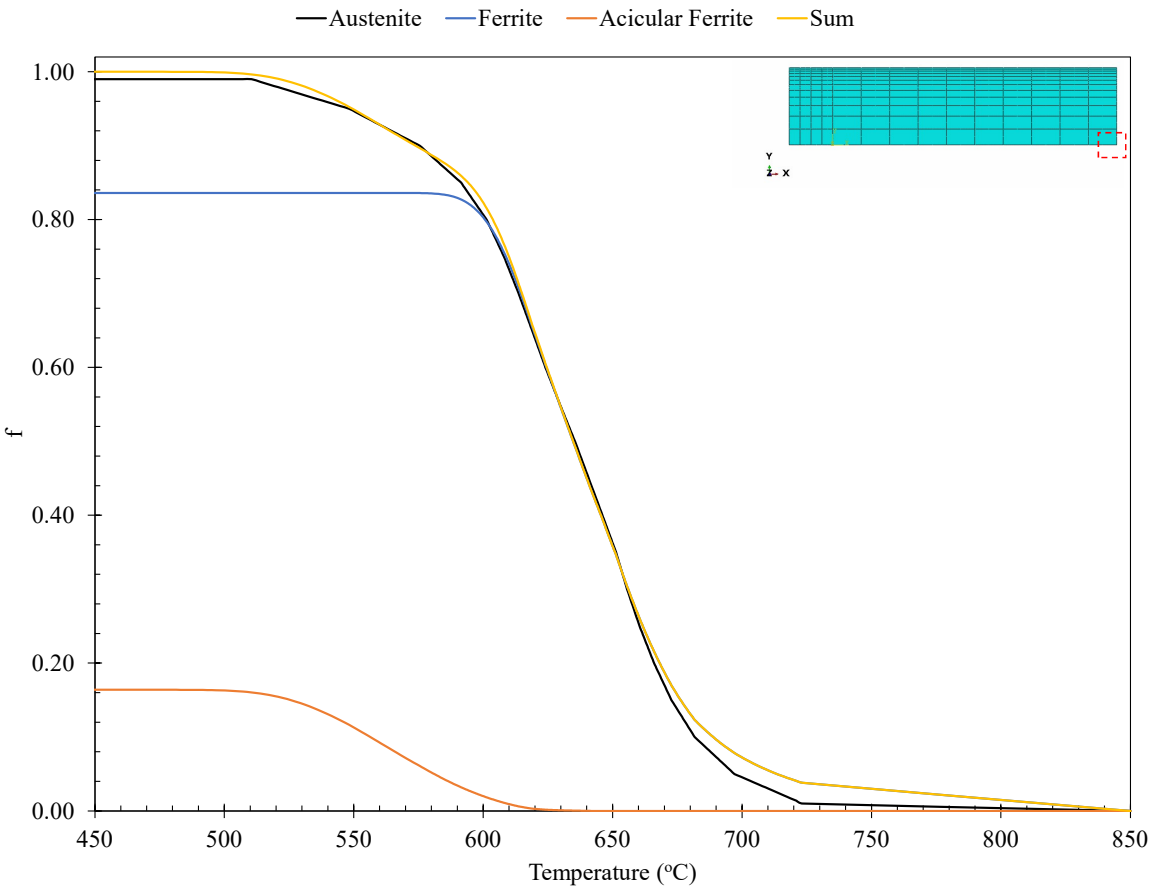

Figure 6.12: Node 5 (center line) microstructure evolution

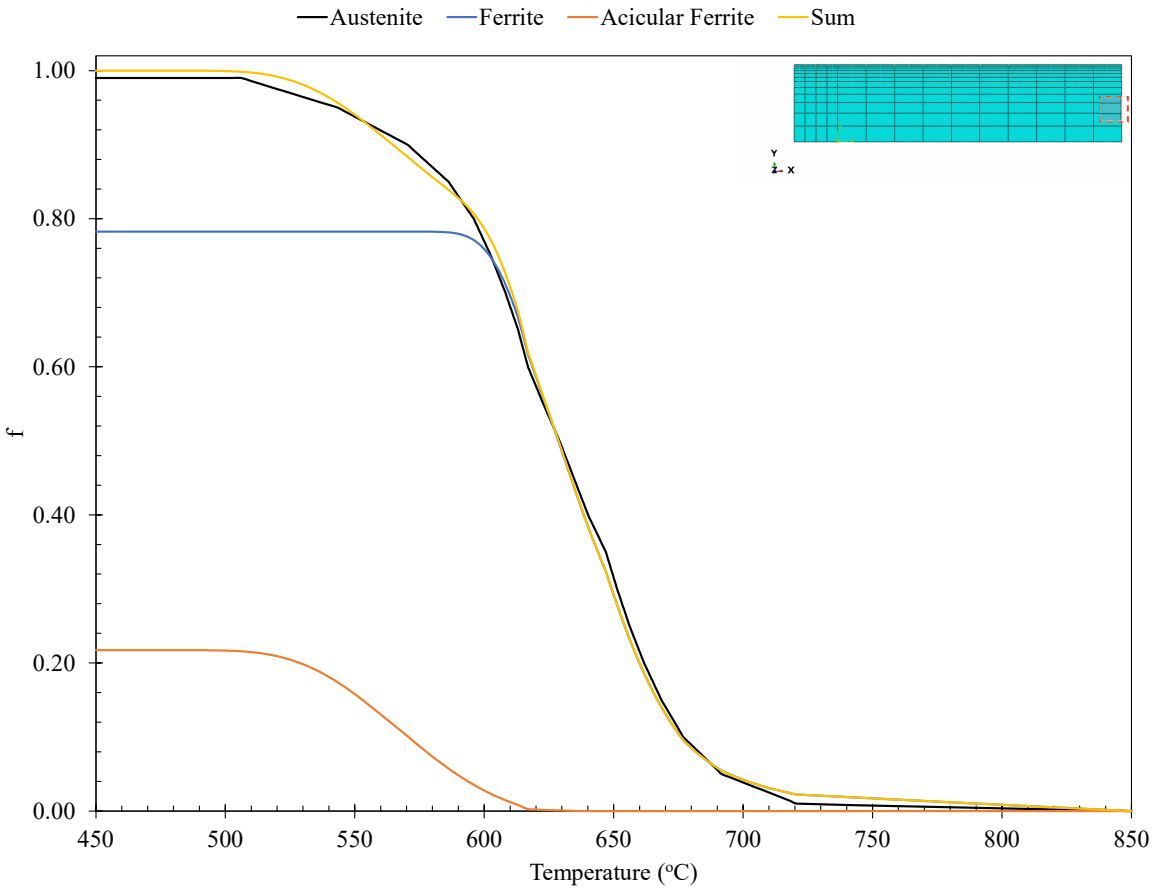

Figure 6.13: Node 360 (quarter line) microstructure evolution

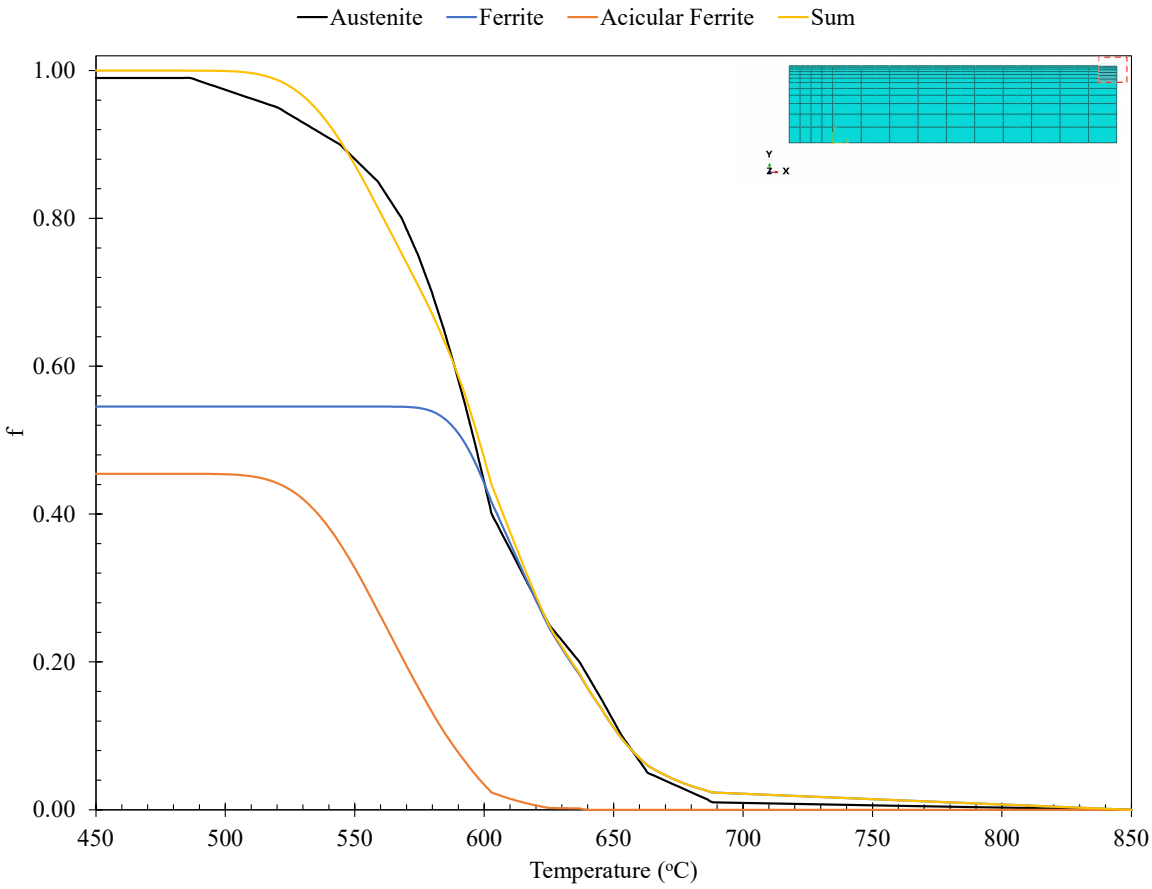

Figure 6.14: Node 501 (surface) microstructure evolution

6.2.4 Model Validation

To assess the efficacy of the model results, three different metrics were used:

1. Whether or not the expected trend of decreasing ferrite towards to the surface was observed

2. How well the results compared to those obtained from EBSD of the ROT sample

3. How well the predicted ferrite and acicular ferrite curves compared to the 5 ℃/s and 15 ℃/s dilatometer sample results

Table 6.3 shows the predicted verses measured phase fractions at the center line, quarter line, and surface. These results show the ability of the model to produce both the expected trends and phase fractions through the thickness of the skelp. The only discrepancy comes from surface results where the amount of ferrite and acicular ferrite differ by a noticeable amount. A potential reason for this deviation may be from approximating the curves to avoid temperature rebounding. When the top 4 mm of the sample were averaged though, the measured and predicted values converged. Further investigation into the effect of temperature rebounding on microstructure evolution is needed to better model this region. Figures 6.15 and 6.16 show the band contrast maps for the the ROT sample at the surface and 4 mm below. From these images it can be observed that the the microstructure at the surface is much more heavily dislocated than 4 mm below it.

Table 6.3: Measured versus predicted phase fractions at center line, quarter line, and surface

Location	Measured/Predicted Ferrite (%)	Measure/Predicted AF (%)
Center line	74:84	24:16
Quarter Line	78:78	21:22
Surface-Top	32:54	62:46
Surface-4mm below	73:54	27:46
Surface-avg	55:54	45:46

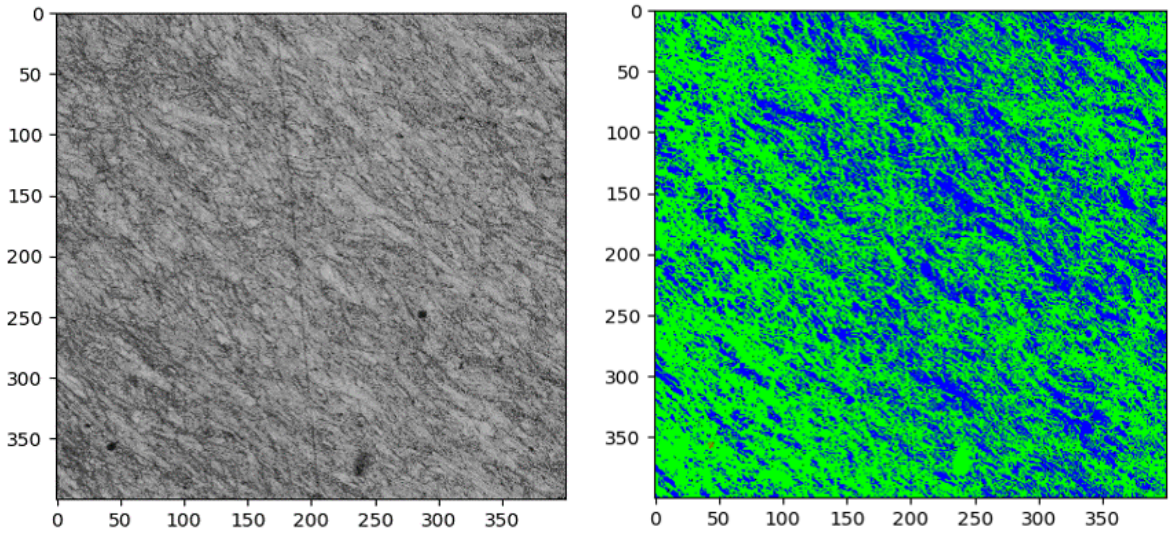

(a) **(b)**

Figure 6.15: EBSD band contrast analysis of ROT sample surface

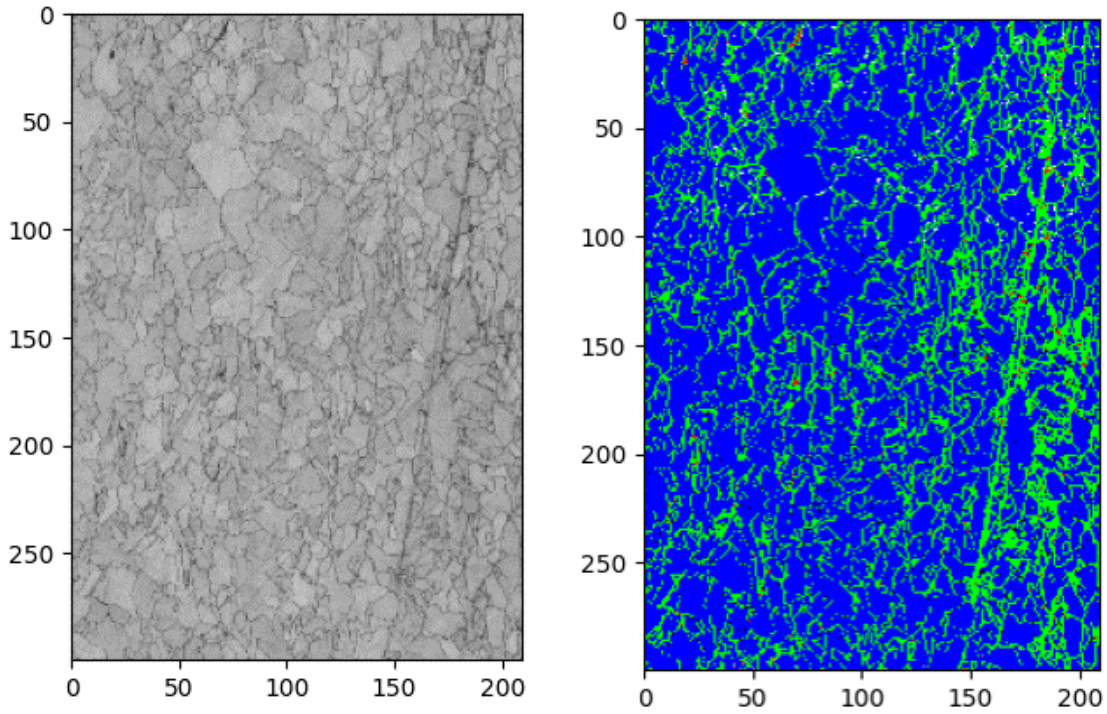

(a) **(b)**

Figure 6.16: EBSD band contrast analysis of ROT sample 4 mm below the surface

Shown by the EBSD analysis, the ROT sample very closely matched the 5 ℃/s and 15 ℃/s dilatometer samples (Figures 3.18, 3.19, and 3.20). Based on this, the predicted transformation curves from the model were expected to align with these samples. Figures 6.17 and 6.18 show a comparison between the transformation curves for ferrite and acicular ferrite at the center line node. For the formation of ferrite, the model is best approximated as the 5 ℃/s sample, while for the acicular ferrite, it is best approximated as the 15 ℃/s sample.

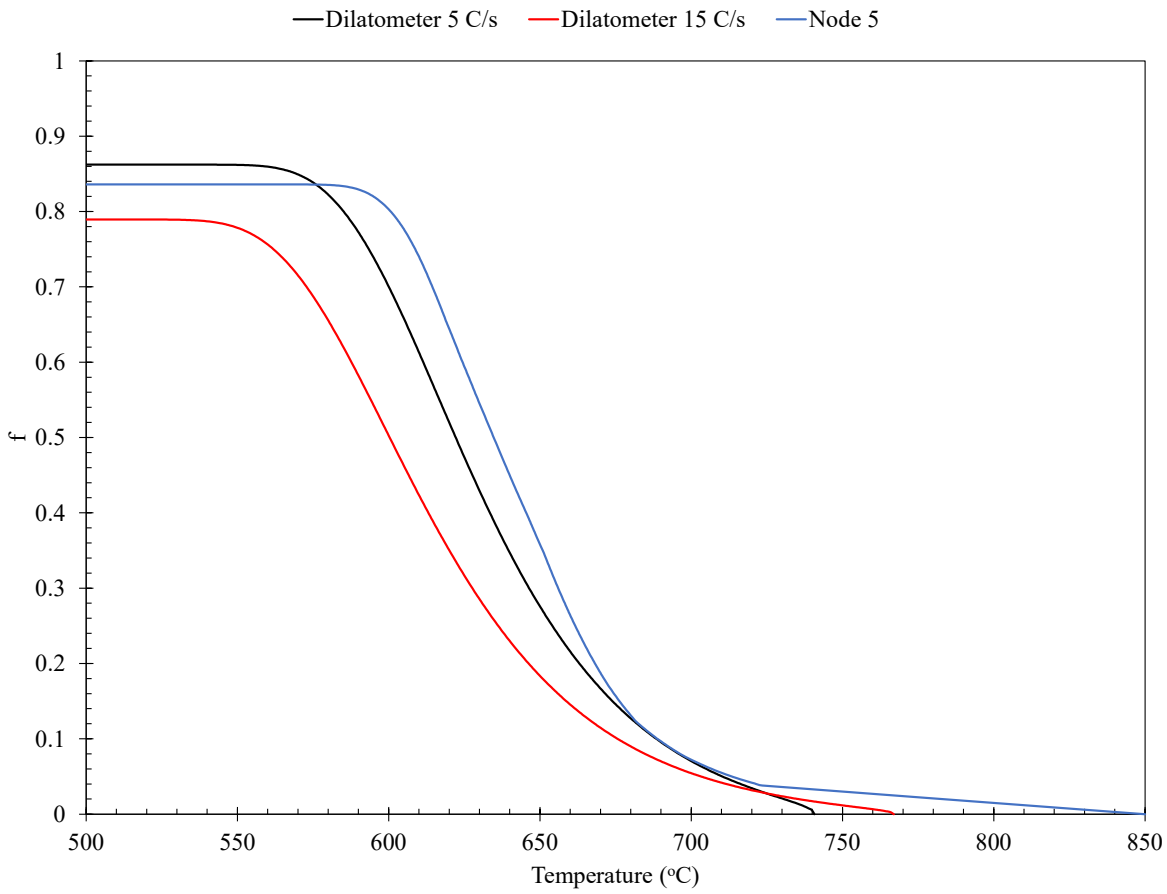

Figure 6.17: Comparison between the ferrite nucleation and growth of the 5 ℃/s and 15 ℃/s dilatometer samples with node 5 from the thermo-microstructure model

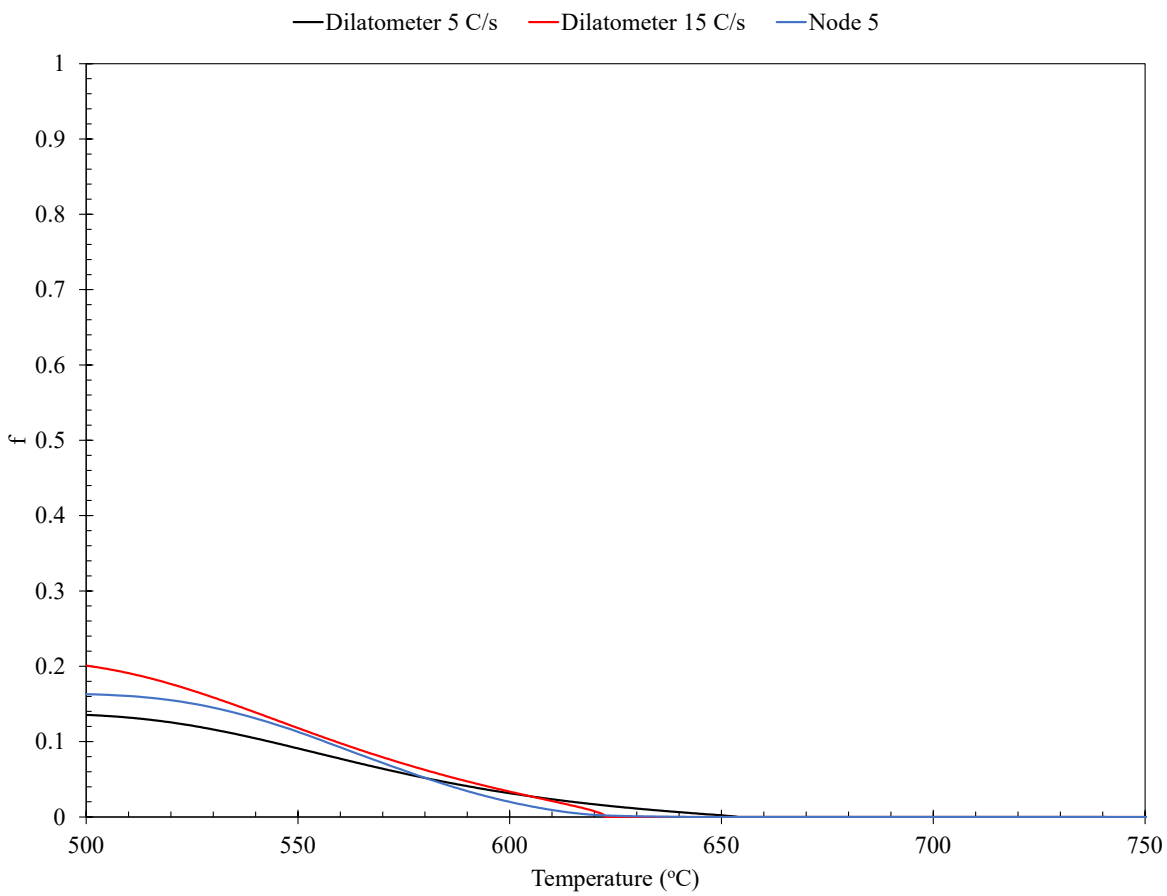

Figure 6.18: Comparison between the acicular ferrite nucleation and growth of the 5 ℃/s and 15 ℃/s dilatometer samples with node 5 from the thermo-microstructure model

6.3 Alternative ROT Configuration Scenarios

In this section, four alternative cooling situations will be assessed. The first is the effect that oxides have on microstructure. Next, the effect of decreasing the CT will be investigated. Lastly, early and late cooling will be explored. The specific ROT configurations used in each simulation can be found in Appendix C. In each situation, only the quarter node away from the nozzle will be assessed.

6.3.1 Effect of Surface Oxides on Microstructure

For the results shown in section 6.2, an ideal situation was assumed where the surface of the skelp is free of any oxides. As shown by the results in chapter 5, the assumption of an oxide free surface is far from what is observed in the mill. From FEA modelling of a 12 mm skelp with oxides (Figures 5.7, 5.8, and 5.9), it was observed that the cooling rate decreased as a result of the oxide. The temperature fluctuations at the surface were also mitigated by the shielding effect of the oxide. To illustrate the differences between microstructures with and without the presence of an oxide, the quarter thickness nodes (away from the nozzle) for 15 mm a) oxide and b) non-oxide models were assessed with the thermo-microstructure model. Figures 6.19 and 6.20 show the differences in cooling paths and the predicted change in austenite decomposition that results from an oxide at the quarter distance of a 15 mm skelp.

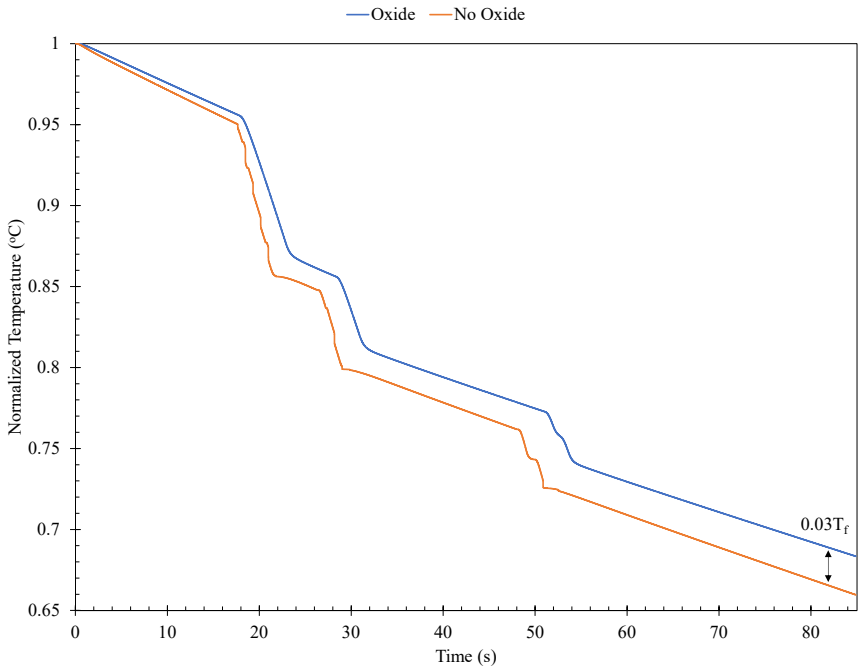

Figure 6.19: Quarter node variation between cooling path for regions with and without a 500 μm oxide

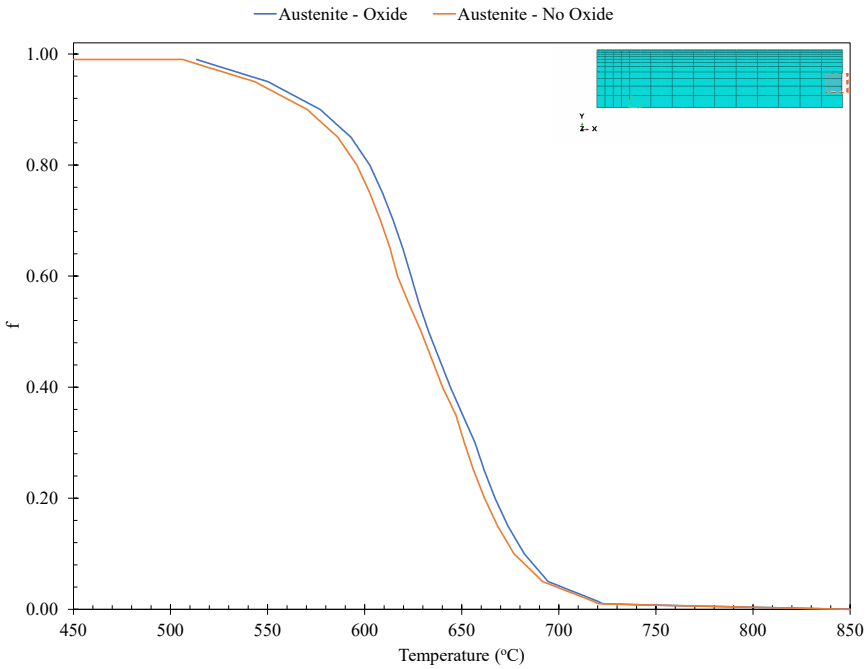

Figure 6.20: Quarter node variation between austenite decomposition for regions with and without a 500 μm oxide

Show in Figure 6.19, the presence of the oxide on the surface decreases the cooling rate imposed by each bank. This also results in a higher CT. By decreasing the cooling rate, the onset of transformation occurs at higher temperatures, and the fraction of ferrite produced increases while the fraction of acicular ferrite decreases. These results align with the trends observed from the CCT shown in chapter 3. Results comparing the microstructure evolution of oxide and oxide free transformations at the quarter node are shown in Figure 6.21. Table 6.4 summarizes the changes in phase fraction between scenarios.

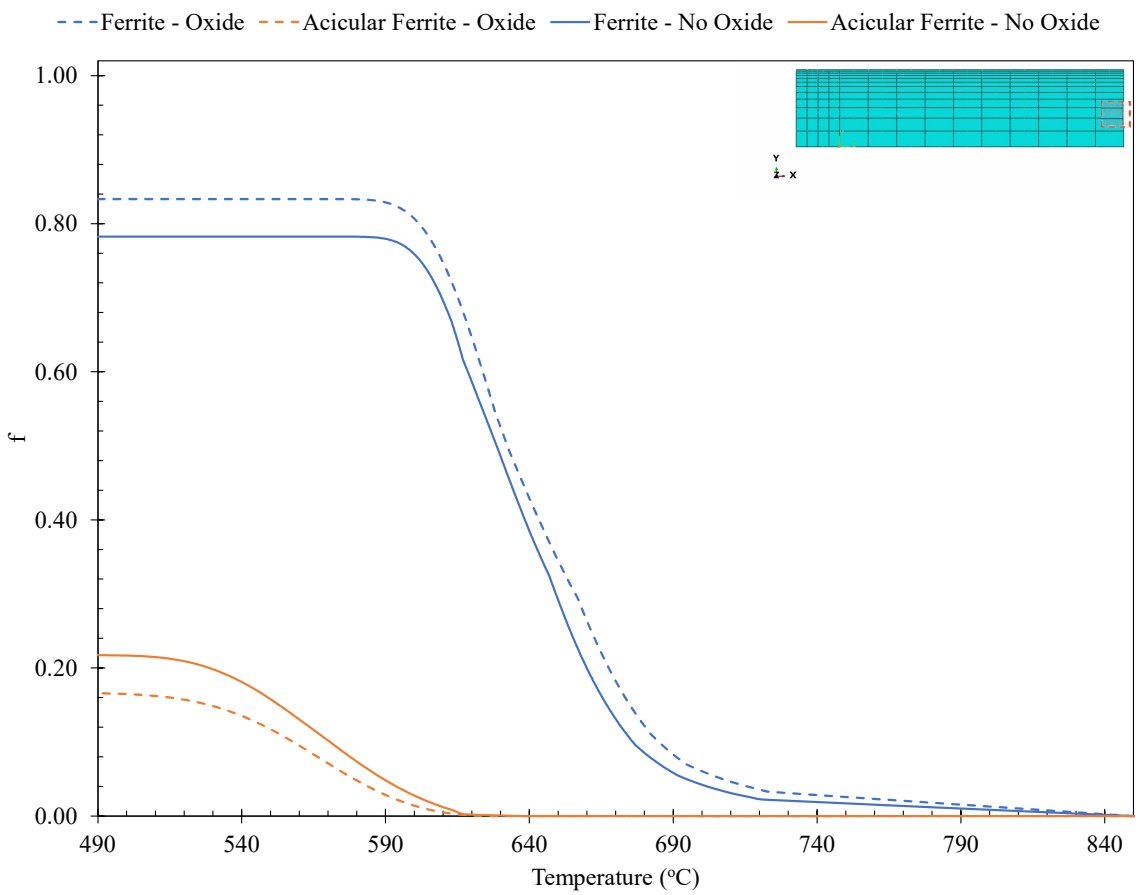

Figure 6.21: Quarter node microstructure evolution comparison between an oxide free and 500 μm oxide region on a 15 mm skelp surface

Table 6.4: Effect of oxides on microstructure evolution at quarter thickness

Model	Ferrite T_s (°C)	AF T_s (°C)	Ferrite:AF (%)
No Oxide	721	639	78:22
Oxide	723	639	83:17

6.3.2 Effect of CT on Microstructure

The effect of a lower CT was also investigated. For the X70 sample being analyzed, a spray pattern to achieve a CT of $0.65T_{finish}$ was used. By changing which headers and banks are in operation, hypothetical cooling scenarios can be created and examined. In this section, the effect of operating alternating and all banks were explored. Figure 6.22 shows the resulting cooling profiles for these hypothetical scenarios. When alternating banks are used, the CT was $0.42T_{finish}$, while when all banks were turned on, it was $0.10T_{finish}$. The effect of the full boiling curve can be observed from these situations, where as the skelp temperature moves out of the film region, a larger magnitude of cooling is experienced. This is shown by the larger temperature drop over each bank towards the end of the simulation.

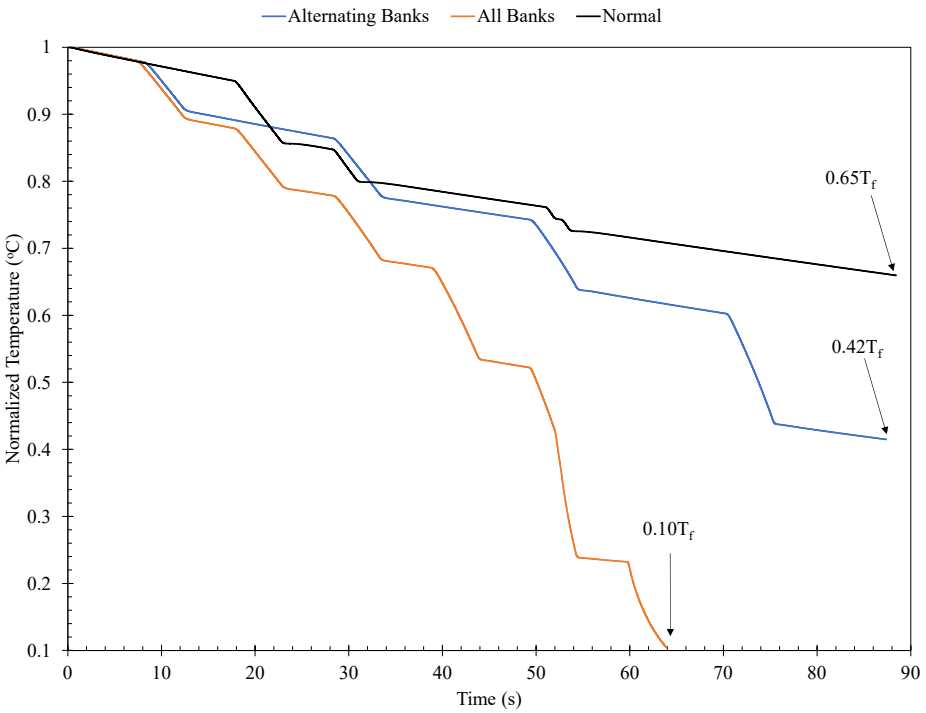

Figure 6.22: Quarter node cooling profiles from regular cooling, alternating banks operating, and all banks operating

The results from running the thermo-microstructure model on each hypothetical cooling scenario is shown in Figures 6.23, 6.24, and 6.25. Between the scenarios, it can be seen that as the number of banks in operation increases (normal - alternating - all) the phase fraction of ferrite and acicular ferrite decrease and increase, respectively. This trend can be explained by the cooling profiles for each scenario and the CCT generated in chapter 3. As the number of banks in operation increases, the amount of time spent at high temperatures decreases. This results in the transformation of less austenite into ferrite prior to the onset acicular ferrite formation. Transformation start temperatures also followed the expected trend where with increasing cooling rates the onset temperatures decreased. Table 6.5 summarizes the changes in phase fraction and start temperatures between scenarios.

Table 6.5: Effect of ROT configuration on microstructure evolution at quarter thickness

Configuration	CT (℃)	Ferrite T_s (℃)	AF T_s (℃)	Ferrite:AF (%)
Normal	$0.65T_{finish}$	721	639	78:22
Alternating	$0.42T_{finish}$	721	639	75:25
All	$0.10T_{finish}$	701	623	72:28

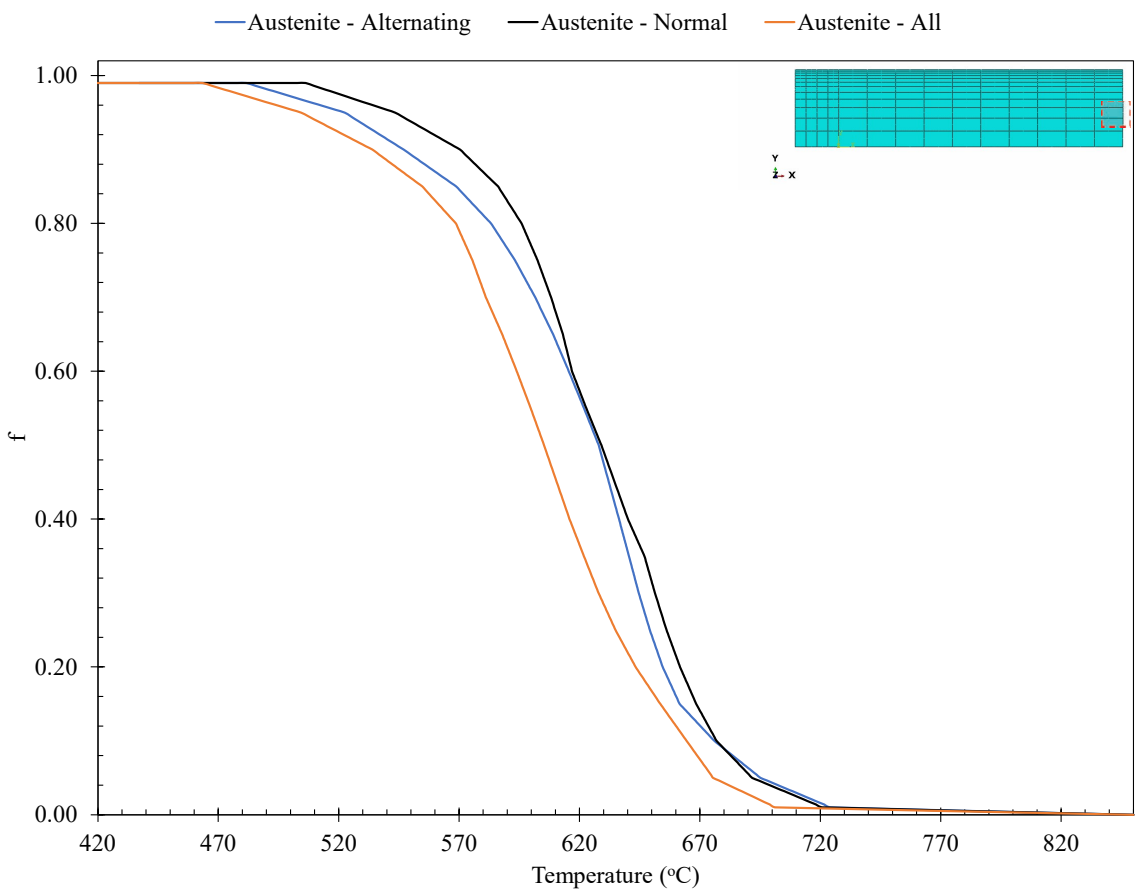

Figure 6.23: Quarter node austenite evolution from regular cooling, alternating banks operating, and all banks operating

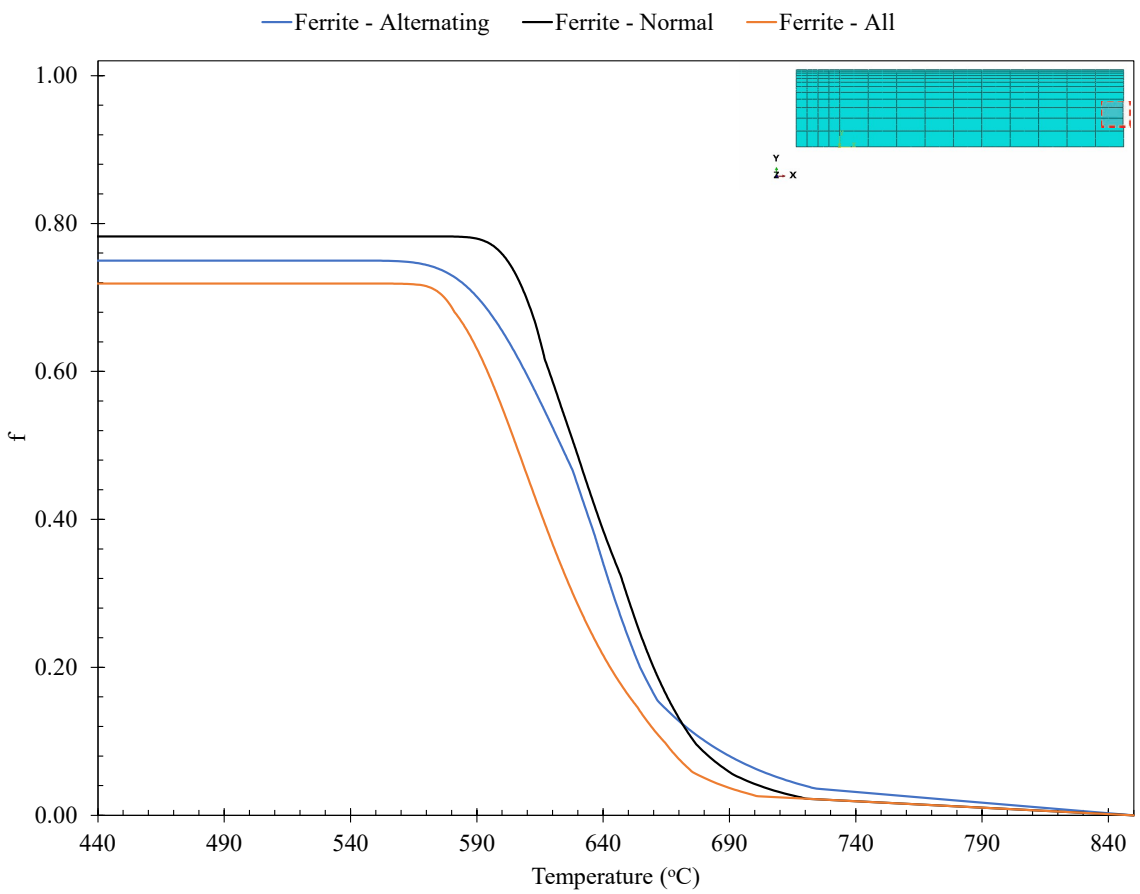

Figure 6.24: Quarter node ferrite evolution from regular cooling, alternating banks operating, and all banks operating

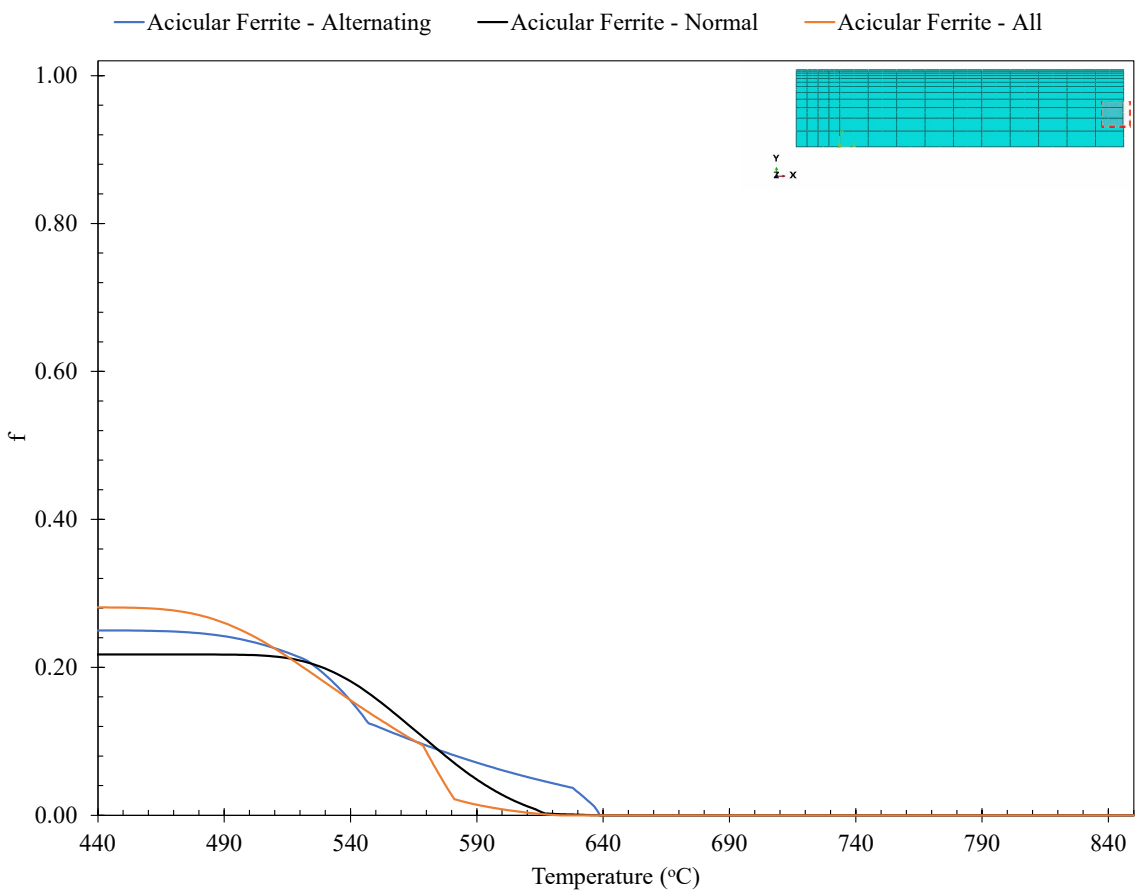

Figure 6.25: Quarter node acicular ferrite evolution from regular cooling, alternating banks operating, and all banks operating

6.3.3 Effect of Early and Late Cooling on Microstructure

The final two ROT configurations explored were those of early and late cooling. For each situation, three banks were turned on. In the early cooling configuration, the first three banks were put into operation, while in late, the last three were turned on. Figure 6.26 shows the simulated temperature profiles for each at the quarter node away from the nozzle.

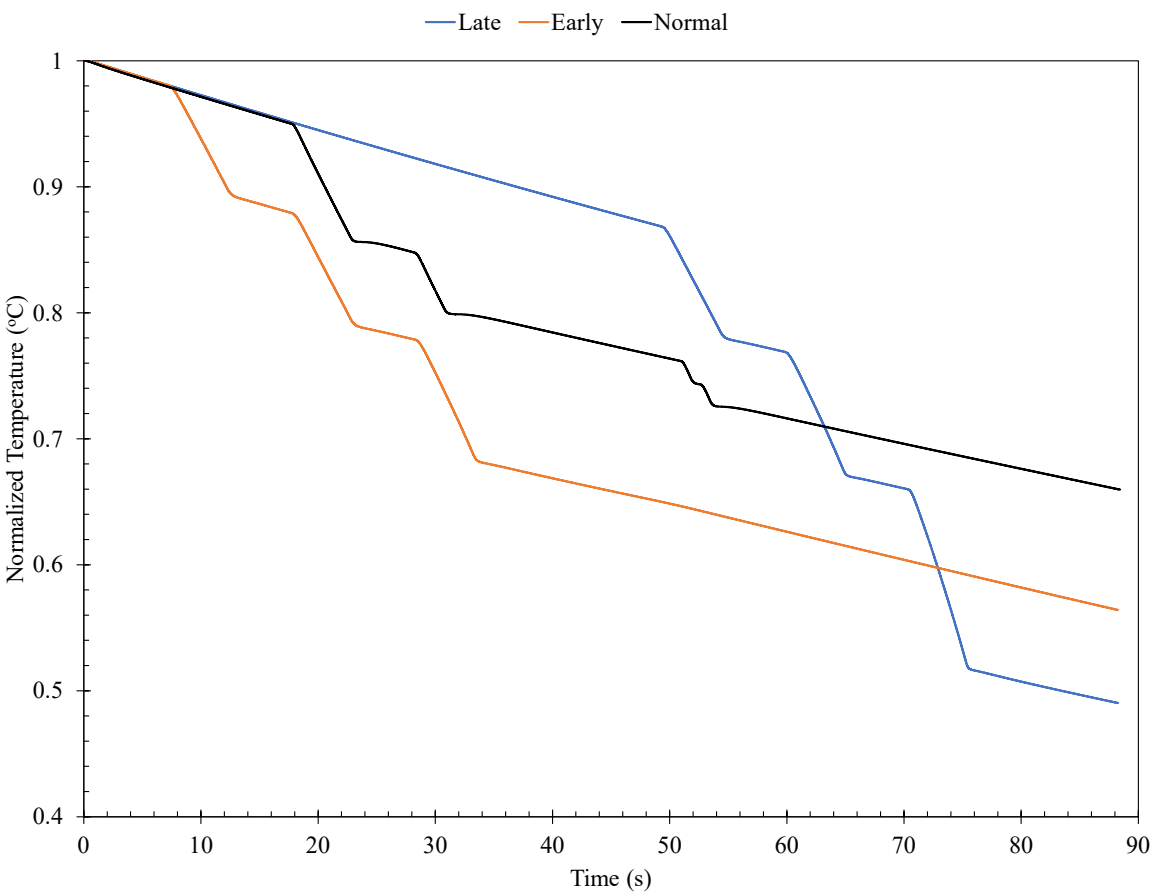

Figure 6.26: Quarter node cooling profiles for normal, early, and late cooling

Figures 6.27, 6.28, and 6.29 show the resulting austenite, ferrite and acicular ferrite transformation curves generated from the thermo-microstructure model. Similar to the observations made for lower CT simulations, the results for early and late cooling follow the same trends. During early cooling, there is less time at higher temperatures, this leads to a lower phase fraction of ferrite (and more acicular ferrite) compared to normal ROT cooling. Conversely, during late cooling, the time at elevated temperatures is similar to normal ROT cooling, which leads to close final phase fractions. Table 6.6 summarizes the changes in phase fraction and start temperatures between scenarios.

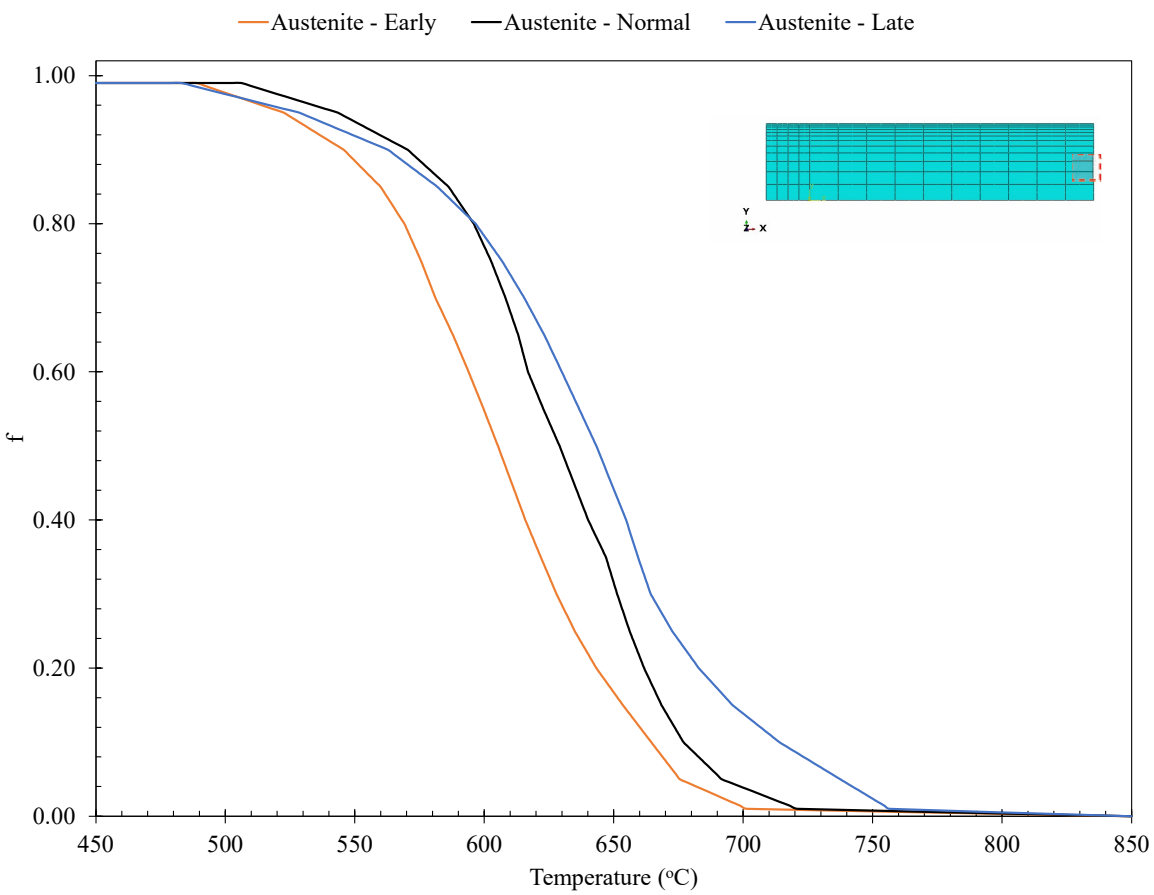

Figure 6.27: Quarter node austenite evolution from regular, early, and late cooling

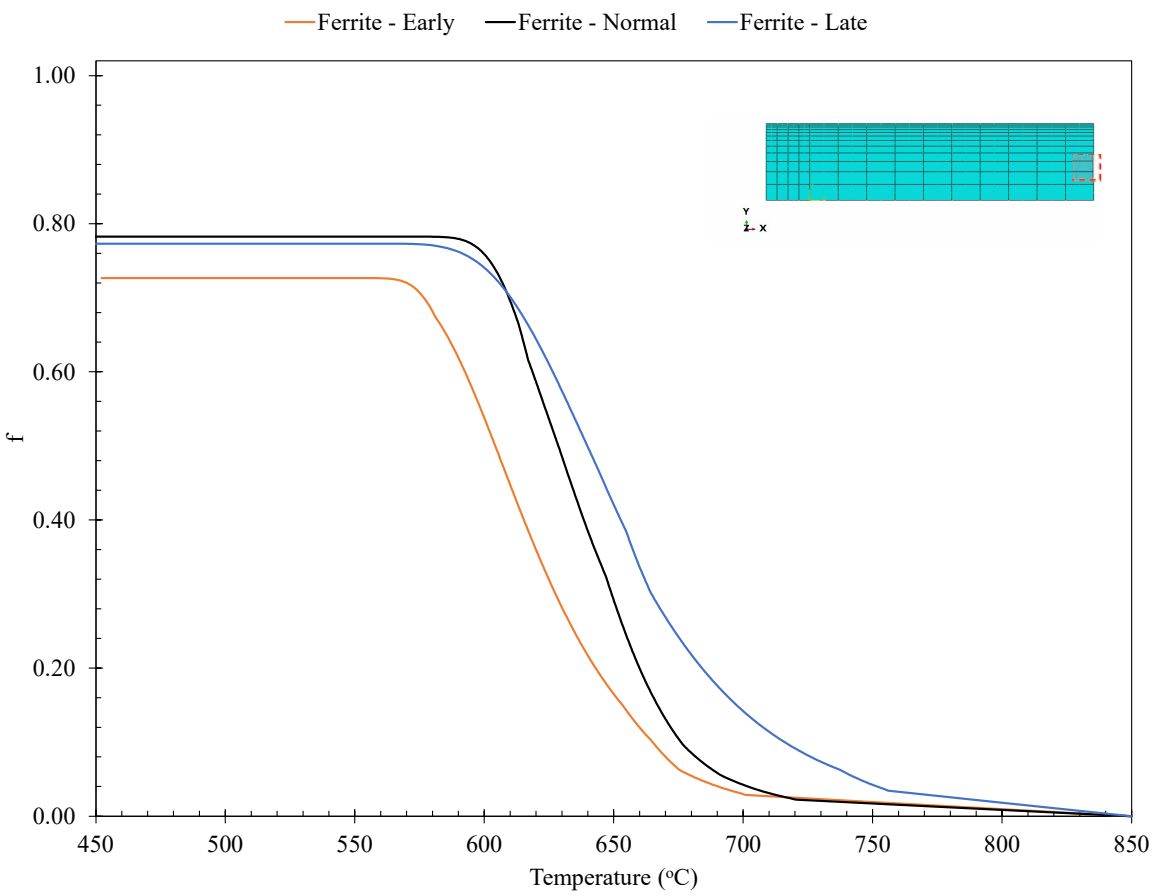

Figure 6.28: Quarter node ferrite evolution from regular, early, and late cooling

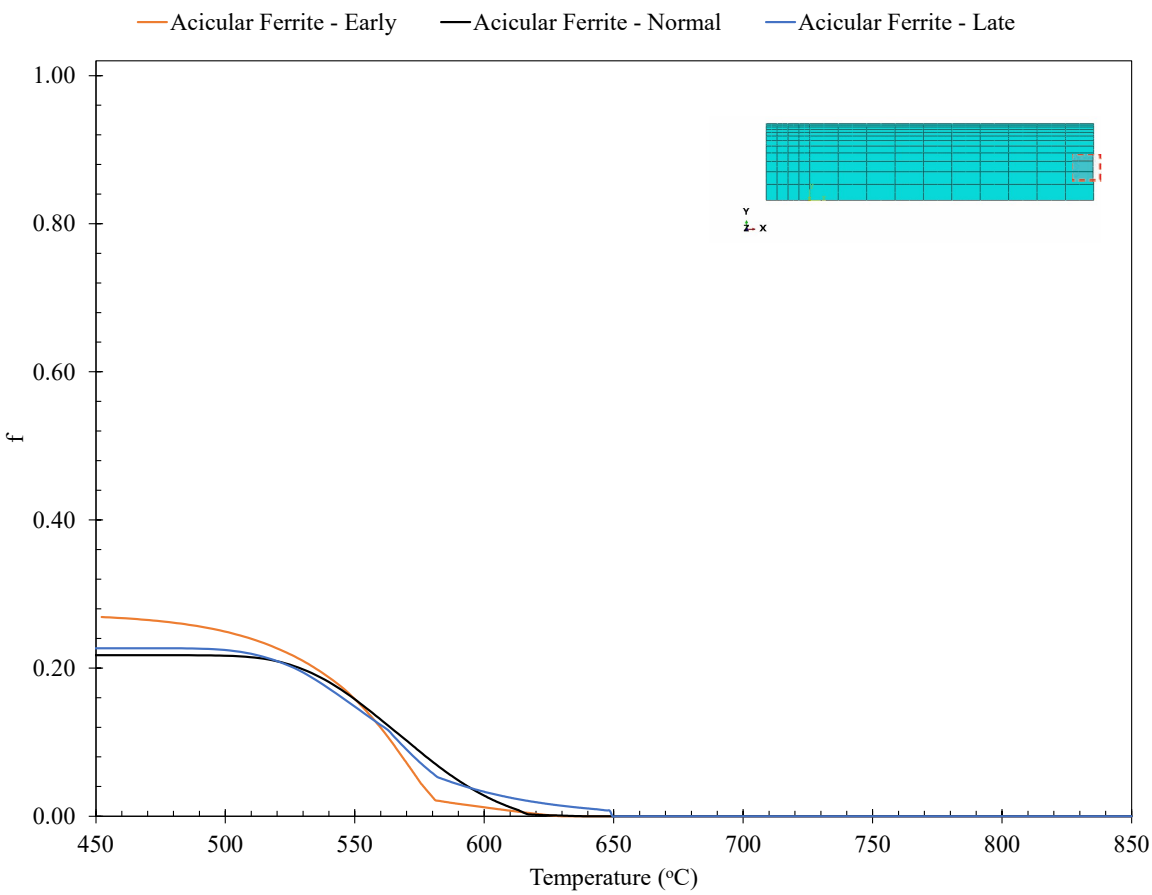

Figure 6.29: Quarter node acicular ferrite evolution from regular, early, and late cooling

Table 6.6: Effect of ROT configuration on microstructure evolution at quarter thickness

Configuration	Ferrite T_s (°C)	AF T_s (°C)	Ferrite:AF (%)
Normal	721	639	78:22
Early	702	630	73:27
Late	756	650	77:23

6.4 Summary

In this chapter, a thermo-microstructure model was developed that could accurately predict the through thickness microstructure and phase fractions of the X70 ROT sample. The non-continuous cooling profile predicted from thermal modelling was first discretized into a series of small isothermal steps. Using the CCT data generated in chapter 3, the fractional incubation was then calculated for each step. Based on the fractional incubation over the entire thermal history, the transformation temperatures for 1-100% were determined, and the austenite decomposition curve could be built. The microstructure model from chapter 3 was then fit to the austenite decomposition data to generate fraction transformed curves for the predicted phases. The performance of the model was validated through its ability to produce expected trends, generate results comparable to those obtained from EBSD, and produce ferrite and acicular ferrite curves with kinetics similar to the 5 ℃/s and 15 ℃/s dilatometer samples. With the model validated, the effect of alternative ROT configurations was explored. From these simulations, it was shown that changing the cooling on the ROT only had minor influences on the predicted end microstructure. This is likely due to the inabililty of the ROT to produce the necessary cooling rates for significant microstructure changes. Shown by the microstructure modelling and EBSD work in chapter 3, a large change to the microstructure was only achieved at cooling rates above 22 ℃/s.

Chapter 7

Summary and Future Work

This chapter contains the major findings and conclusions from this work. Additionally, for the oxide and thermo-microstructure model work conducted during this thesis, recommendations for the next steps are given.

7.1 Conclusions

In this work, a thermo-microstructural model was developed to predict the through thickness microstructure evolution on the ROT. This was achieved through the development of both a thermal model in ABAQUS and a microstructural model that could account for the simultaneous formation of two different phases. Through use of a modified form of the Scheil additive principle, these two models were combined into a unified model that could accurately predict the through thickness microstructure of a 15 mm X70 sample from Stelco Ltds. ROT.

A microstructural model was developed by modifying the JMAK equation by Jones et al [6] which accounts for simultaneous nucleation and growth of two phases. For the model used in this work, the K(T) portion of the equation was replaced with a $(\frac{1}{\tau})^n$ dependency, and the shape factor n was used as a fitting parameter to accommodate for varying particle geometries. Using this equation, austenite curves produced from

dilatometric testing were decomposed into fraction transformed curves for two phases. Dilatometric testing was carried out using cooling rates of 1-, 5-, 15-, 22-, 30-, 50-, 80-, and 120 °C/s, where from OM and SEM, it was determined that below 50 °C/s the primary phases were ferrite and acicular ferrite, and above they were acicular ferrite and bainite. Validation of model results was done through the use of EBSD band contrasting on each dilatometer sample, where the fraction of each phase was determined by the pattern quality of each pixel.

The thermal model based on the work of Wiskel et al [41] accurately captured the effect of different cooling mechanisms and ROT configurations on through thickness temperature profiles of 8-, 11-, 12-, and 15 mm skelp. Using a user-defined subroutine and a modifed version of the film boiling curve derived by Wendelstorf et al [36], the thermal model was able to accurately predict coiling temperatures. Validation of the model was done through the use of IR thermography where the full surface temperature profile was determined. When comparing transverse temperature profiles predicted from modelling and IR thermography, a discrepancy between the two was observed. Abnormal fluctuations were measured with the IR camera, resulting in temperature changes in excess of 20 °C. A method to access these abnormal temperature values was developed, and they were determined to be the result of oxides on the skelp surface. As a result of the presence of oxides on the surface, a program written in Python was developed to track their size and location, and supplementary thermal models that included the presence of oxides were made. From thermal modelling with oxides, it was determined that they inhibited extreme surface fluctuations on the skelp surface which subsequently resulted in reduced cooling through thickness.

Using a modified version of the Scheil additive principle developed by Rios [115], the thermal and microstructural models were combined. Through this approach, the volume fraction of ferrite and acicular ferrite in a 15 mm X70 ROT sample was predicted. Away

from the nozzle, ferrite percentages were predicted to be 54 %, 78 %, and 84 % at the surface, quarter, and center lines, respectively. Acicular ferrite values varied from 46 %, 22 %, and 16 % at the surface, quarter, and center lines, respectively. These results compared very good to those measured through band contrasting on the corresponding ROT sample, where the amount of ferrite and acicular ferrite at the center and quarter lines were measured to be 74 % and 24 %, and 78% and 21%, respectively. Surface measurements were hard to quantify with band contrasting as the cooling is complex in this region, but results of 32 % ferrite and 62 % acicular ferrite were produced which still show the trend of decreasing ferrite and increasing acicular ferrite towards the surface. Due to the limited amount of ROT samples for model validation, a comparison with dilatometer sample grain areas, aspect ratios, and misorientaion angles was also done as an additional means of validation. From comparison of these values with those measured for ROT sample, it was found that the 5 °C/s and 15 °C/s dilatometer samples provided the best fit. When model predictions were then compared with these samples, it was shown that the kinetics matched closely as well.

7.2 Future Work

Although the thermo-microstructure results show good prediction capabilities for the X70 sample provided, it is only calibrated to one specific steel chemistry and processing route. As such, any future work on this model should be aimed at increasing the breadth and generality of its predictive capabilities. To do this, potential aspects of future work are suggested below:

- From IR thermography, the presence of oxides on the surface of the skelp were confirmed, but specifics regarding them are still unknown. Important characteristics of these oxides that are unknown at this time include the specific thickness, com-

position, and emissivity. Any future work aimed at their presence and influence on microstructure evolution on the ROT must address these uncertainties. A potential route one may take to accomplish this would be to first carry out emissivity tests in accordance with ISO 19618:2017 on varying oxide thicknesses. Characterization techniques such as SEM and XRD could then be used to determine the type and proportion of each oxide present. From this, it may be possible to determine a correlation between thickness, composition, and emissivity. Then, using IR thermography, the emissivity of each spot along the skelp surface can be calculated. This can be done in a similar method as that done in chapter 5. Using the correlation between thickness and emissivity previously found, there is now the potential to be able to fully characterize the skelp surface. With true oxide thicknesses potentially known, more accurate thermal models can be generated to determine the temperature-time profiles.

- The thermo-microstructure model developed in this work is calibrated to the specific steel under investigation. Shown in the literature review section of this thesis, factors such as the prior austenite grain size, steel chemistry, and amount of strain, all have an effect on the transformation kinetics. Since the thermo-microstructure model specifically relies on the CCT of the given steel, understanding how each of these factors effect it is crucial in increasing its generality. Conducting dilatometric testing that investigates each of these factors may illustrate specific trends that can then be incorporated into the model presented in this thesis. Validating the model performance through additional dilatometer tests is also recommended. A dilatometer sample could be processed with a thermal history similar to that experienced on the ROT. The resulting microstructure from that sample could then be used as validation of model performance.

References

[1] J Malcolm Gray. Technology of microalloyed steel for large diameter pipe. *International Journal of Pressure Vessels and Piping*, 2(2):95–122, 1974.

[2] Debanshu Bhattacharya. Microalloyed steels for the automotive industry. *Tecnologia em Metalurgia, Materiais e Mineração*, 11(4):371, 2014.

[3] Paul C Lynch and Tyler J Grimm. Reducing microsegregation in next-generation high-strength low-alloy cast steels. *International Journal of Metalcasting*, 13:783–792, 2019.

[4] Imao Tamura, Hiroshi Sekine, and Tomo Tanaka. *Thermomechanical processing of high-strength low-alloy steels*. Butterworth-Heinemann, 2013.

[5] EI Poliak, NS Pottore, RM Skolly, WP Umlauf, and JC Brannbacka. Thermomechanical processing of advanced high strength steels in production hot strip rolling. *la metallurgia italiana*, 2009.

[6] SJ Jones and HKDH Bhadeshia. Kinetics of the simultaneous decomposition of austenite into several transformation products. *Acta Materialia*, 45(7):2911–2920, 1997.

[7] T. Gladman. *The physical metallurgy of microalloyed steels. [electronic resource]*. Book: 0792. Maney, 2002.

[8] Joseph R Davis et al. High-strength low-alloy steels. *Alloying: Understanding the Basics, ASM International, Metals Park, Ohio*, 2001.

[9] Junfang Lu et al. *Quantitative microstructural characterization of microalloyed steels*. PhD thesis, University of Alberta, 2009.

[10] GK Bansal, VC Srivastava, and S Ghosh Chowdhury. Role of solute nb in altering phase transformations during continuous cooling of a low-carbon steel. *Materials Science and Engineering: A*, 767:138416, 2019.

[11] Sarma DS, Karasev AV, and Jönsson PG. On the role of non-metallic inclusions in the nucleation of acicular ferrite in steels. *ISIJ international*, 49(7):1063–1074, 2009.

[12] Vahid Javaheri, Nasseh Khodaie, Antti Kaijalainen, and David Porter. Effect of niobium and phase transformation temperature on the microstructure and texture of a novel 0.40% c thermomechanically processed steel. *Materials Characterization*, 142:295–308, 2018.

[13] J Hu, LX Du, M Zang, SJ Yin, YG Wang, XY Qi, XH Gao, and RDK Misra. On the determining role of acicular ferrite in vn microalloyed steel in increasing strength-toughness combination. *Materials Characterization*, 118:446–453, 2016.

[14] Zhenghua Tang and Waldo Stumpf. The role of molybdenum additions and prior deformation on acicular ferrite formation in microalloyed nb–ti low-carbon line-pipe steels. *Materials Characterization*, 59(6):717–728, 2008.

[15] C Garcia de Andres, Carlos Capdevila, I Madariaga, and I Gutierrez. Role of molybdenum in acicular ferrite formation under continuous cooling in a medium carbon microalloyed forging steel. *Scripta materialia*, 45(6):709–716, 2001.

[16] Guomin Hua, Changsheng Li, Xiaonong Cheng, Xinluo Zhao, Quan Feng, Zhijie Li, Dongyang Li, and Jerzy A Szpunar. First-principles study on influence of molybdenum on acicular ferrite formation on tic particles in microallyed steels. *Solid State Communications*, 269:102–107, 2018.

[17] M Victor Li, David V Niebuhr, Lemmy L Meekisho, and David G Atteridge. A computational model for the prediction of steel hardenability. *Metallurgical and Materials transactions B*, 29:661–672, 1998.

[18] JS Kirkaldy and EA Baganis. Thermodynamic prediction of the ae 3 temperature of steels with additions of mn, si, ni, cr, mo, cu. *Metallurgical Transactions A*, 9:495–501, 1978.

[19] Dengqi Bai, Michael Ambrose Cooke, James Asante, and Jonathan Dorricott. Process for making high strength micro-alloy steel, January 27 2004. US Patent 6,682,613.

[20] A Ghosh. Segregation in cast products. *Sadhana*, 26:5–24, 2001.

[21] Anthony J DeArdo, Mingjian Hua, and Calixto I Garcia. Basic metallurgy of modern niobium steels. In *International Symposium on Niobium Microalloyed Sheet Steel for Automotive Applications*, pages 5–8, 2006.

[22] LJ Cuddy. Thermomechanical processing of microalloyed austenite. *TMS, Warrendale (Pa)*, 129, 1982.

[23] William D Callister and David G Rethwisch. *Materials science and engineering: an introduction*, volume 7. wiley New York, 2020.

[24] Rostislav Kawulok, Petr Kawulok, Ivo Schindler, Petr Opěla, Stanislav Rusz, Vojtěch Ševčák, and Zdeněk Solowski. Study of the effect of deformation on transformation diagrams of two low-alloy manganese-chromium steels. *Archives of Metallurgy and Materials*, 63, 2018.

[25] Shu-biao Yin, Xin-jun Sun, Qing-you Liu, and Zhi-bo Zhang. Influence of deformation on transformation of low-carbon and high nb-containing steel during continuous cooling. *Journal of iron and steel research, international*, 17(2):43–47, 2010.

[26] Rostislav Kawulok, Ivo Schindler, Jaroslav Sojka, Petr Kawulok, Petr Opěla, Lukáš Pindor, Eduard Grycz, Stanislav Rusz, and Vojtěch Ševčák. Effect of strain on transformation diagrams of 100cr6 steel. *Crystals*, 10(4):326, 2020.

[27] G Tacke, H Litzke, and E Raquet. Investigations into the efficiency of cooling systems for wide-strip hot rolling mills and computer-aided control of strip cooling. *Accelerated Cooling of Steel*, pages 35–54, 1985.

[28] GG Nasr, AJ Yule, L Bendig, GG Nasr, AJ Yule, and L Bendig. Spraying hot surfaces for making steel and other metals. *Industrial Sprays and Atomization: Design, Analysis and Applications*, pages 379–440, 2002.

[29] J Lee, S Samanta, and M Steeper. Review of accelerated cooling of steel plate. *Ironmaking & Steelmaking*, 42(4):268–273, 2015.

[30] Fuchang Xu. *Finite element simulation of water cooling process of steel strips on runout table*. PhD thesis, University of British Columbia, 2006.

[31] Zbigniew Malinowski, Tadeusz Telejko, Beata Hadala, and Agnieszka Cebo-Rudnicka. Implementation of the axially symmetrical and three dimensional finite element models to the determination of the heat transfer coefficient distribution on the hot plate surface cooled by the water spray nozzle. In *Key Engineering Materials*, volume 504, pages 1055–1060. Trans Tech Publ, 2012.

[32] DA Zumbrunnen. Method and apparatus for measuring heat transfer distributions on moving and stationary plates cooled by a planar liquid jet. *Experimental Thermal and Fluid Science*, 3(2):202–213, 1990.

[33] K Jondhale. *Heat Transfer During Multiple Jet Impingement on the Top Surface of Hot Rolled Steel Strip, MA. Sc.* PhD thesis, Thesis. 2007, University of British Columbia, Vancouver, 2007.

[34] G. P. Peterson. Heat transfer fundamentals. In *Eshbach's Handbook of Engineering Fundamentals*, pages 818–869. John Wiley & Sons, Ltd, 2009. Section: 15 _eprint: https://onlinelibrary.wiley.com/doi/pdf/10.1002/9780470432754.ch15.

[35] PC Campbell, EB Hawbolt, and JK Brimacombe. Microstructural engineering applied to the controlled cooling of steel wire rod: Part i. experimental design and heat transfer. *Metallurgical Transactions A*, 22:2769–2778, 1991.

[36] Jens Wendelstorf, K-H Spitzer, and R Wendelstorf. Spray water cooling heat transfer at high temperatures and liquid mass fluxes. *International Journal of heat and mass transfer*, 51(19-20):4902–4910, 2008.

[37] Jovan Filipovic, Raymond Viskanta, Frank P Incropera, and Timothy A Veslocki. Cooling of a moving steel strip by an array of round jets. *Steel research*, 65(12):541–547, 1994.

[38] Ichirō Tanasawa and Noam Lior. Heat and mass transfer in materials processing. 1992.

[39] Ananya Mukhopadhyay and Sudipta Sikdar. Implementation of an on-line run-out table model in a hot strip mill. *Journal of Materials Processing Technology*, 169(2):164–172, 2005.

[40] Siamak Serajzadeh. Prediction of temperature distribution and phase transformation on the run-out table in the process of hot strip rolling. *Applied Mathematical Modelling*, 27(11):861–875, 2003.

[41] JB Wiskel, H Deng, C Jefferies, and H Henein. Infrared thermography of tmcp microalloyed steel skelp at upcoiler and its application in quantifying laminar jet/skelp interaction. *Ironmaking & Steelmaking*, 38(1):35–44, 2011.

[42] Carosena Meola. Infrared thermography recent advances and future trends. 2012.

[43] M Vollmer. Fundamentals of infrared thermal imaging. In *Infrared Thermal Imaging*, pages 1–106. John Wiley & Sons, Ltd, 2017. Section: 1 _eprint: https://onlinelibrary.wiley.com/doi/pdf/10.1002/9783527693306.ch1.

[44] Carosena Meola, Simone Boccardi, and Giovanni maria Carlomagno. Chapter 2 - nondestructive evaluation. In Carosena Meola, Simone Boccardi, and Giovanni maria Carlomagno, editors, *Infrared Thermography in the Evaluation of Aerospace Composite Materials*, pages 25–56. Woodhead Publishing, 2017.

[45] H Abuluwefa, RIL Guthrie, JH Root, and F Ajersch. Real-time observations of the oxidation of mild steel at high temperature by neutron diffraction. *Metallurgical and Materials Transactions B*, 27:993–997, 1996.

[46] Weihua Sun, AK Tieu, Zhengyi Jiang, and Cheng Lu. High temperature oxide scale characteristics of low carbon steel in hot rolling. *Journal of Materials Processing Technology*, 155:1307–1312, 2004.

[47] RY Chen and WYD Yuen. Oxide-scale structures formed on commercial hot-rolled steel strip and their formation mechanisms. *Oxidation of metals*, 56(1-2):89–118, 2001.

[48] Huiquan Han, Tianpeng Zhou, Wanhui Wang, Zejun Chen, and Chunmei Yang. Effect of rolling reduction and temperature on the oxide scale of hot rolled mild steel strip. *Materials Research*, 22, 2019.

[49] RY Chen and WYD Yuen. Examination of oxide scales of hot rolled steel products. *ISIJ international*, 45(1):52–59, 2005.

[50] HangJin Jo, Jonathan L King, Kyle Blomstrand, and Kumar Sridharan. Spectral emissivity of oxidized and roughened metal surfaces. *International Journal of Heat and Mass Transfer*, 115:1065–1071, 2017.

[51] Vladimir B Ginzburg. *Steel-rolling technology: theory and practice*. CRC Press, 1989.

[52] Xiang Long Yu, Zheng Yi Jiang, Jing Wei Zhao, Dong Bin Wei, and Ji Zhou. A review of microstructure and microtexture of tertiary oxide scale in a hot strip mill. *Key Engineering Materials*, 716:843–855, 2016.

[53] M Graf and R Kawalla. Scale development on steel during hot strip rolling. *La Metallurgia Italiana*, 2014.

[54] RY Chen and WYD Yuen. Examination of oxide scales of hot rolled steel products. *ISIJ international*, 45(1):52–59, 2005.

[55] Weihua Sun, AK Tieu, Zhengyi Jiang, Cheng Lu, and Hongtao Zhu. Surface characteristics of oxide scale in hot strip rolling. *Journal of Materials Processing Technology*, 140(1-3):76–83, 2003.

[56] Michal Krzyzanowski and John Howard Beynon. Modelling the behaviour of oxide scale in hot rolling. *ISIJ international*, 46(11):1533–1547, 2006.

[57] Leire Del Campo, Raul B Perez-Saez, and Manuel J Tello. Iron oxidation kinetics study by using infrared spectral emissivity measurements below 570 c. *Corrosion Science*, 50(1):194–199, 2008.

[58] Leire del Campo, Raúl B Pérez-Sáez, Xabier Esquisabel, Ignacio Fernández, and Manuel J Tello. New experimental device for infrared spectral directional emissivity measurements in a controlled environment. *Review of scientific instruments*, 77(11):113111, 2006.

[59] Chang-Da Wen. Investigation of steel emissivity behaviors: Examination of multi-spectral radiation thermometry (mrt) emissivity models. *International Journal of Heat and Mass Transfer*, 53(9-10):2035–2043, 2010.

[60] RY Chen and WYD Yuen. A study of the scale structure of hot-rolled steel strip by simulated coiling and cooling. *Oxidation of Metals*, 53(5-6):539–560, 2000.

[61] PODHLADITEV IN PREKRIVANJE PODRO and IJ MED. Overcooling in overlap areas during hydraulic descaling. *Materiali in tehnologije*, 50(4):575–578, 2016.

[62] D Farrugia, Andrew Richardson, and Yong Jun Lan. Advancement in understanding of descalability during high pressure descaling. In *Key Engineering Materials*, volume 622, pages 29–36. Trans Tech Publ, 2014.

[63] M Krzyzanowski, JH Beynon, et al. Effect of oxide scale failure in hot steel rolling on subsequent hydraulic descaling: numerical simulation. In *Proceedings of the 3rd international conference on hydraulic descaling, London, United Kingdom*, pages 14–15, 2000.

[64] Takayuki NAKAMURA and Motoo SATO. Descalability on reheated steel slabs at high temperature. *Tetsu-to-hagané*, 80(3):237–242, 1994.

[65] Huiquan Han, Tianpeng Zhou, Wanhui Wang, Zejun Chen, and Chunmei Yang. Effect of rolling reduction and temperature on the oxide scale of hot rolled mild steel strip. *Materials Research*, 22, 2019.

[66] Michal Krzyzanowski, John H Beynon, and Didier CJ Farrugia. *Oxide scale behavior in high temperature metal processing*. John Wiley & Sons, 2010.

[67] Jung Hyun Jang, Dong Eun Lee, Man Young Kim, and Hyong Gon Kim. Investigation of the slab heating characteristics in a reheating furnace with the formation and growth of scale on the slab surface. *International Journal of Heat and Mass Transfer*, 53(19-20):4326–4332, 2010.

[68] DP Fairchild, BD Newbury, TD Anderson, and NS Thirumalai. Local hard zones in sour service steels. In *International Conference on Offshore Mechanics and Arctic Engineering*, volume 58790, page V004T03A015. American Society of Mechanical Engineers, 2019.

[69] D Matlock. Metallurgy of induction hardening of steel. *ASM Handbook*, 4:45–57, 2014.

[70] David A Porter, Kenneth E Easterling, and Mohamed Y Sherif. *Phase transformations in metals and alloys*. CRC press, 2021.

[71] Melvin Avrami. Kinetics of phase change. i general theory. *The Journal of chemical physics*, 7(12):1103–1112, 1939.

[72] W.A. Johnson and R.F. Mehl. Reaction kinetics in processes of nucleation and growth. *Trans. AIME*, 135(8):396–415, 1939.

[73] H Chen, YC Liu, DJ Wang, ZS Yan, JC Fu, and QZ Shi. A jmak-like approach for isochronal austenite–ferrite transformation kinetics in fe–0· 055 wt-% n alloy. *Materials Science and Technology*, 26(5):572–578, 2010.

[74] M Umemoto, N Komatsubara, and I Tamura. Prediction of hardenability effects from isothermal transformation kinetics. *Journal of Heat Treating*, 1:57–64, 1980.

[75] M Venkatraman, ON Mohanty, and RN Ghosh. Modelling of transformation kinetics in hsla 100 steel during continuous cooling. *Scandinavian journal of metallurgy*, 30(1):8–13, 2001.

[76] Erich Scheil. Austenite transformation ramp-up time. *Archive for the ironworks*, 8(12):565–567, 1935.

[77] Minoru Umemoto, Kazunari Horiuchi, and Imao Tamura. Transformation kinetics of bainite during isothermal holding and continuous cooling. *Tetsu-to-Hagane*, 68(3):461–470, 1982.

[78] Aarne Pohjonen, Mahesh Somani, and David Porter. Modelling of austenite transformation along arbitrary cooling paths. *Computational Materials Science*, 150:244–251, 2018.

[79] Prakash K Agarwal and JK Brimacombe. Mathematical model of heat flow and austenite-pearlite transformation in eutectoid carbon steel rods for wire. *Metallurgical Transactions B*, 12:121–133, 1981.

[80] Yazhu Ma, Yubing Zhang, and Feng Liu. A non-isokinetic approach for modeling solid-state transformations: Application to crystallization of a fe-b amorphous alloy. *Materials*, 14(2):292, 2021.

[81] John Christian. *The theory of transformations in metals and alloys*. Newnes, 2002.

[82] Jun-Yun Kang, Hyun Kim Do, Sung-Il Baik, Tae-Hong Ahn, Young-Woon Kim, Heung Nam Han, Kyu Hwan Oh, Hu-Chul Lee, and Seong Ho Han. Phase analysis of steels by grain-averaged ebsd functions. *ISIJ international*, 51(1):130–136, 2011.

[83] Stuart I Wright and Matthew M Nowell. Ebsd image quality mapping. *Microscopy and microanalysis*, 12(1):72–84, 2006.

[84] AW Wilson, JD Madison, and G Spanos. Determining phase volume fraction in steels by electron backscattered diffraction. *Scripta materialia*, 45(12):1335–1340, 2001.

[85] AJ de DeArdo, CI Garcia, K Cho, and M Hua. New method of characterizing and quantifying complex microstructures in steels. *Materials and Manufacturing Processes*, 25(1-3):33–40, 2010.

[86] Haitao Zhao, BP Wynne, and EJ Palmiere. A phase quantification method based on ebsd data for a continuously cooled microalloyed steel. *Materials Characterization*, 123:339–348, 2017.

[87] JR Yang and HKDH Bhadeshia. The dislocation density of acicular ferrite in steel welds. *Weld. J*, 69:305–307, 1990.

[88] Jian Zhu, Gary Barber, and Xichen Sun. Effects of isothermal temperature on dislocation density in bainite transformation of 4140 steel. *Materials*, 15(17):6066, 2022.

[89] William Fortune Smith. Structure and properties of engineering alloys. *McGraw-Hill Book Co., xiv+ 512, 23 x 16 cm, illustrated(16. 95)*, 1981.

[90] Etienne Girault, Pascal Jacques, Ph Harlet, Koen Mols, Jan Van Humbeeck, Etienne Aernoudt, and Francis Delannay. Metallographic methods for revealing the multiphase microstructure of trip-assisted steels. *Materials Characterization*, 40(2):111–118, 1998.

[91] Jinghui Wu, Peter J Wray, Calixto I Garcia, Mingjian Hua, and Anthony J DeArdo. Image quality analysis: A new method of characterizing microstructures. *ISIJ international*, 45(2):254–262, 2005.

[92] Sachin L Shrestha, Andrew J Breen, Patrick Trimby, Gwénaëlle Proust, Simon P Ringer, and Julie M Cairney. An automated method of quantifying ferrite microstructures using electron backscatter diffraction (ebsd) data. *Ultramicroscopy*, 137:40–47, 2014.

[93] Kyung-Tae Park, Si Woo Hwang, Jung Hoon Ji, and Chang Hee Lee. Inclusions nucleating intragranular polygonal ferrite and acicular ferrite in low alloyed carbon manganese steel welds. *Metals and Materials International*, 17:349–356, 2011.

[94] Gourgues A.-F., HM Flower, and TC Lindley. Electron backscattering diffraction study of acicular ferrite, bainite, and martensite steel microstructures. *Materials Science and Technology*, 16(1):26–40, 2000.

[95] H Landheer, SE Offerman, RH Petrov, and LAI Kestens. The role of crystal misorientations during solid-state nucleation of ferrite in austenite. *Acta materialia*, 57(5):1486–1496, 2009.

[96] JCF Jorge, LFG De Souza, MC Mendes, IS Bott, LS Araújo, VR Dos Santos, JMA Rebello, and GM Evans. Microstructure characterization and its relationship with impact toughness of c–mn and high strength low alloy steel weld metals–a review. *Journal of Materials Research and Technology*, 10:471–501, 2021.

[97] Zhang Jian, Chen Deng-Fu, Zhang Cheng-Qian, Hwang Weng-Sing, and Han Ming-Rong. The effects of heating/cooling rate on the phase transformations and thermal expansion coefficient of c–mn as-cast steel at elevated temperatures. *Journal of Materials Research*, 30(13):2081–2089, 2015.

[98] Hamid Azizi-Alizamini, Matthias Militzer, and Warren J Poole. Austenite formation in plain low-carbon steels. *Metallurgical and Materials Transactions A*, 42:1544–1557, 2011.

[99] Th A Kop, J Sietsma, and S Van Der Zwaag. Dilatometric analysis of phase transformations in hypo-eutectoid steels. *Journal of Materials Science*, 36:519–526, 2001.

[100] Leon S Lasdon, Richard L Fox, and Margery W Ratner. Nonlinear optimization using the generalized reduced gradient method. *Revue française d'automatique, informatique, recherche opérationnelle. Recherche opérationnelle*, 8(V3):73–103, 1974.

[101] Ming-Chun Zhao, Ke Yang, Fu-Ren Xiao, and Yi-Yin Shan. Continuous cooling transformation of undeformed and deformed low carbon pipeline steels. *Materials Science and Engineering: A*, 355(1-2):126–136, 2003.

[102] RL Bodnar and SS Hansen. Effects of austenite grain size and cooling rate on widmanstätten ferrite formation in low-alloy steels. *Metallurgical and Materials Transactions A*, 25:665–675, 1994.

[103] YJ Lan, DZ Li, and YY Li. Modeling austenite decomposition into ferrite at different cooling rate in low-carbon steel with cellular automaton method. *Acta Materialia*, 52(6):1721–1729, 2004.

[104] SW Thompson, DJ Colvin, and G Krauss. Austenite decomposition during continuous cooling of an hsla-80 plate steel. *Metallurgical and Materials Transactions A*, 27:1557–1571, 1996.

[105] D Rasouli, Sh Khameneh Asl, A Akbarzadeh, and GH Daneshi. Effect of cooling rate on the microstructure and mechanical properties of microalloyed forging steel. *Journal of materials processing technology*, 206(1-3):92–98, 2008.

[106] Mingming Tong, Dianzhong Li, and Yiyi Li. Modeling the austenite–ferrite diffusive transformation during continuous cooling on a mesoscale using monte carlo method. *Acta materialia*, 52(5):1155–1162, 2004.

[107] YB Guo, GF Sui, YC Liu, Y Chen, and DT Zhang. Phase transformation mechanism of low-carbon high strength low alloy steel upon continuous cooling. *Materials Research Innovations*, 19(sup8):S8–416, 2015.

[108] Yongkun Yang, Dongping Zhan, Hong Lei, Guoxing Qiu, Yulu Li, Zhouhua Jiang, and Huishu Zhang. In situ observation of acicular ferrite nucleation and growth at different cooling rate in ti-zr deoxidized steel. *Metallurgical and Materials Transactions B*, 50:2536–2546, 2019.

[109] Young Min Kim, Hakcheol Lee, and Nack J Kim. Transformation behavior and microstructural characteristics of acicular ferrite in linepipe steels. *Materials Science and Engineering: A*, 478(1-2):361–370, 2008.

[110] Yi Shao, Chenxi Liu, Zesheng Yan, Huijun Li, and Yongchang Liu. Formation mechanism and control methods of acicular ferrite in hsla steels: A review. *Journal of Materials Science & Technology*, 34(5):737–744, 2018.

[111] Harshad Kumar Dharamshi Hansraj Bhadeshia and JW Christian. Bainite in steels. *Metallurgical transactions A*, 21:767–797, 1990.

[112] Shih-Jiun Chen and Ampere A Tseng. Spray and jet cooling in steel rolling. *International Journal of Heat and Fluid Flow*, 13(4):358–369, 1992.

[113] Jye-Long Lee, Chen JK, Pan YT, and Hsieh KC. Evaluation of transformation latent heat in c-mn steels. *ISIJ international*, 39(3):281–287, 1999.

[114] H Abuluwefa, RIL Guthrie, JH Root, and F Ajersch. Real-time observations of the oxidation of mild steel at high temperature by neutron diffraction. *Metallurgical and Materials Transactions B*, 27:993–997, 1996.

[115] PR Rios. Relationship between non-isothermal transformation curves and isothermal and non-isothermal kinetics. *Acta Materialia*, 53(18):4893–4901, 2005.

[116] JB Wiskel, J Prescott, and H Henein. Finite element thermal analysis of surface cold spots observed during infrared video imaging of a moving hot steel strip. QIRT, 2014.

Appendix A. Run-Out Table Sample

Appendix A contains supplementary OM and SEM images of the ROT sample. Additionally, all EBSD band contrast images and results are presented.

A.1 X70 Properties

Table A.1: Latent heat of transformation of X70 steel [41]

Latent Heat (J/kg)	Solidus Temperature (℃)	Liquidus Temperature (℃)
18000	550	700

Table A.2: Specific thermal conductivity of X70 steel [41]

Temperature (℃)	Thermal Conductivity ($\frac{W}{mK}$)
0	59.5
100	57.8
200	53.2
300	49.4
400	45.6
500	41
600	36.9
700	33.1

Table A.3: Specific heat capacity of X70 steel [41]

Temperature (℃)	Heat Capacity ($\frac{J}{kg*K}$)
50	481
150	519
250	536
300	553
350	547
400	595
500	662
600	754

A.2 ROT Optical Microscopy

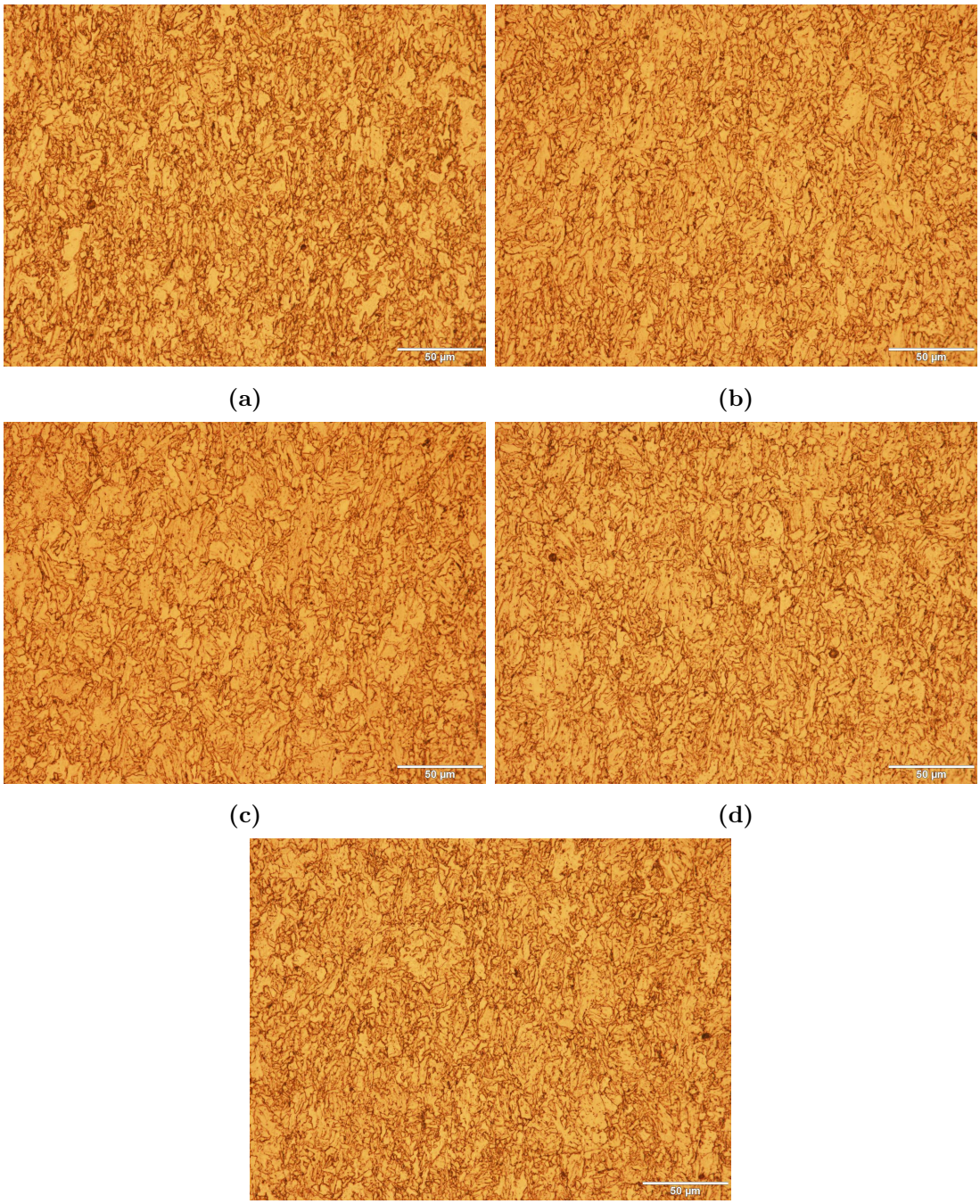

(a) **(b)**

(c) **(d)**

(e)

Figure A.1: OM images of ROT sample (a) top surface (b) top quarter (c) center (d) bottom quarter and (e) bottom surface

A.3 ROT SEM

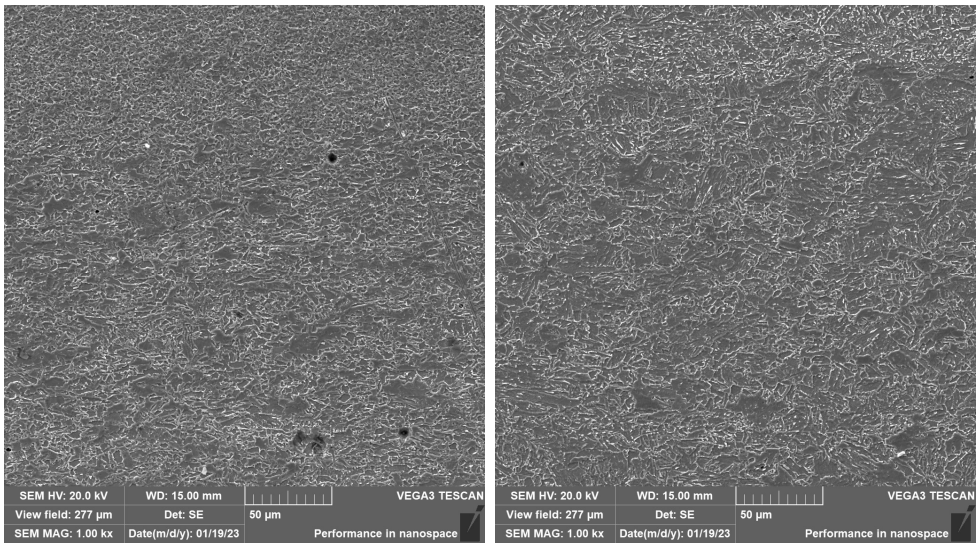

(a) **(b)**

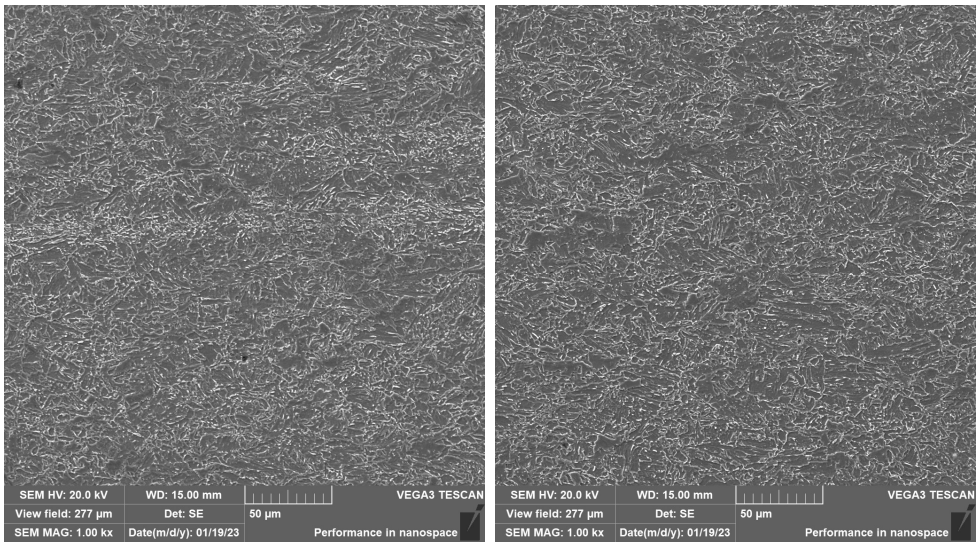

(c) **(d)**

Figure A.2: SEM images of ROT sample (a) top surface (b) top quarter (c) center and (d) bottom quarter at 1000X magnification

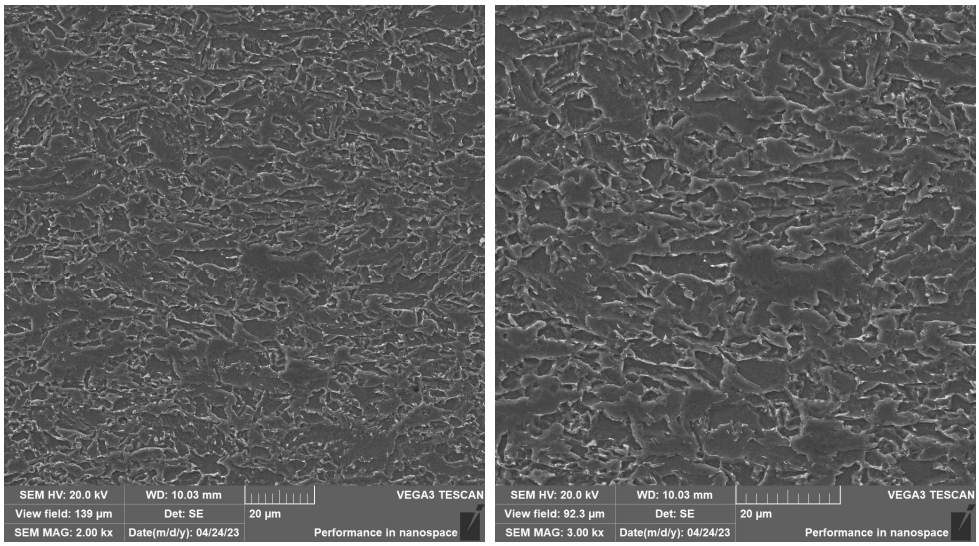

(a) **(b)**

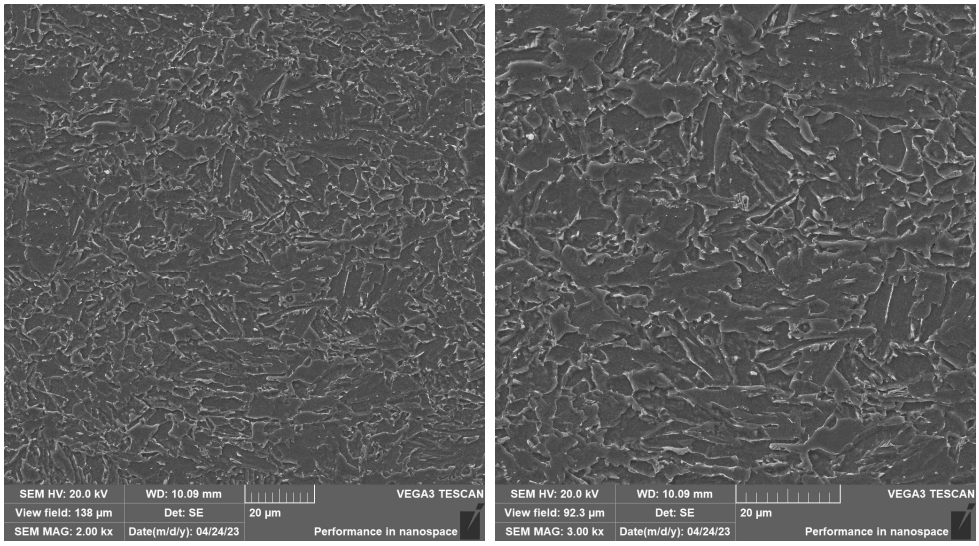

(c) **(d)**

Figure A.3: SEM images of ROT sample quarter (a-b) and center (c-d) at 2000X (a and c) and 3000X (b and d) magnification

A.4 ROT EBSD

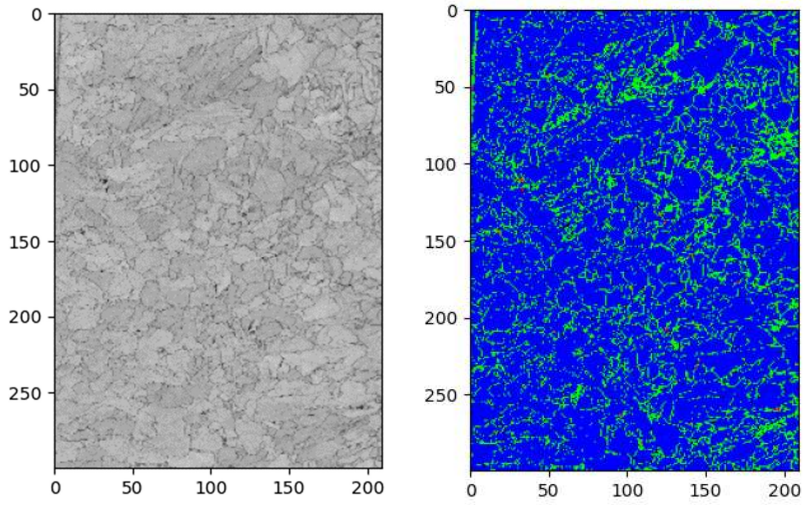

Figure A.4: EBSD band contrast of ROT sample quarter line

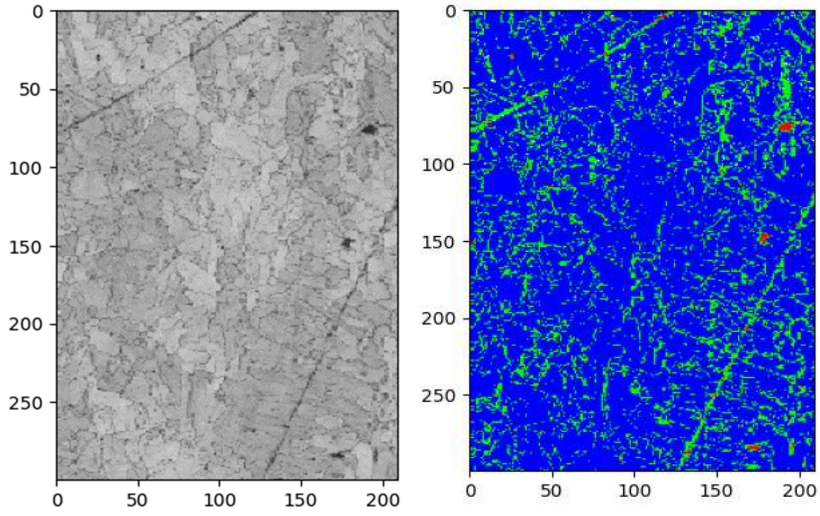

Figure A.5: EBSD band contrast of ROT sample center line

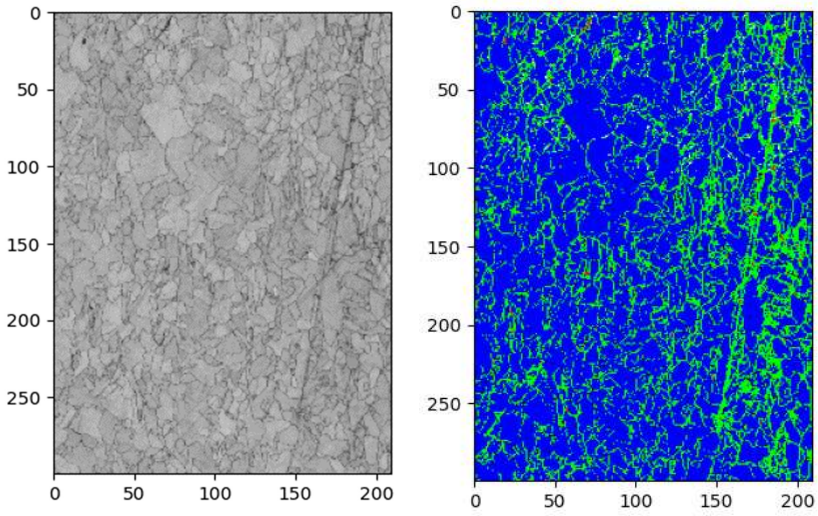

Figure A.6: EBSD band contrast of ROT sample top surface

Appendix B. Dilatometer Samples

Appendix B contains all the results for each dilatometer sample. This includes dilation curves, transformation curves, SEM images, and EBSD band contrast.

B.1 Dilation Curves

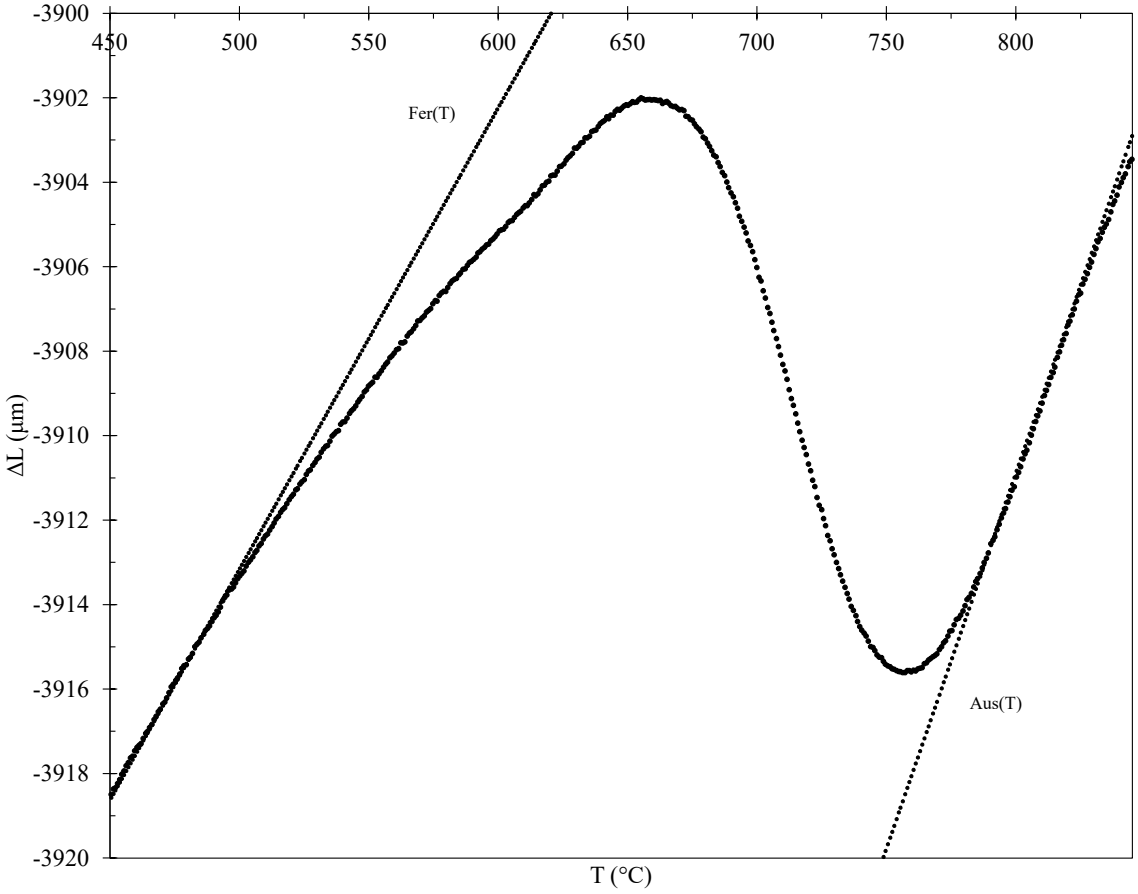

Figure B.1: 1 °C/s dilation curve

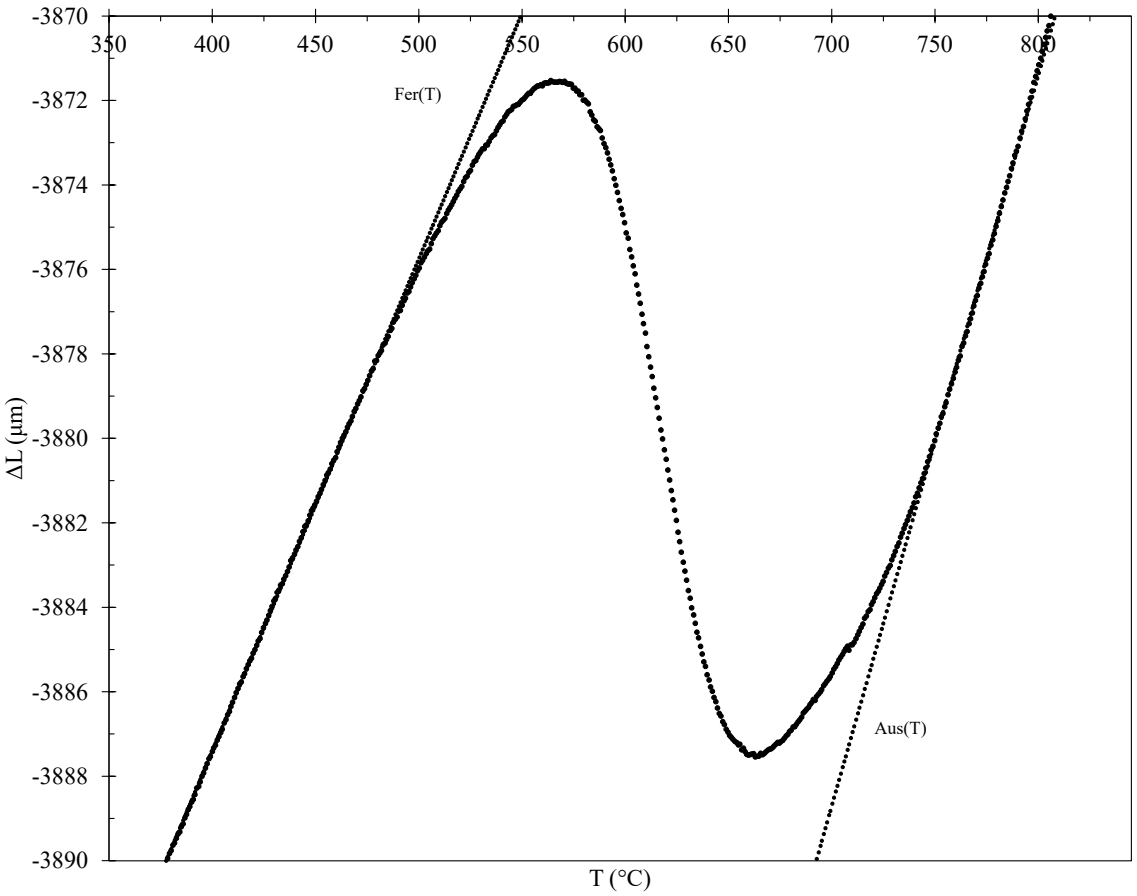

Figure B.2: 5 °C/s dilation curve

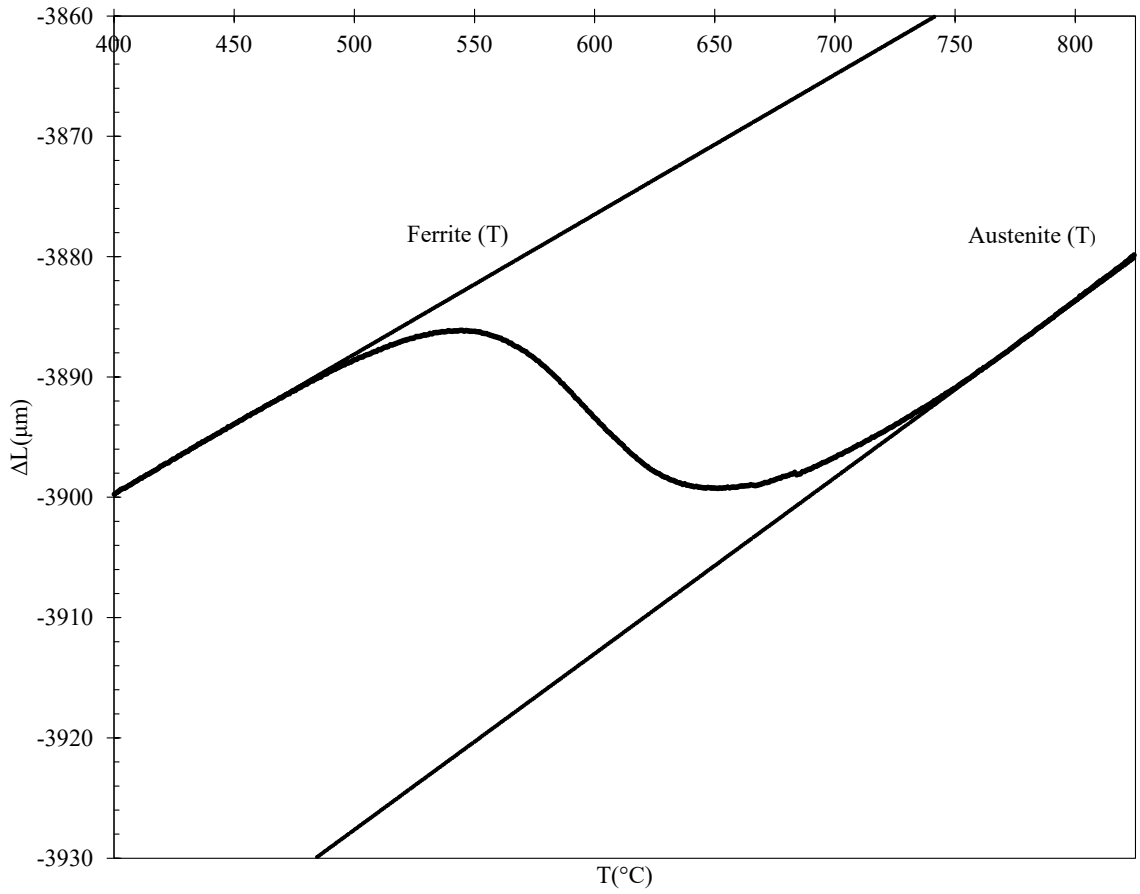

Figure B.3: 15 ℃/s dilation curve

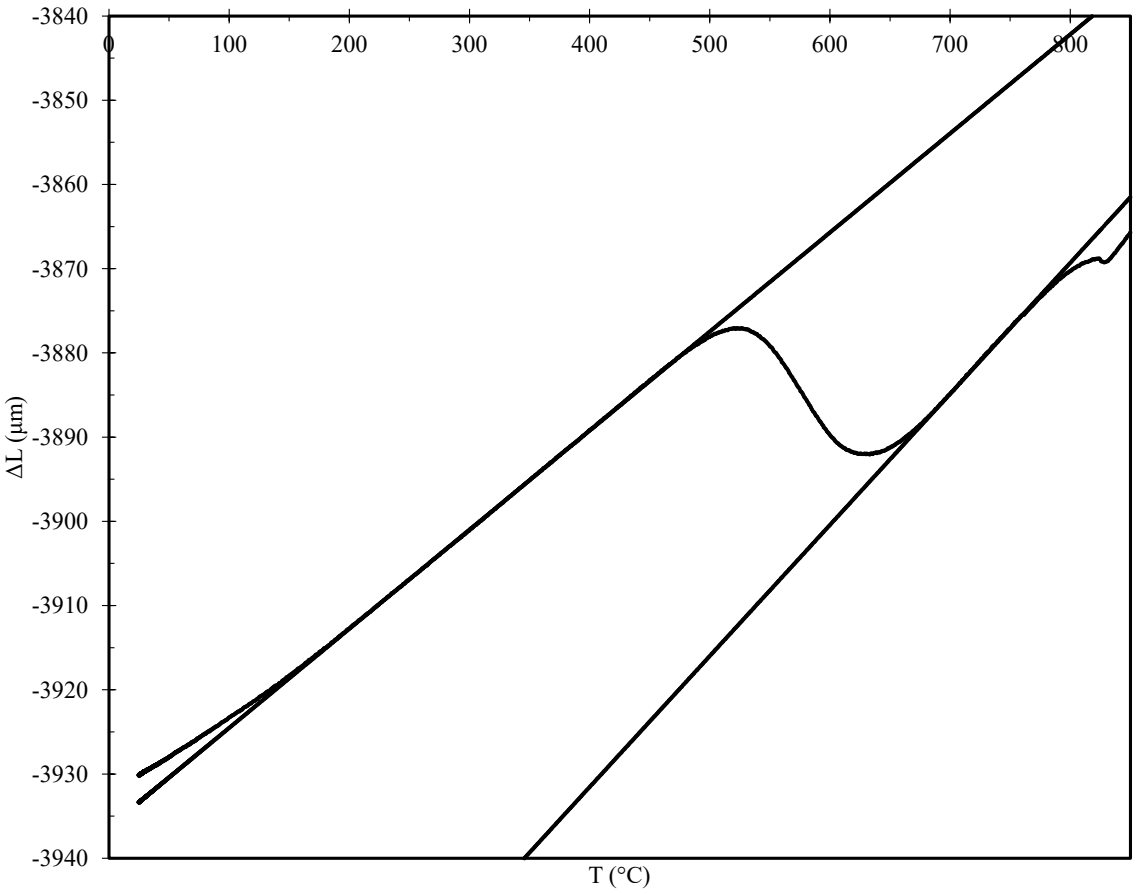

Figure B.4: 22 ℃/s dilation curve

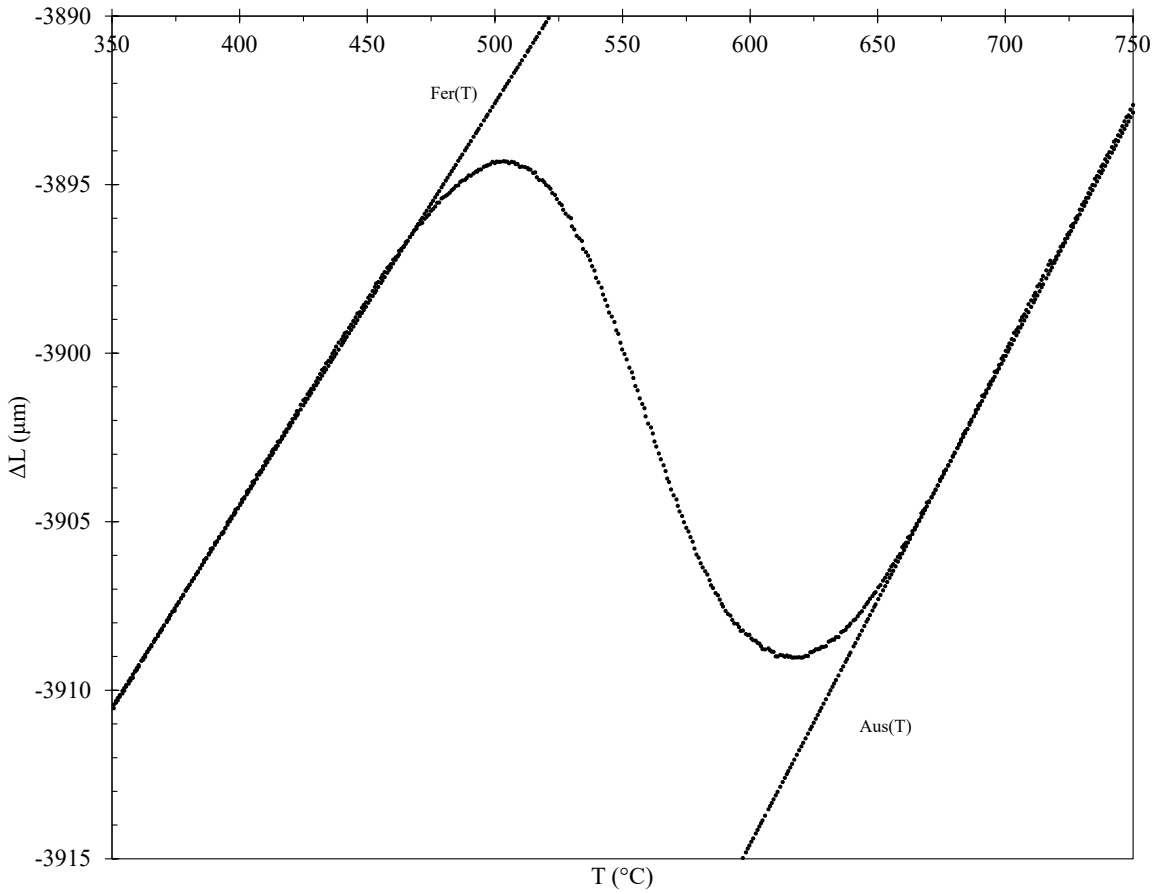

Figure B.5: 30 ℃/s dilation curve

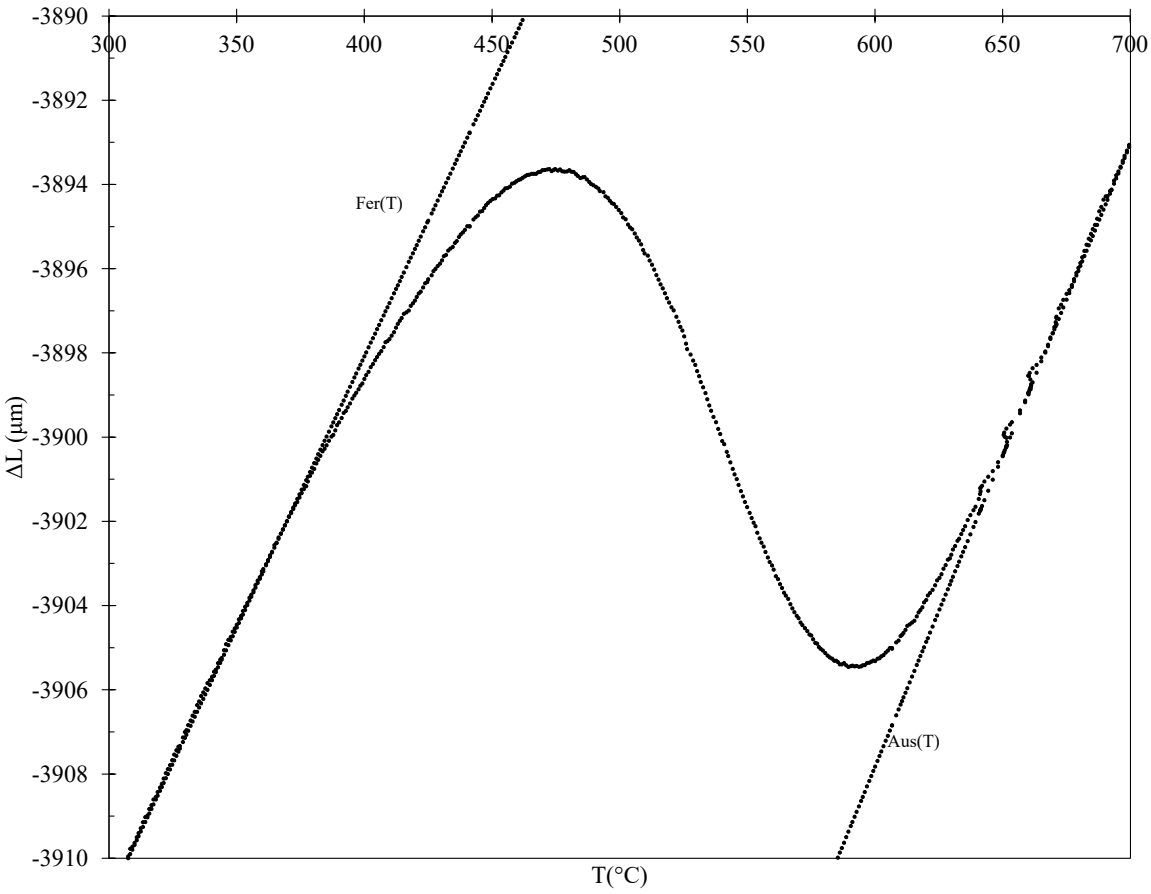

Figure B.6: 50 ℃/s dilation curve

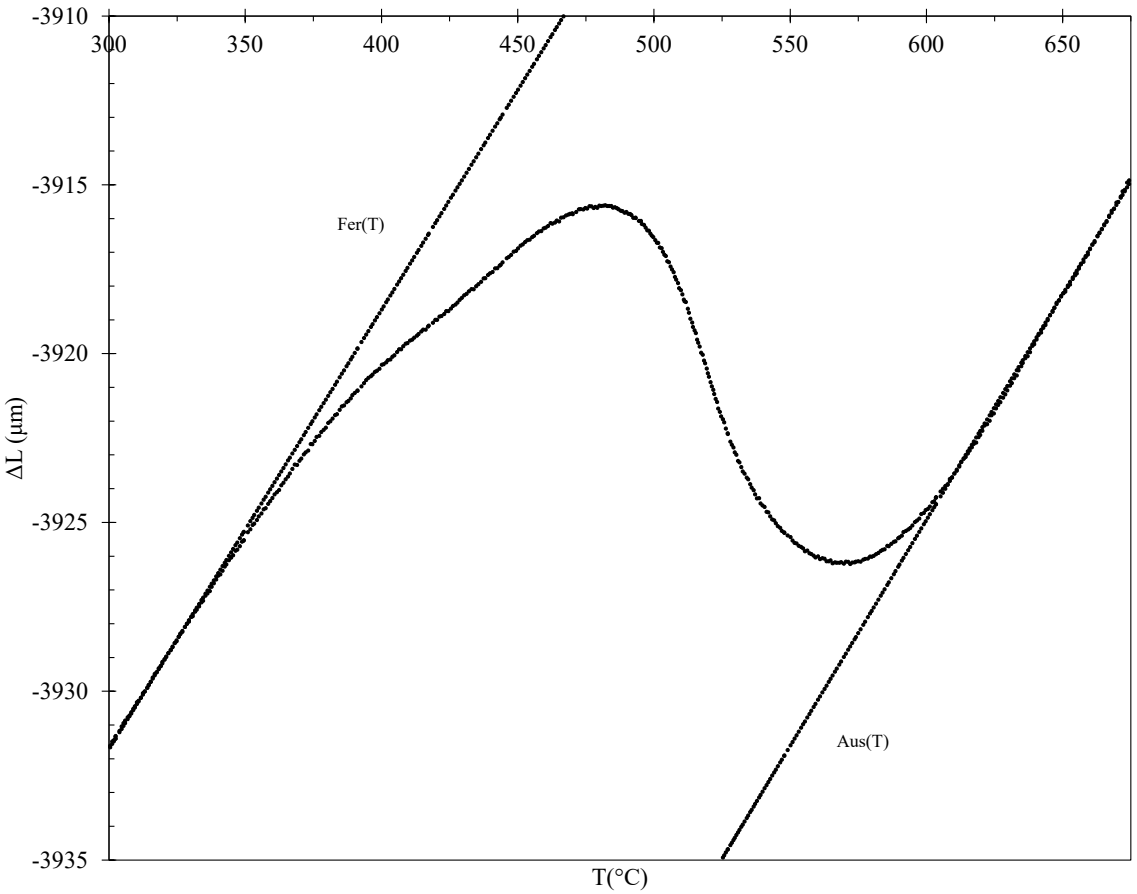

Figure B.7: 80 ℃/s dilation curve

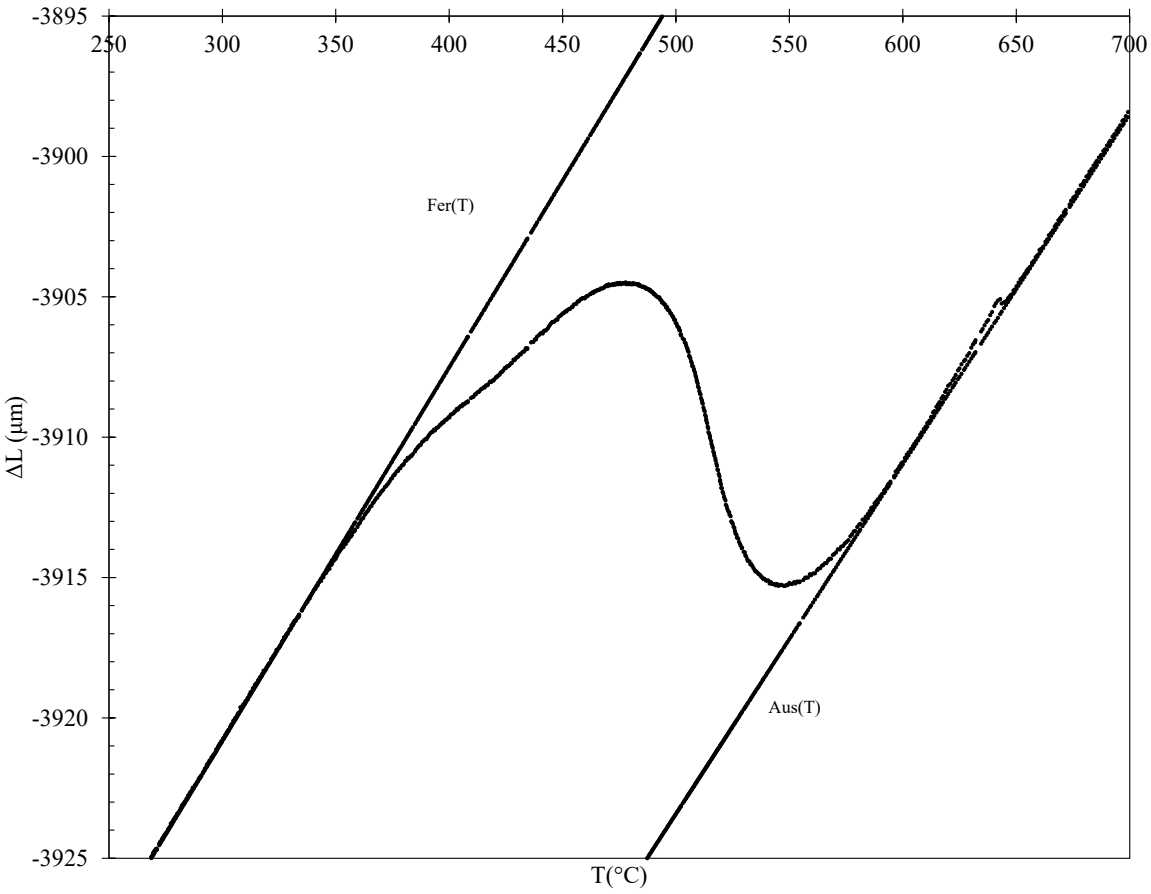

Figure B.8: 120 °C/s dilation curve

B.2 Fraction Transformed Curves

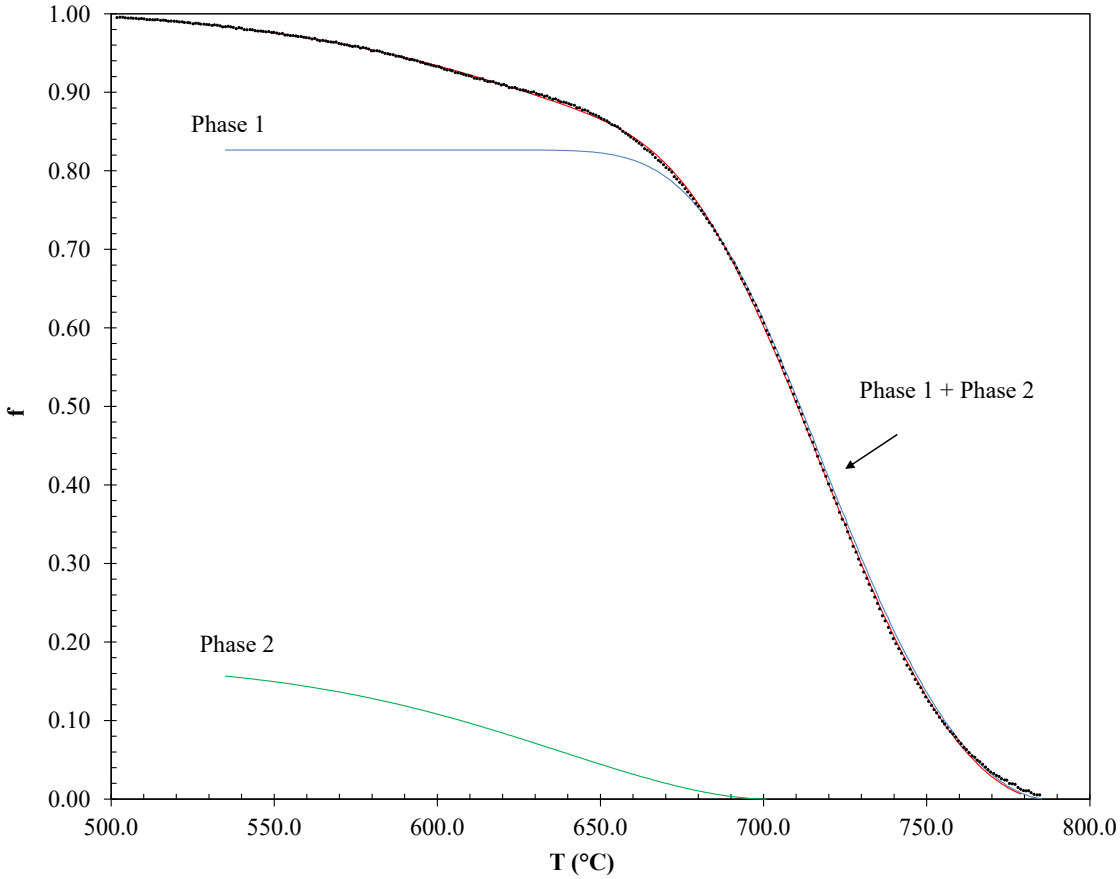

Figure B.9: 1 ℃/s transformation curve

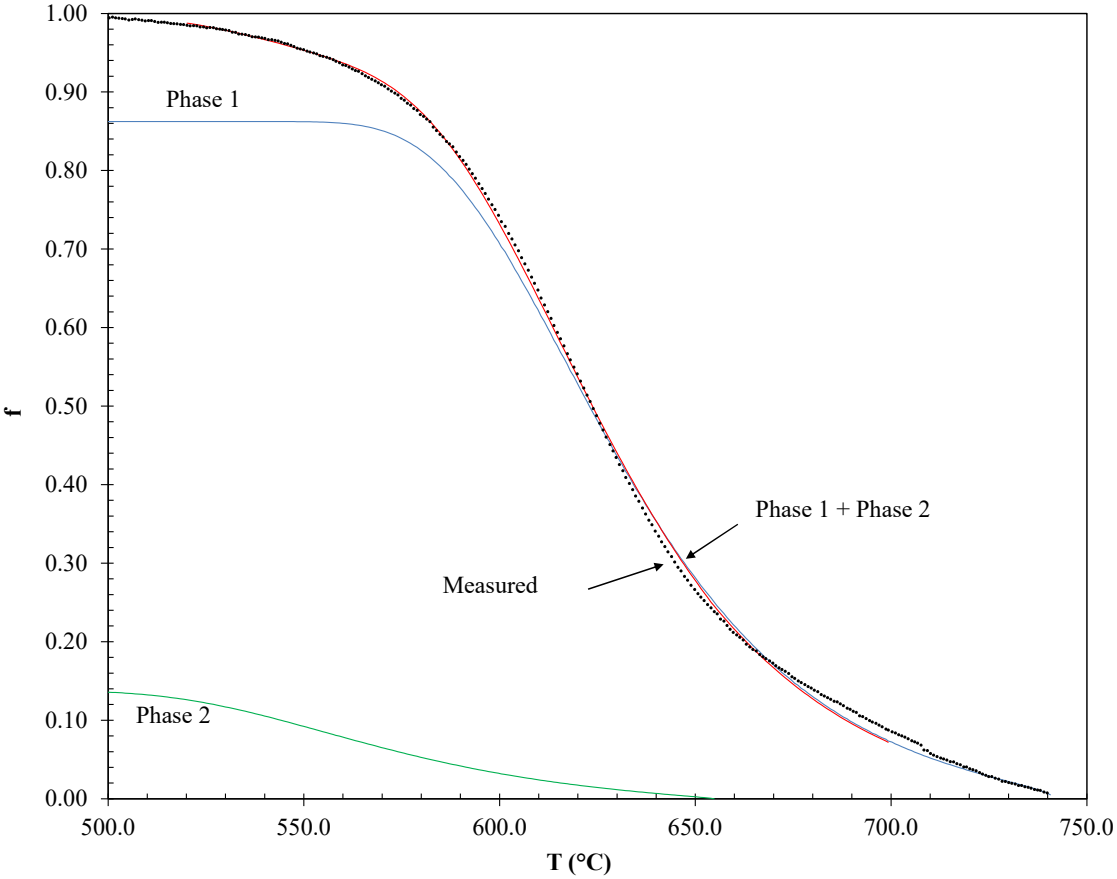

Figure B.10: 5 ℃/s transformation curve

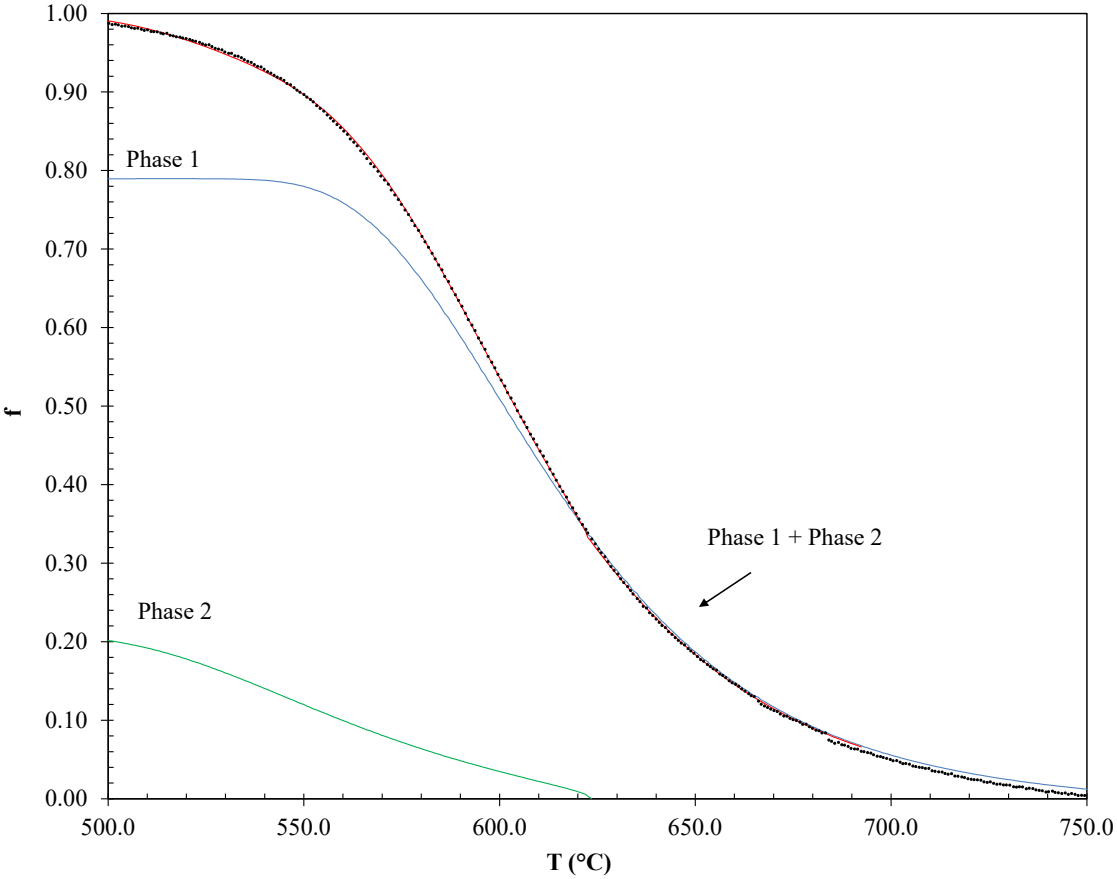

Figure B.11: 15 ℃/s transformation curve

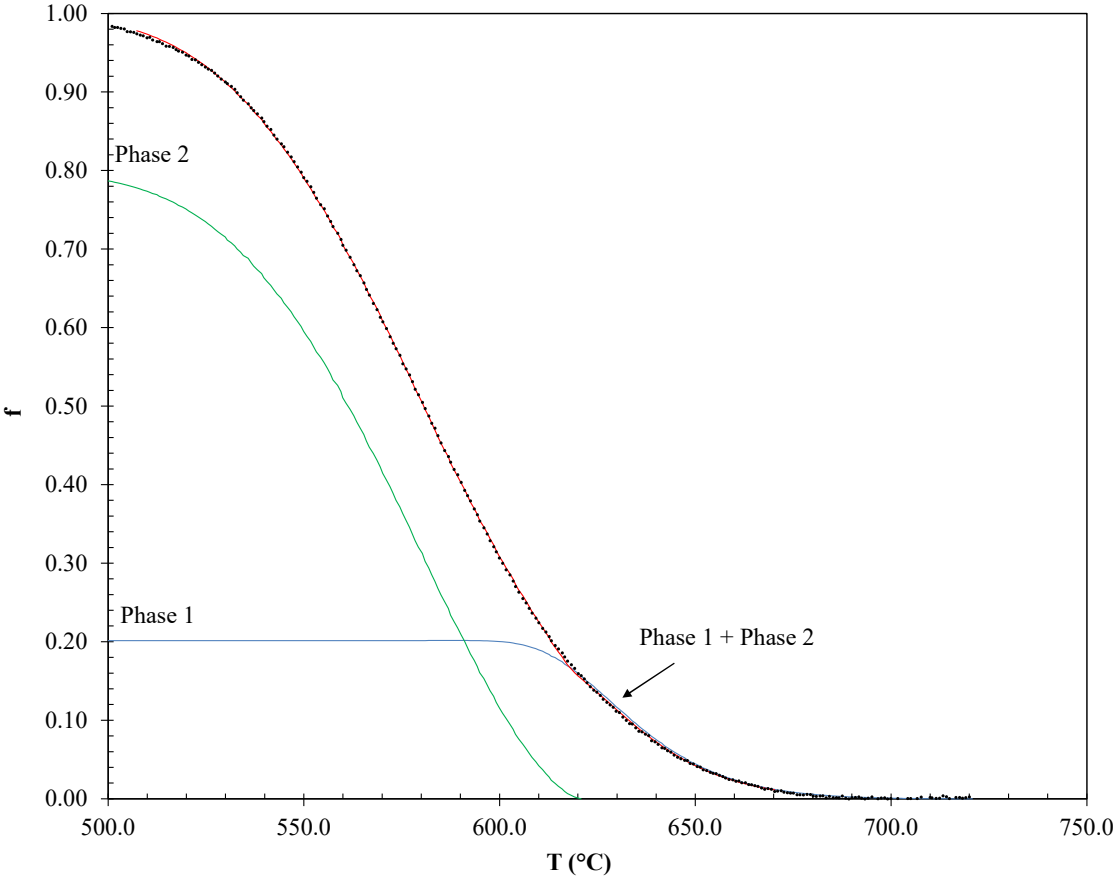

Figure B.12: 22 ℃/s transformation curve

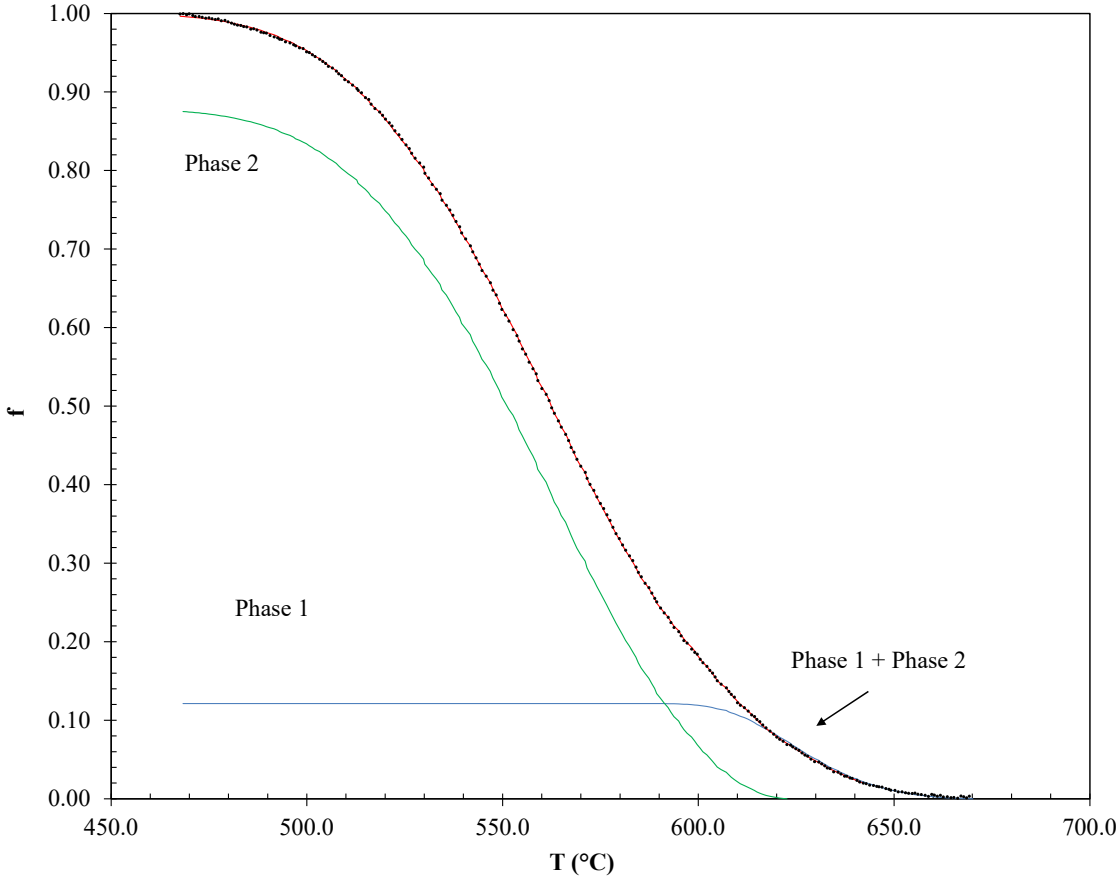

Figure B.13: 30 ℃/s transformation curve

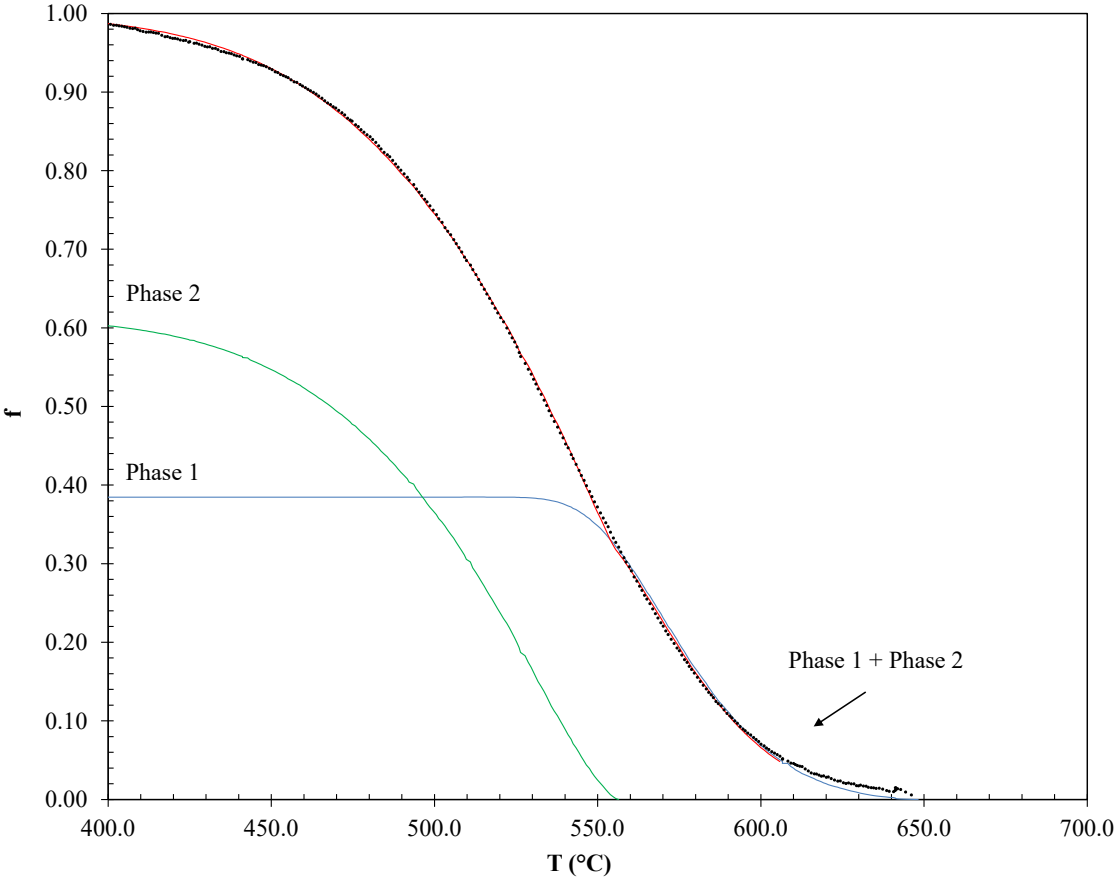

Figure B.14: 50 ℃/s transformation curve

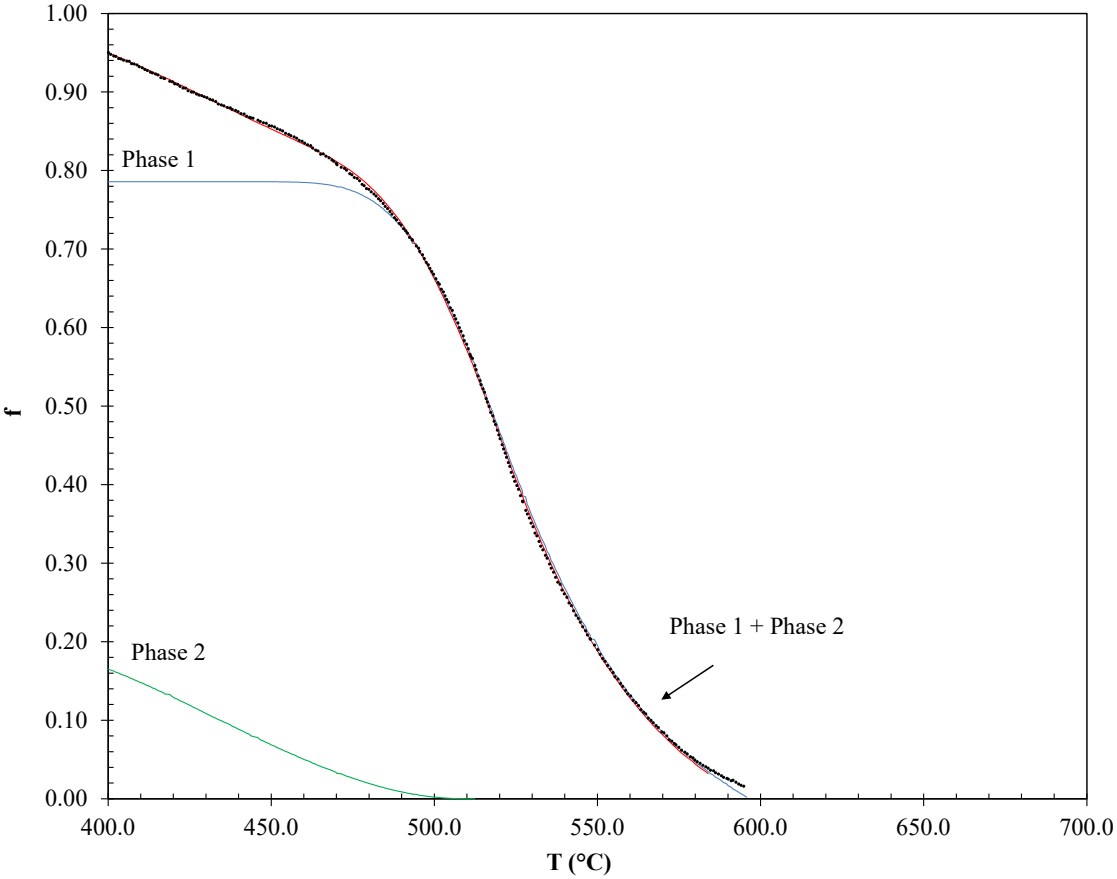

Figure B.15: 80 ℃/s transformation curve

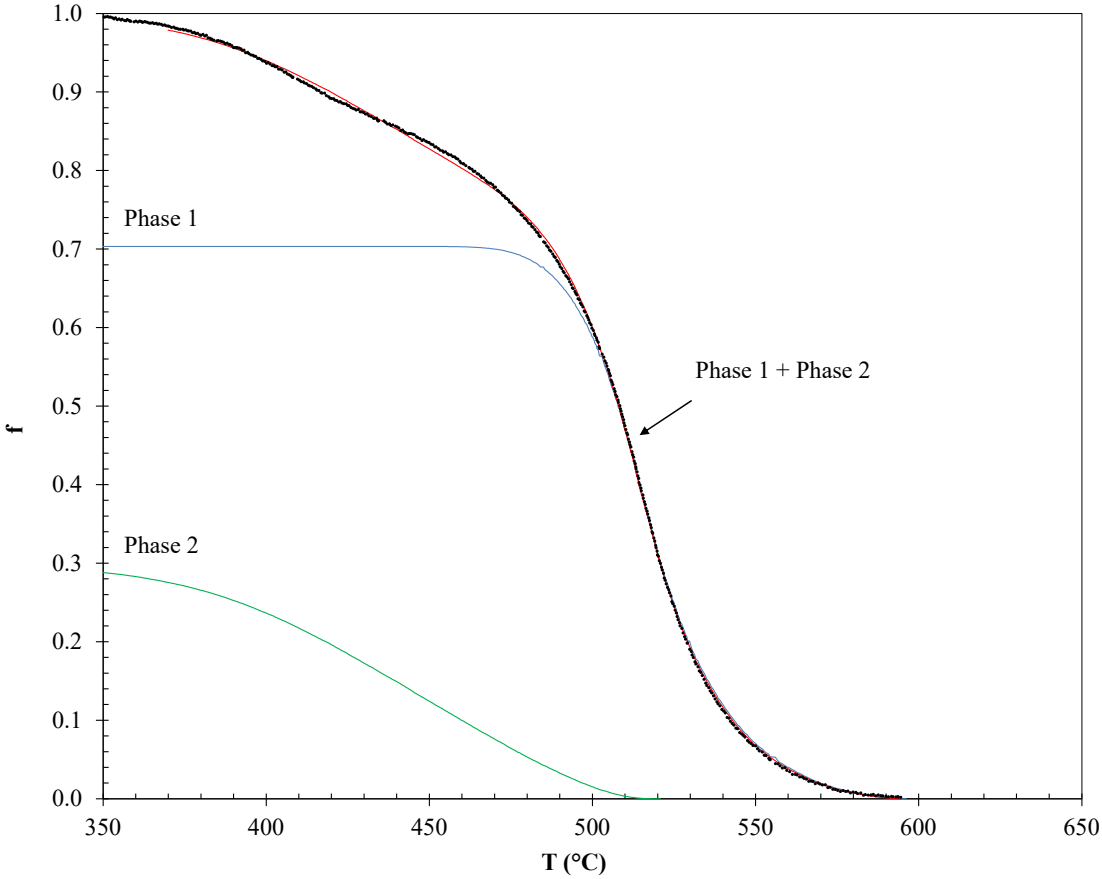

Figure B.16: 120 ℃/s transformation curve

B.3 Constants for Microstructure Modelling

Table B.4: Equation constants for modified Avrami equation

Cooling Rate (℃)	K	τ_{1o}	n_1	Q_1(J/mol)	τ_{2o}	n_2	Q_2 (J/mol)
1	4.77	1.09E5	1.64	58204	2.85E2	1.74	150
5	6.26	6.79E22	0.47	363045	6.75E11	0.75	148301
15	3.75	8.17E22	0.44	361671	1.81E14	0.56	192688
22	0.25	3.46E8	2	130198	5.64E1	1.56	20000
30	1.92	4.62E8	1.70	135211	2.14E1	1.92	13852
50	0.63	5.16E8	1.36	131877	1.69	1.45	10
80	3.67	5.38E8	0.89	129228	2.41	2.61	10
120	2.37	1.00E4	1.65	57848	2.57	2.68	100

B.4 Dilatometer SEM Images

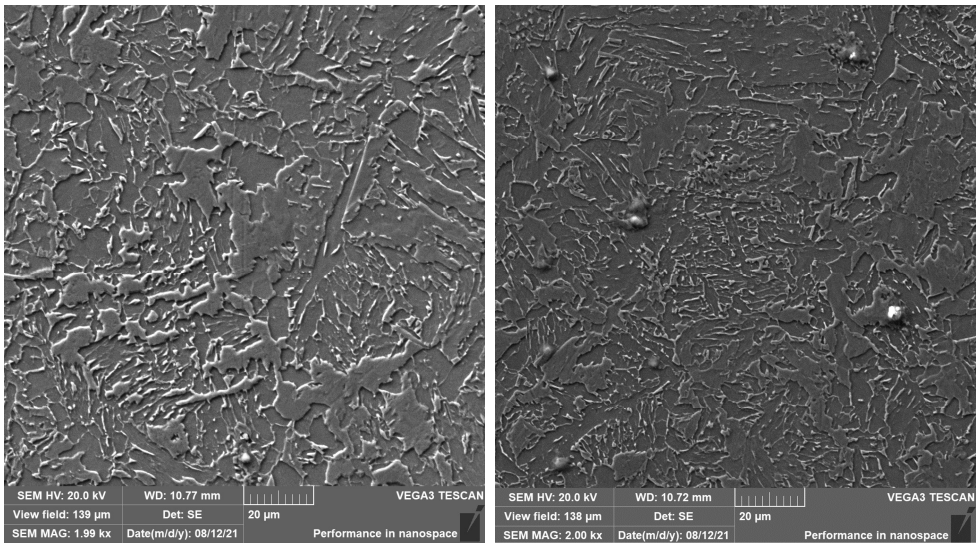

(a) **(b)**

Figure B.17: SEM images of 5 and 15 ℃/s dilatometer samples

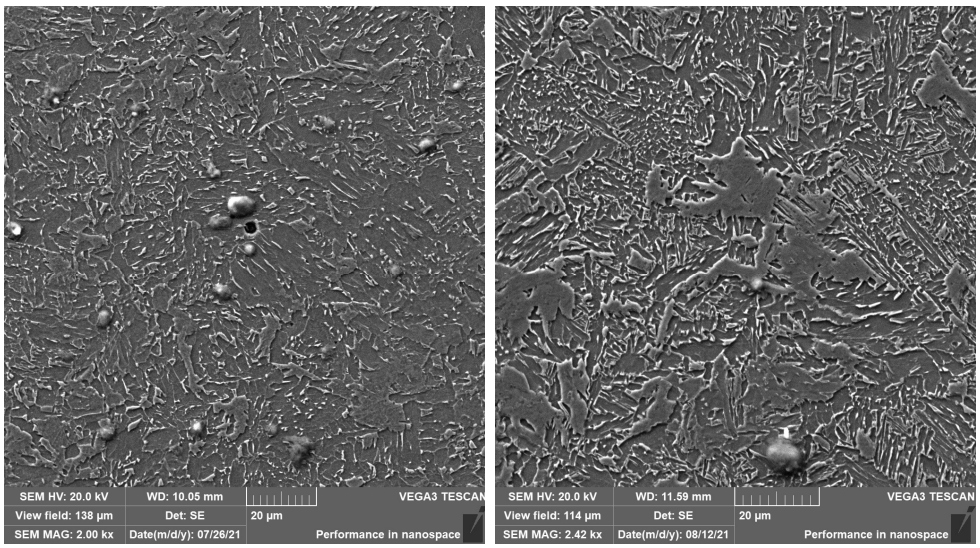

(a) **(b)**

Figure B.18: SEM images of 22 and 30 ℃/s dilatometer samples

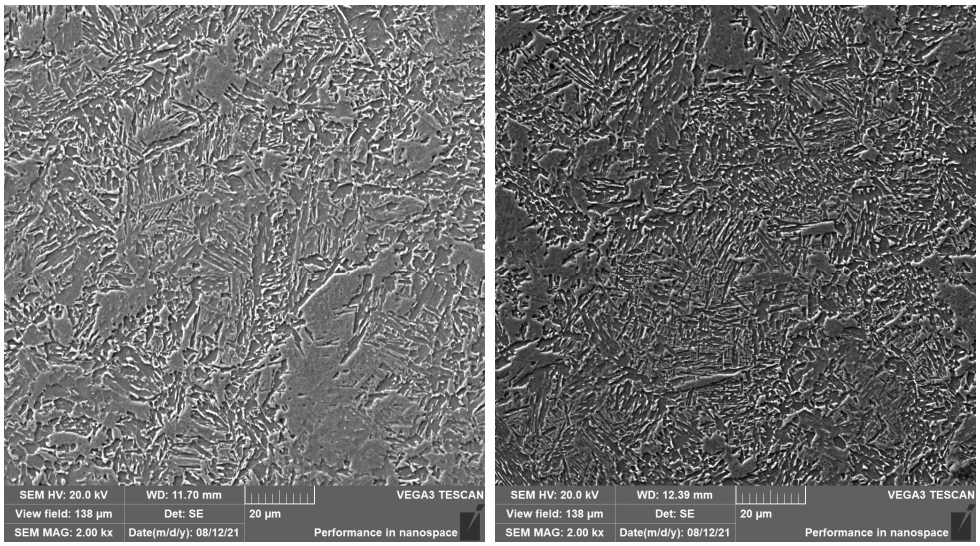

(a) **(b)**

Figure B.19: SEM images of 50 and 120 ℃/s dilatometer samples

B.5 Dilatometer EBSD

B.5.1 Dilatometer Aspect Ratio

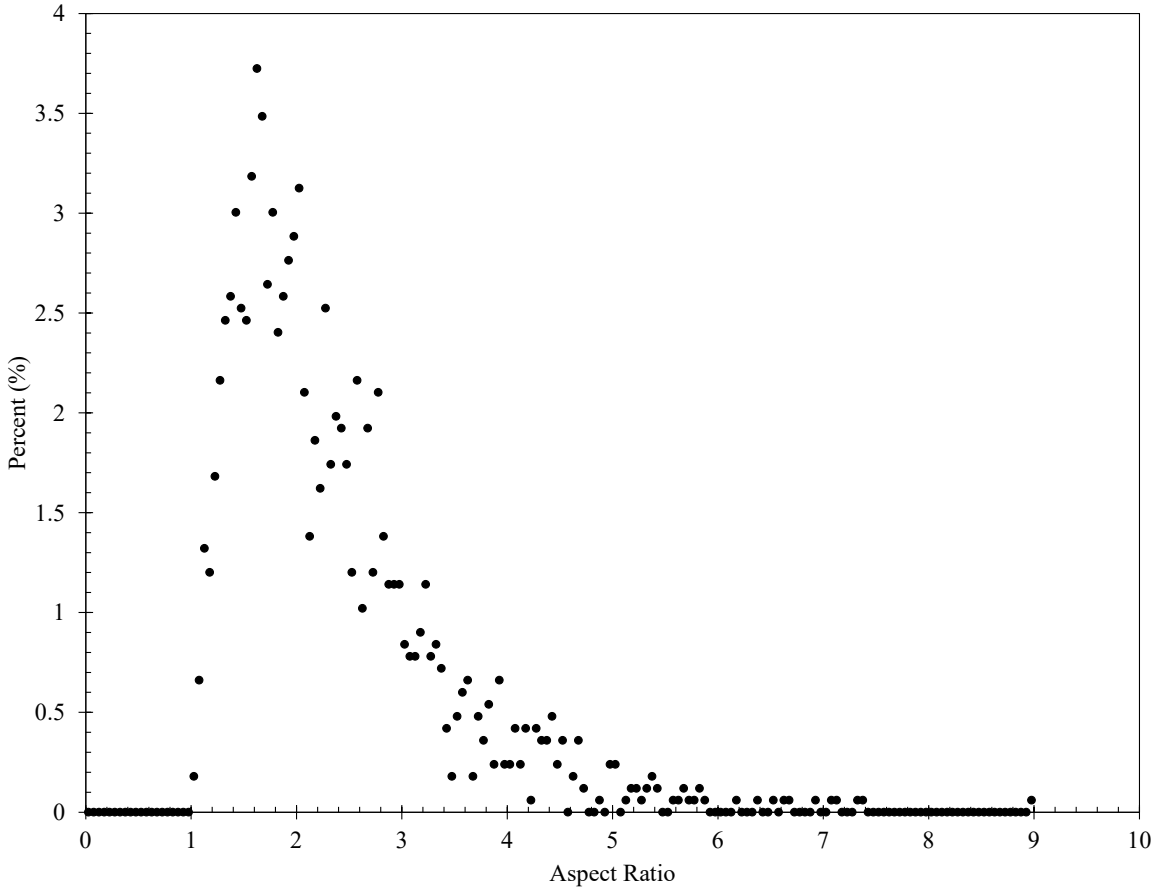

Figure B.20: 1 ℃/s aspect ratio distribution

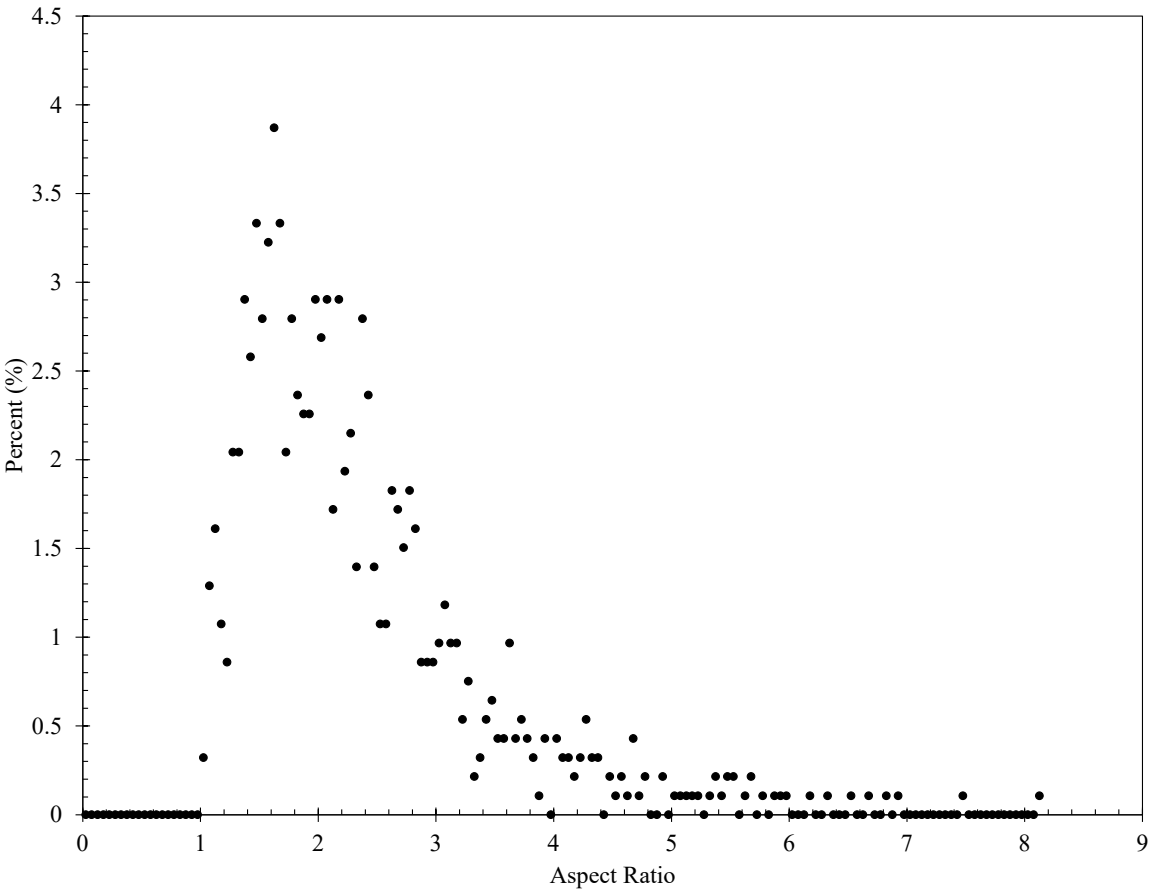

Figure B.21: 5 ℃/s aspect ratio distribution

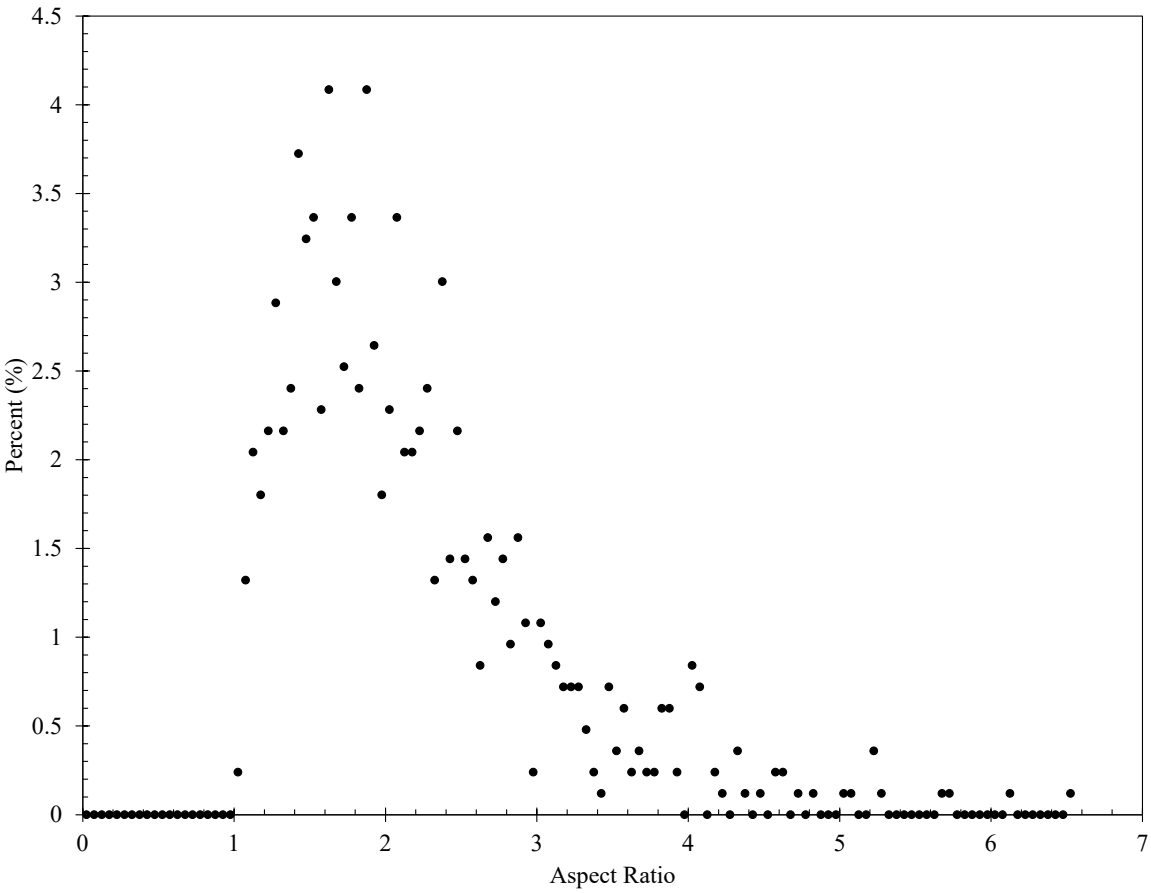

Figure B.22: 15 ℃/s aspect ratio distribution

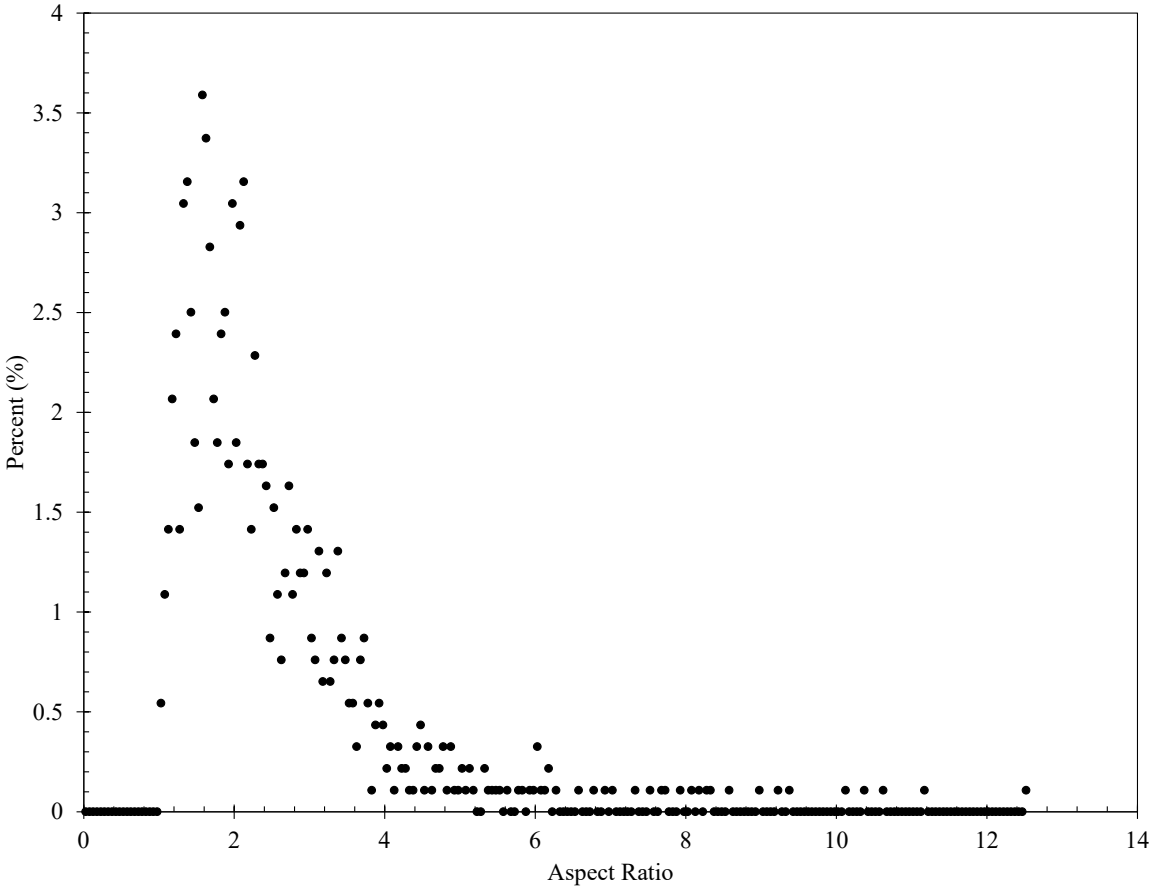

Figure B.23: 22 ℃/s aspect ratio distribution

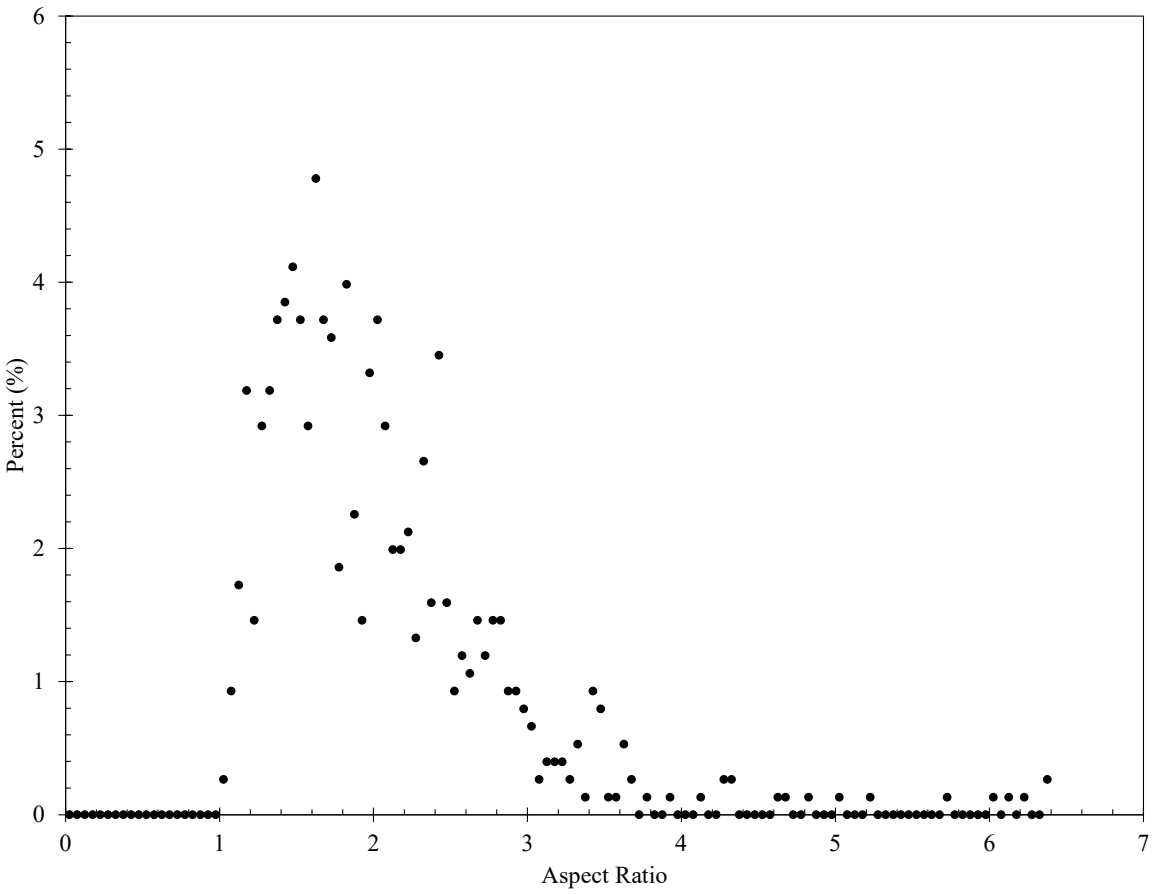

Figure B.24: 30 ℃/s aspect ratio distribution

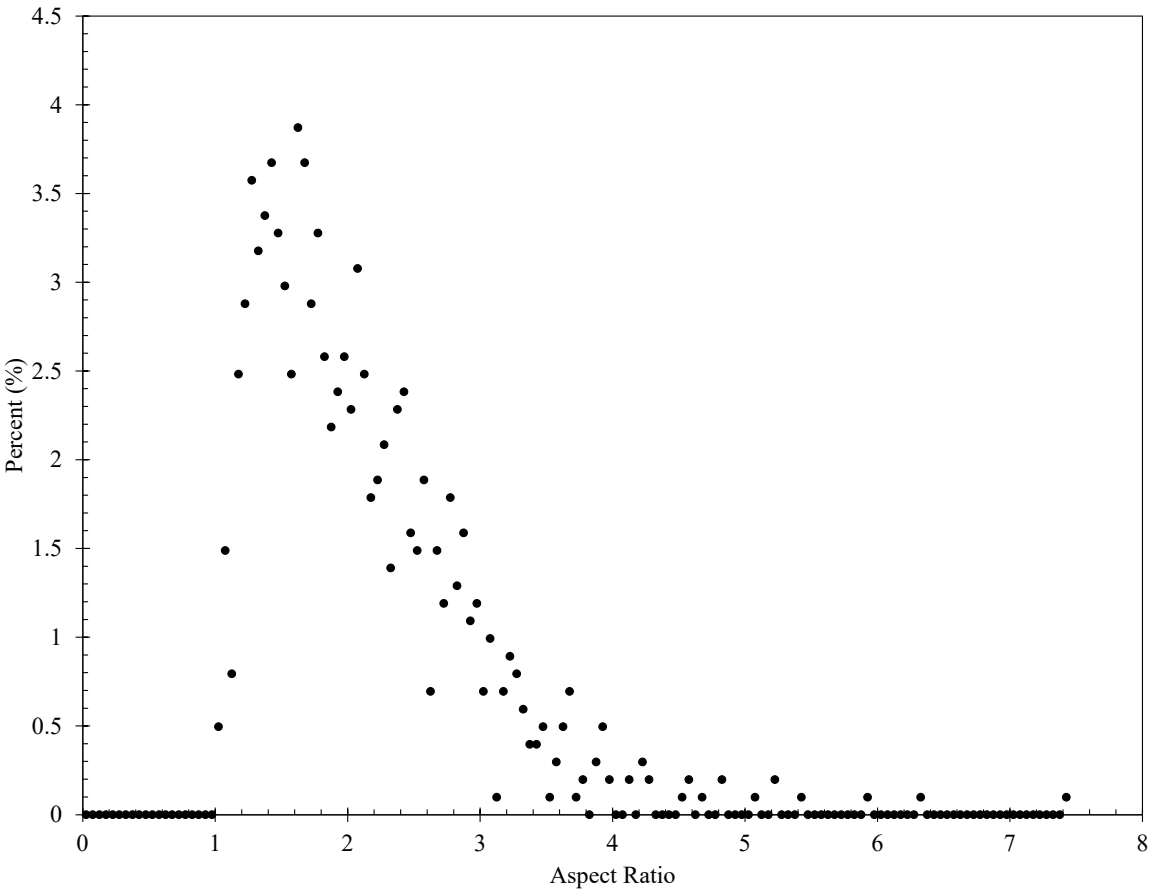

Figure B.25: 50 ℃/s aspect ratio distribution

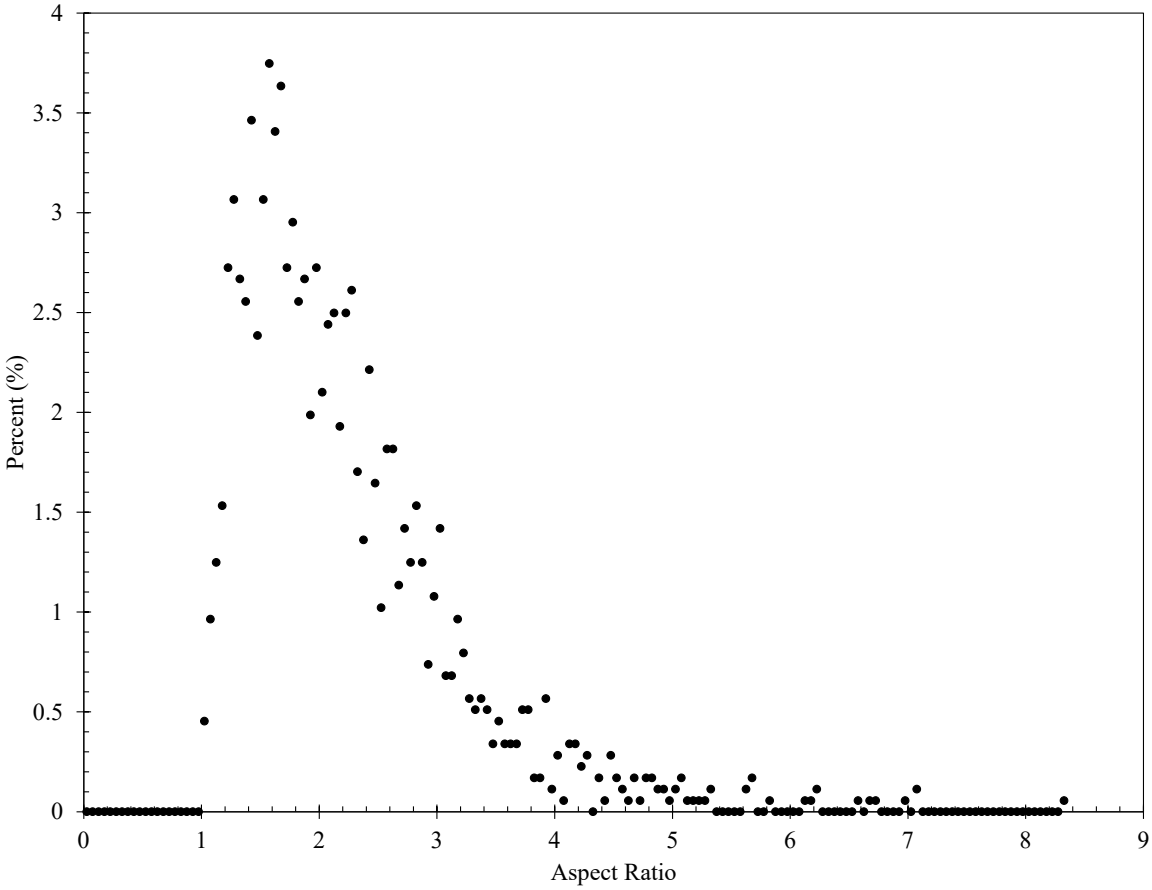

Figure B.26: 80 ℃/s aspect ratio distribution

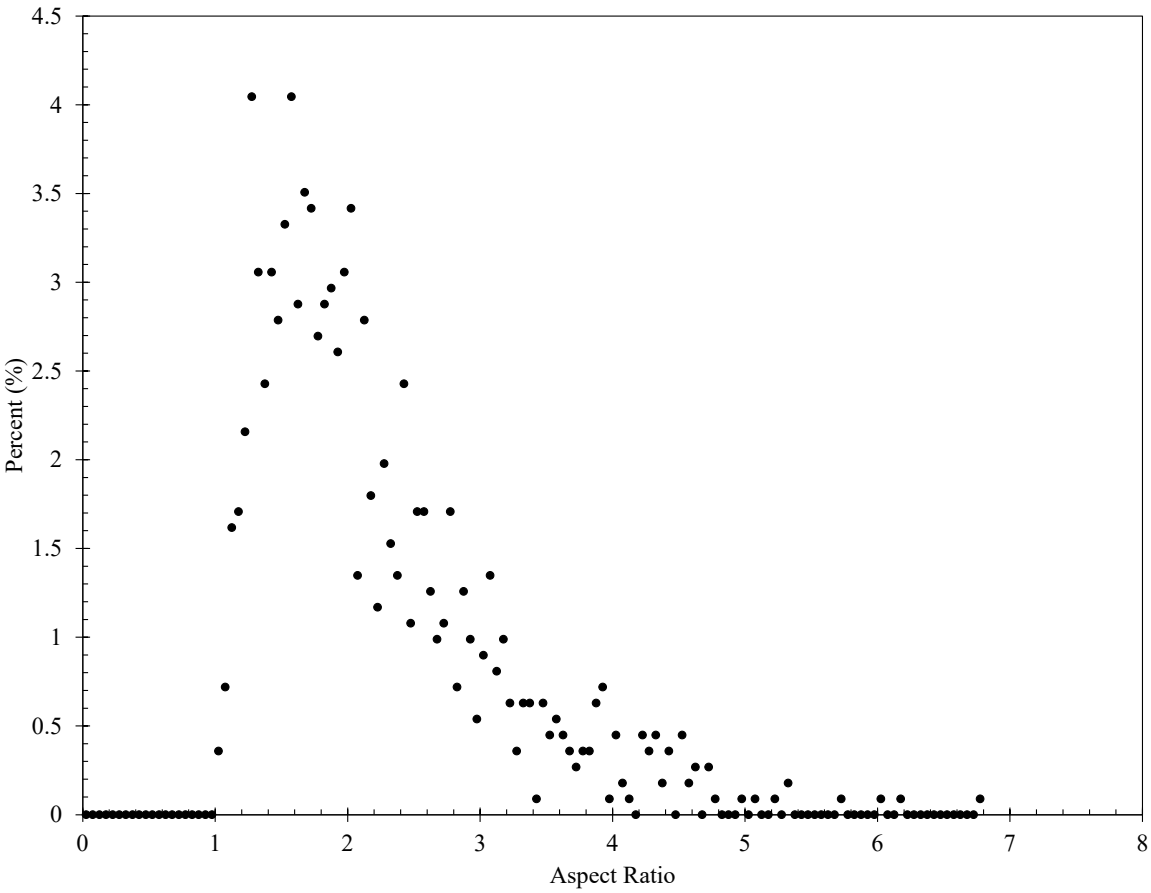

Figure B.27: 120 ℃/s aspect ratio distribution

B.5.2 Dilatometer Grain Area

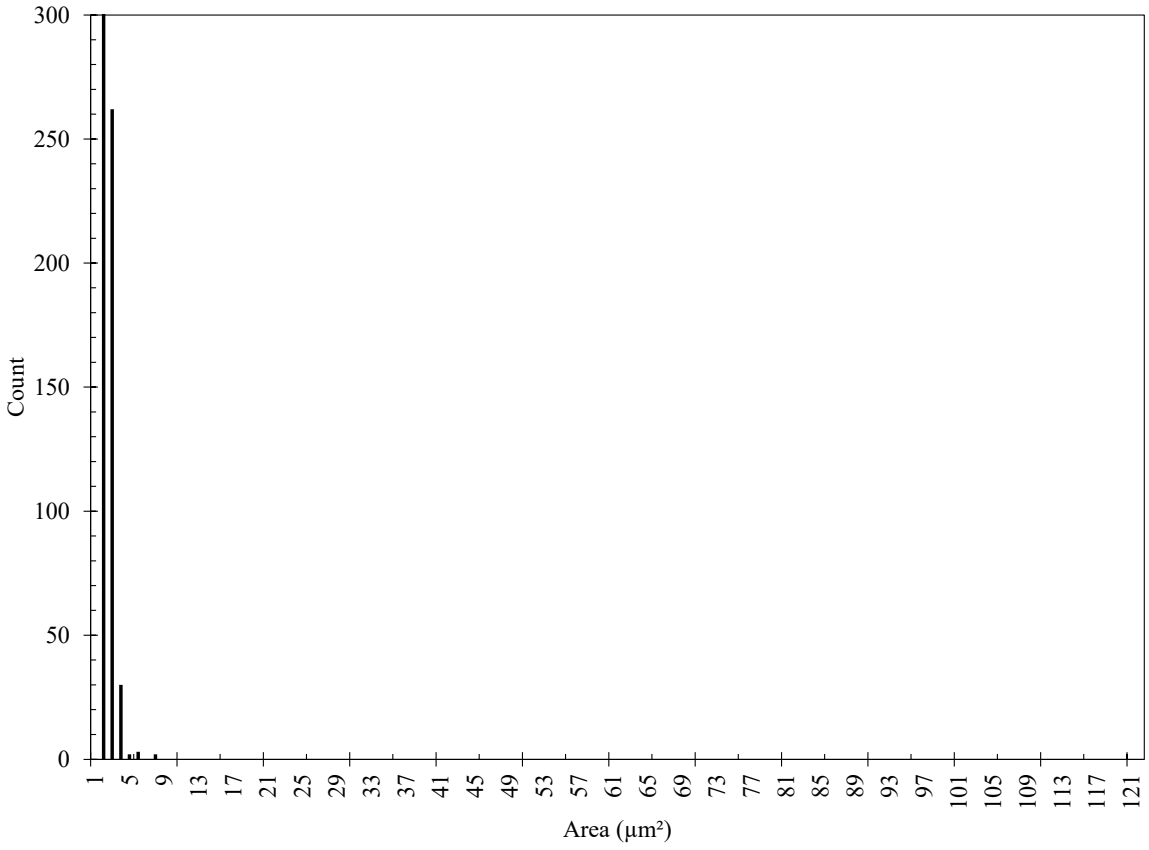

Figure B.28: 1 ℃/s grain area distribution

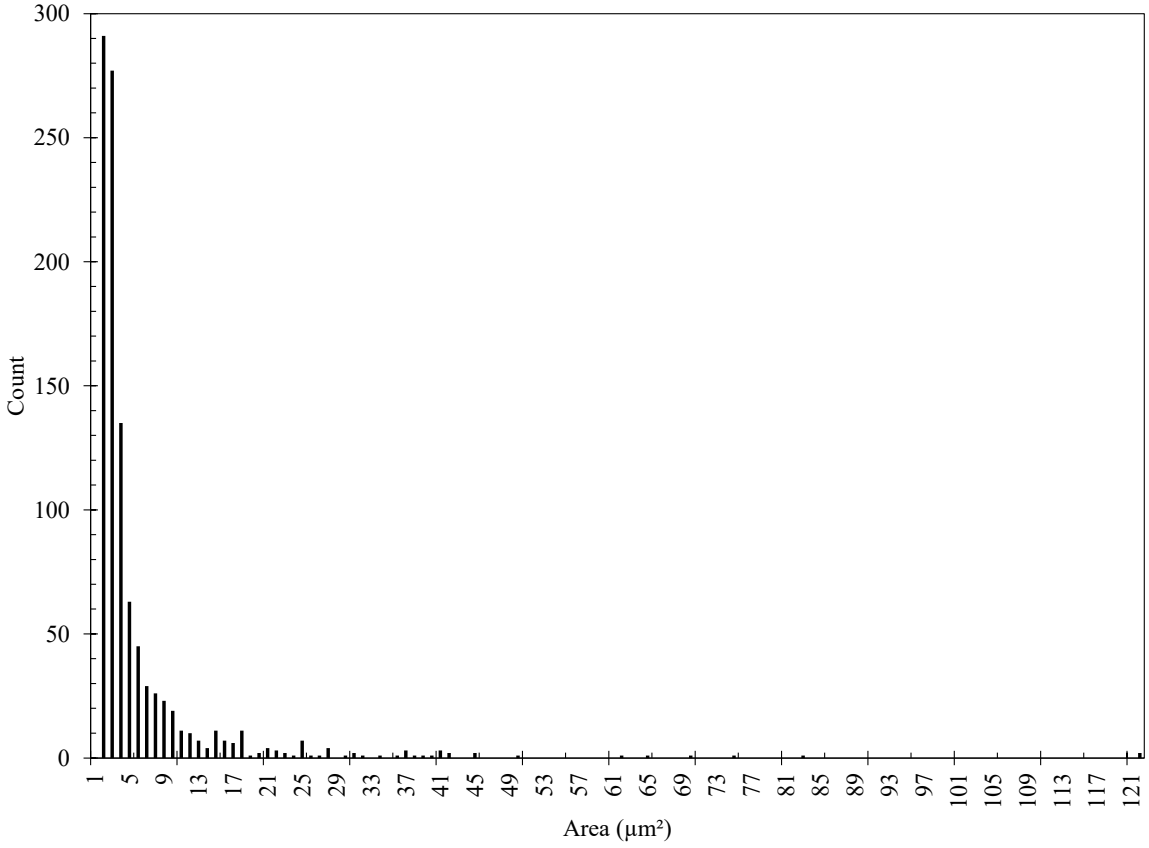

Figure B.29: 5 ℃/s grain area distribution

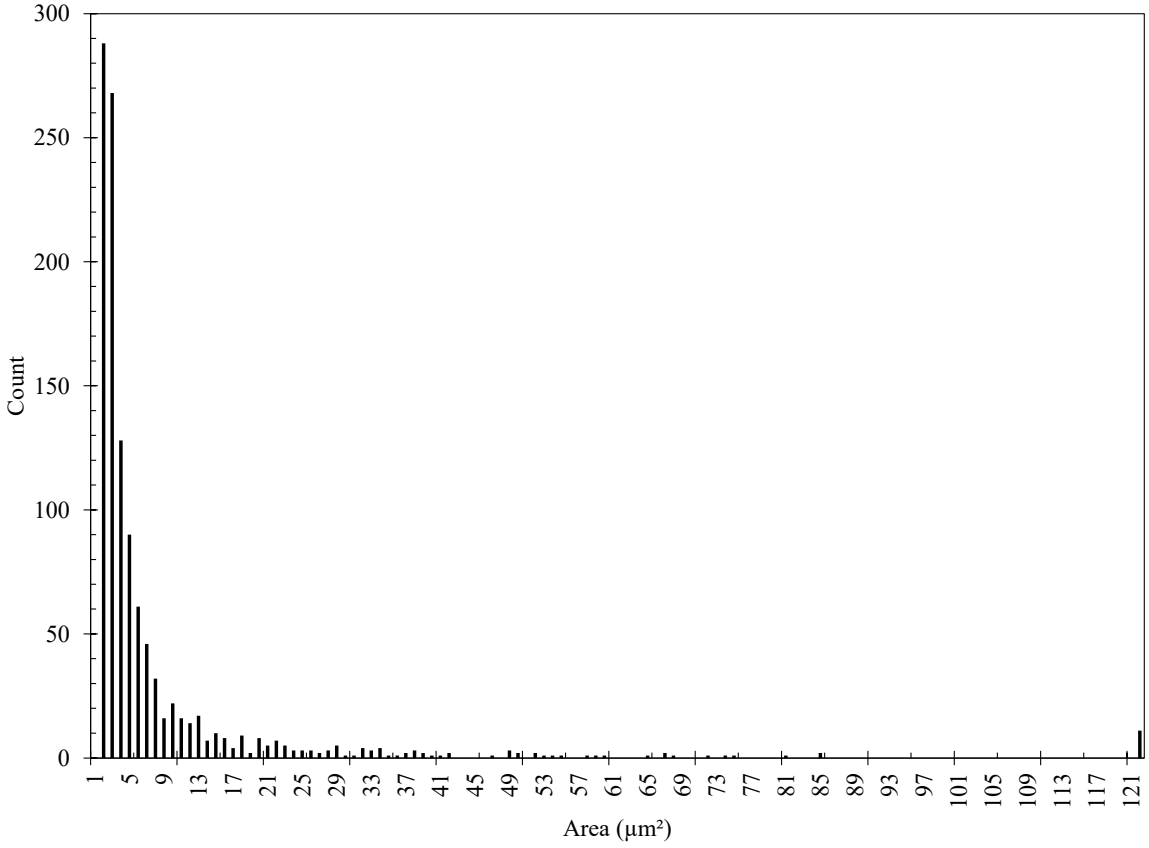

Figure B.30: 15 ℃/s grain area distribution

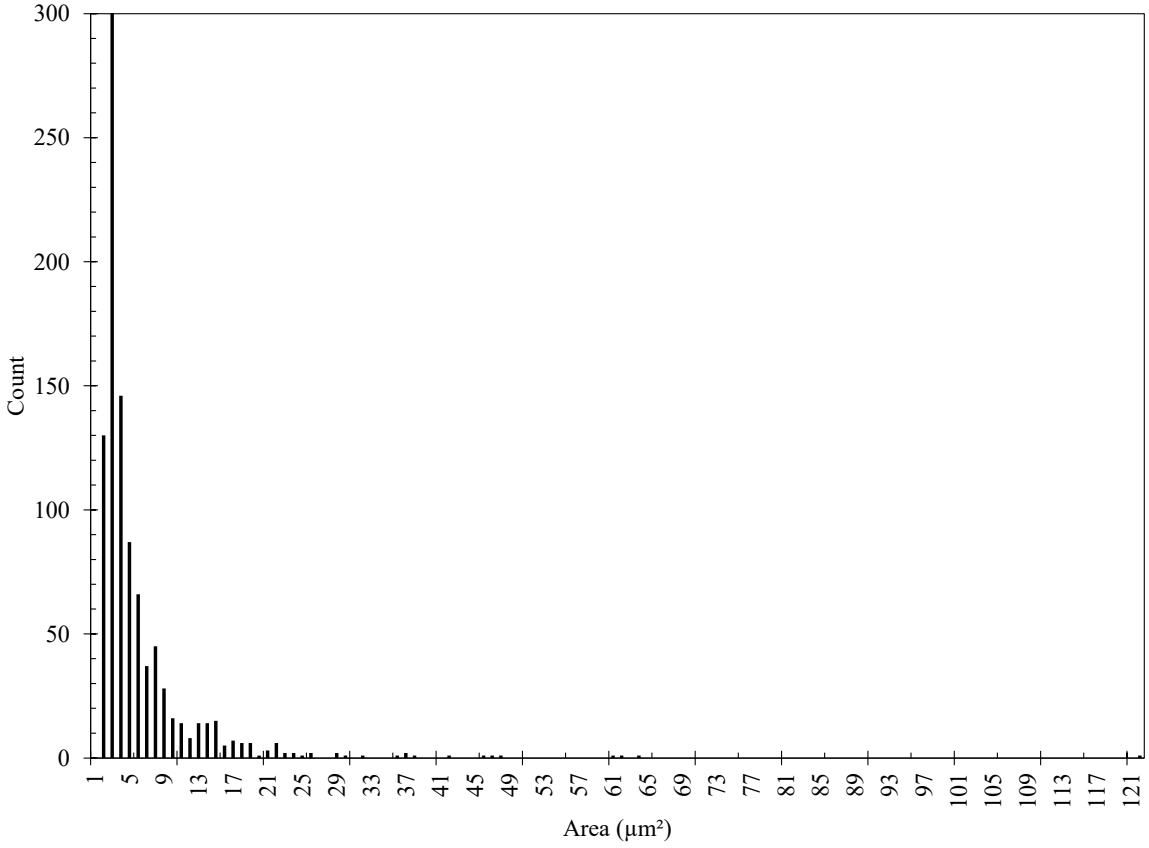

Figure B.31: 22 ℃/s grain area distribution

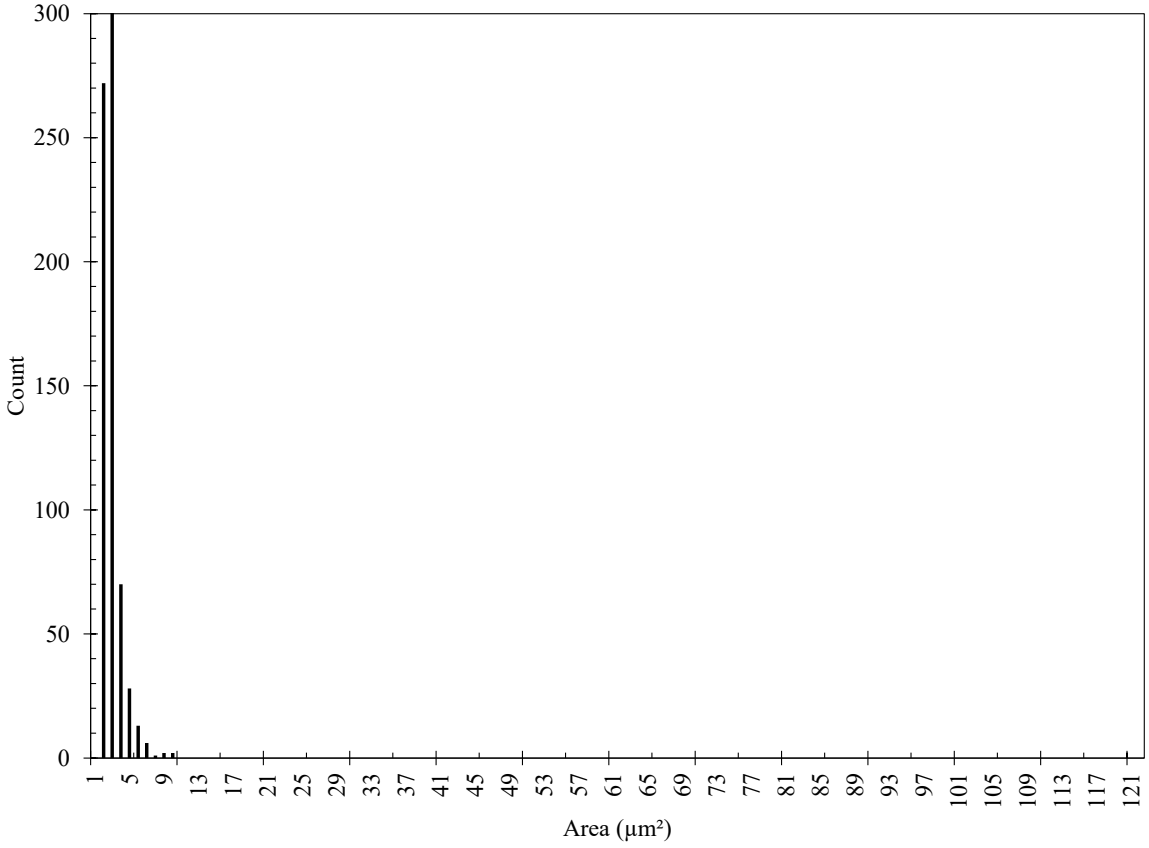

Figure B.32: 30 ℃/s grain area distribution

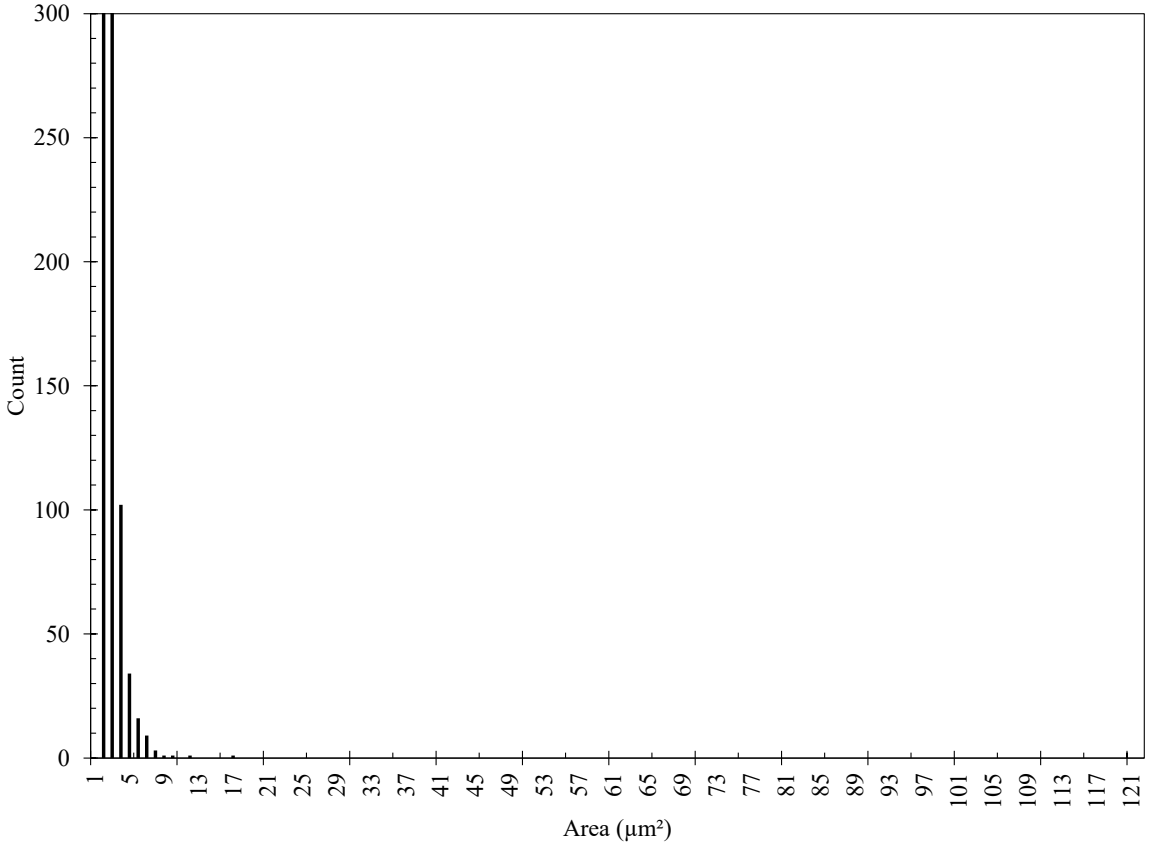

Figure B.33: 50 ℃/s grain area distribution

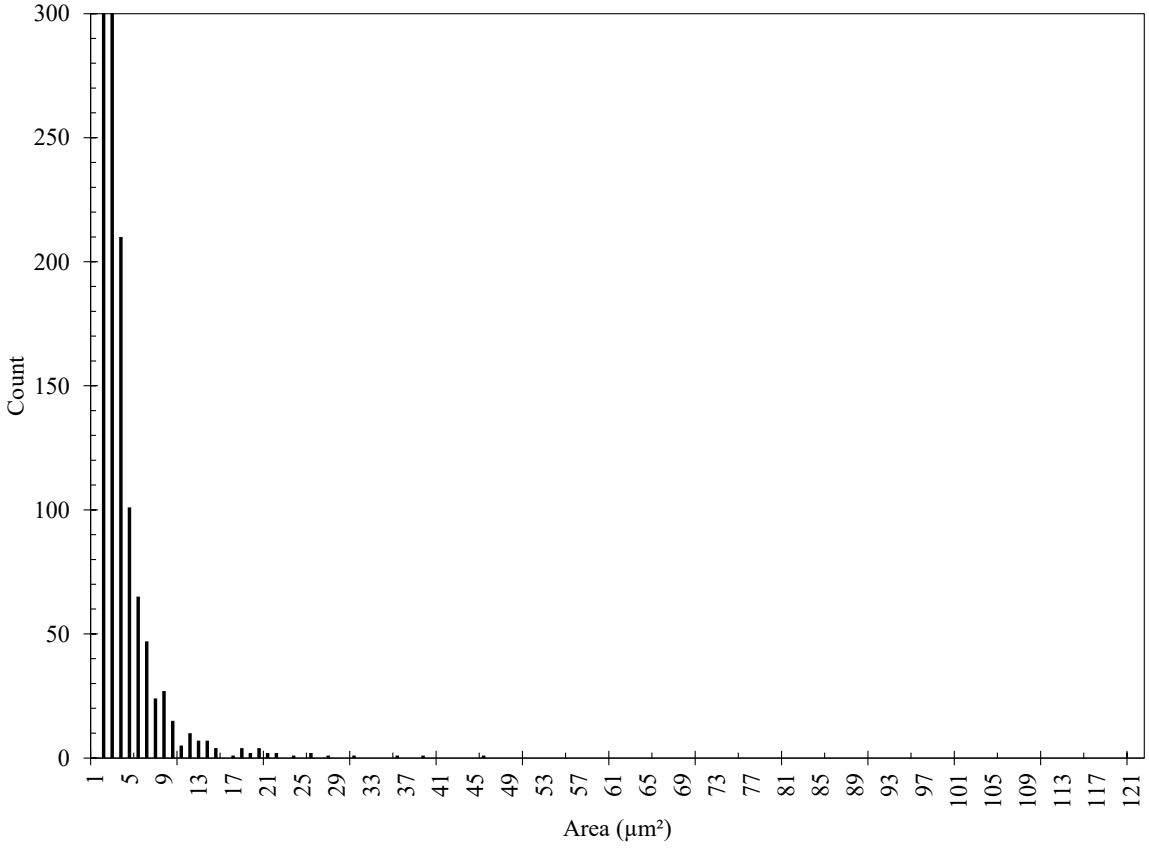

Figure B.34: 80 ℃/s grain area distribution

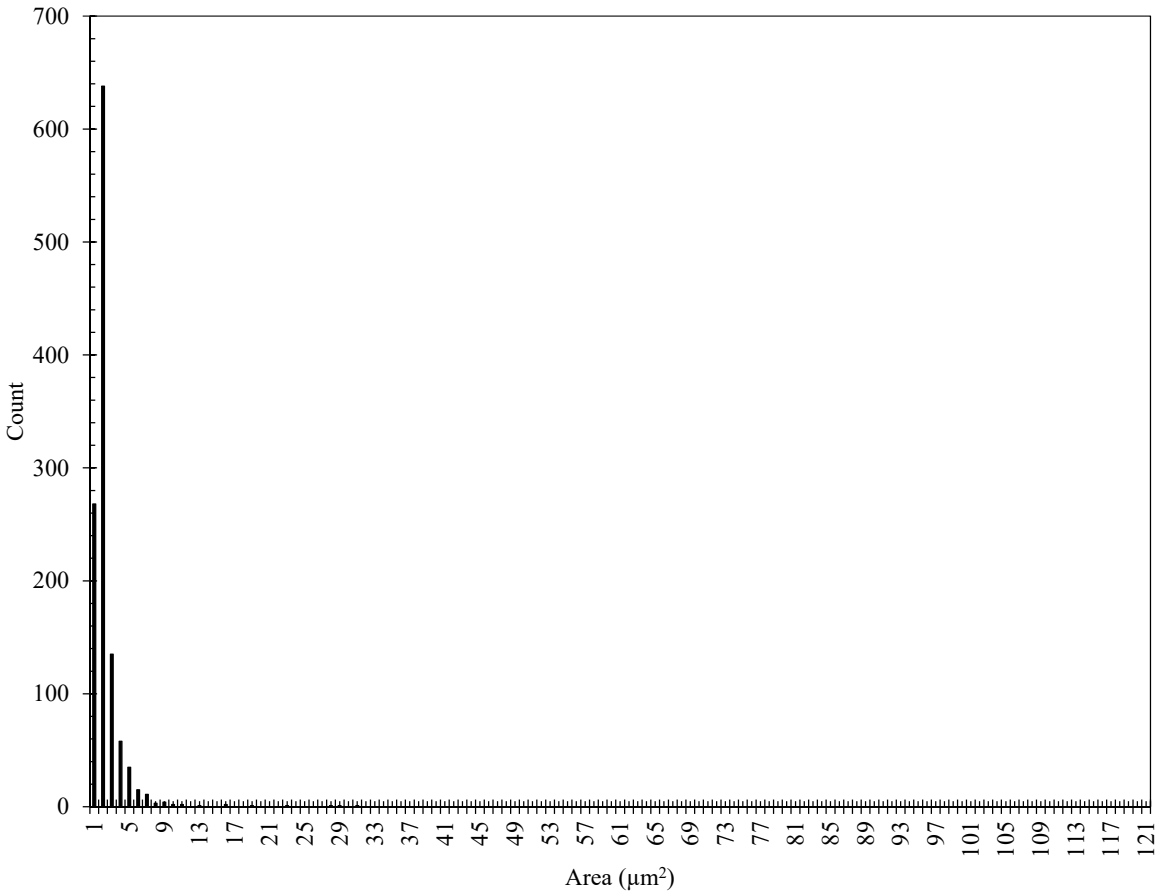

Figure B.35: 120 ℃/s grain area distribution

B.5.3 Dilatometer Misorienttion Angles

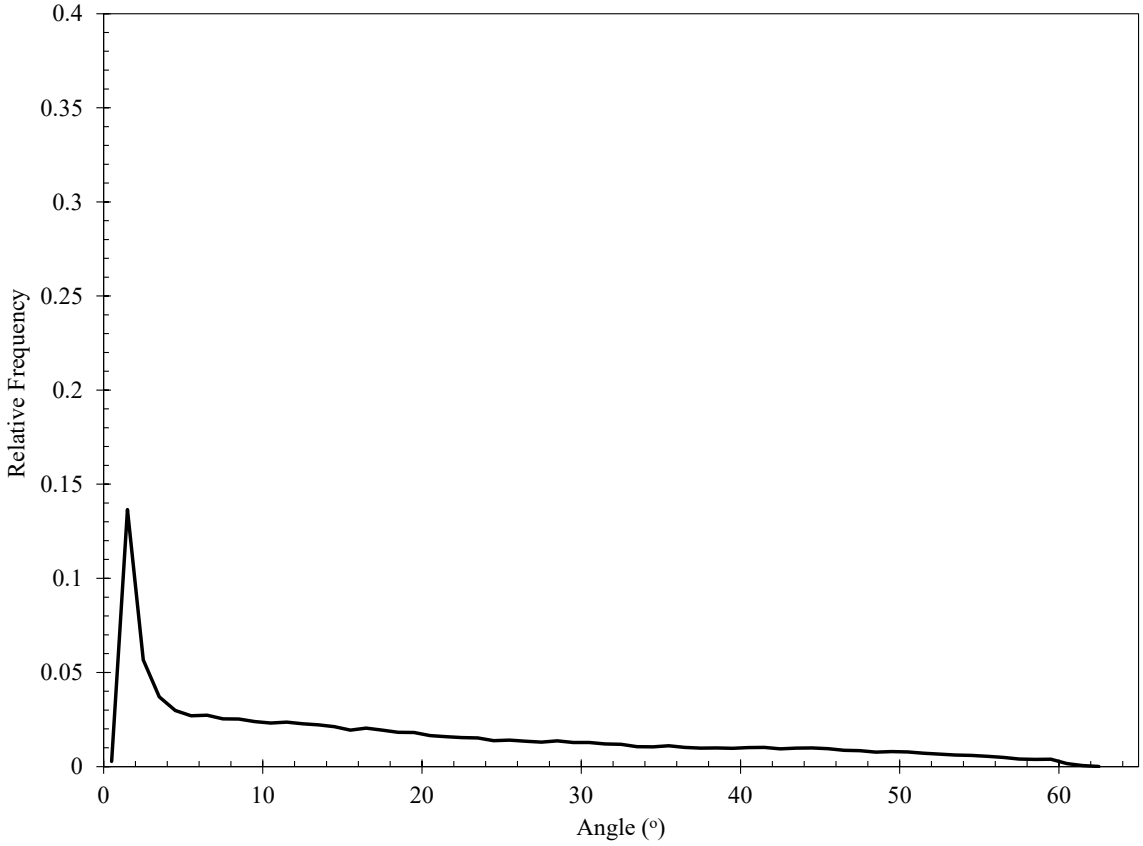

Figure B.36: 1 ℃/s misorientation angle distribution

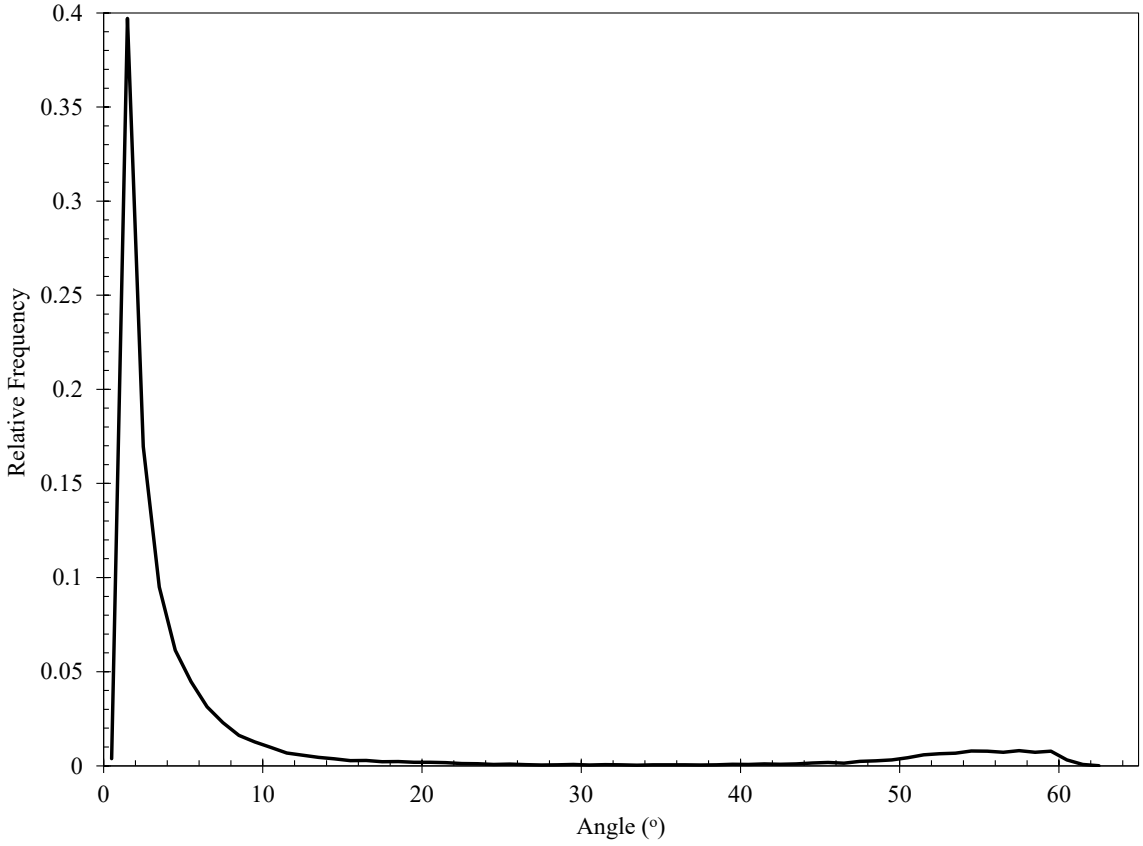

Figure B.37: 5 ℃/s misorientation angle distribution

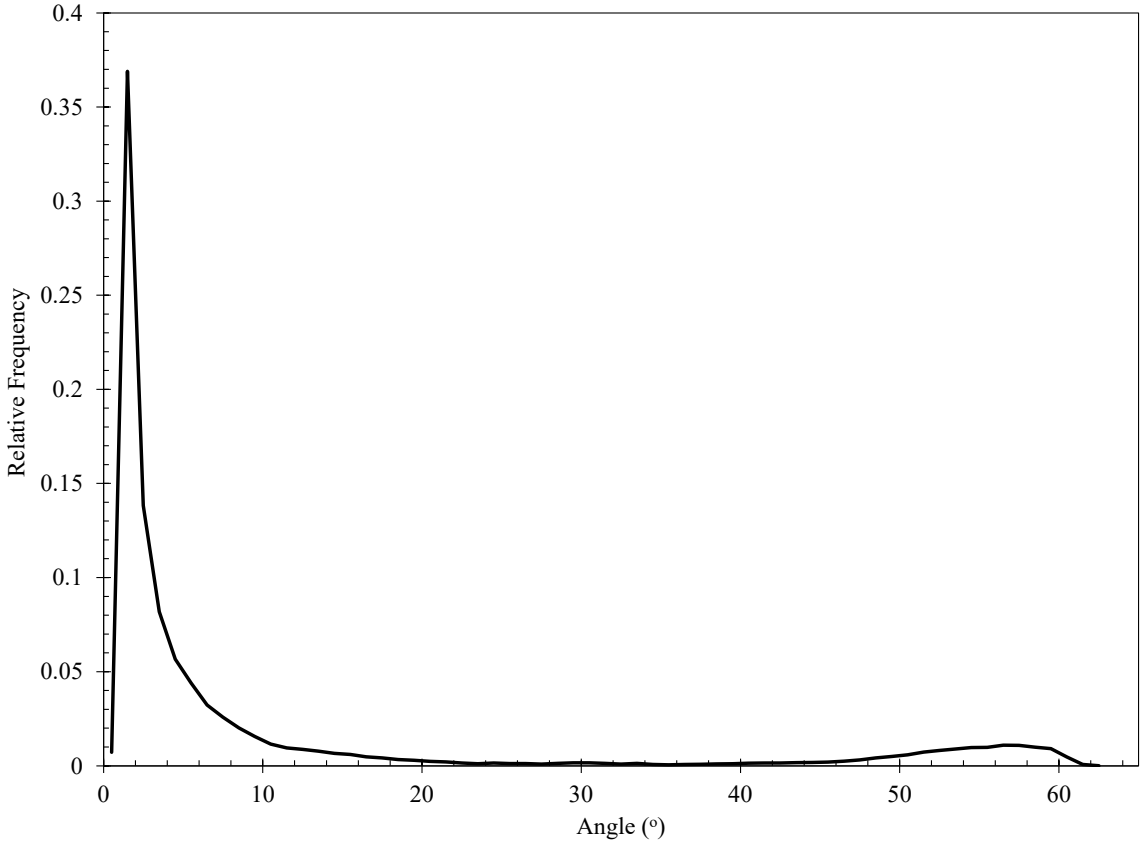

Figure B.38: 15 ℃/s misorientation angle distribution

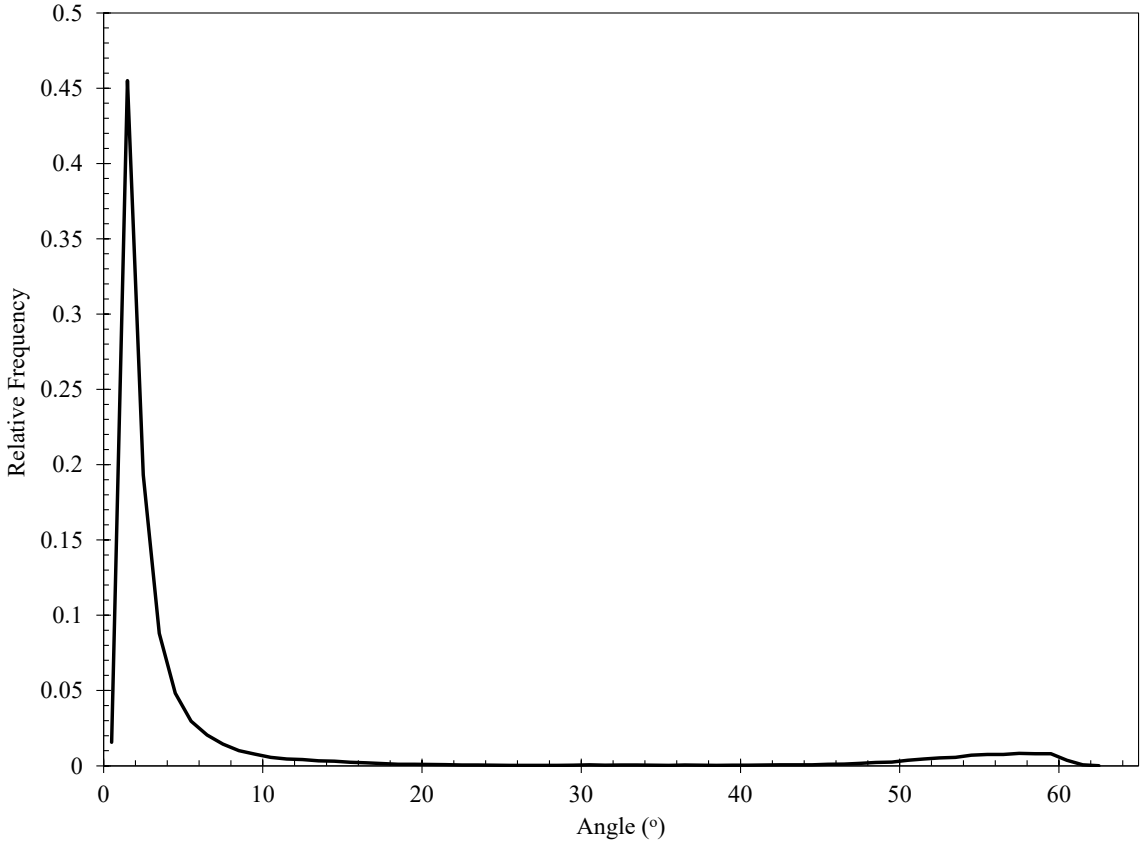

Figure B.39: 22 ℃/s misorientation angle distribution

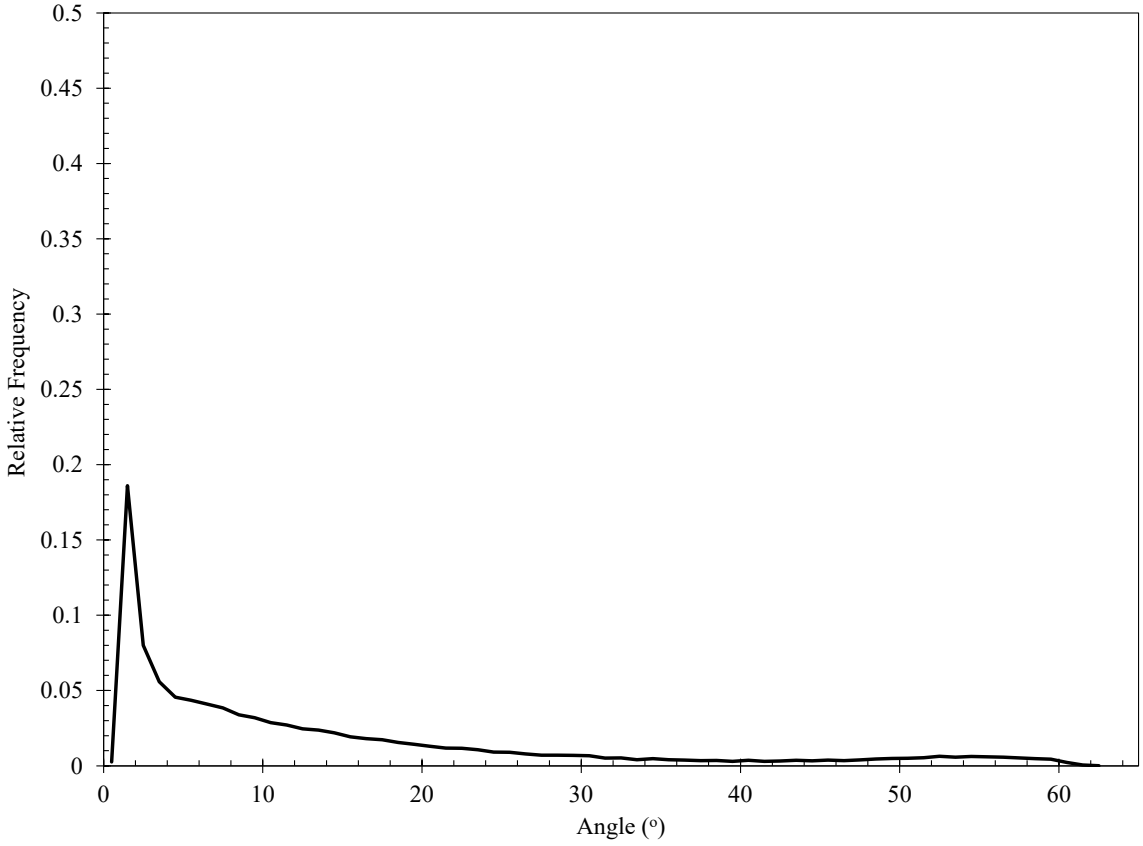

Figure B.40: 30 ℃/s misorientation angle distribution

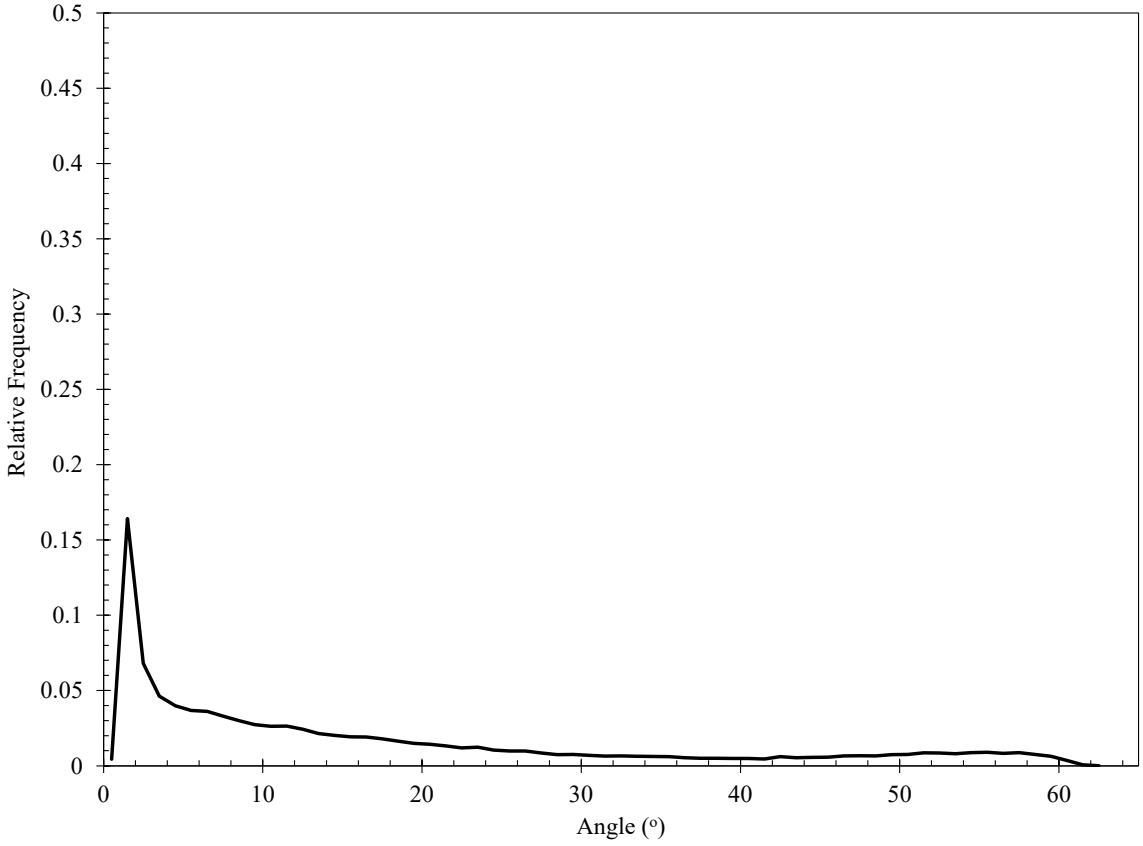

Figure B.41: 50 ℃/s misorientation angle distribution

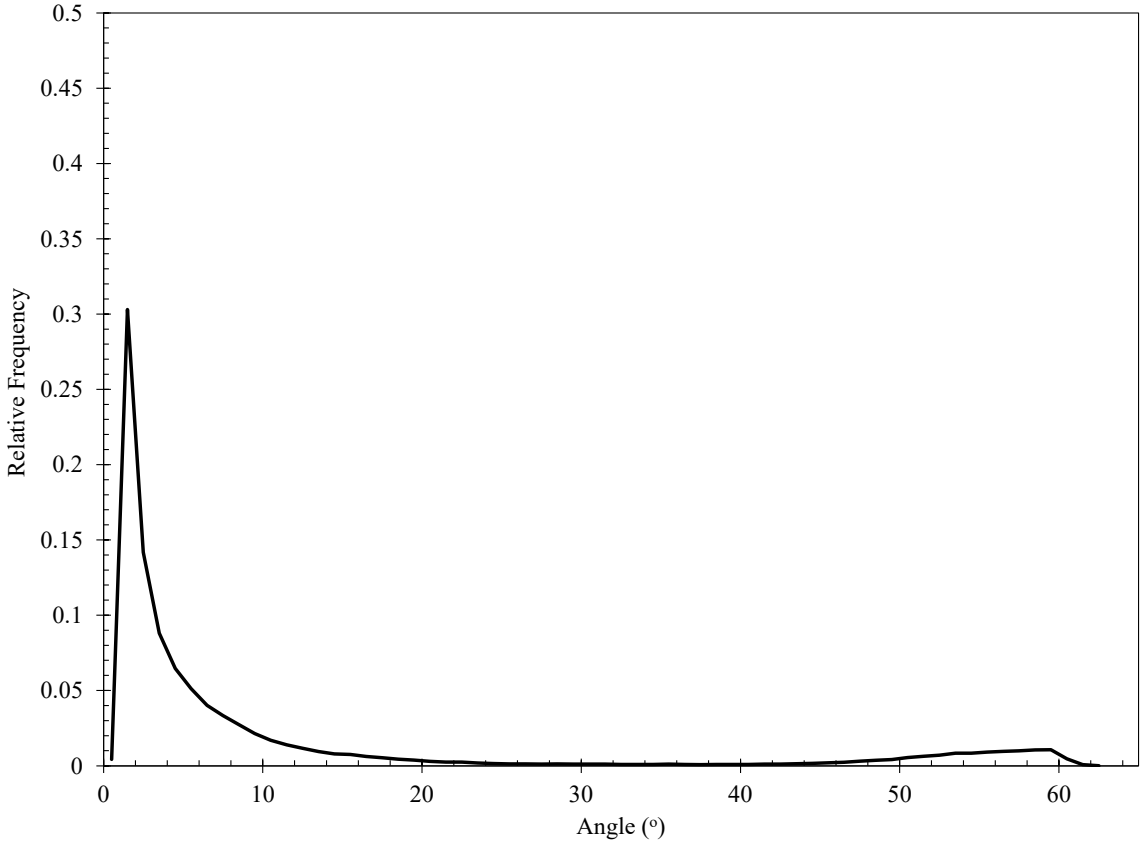

Figure B.42: 80 ℃/s misorientation angle distribution

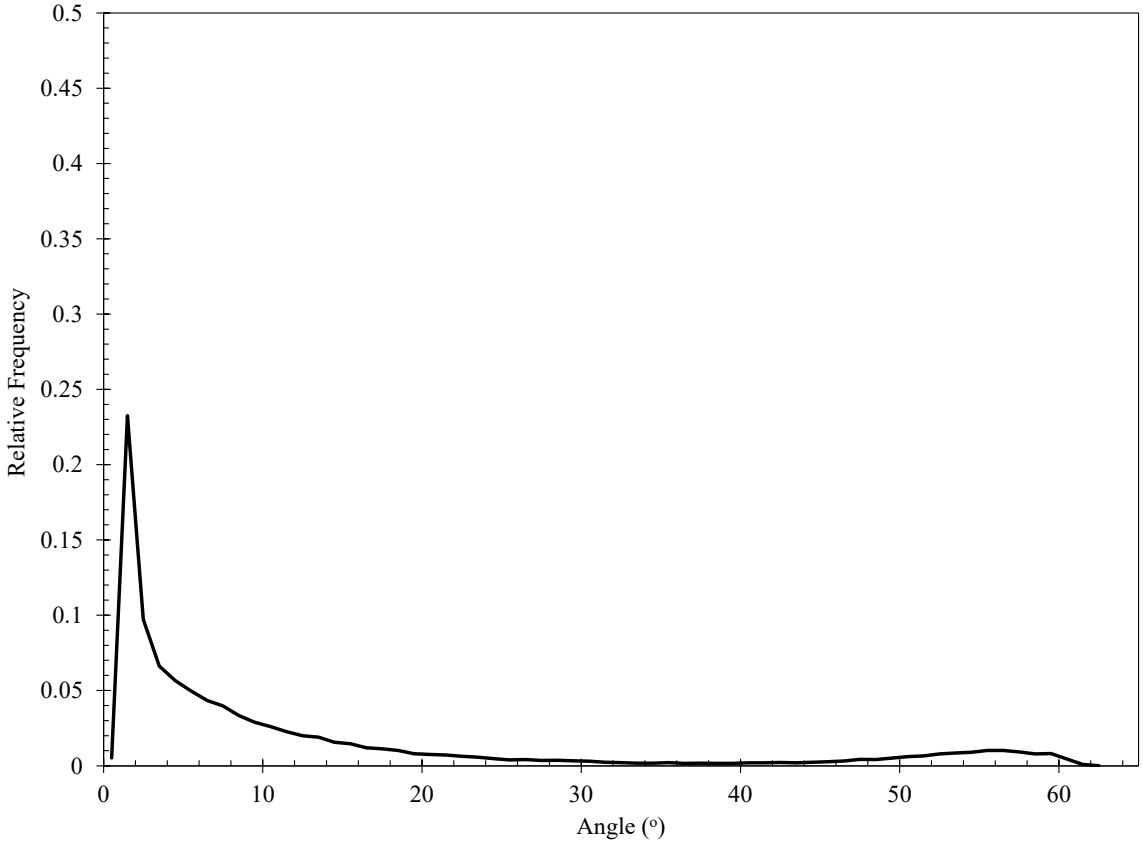

Figure B.43: 120 ℃/s misorientation angle distribution

B.5.4 Dilatometer Band Contrast

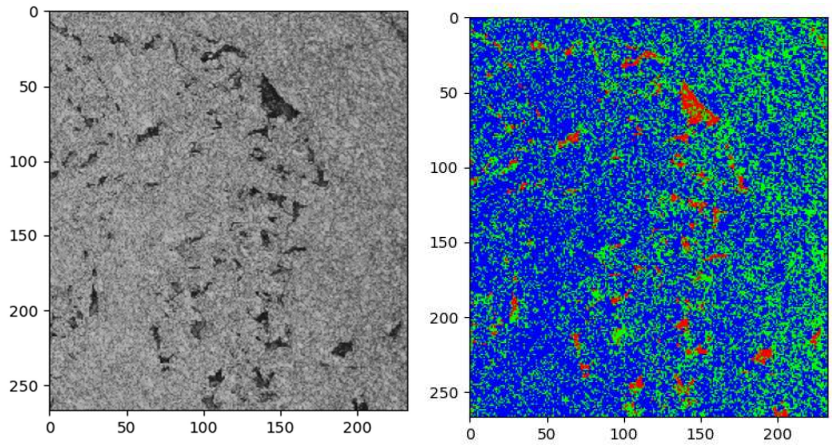

Figure B.44: EBSD band contrast of 1 ℃/s dilatometer samples

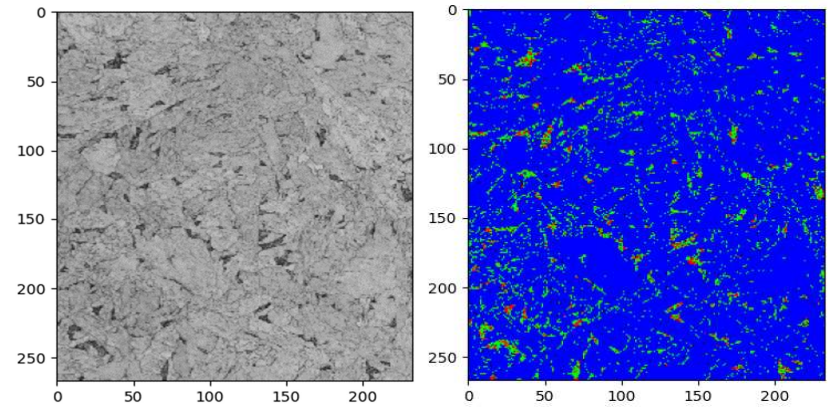

Figure B.45: EBSD band contrast of 5 ℃/s dilatometer samples

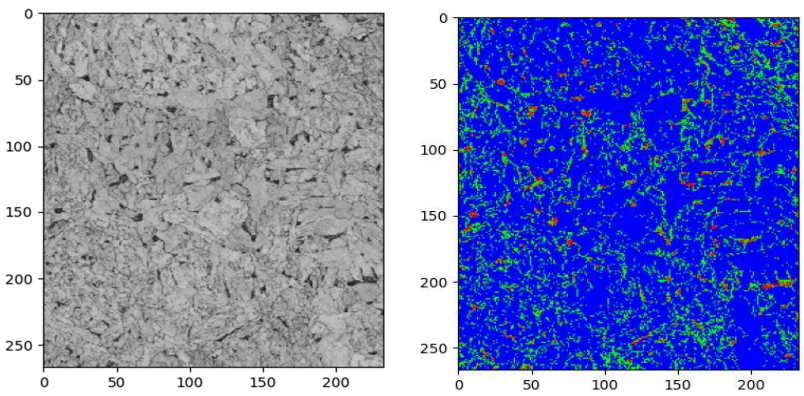

Figure B.46: EBSD band contrast of 15 ℃/s dilatometer samples

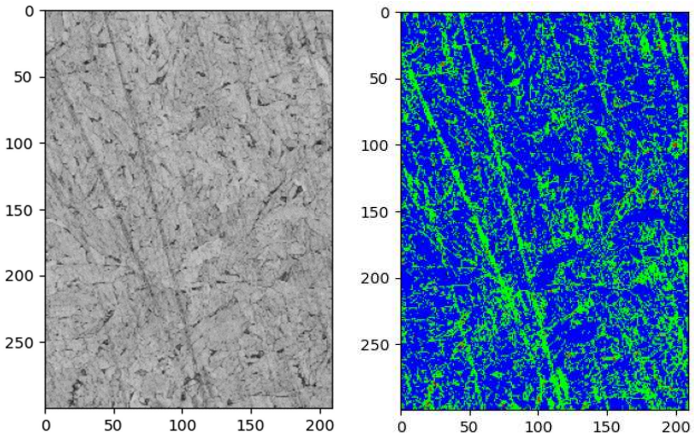

Figure B.47: EBSD band contrast of 22 ℃/s dilatometer samples

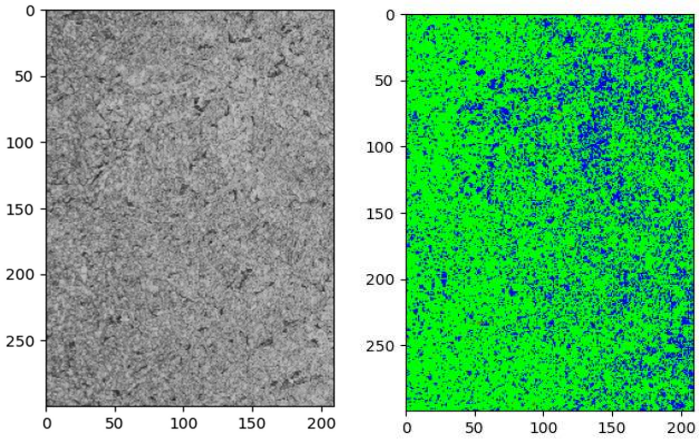

Figure B.48: EBSD band contrast of 30 ℃/s dilatometer samples

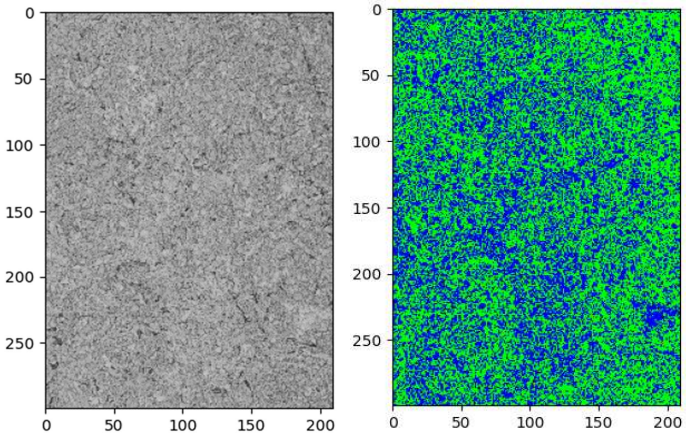

Figure B.49: EBSD band contrast of 50 ℃/s dilatometer samples

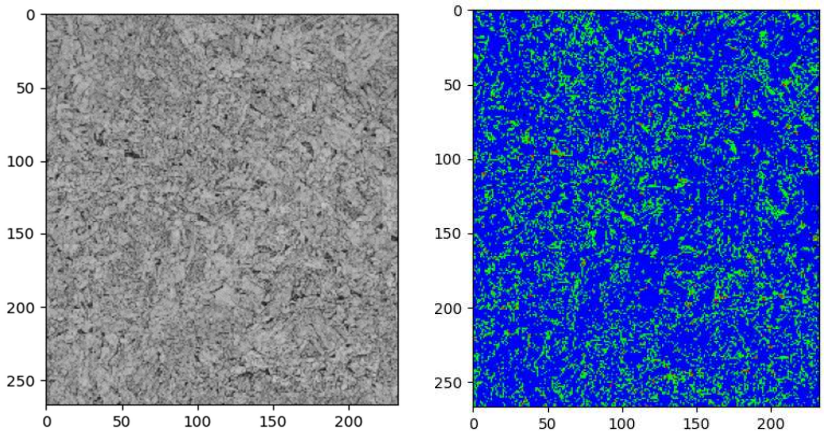

Figure B.50: EBSD band contrast of 80 ℃/s dilatometer samples

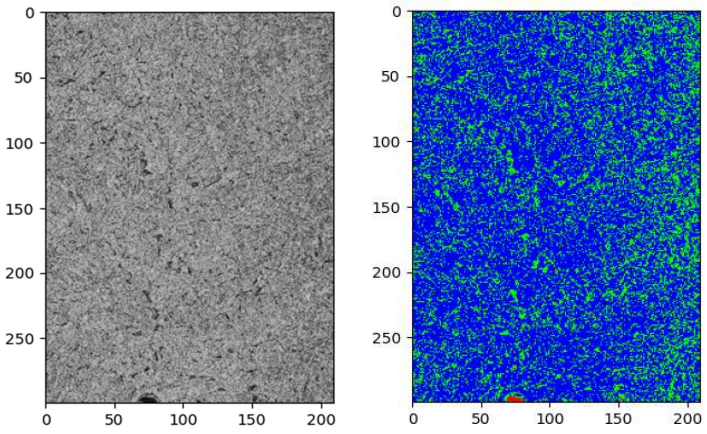

Figure B.51: EBSD band contrast of 120 ℃/s dilatometer samples

Appendix C. Thermal Model

Appendix C contains all the results from thermal modelling. This includes temperature profiles, spray patterns, and calibration for IR.

C.1 8-, 11-, and 12 mm Models Results

C.1.1 8 mm Results

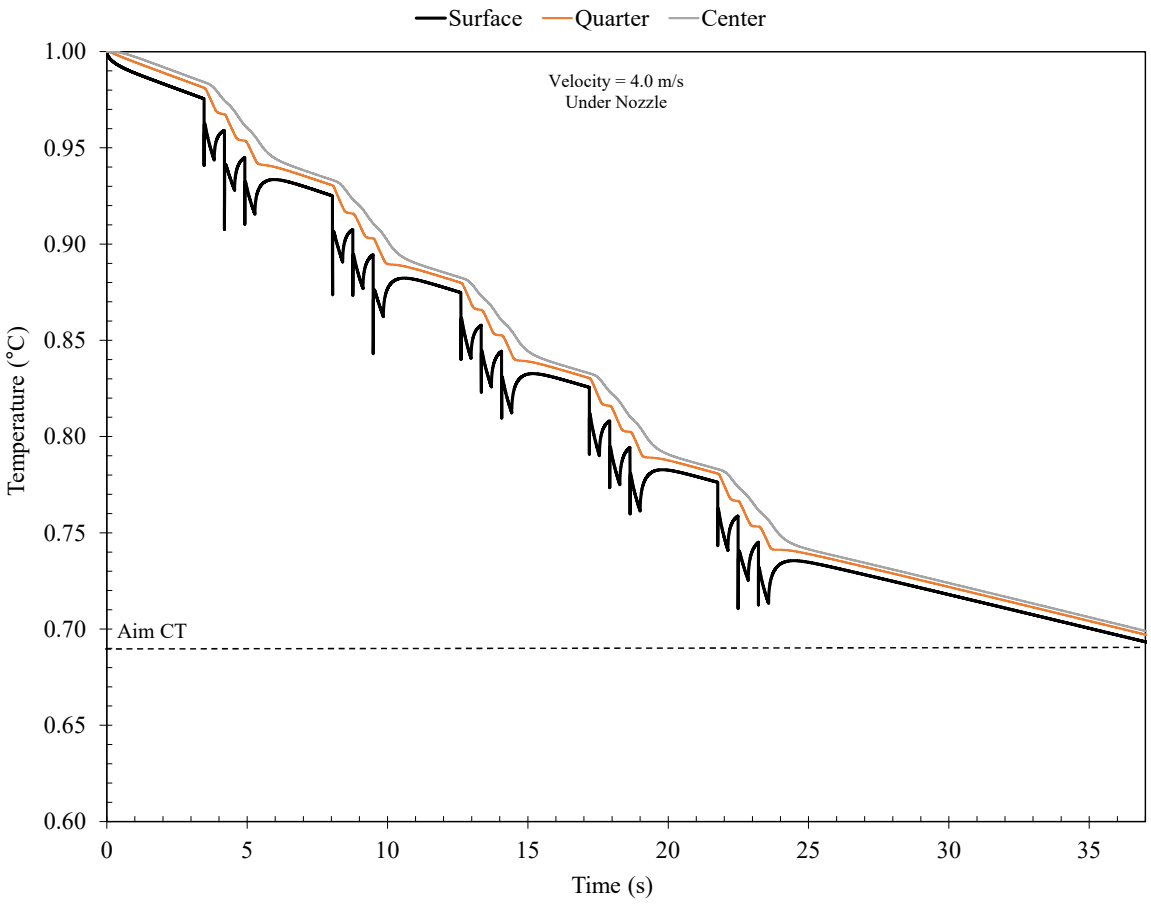

Figure C.1: 8 mm X70 simulation temperature profile under nozzle

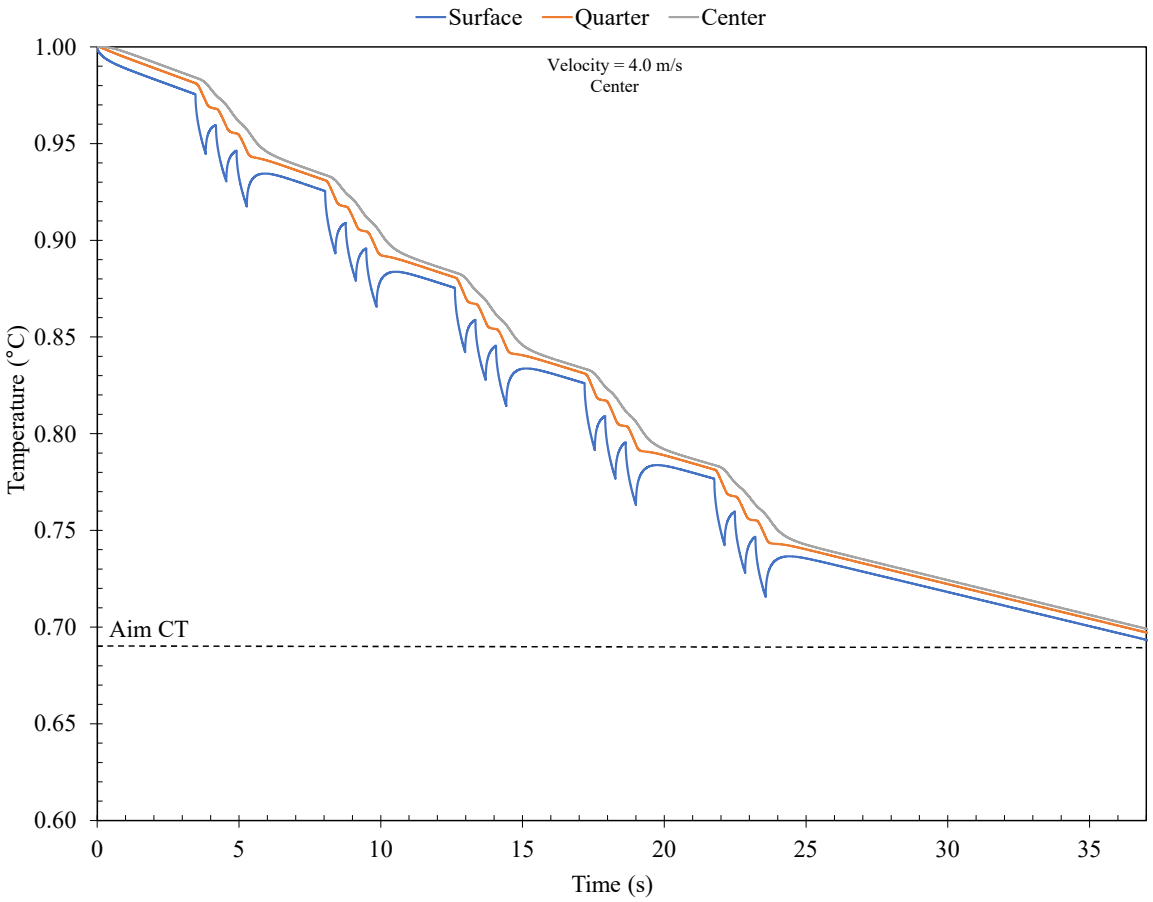

Figure C.2: 8 mm X70 simulation temperature profile quarter distance to next nozzle

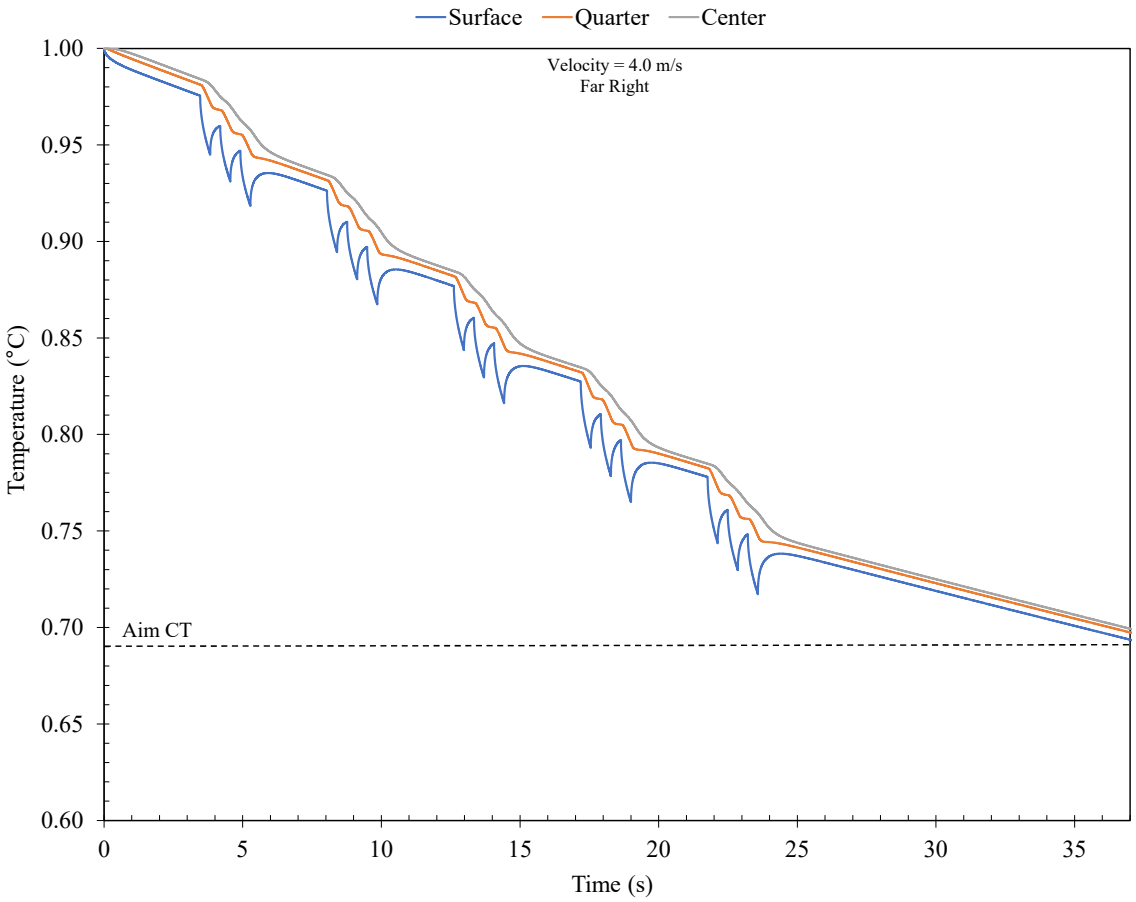

Figure C.3: 8 mm X70 simulation temperature profile half distance to next nozzle

C.1.2 11 mm Results

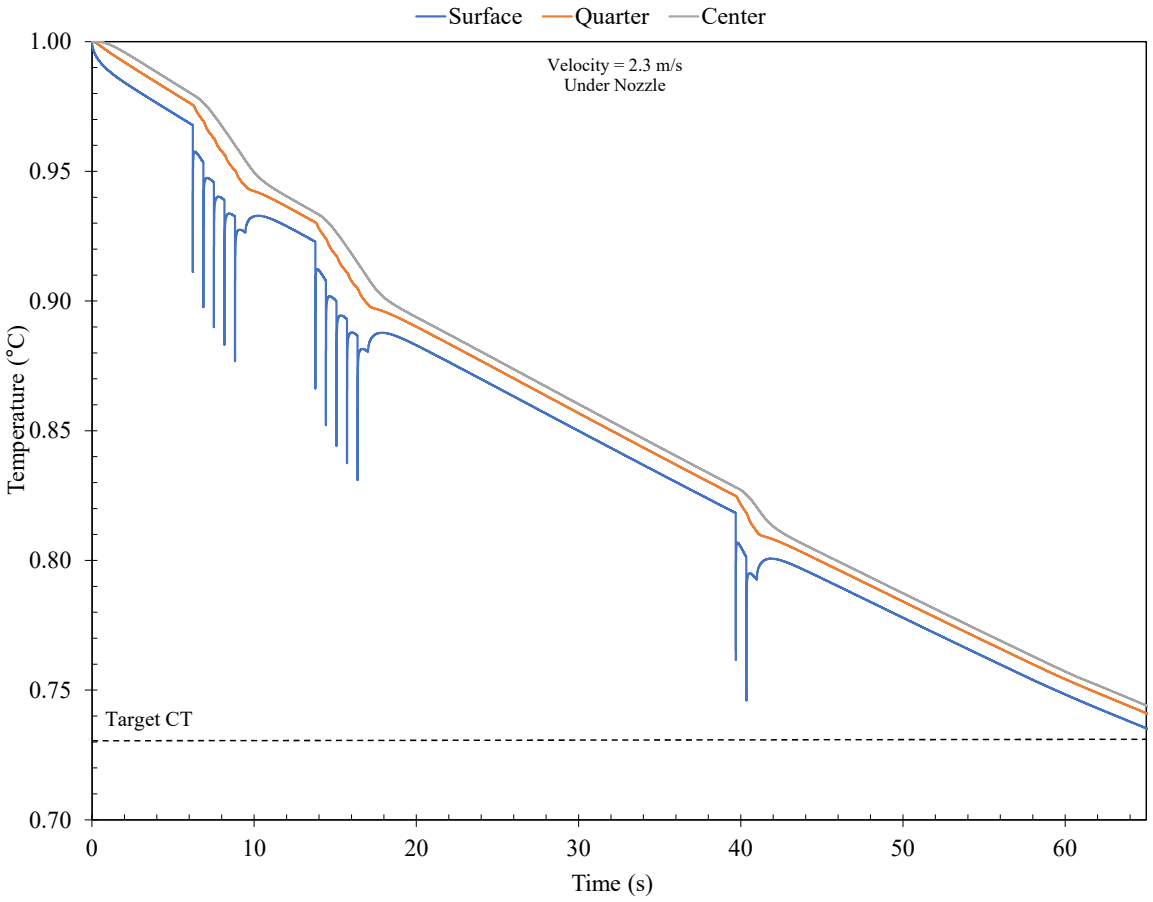

Figure C.4: 11 mm X70 simulation temperature profile under nozzle

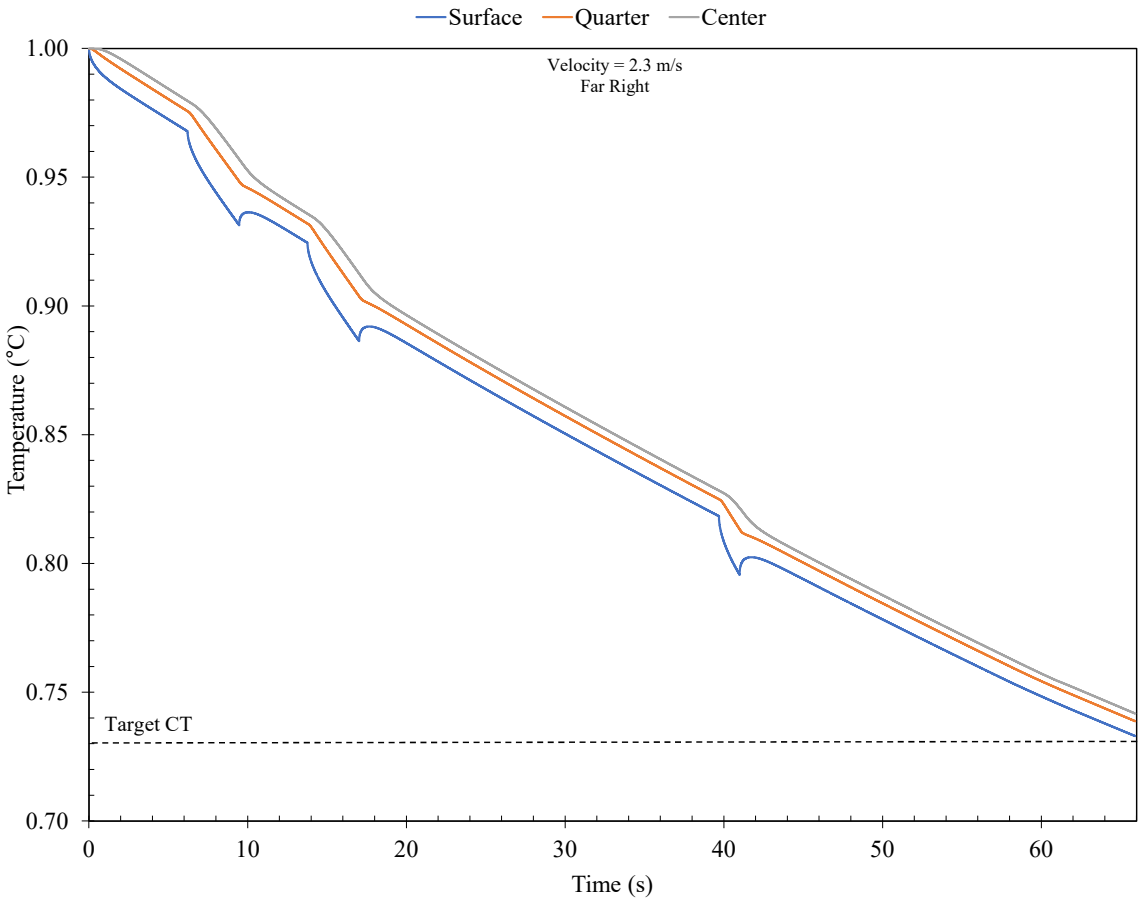

Figure C.5: 11 mm X70 simulation temperature profile half distance to next nozzle

C.1.3 12 mm Results

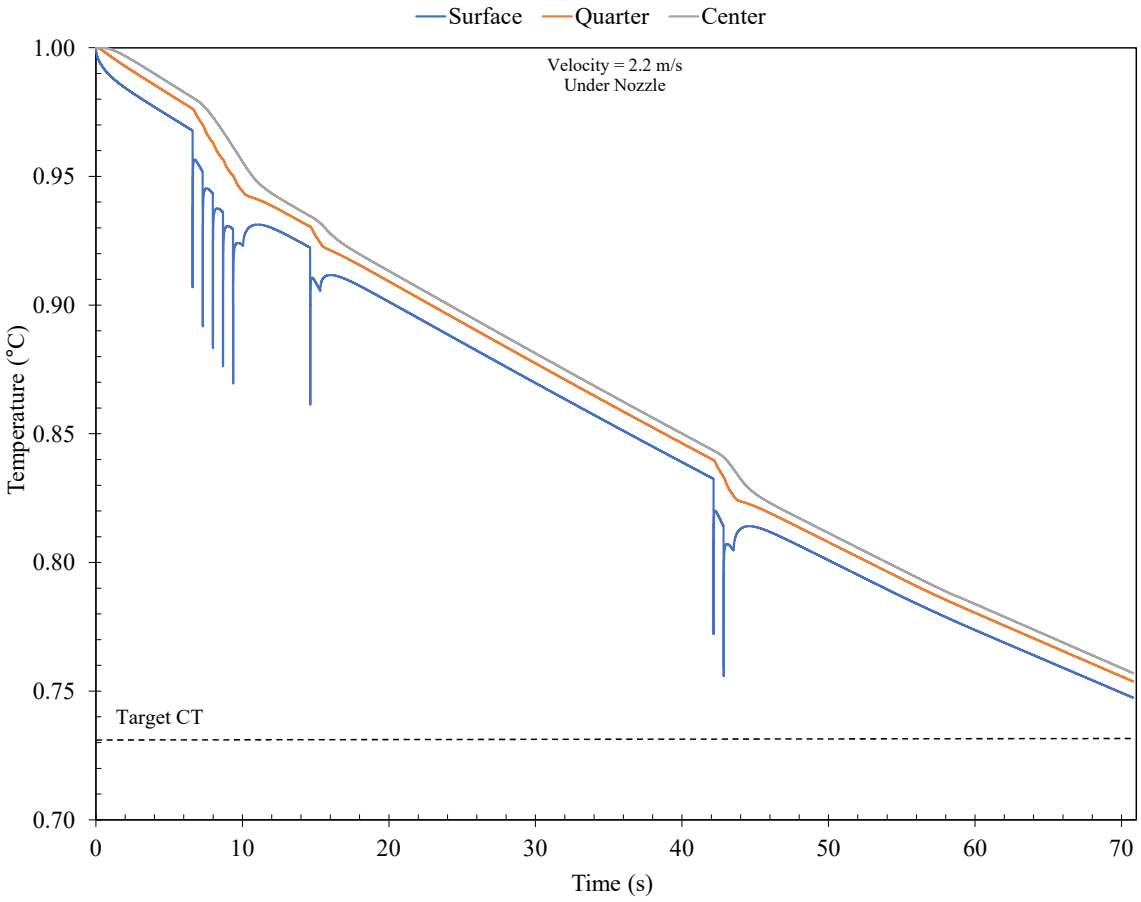

Figure C.6: 12 mm X70 simulation temperature profile under nozzle

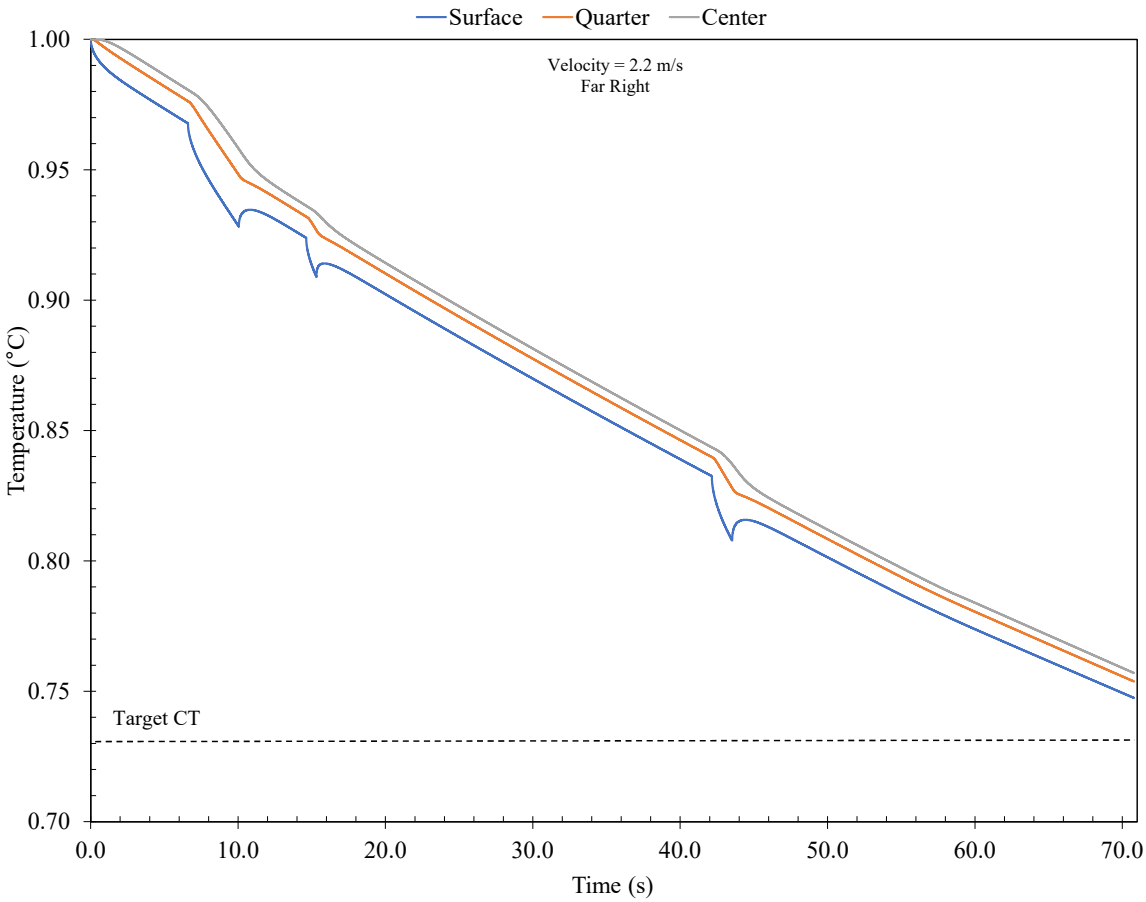

Figure C.7: 12 mm X70 simulation temperature profile half distance to next nozzle

C.2 Spray patterns

Velocity (m/s)			4.0			
FT (°C)			1			
CIT (°C) IR / FEM			0.681T / 0.691			
ROT Configuration						
	H1	H2	H3	H4	H5	H6
Bank 1	Off	On	Off	On	Off	On
Bank 2	Off	On	Off	On	Off	On
Bank 3	Off	On	Off	On	Off	On
Bank 4	Off	On	Off	On	Off	On
Bank 5	Off	On	Off	On	Off	On
Bank 6	Off	Off	Off	Off	Off	Off
Bank 7	Off	Off	Off	Off	Off	Off

Figure C.8: 8 mm X70 ROT configuration

Velocity (m/s)	2.3					
FT (°C)	1					
CIT (°C) IR / FEM	0.733T / 0.733T					
ROT Configuration						
	H1	H2	H3	H4	H5	H6
Bank 1	Off	On	On	On	On	On
Bank 2	On	On	On	On	On	Off
Bank 3	Off	Off	Off	Off	Off	Off
Bank 4	Off	Off	Off	Off	Off	Off
Bank 5	Off	Off	On	On	Off	Off
Bank 6	Off	Off	Off	Off	Off	Off
Bank 7	Off	Off	Off	Off	Off	Off

Figure C.9: 11 mm X70 ROT configuration

Velocity (m/s)			2.2			
FT (°C)			1			
CIT (°C) IR / FEM			0.760T / 0.726T			
ROT Configuration						
	H1	H2	H3	H4	H5	H6
Bank 1	Off	On	On	On	On	On
Bank 2	On	Off	Off	Off	Off	Off
Bank 3	Off	Off	Off	Off	Off	Off
Bank 4	Off	Off	Off	Off	Off	Off
Bank 5	Off	Off	On	On	Off	Off
Bank 6	Off	Off	Off	Off	Off	Off
Bank 7	Off	Off	Off	Off	Off	Off

Figure C.10: 12 mm X70 ROT configuration

Velocity (m/s)			2.00			
FT (°C)			1			
CIT (°C) IR / FEM			0.635T / 0.662T			
ROT Configuration						
	H1	H2	H3	H4	H5	H6
Bank 1	Off	Off	Off	Off	Off	Off
Bank 2	On	On	On	On	On	On
Bank 3	On	On	On	Off	Off	Off
Bank 4	Off	Off	Off	Off	Off	Off
Bank 5	Off	Off	On	Off	On	Off
Bank 6	Off	Off	Off	Off	Off	Off
Bank 7	Off	Off	Off	Off	Off	Off

Figure C.11: 15 mm X70 ROT configuration

Velocity (m/s)			2.00			
FT (°C)			1			
ROT Configuration						
	H1	H2	H3	H4	H5	H6
Bank 1	Off	Off	Off	Off	Off	Off
Bank 2	On	On	On	On	On	On
Bank 3	Off	Off	Off	Off	Off	Off
Bank 4	On	On	On	On	On	On
Bank 5	Off	Off	Off	Off	Off	Off
Bank 6	On	On	On	On	On	On
Bank 7	Off	Off	Off	Off	Off	Off

Figure C.12: 15 mm X70 alternating banks ROT configuration

Velocity (m/s)			2.00			
FT (°C)			1			
ROT Configuration						
	H1	H2	H3	H4	H5	H6
Bank 1	On	On	On	On	On	On
Bank 2	On	On	On	On	On	On
Bank 3	On	On	On	On	On	On
Bank 4	On	On	On	On	On	On
Bank 5	On	On	On	On	On	On
Bank 6	On	On	On	On	On	On
Bank 7	On	On	On	On	On	On

Figure C.13: 15 mm X70 all banks ROT configuration

Velocity (m/s)				2.00		
FT (°C)				1		
ROT Configuration						
	H1	H2	H3	H4	H5	H6
Bank 1	On	On	On	On	On	On
Bank 2	On	On	On	On	On	On
Bank 3	On	On	On	On	On	On
Bank 4	Off	Off	Off	Off	Off	Off
Bank 5	Off	Off	Off	Off	Off	Off
Bank 6	Off	Off	Off	Off	Off	Off
Bank 7	Off	Off	Off	Off	Off	Off

Figure C.14: 15 mm X70 early cooling ROT configuration

Velocity (m/s)				2.00		
FT (°C)				1		
ROT Configuration						
	H1	H2	H3	H4	H5	H6
Bank 1	Off	Off	Off	Off	Off	Off
Bank 2	Off	Off	Off	Off	Off	Off
Bank 3	Off	Off	Off	Off	Off	Off
Bank 4	Off	Off	Off	Off	Off	Off
Bank 5	On	On	On	On	On	On
Bank 6	On	On	On	On	On	On
Bank 7	On	On	On	On	On	On

Figure C.15: 15 mm X70 late cooling ROT configuration

C.3 IR Calibration and Validation

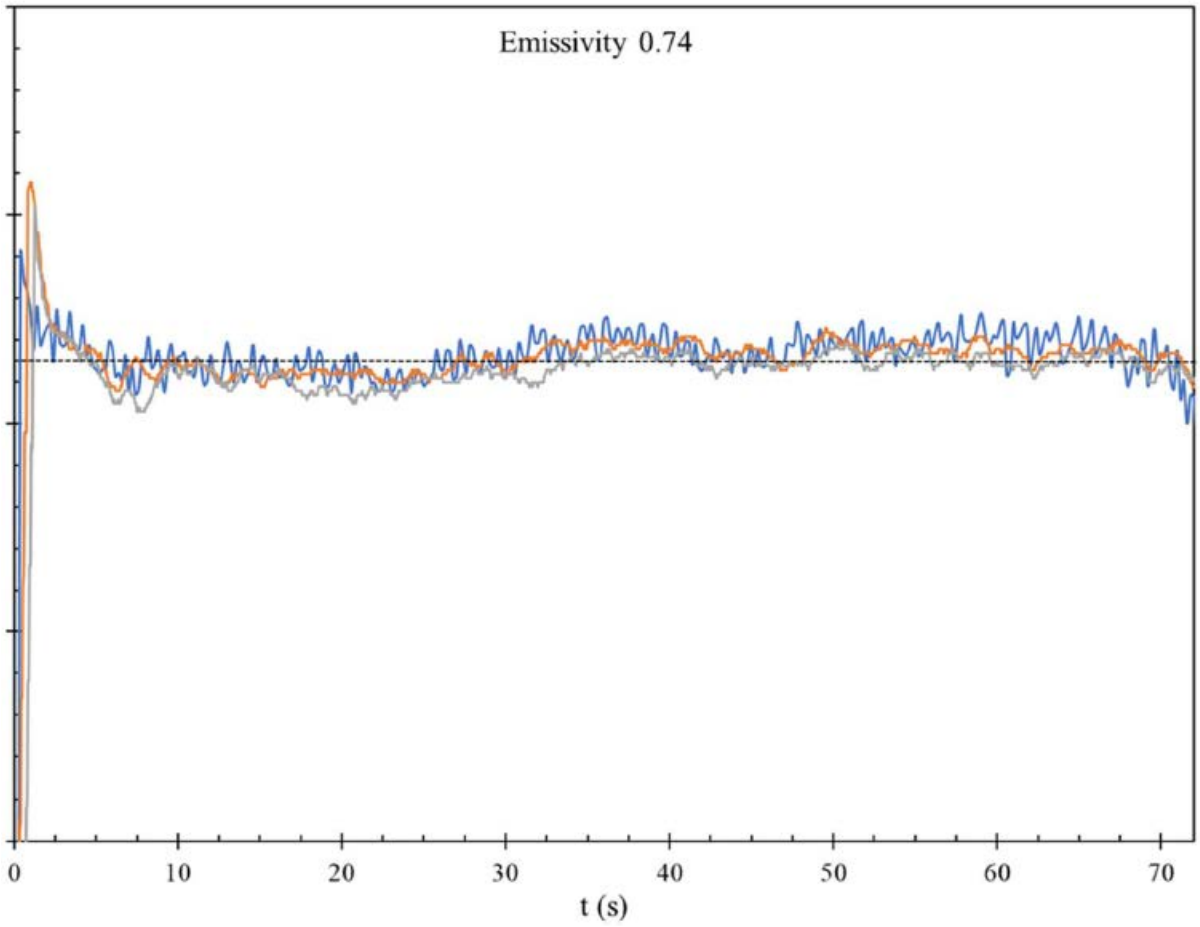

Figure C.16: Calibrated 8 mm IR data using emissivity of 0.74

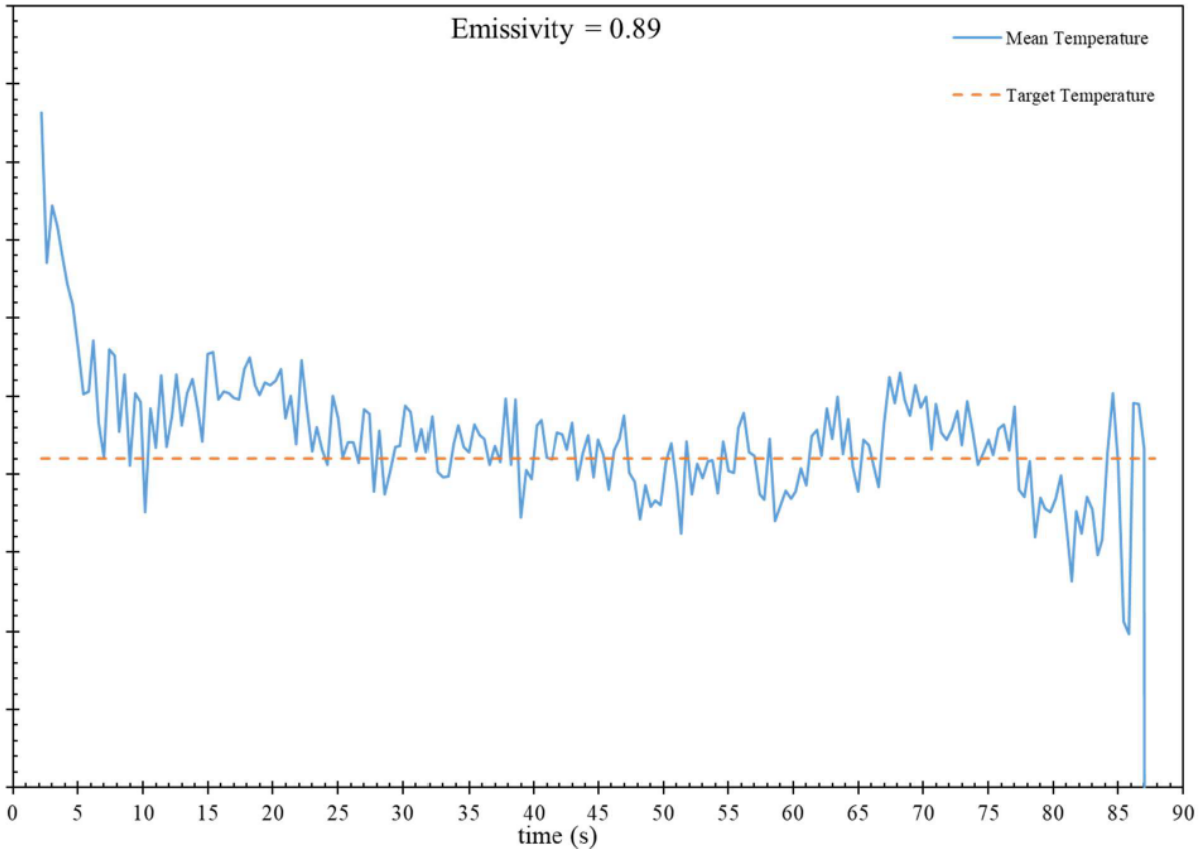

Figure C.17: Calibrated 11 mm IR data using emissivity of 0.89

Appendix D. Oxides

Appendix D covers the oxide properties used for modelling. All values were previously gathered by Prescott et al [116].

D.1 Oxide Properties

Table D.5: Density of various oxides $\frac{kg}{m^3}$

Wustite	Hematite	Magnetite
5700	5260	5046

Table D.6: Specific thermal conductivity of various oxides ($\frac{W}{m*K}$)

Temperature (℃)	Wustite	Hematite	Magnetite
273	5.6	19.9	21.6
323	5.3	16.8	18.3
373	5.0	14.5	15.8
423	4.7	12.8	14.0
473	4.5	11.5	12.5
523	4.2	10.4	11.3
573	4.0	9.5	10.3
623	3.9	8.7	9.5
673	3.7	8.1	8.8
723	3.5	7.5	8.2
773	3.4	7.0	7.6
823	3.3	6.6	7.2
873	3.3	6.2	6.8
923	3.4	5.9	6.5
973	3.4	5.8	6.5
1023	3.5	5.6	6.5
1073	3.6	5.5	6.5

Table D.7: Specific heat capacity of various oxides ($\frac{J}{kg*K}$)

Temperature (°C)	Wustite	Hematite	Magnetite
273	686	944	993
323	707	944	1012
373	723	944	1026
423	736	944	1037
473	746	944	1046
523	756	944	1054
573	764	944	1062
623	772	944	1069
673	780	944	1075
723	787	944	1082
773	794	944	1088
823	801	944	1094
873	808	944	1100
923	814	944	868
973	821	944	868
1023	827	944	868
1073	834	944	868

Appendix E. Curve Fitting

Appendix E contains all the dilatometer data fit to a single set of constants

E.1 Curve Fitting of Dilatometer Curves

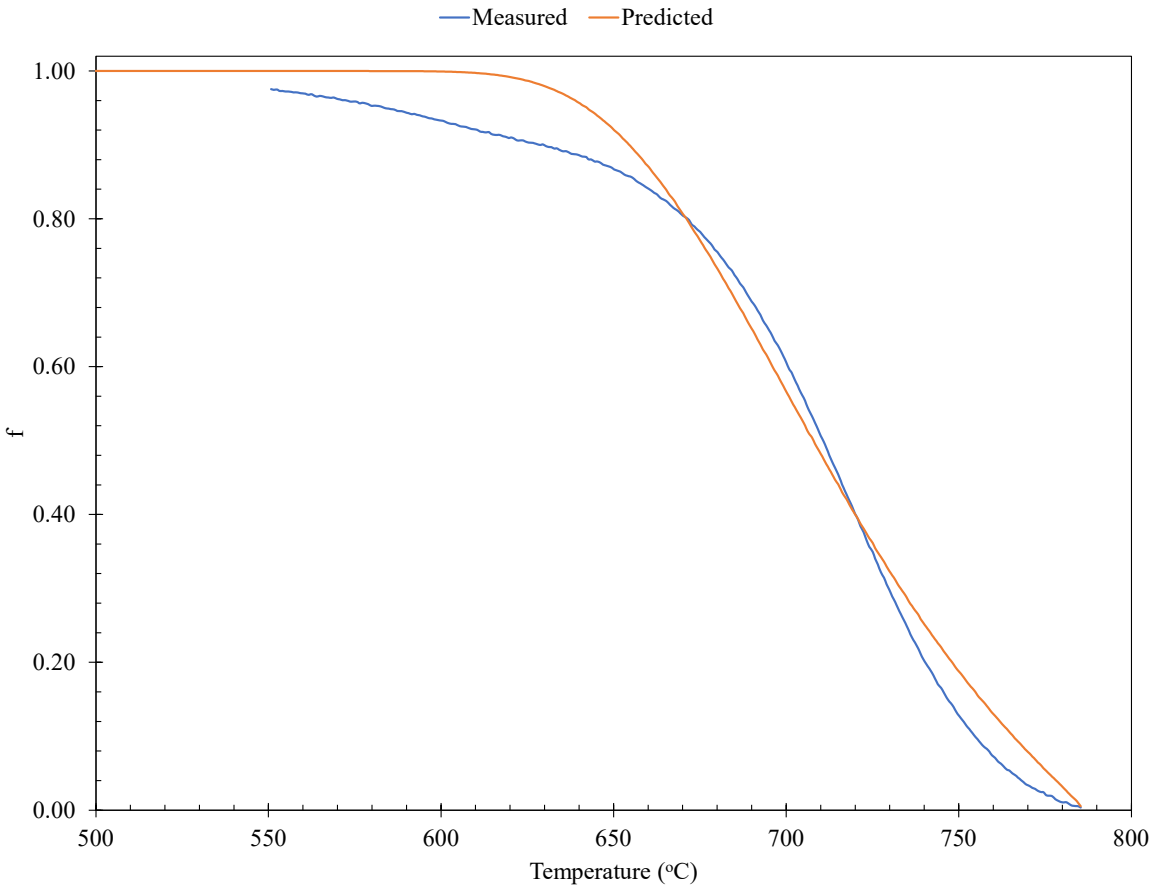

Figure E.1: 1 ℃/s dilatometer data fit to a single set of constants

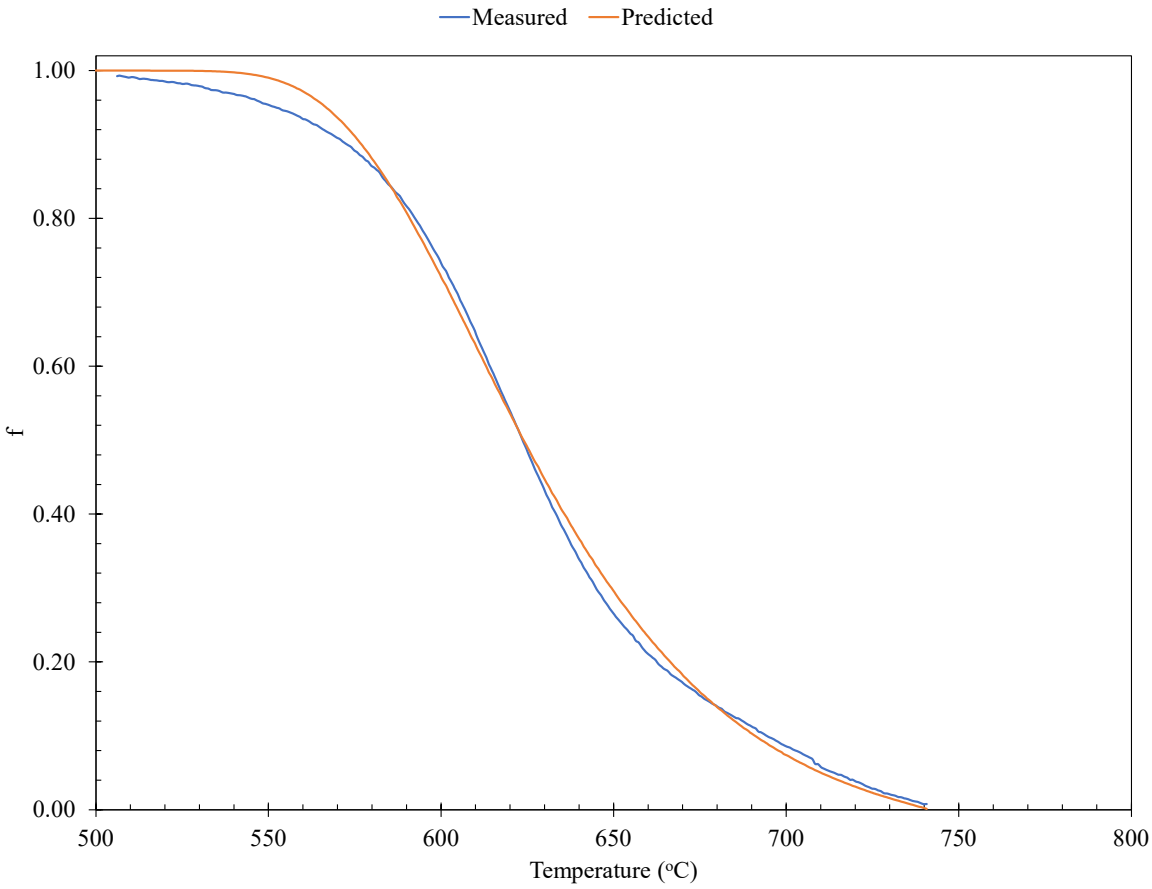

Figure E.2: 5 ℃/s dilatometer data fit to a single set of constants

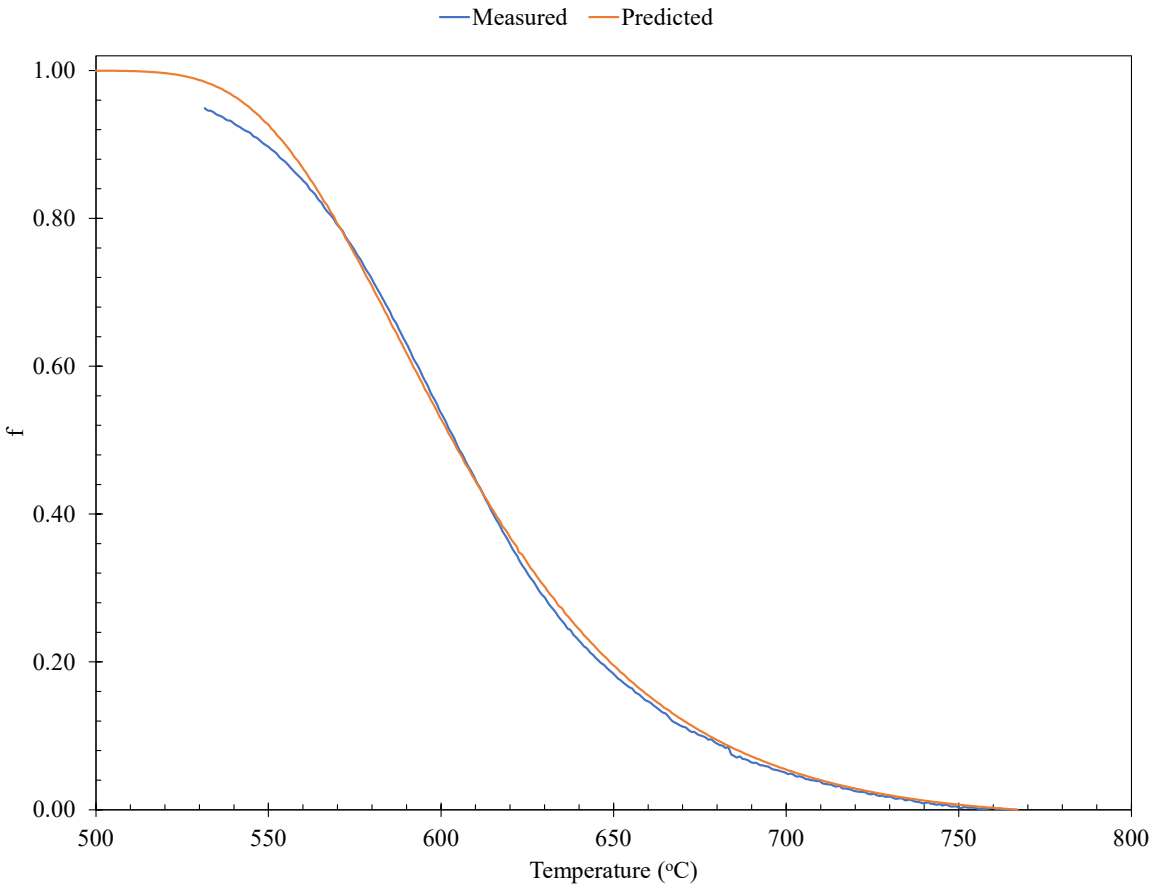

Figure E.3: 15 ℃/s dilatometer data fit to a single set of constants

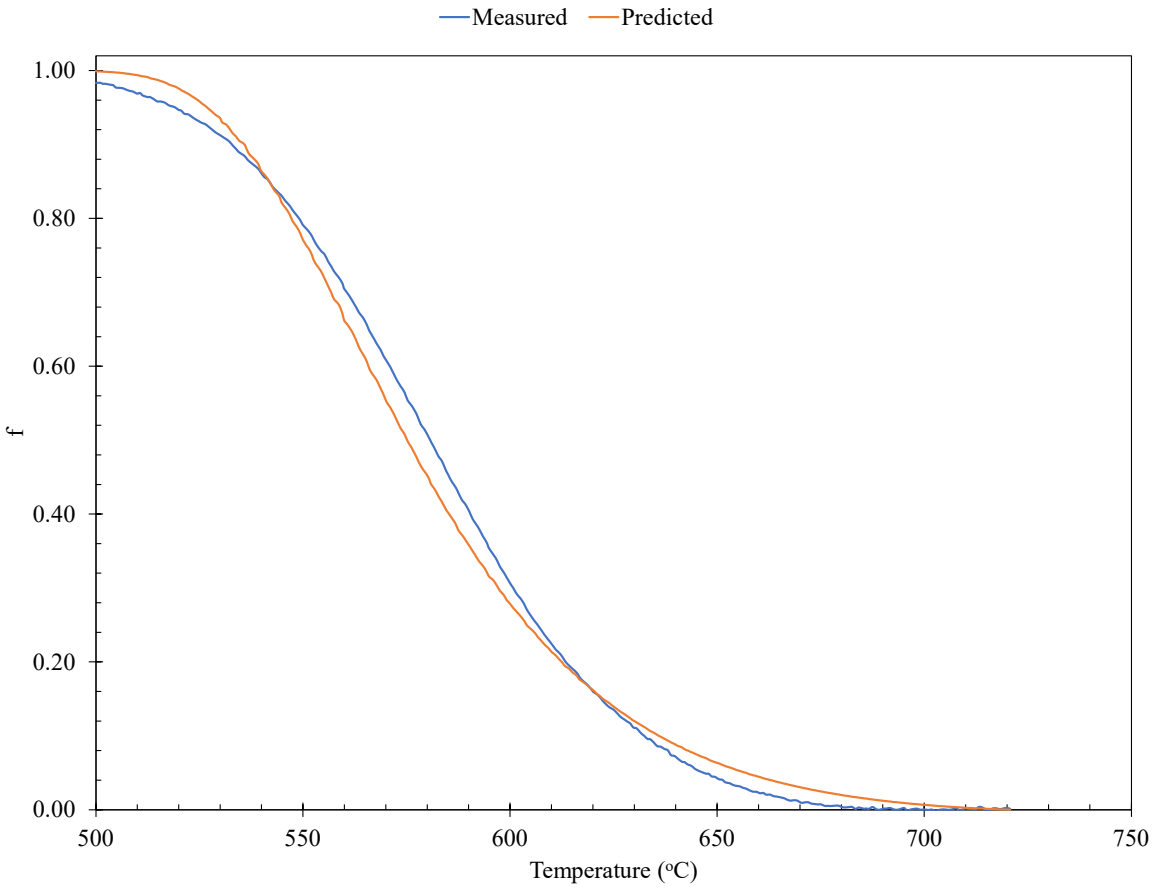

Figure E.4: 22 ℃/s dilatometer data fit to a single set of constants

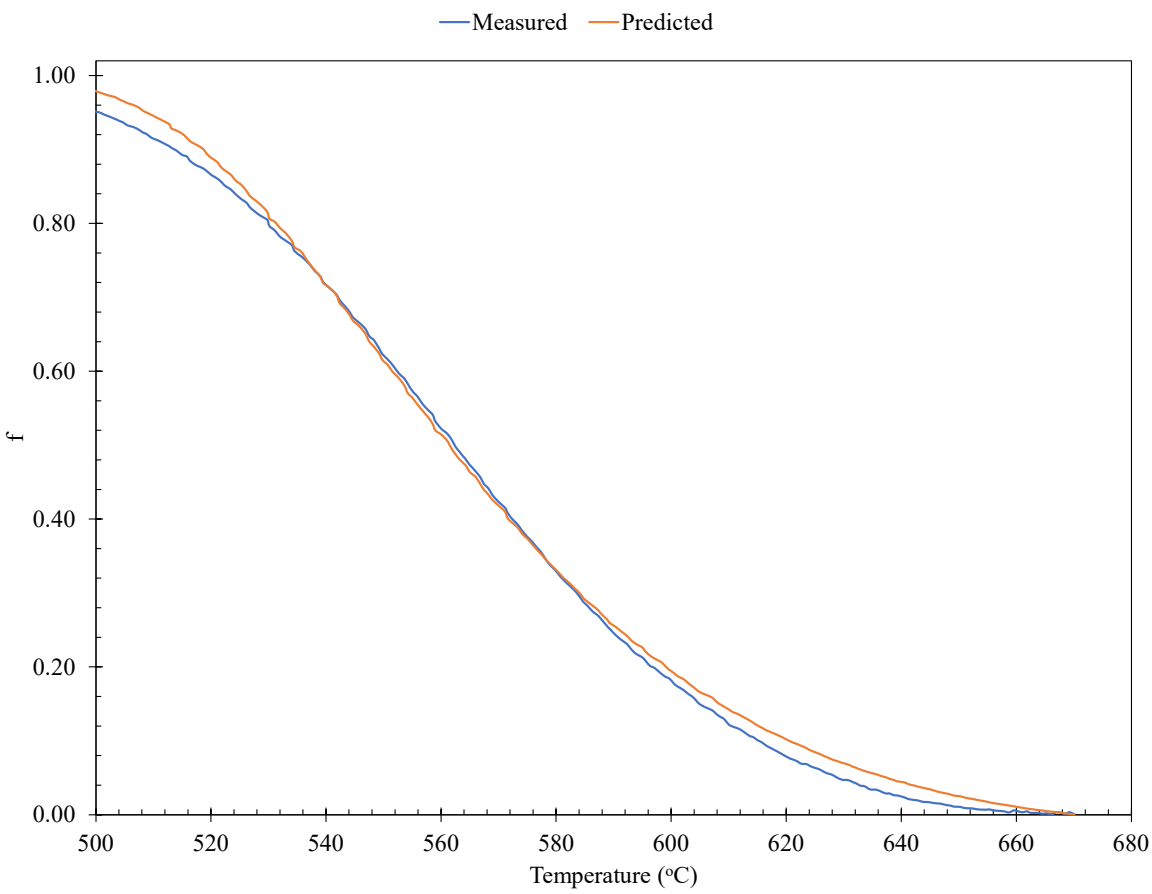

Figure E.5: 30 ℃/s dilatometer data fit to a single set of constants

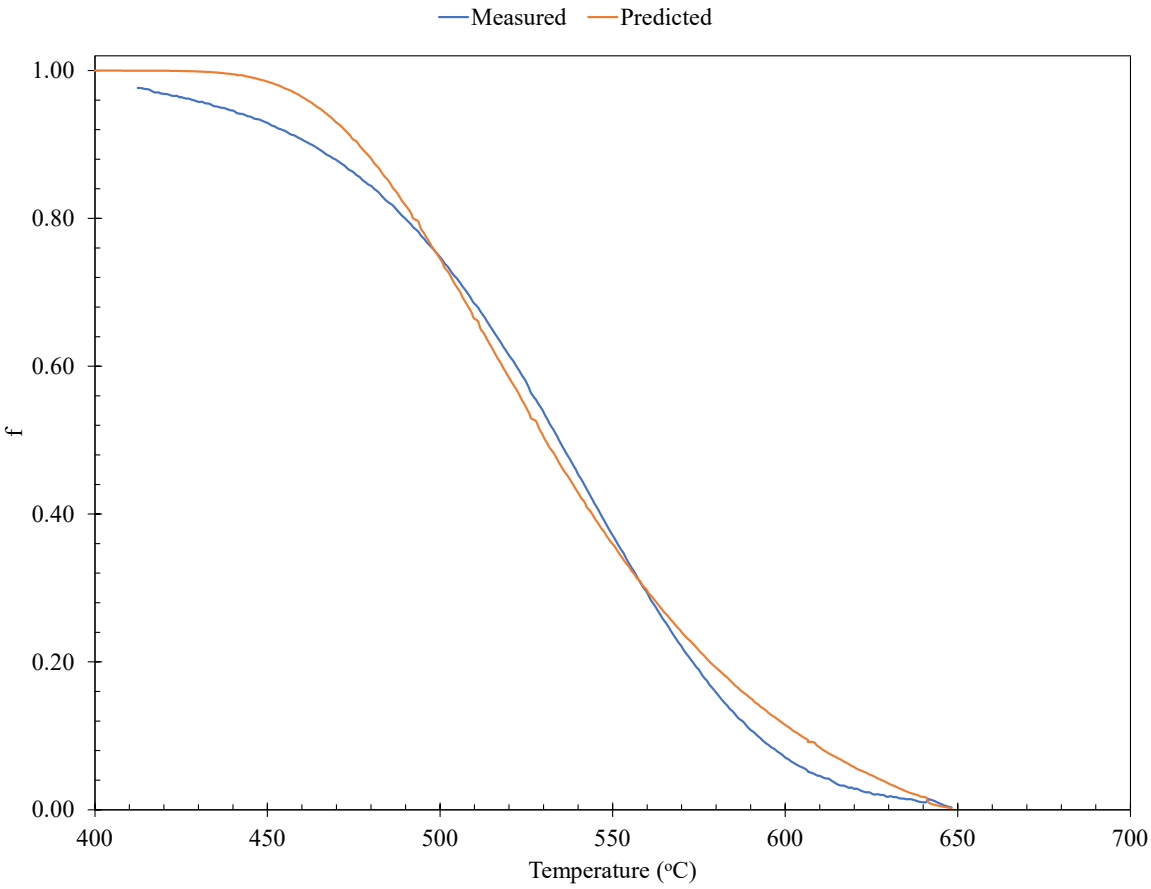

Figure E.6: 50 ℃/s dilatometer data fit to a single set of constants

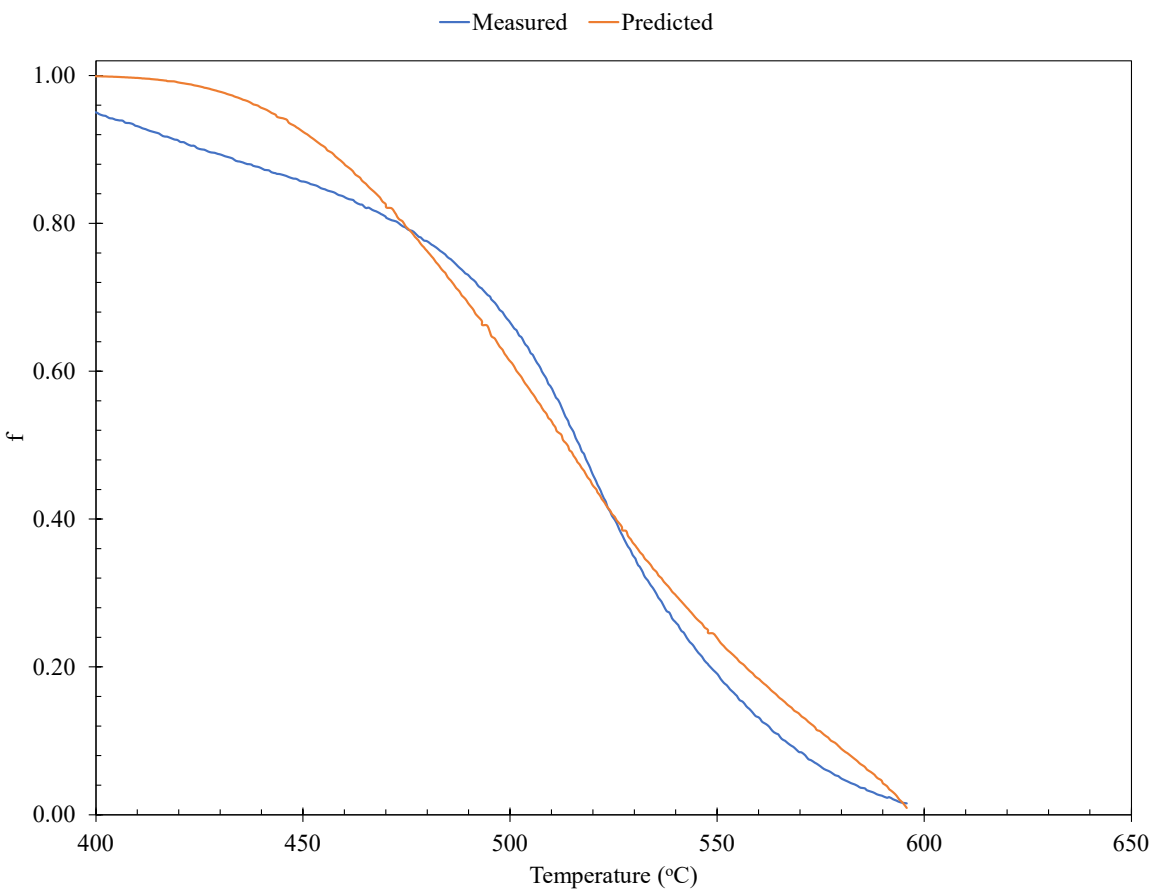

Figure E.7: 80 ℃/s dilatometer data fit to a single set of constants

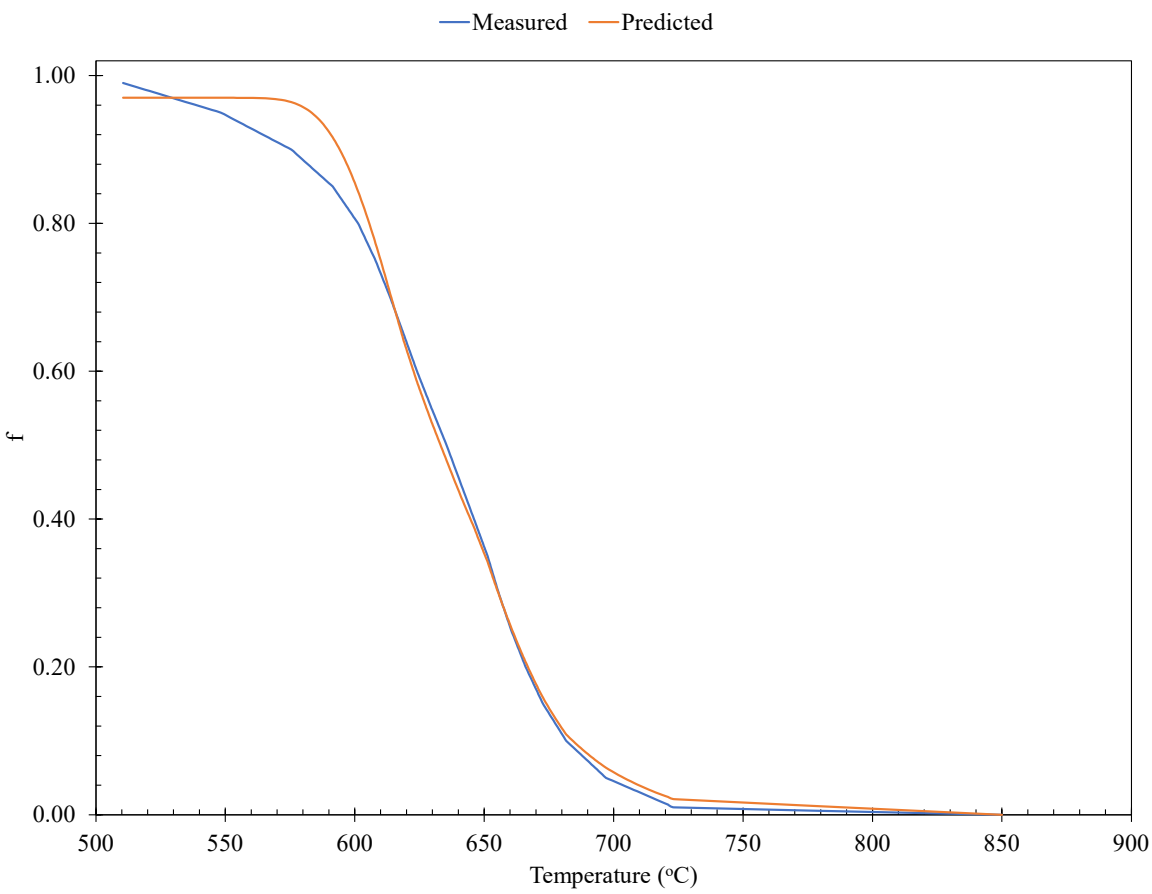

Figure E.8: 120 ℃/s dilatometer data fit to a single set of constants